TECHNISCHE UNIVERSITÄT MÜNCHEN

Experimentelle und numerische Studie zur Bewehrungskorrosion in gerissenem Beton

Wei Tian

2013

TECHNISCHE UNIVERSITÄT MÜNCHEN

Lehrstuhl für Baustoffkunde und Werkstoffprüfung

Centrum Baustoffe und Materialprüfung

Experimentelle und numerische Studie zur Bewehrungskorrosion in gerissenem Beton

Wei Tian

Vollständiger Abdruck der von der Ingenieurfakultät Bau Geo Umwelt der Technischen Universität München zur Erlangung des akademischen Grades eines

Doktor - Ingenieurs (Dr.-Ing.)

genehmigten Dissertation.

Vorsitzender:	Univ.-Prof. Dr.-Ing. Detlef Heinz
Prüfer der Dissertation:	1. Univ.-Prof. Dr.-Ing. Dr.-Ing. E.h. Peter Schießl, i.R.
	2. Univ.-Prof. Dr.-Ing. Christoph Gehlen
	3. Univ.-Prof. Dr.-Ing. Michael Raupach (Rheinisch-Westfälische Technische Hochschule Aachen)

Die Dissertation wurde am 04.10.2013 bei der Technischen Universität München eingereicht und durch die Ingenieur Fakultät Bau Geo Umwelt am 26.02.2014 angenommen.

TECHNICAL UNIVERSITY OF MUNICH

Faculty of Civil, Geo and Environmental Engineering

Centre for Building Materials

Experimental and Numerical Study on Reinforcement Corrosion in Cracked Concrete

Wei Tian

Complete copy of the dissertation approved by responsible Faculty of Civil, Geo and Environmental Engineering of the Technical University of Munich in partial fulfilment of the requirements for the degree of

Doktor - Ingenieurs (Dr.-Ing.)

Chair:	Univ.-Prof. Dr.-Ing. Detlef Heinz
Dissertation Examiners:	1. Univ.-Prof. Dr.-Ing. Dr.-Ing. E.h. Peter Schießl, i.R.
	2. Univ.-Prof. Dr.-Ing. Christoph Gehlen
	3. Univ.-Prof. Dr.-Ing. Michael Raupach (Rheinisch-Westfälische Technische Hochschule Aachen)

The dissertation was submitted to the Technical University of Munich on 04.10.2013 and accepted by the responsible Faculty of Civil, Geo and Environmental Engineering on 26.02.2014

Abstract

Concrete is the most commonly used building material, however, is not always crack free. When cracks occur, a preferable path for corrosion promoting substances (CO_2, Cl^- ions, etc.) is created and corrosion might take place. For uncracked concrete the corrosion mechanism is clear and corrosion model is relatively mature. However, research on reinforcement corrosion in cracked concrete is rare. The motivation of this research is to reach a better understanding of the physical mechanisms underlying the deterioration process of reinforcement in cracked concrete subjected to cyclic chloride and to propose a reliable method for estimating these processes.

Laboratory tests were carried out on central cracked concrete beams, in which corrosion systems with single anode and multiple cathodes with different cover depth were arranged. The beams are subjected to both chloride/water wetting-drying cycle and natural exposures. Results indicate that the corrosion mechanism in cracked concrete is macro-cell corrosion which is mainly under concrete resistance control. The time development of corrosion rate is characterized as a three-phase process: the ascending phase, the descending phase and the equilibrium phase. The equilibrium corrosion state enables the prediction of the residual service life. An unconventional effect that corrosion intensity increased with concrete cover depth was observed in the laboratory tests. In order to confirm and explore this effect, numerical modelling on both the process of chloride/moisture penetration into cracked concrete and the simulation of corrosion state in propagation period was conducted.

The mechanisms of chloride transportation into non-saturated cracked concrete is considered as diffusion coupled with convection with flowing moisture, associated with chloride binding which is described by Freundlich and Langmuir binding isotherms. Basic equations were built based on modified Fick's second law and solved by Alternating-Direction Implicit finite difference method, with required boundary and initial conditions. To figure out the moisture evaporation rate in the crack, laboratory tests were carried out and a half logarithm relationship between the evaporation rate and exposure duration was found. Main parameters for the numerical simulation (diffusion coefficients of chloride and relative humidity, chloride binding capacity and moisture capacity) were estimated by factorial approach. The chloride/moisture penetration process was successfully simulated by the proposed model. The unconventional effect of concrete cover that observed in experimental study was well explained.

The numerical simulation of corrosion state after depassivation was carried out with a self-developed FEM program 'MCRC' (Macro-cell Corrosion of Reinforcement in Concrete). Measured polarization curves were used as boundary conditions for the numerical modelling; a three-dimensional-location-dependent resistivity field was built to describe the electrolytic properties of the cracked beam. Corrosion potential and current density of both concrete and steel were obtained. Corrosion in cracked concrete was confirmed as under concrete resistance control.

The accordance between the numerical and experimental results proved the validity of experiment results, meanwhile confirmed the efficiency of the numerical tools.

Based on the chloride/moisture penetration model and the corrosion state model, both the initiation period and propagation period could be estimated.

Keywords: macro-cell corrosion, cracked concrete, chloride penetration, numerical modelling, cover depth

Abstrakt

Beton ist der meist verwendete Baustoff, doch ist der Beton nicht immer rissfrei. Wenn Risse auftreten, können korrosionsverursachende Substanzen (CO_2, Cl^--Ionen, etc.) ungehindert zur Bewehrung gelangen und Korrosion auslösen. Für ungerissenen Beton ist der Korrosionsmechanismus weitestgehend bekannt, während für Korrosion im gerissenen Beton noch viele Fragen unbeantwortet sind. Das Ziel dieser Arbeit ist, ein besseres Verständnis für die physikalischen Mechanismen des Schädigungsprozesses Korrosion in gerissenen Beton unter zyklische Chloridbeaufschlagung zu gewinnen und eine zuverlässige Methode zur Abschätzung dieses Schädigungsprozesses zu erarbeiten.

Es wurden Laborversuche an zentral gerissenen Betonbalken durchgeführt, in denen ein Korrosionssystem mit einer einzelnen Anode und multiplen Kathoden mit unterschiedlichen Betondeckungen angeordnet waren. Die Balken wurden zyklisch mit Chloridlösung und natürlich beaufschlagt. Die Ergebnisse weisen darauf hin, dass der Korrosionsmechanismus in gerissenem Beton dem einer Makrozellkorrosion entspricht, die unter Kontrolle des Elektrolytwiderstandes des Betons liegt. Die zeitliche Entwicklung der Korrosionsrate ist durch drei Phasen charakterisiert: die Aufstiegsphase, die Abstiegsphase und die Gleichgewichtsphase. Der Gleichgewichtszustand der Korrosion ermöglicht die Vorhersage der verbleibenden Lebensdauer. Die Korrosionsintensität steigt mit größer werdender Betondeckung. Zur Untersuchung dieses unerwarteten Effektes wurden numerische Simulationen sowohl des Chlorid/Feuchtigkeitstransport in den gerissenen Beton als auch des Korrosionszustands in der Schädigungsphase durchgeführt.

Zur Simulation des Chloridtransportmechanismus in den ungesättigten Beton wurde sowohl die Diffusion gekoppelt mit der Konvektion und die Chloridbindekapazität nach Freundlich und Langmuir berücksichtigt. Die Gleichungen basieren auf dem modifizierten 2. Fick'schen Gesetz, die mit Hilfe der Finiten Differenzen Methode gelöst werden. Zur Bestimmung der Verdunstungsraten im Riss wurden Laborversuche durchgeführt, die als Ergebnis eine halblogarithmische Beziehung zwischen der Verdunstungsrate und Expositionsdauer ergaben. Die wichtigsten Parameter für die numerische Simulation (Chloriddiffusionskoeffizient, relative Luftfeuchtigkeit. Chloridbindekapazität und Feuchtekapazität) wurden durch einen Faktoransatz bestimmt. Der Chlorid/Feuchtigkeitseintrag wurde erfolgreich mit diesem Modell simuliert. Der unerwartete Effekt der Betondeckung auf die Korrosionsintensität konnte erklärt werden.

Die numerische Simulation des Korrosionszustandes nach der Depassivierung wurde mit einem selbstentwickelten FEM Programm “MCRC” (Macro-cell Corrosion of Reinforcement in Concrete) untersucht. Als Randbedingung wurden experimentell bestimmte Polarisationskurven verwendet. Zur Beschreibung der elektrolytischen Eigenschaften im gerissenen Beton wurde ein dreidimensionales ortsabhängiges Widerstandsfeld verwendet. Berechnet wurden sowohl das Korrosionspotential als auch die Korrosionsstromdichten. Durch die numerische Simulationen konnte bestätigt werden, dass die Korrosion in gerissenem Beton einer elektrolytischen Kontrolle unterliegt.

Die Übereinstimmung der numerischen und experimentellen Ergebnisse beweist die Gültigkeit der experimentellen Ergebnisse und bestätigt die Effizient der Numerik.

Basierend auf dem Model des Chlorid/Feuchtigkeitstransports und des Korrosionsmodells können die Initiierungsphase und die Schädigungsphase bestimmt werden.

Stichworte: Makrozellkorrosion, gerissener Beton, Chlorideintrag, numerische Simulation, Betondeckung

Acknowledgements

This thesis could not have been written without the continual encouragement and generous devotion of time from my academic advisors Prof. Peter Schießl and Prof. Christoph Gehlen. They provided a wealth of ideas and encouragement, and were always available to discuss this work.

I would like to thank Kai Osterminski, Stefanie von Dierfeld, Marc Zintel, and Sylvia Kessler for their hands on assistance with all aspects of the research work. Osterminski's mentorship and inquisitiveness will always be valued. In addition to the above mentioned individuals, I would also like to recognize Daniel and Carsten for their contributions to my experience in Centre for Building and Testing.

The research presented in this thesis was sponsored by the German research foundation under contract number DFG-537, which is gratefully acknowledged. The study was a part of multi-institution project under the overall direction of Prof. Schießl. In addition, I am indebted to China Scholarship Council for the financial sponsorship in the past four years.

Words are not enough to thank my family for the support they have given me during this long and sometimes difficult journey.

(Blank page)

Contents

(Blank page)

List of Figures

(Blank page)

List of Tables

(Blank page)

Notations

A- total corrosion area of a single steel bar, [mm^2]

$A_{i,j}$- real corrosion area in each grid, [mm^2]

$A_{measured\ i,j}$- measured corrosion area in each grid, [mm^2]

C_{bm} - bound chloride content at saturated monolayer adsorption.

C_i - the conductance between anode and each cathode, [$1/\Omega$]

Cl_{TH}- chloride threshold value Cl_{TH}, [% by mass of cement]

c_t - the total chloride concentration (g/g of cement), which is the summation of the free chloride concentration (c_f) and the bound chloride concentration (c_b)

C_a , C_c and C_{el} - the controlling factor of anode, cathode and electrolytic resistance respectively.

$c_b^{'}$ - bound chloride concentration in milligram of Cl per gram of C-S-H;

$c_f^{'}$ - free chloride concentration in moles per liter of pore solution, [mole/l].

D_c - chloride diffusion coefficient (cm^2/s);

D_{cl} - the effective diffusion coefficient considering linear binding of concrete, [cm^2/s]

D_h - humidity diffusion coefficient (cm^2/s). g_i - the volume fraction of aggregates of the concrete;

$D_{c,agg}$ and $D_{c,cp}$ - chloride diffusion coefficient of aggregate and cement paste respectively .

$D_{h,cp}$and $D_{h,agg}$ - the diffusion coefficient of humidity of the cement paste and aggregate respectively, in [cm^2/s].

$\frac{dc_t}{dc_f}$ - chloride binding capacity, which reflects the relationship between the bound chloride concentration and the free chloride concentration.

E - the corresponding potential on the polarization curve [mV].

E_0 - the free corrosion potential $[\mathrm{mV}]$of either anode or cathode.

$E_{0,a}$ and $E_{0,c}$ - free corrosion potential for the anodic and cathodic reaction, in [mV].

E_a and E_c - the calculated anodic and cathodic potential, in [mV].

$E_{a,N}$ and $E_{c,N}$ - the node potential, in [mV].

f_{agg} and f_{cp} - weight fraction of aggregate and cement paste;

g_i - the volume fraction of aggregates of the concrete;

h - pore relative humidity;

h_c - the critical humidity at which the diffusion coefficient drops halfway between its maximum and minimum values (h_c=0.75)

I_{equ}- equilibrium macro-cell corrosion current, in [μA]

I_a and I_c - the anodic and cathodic current, in [μA].

$I_{a,e}$ and $I_{c,e}$ - the anodic and cathodic element current, in [μA].

$I_{a,N}$ and $I_{c,N}$ - the anodic and cathodic current on nodes, in [μA].

i - the corrosion current density [mA/m^2]

i_0 - either the anodic or cathodic exchange current density, [mA/m^2].

$i_{0,a}$ and $i_{0,c}$ - Anodic and cathodic exchange current density, [mA/m^2]

$[J]$- the Jacobi matrix for integration point transferring from global coordination to local coordination.

J_x and J_y – chloride penetration flux along x and y direction respectively, in [g of chloride iron per cm^2 per day].

J_x' and J_y' - moisture flux along x and y direction [g of pore water per cm^2 per s], which are mainly induced by the moisture gradients around the point.

$k^{'}$ - adsorption constant;

k_{cl} - factor which depends on the external ionic concentration, [-]

k_x, k_y, k_z - the concrete electric conductivities along x, y, z directions.

$1/k_{in}$ - the equivalent resistance of the interface layer, which represents the anodic or cathodic polarization resistance.

n - number of intervals along longitudinal direction, [-]

P_{ave}, - the averaged l radius loss of the rebar cross section, in [μm /year]

P_i - the conductance portion of each cathode, [%]

P_{max} - maximum radius loss of the rebar cross section, in [μm /year]

Q- Accumulated macro-cell corrosion current, in [C]

R_i - the resistance between anode and each cathode, in [Ω]

r_{cl} - the binding factor, [-]

$R_{p,a}$ and $R_{p,c}$ - the anodic and cathodic polarization resistance, in[Ω].

S_i - the other parts of boundary through which the electrical current density is fixed as $\overline{i_n}$.

S_ϕ - the partial boundary with constant electrical potential, $\overline{\phi}$.

t - the thickness of the interface layer, [mm].

U_{el} - the voltage consumed by electrolytic charge transfer, in [mV].

U - activation energy.

V_{sol} - the volume of solution;

w- moisture content (g of solution/g of concrete), including both evaporable water and non-evaporable water.

$\frac{\partial w}{\partial h}$ - concrete moisture capacity.

$\left(\frac{\partial w}{\partial h}\right)_{agg}$ and $\left(\frac{\partial w}{\partial h}\right)_{cp}$ - the moisture capacity of aggregate and cement paste respectively,

w_{conc} - weight of concrete, in [g].

w_{sol} - weight of solution, in [g];

w_{C-S-H} and w_{cp} - weight of C-S-H gel and cement paste respectively, in [g];

α - the integration weighting coefficient.

α_h - the degree of hydration of the cement, [-].

β_a and β_c - anodic and cathodic Tafel slopes.

β_{C-S-H} - the weight ratio of $C-S-H$ gel to concrete [g/g].

β_{curv} - bow factor, [-]

β_{sol} - the ratio of pore solution to concrete, in liters of pore solution per gram of concrete [l/g]

ε - the specified convergence accuracy.

ρ_{es} - the concrete resistivity in saturated conditions, [Ωm]

ρ_{sol} - density of solution [g/l], which is simply taken as water density [1000g/l];

$\phi(x,y,z)$ - the electrical potential.

μ - pore solution content, i.e., mass ratio of concrete to pore solution, in (g of concrete/g of pore solution);

$\|\cdot\|$ - the 2-norm of a vector.

Chapter 1 Introduction

1.1 General

Reinforced concrete is the most widely used construction material. Yet, many of these concrete structures exhibit early deterioration caused by reinforcement corrosion. Chloride contamination is one of the major causes, especially for highway bridges, parking garages, and marine structures exposed to either de-icing salts or sea water/atmosphere. These structures are among the structures most affected by corrosion. Damages include structural distress due to either reduction of the cross-section of the reinforcing bars or loss of bond strength along the steel/concrete interface, as well as the cracking and spalling of the concrete cover due to the expansion of corrosion products accumulating around the reinforcement.

The immense costs for maintaining reinforced concrete structures and repairing damage caused by reinforcement corrosion appeal for the estimation of deterioration that structures may suffer during its service life. The durability of reinforced concrete structures is of great concern for engineers throughout planning and execution. Better understanding of the corrosion mechanism and especially the corrosion intensity can help engineers to make decisions on the type of materials used and concrete covers required to ensure the designed service life of the structures.

Previous research on corrosion of reinforcement in concrete has primarily focused on uncracked concrete. The factors influencing corrosion and the methods for determining the corrosion rate have been extensively studied [1, 2, 3, 4, 5, 6, 7, 8, 9]. Thick and dense concrete cover is considered to provide excellent protection to embedded reinforcement against corrosion by forming a passive layer. Therefore, the steel in sound reinforced concrete structures usually exhibits prolonged corrosion initiation period.

Although concrete has superior properties in load bearing capacity and durability, its tensile strength and strain capacity are modest. Therefore even small imposed tensile strain due to hygral or thermal shrinkage or by mechanical loads or a combination thereof leads to crack formation. Once a crack is formed in reinforced concrete, it provides an easy and fast access for corrosion promoting substances (chloride ions, carbon dioxide, etc.) and moisture, as well as oxygen to the steel surface[10]. When the carbonation front reaches the steel surface or the critical chloride content is exceeded, the embedded steel is depassivated.

However, contributions on the corrosion of steel embedded in cracked concrete are relatively rare.

Cracks up to a critical width are directly or indirectly allowed by most concrete structural design codes, which indicates the agreement about the possibility of crack-induced corrosion [11]. Up to the present day, researchers have questioned if the approach of corrosion control suggested and required in the existing codes are enough. To answer this question, the corrosion mechanism in cracked concrete and the relationship between the crack and corrosion rate should be clarified, factors which probably influence the corrosion process in cracked concrete should be investigated as well.

1.2 Objectives and main content of the study

In this study, reinforcement corrosion in cracked concrete is studied using both laboratory experimental tests and numerical simulation. The motivation of this dissertation is to get better understanding of the physical mechanisms underlying the corrosion process of reinforcement in cracked concrete which is subjected to cyclic chloride contamination and meanwhile, to develop effective numerical tools that could serve as a complement to engineering decisions related to durability-based design and assessment of cracked/uncracked reinforced concrete structures.

The laboratory study and numerical simulation validated each other and together integrate all of the aspects related to chloride induced corrosion of reinforcing steel, namely the time to steel depassivation, the process of active corrosion, and the damage patterns thereafter. It is an objective to formulate the numerical model upon general physical laws so it would not be limited to a specific type of concrete or environmental conditions. Although the model is intended to be as general as possible, the main content of this research focuses on reinforcement corrosion in cracked concrete subjected to cyclic chloride contamination.

The dissertation consists of six chapters. Chapter 2 outlines a literature survey of researches which relates to corrosion of reinforcement in concrete, especially in cracked concrete. The review focuses on published experimental studies and numerical models on both the initiation and propagation period of reinforcement corrosion. Therefore both chloride ingress process and active corrosion of steel reinforcement are introduced. The effects of crack on the physical process of corrosion are particularly included.

Laboratory study on reinforcement corrosion in cracked concrete is presented in Chapter 3. Experiments are carried out on central cracked concrete beams, in which corrosion systems with single anode and multiple cathodes with different cover depth are arranged. The beams are subjected to both chloride/water wetting-drying cycle and natural exposures. The effects of concrete composition, exposure conditions and member geometry are investigated. The corrosion mechanism in cracked concrete is found to be macro-cell corrosion under resistance control. The active corrosion state is characterized as 3-phase process: the ascending phase, the descending phase and the equilibrium phase.

In Chapter 4, a numerical model is developed to simulate the chloride penetration process into cracked concrete. The mechanism is diffusion coupled with convection with flowing moisture, taking into account chloride binding. Moisture evaporation rate tests are carried out to obtain the cyclic varying water level in crack and chloride concentration in crack solution. Main parameters (diffusion coefficients of chloride and relative humidity, chloride binding capacity and moisture capacity) for the numerical calculation are estimated by a factorial approach. Numerical results are compared with experimental results and found to agree with each other well.

In Chapter 5, numerical simulation of corrosion state is carried out with a self-developed FEM program 'MCRC'. Polarization curves are measured and a three-dimensional and location-dependent resistivity field is built, both of which serve as boundary conditions for the numerical modelling. The corrosion potential and current (density) at arbitrary location in the model are obtained after calculation. The controlling factor and cell constant of the corrosion cell are discussed. A parametric study is also conducted to quantify the effects of driving potential and concrete resistivity on corrosion intensity.

Finally, conclusions drawn from this research as well as recommendations for future work are given in Chapter 6.

(Blank page)

Chapter 2 Literature Review

2.1 Principles about reinforcement corrosion

2.1.1 Cause of corrosion in concrete

Nowadays, reinforced concrete is one of the most commonly used building materials due to its high strength, good durability and low cost. As a material which offers long term performance, reinforced concrete is expected to last for decades. However, concrete structures are not free from deteriorating. Their service lives could be greatly shortened by the corrosion of embedded reinforcements when the concrete cover is insufficient or poorly designed and aggressive agents are presented.

Corrosion is the result of a chemical reaction between a metal and its environment. However, experience shows that steel in good quality concrete does not corrode even if sufficient moisture and oxygen are available. This is because that concrete provides a high degree of protection for the embedded reinforcing steel against corrosion. Physically, protection is provided by the concrete cover, which acts as a barrier against the access of aggressive agents and reduces the flow of electrical currents especially when the electrolytic resistivity is high. Chemically, the high alkaline medium (12.0-13.0) within the pore structures of cement matrix contains high concentrations of soluble calcium, sodium and potassium oxides, maintaining the reinforcement in an inactive state by the formation of a layer of iron oxide (Fe_2O_3), i.e. the passive layer. The passive layer is a dense, impenetrable film, which suppresses the ion dissolution to a negligible low corrosion rate if it is fully established. It is an ideal coating since it could form automatically and will maintain and even self-repair if it is damaged as long as the environmental pH is kept above 11.5. The stability of the passive layer depends on the quality and the thickness of concrete cover. Normally the passive layer is in stable state during the whole service life of the reinforced concrete structure. However, the passivity cannot be always maintained. There are two different mechanisms which can depassivate the reinforcing steel: (1) neutralization of the Portland cement paste by atmospheric CO_2, reducing the pH to about 9 (carbonation-induced corrosion); and (2) localized breakdown of the passive layer when there is a sufficient amount of chloride ions dissolved in the pore solution in contact with the reinforcing steel (chloride-induced corrosion).

Carbonation induced depassivation

When exposed to atmosphere, especially urban or industry environments, concrete structures are subjected to the risk of carbonation. Carbon dioxide (CO_2) diffuses from the surrounding air into porous concrete and reacts with the cement paste compounds in the presence of water. Consequently the $Ca(OH)_2$ is consumed which results in an overall decrease of the pH of the concrete surrounding the steel:

$$Ca(OH)_2 + CO_2 \rightarrow CaCO_3 + H_2O \qquad (2.1)$$

The diffusivity of CO_2 depends on the pore structure of cementitious phase and the humidity inside concrete. Carbonation would not take place either when the concrete pore structures are extremely dry or saturated (diffusivity of CO_2 is about 10^4 times lower in liquid than in air). Only when the pores are partly saturated, which is normally the case in practice, carbonation proceeds rapidly.

Chloride induced depassivation

Chlorides can be introduced into the concrete either by casted in (use of sea water, contaminated aggregates) or subsequently penetrate from the environment (highway and garage which are subjected to deicing salts, coastal structures which are subjected to direct seawater or ocean atmosphere, brine tanks, aquaria, etc.).

Unlike carbonation which reduces the overall alkalinity, chloride ions act as catalyst to corrosion reaction instead of reactant. When they are present at the steel surface with a certain concentration (threshold value), they promote the breakdown of the passive film at localized sites, resulting in pitting corrosion:

$$\begin{aligned} Fe^{2+} + 2Cl^- &\rightarrow FeCl_2 \\ FeCl_2 + 2OH^- &\rightarrow Fe(OH)_2 + Cl^- \end{aligned} \qquad (2.2)$$

2.1.2 Corrosion mechanisms

Corrosion of reinforcement is associated with anodic and cathodic reactions which consist of the dissolution of iron into solution and reduction of oxygen respectively (see in Figure 2-1):

- The anodic reaction occurs at depassivated area, where iron ions dissolve into concrete pore solution, releasing electrons and becoming Fe^{2+}.

$$Fe \Leftrightarrow Fe^{2+} + 2e^- \qquad (2.3)$$

- The cathodic reaction takes place at passive area, at where the free electrons react with water and oxygen, forming hydroxyl ions.

$$O_2 + 2H_2O + 4e^- \Leftrightarrow 4OH^- \tag{2.4}$$

- The hydroxyl ions released at the cathode migrate through the electrolyte under the drive of an electric field which is created by the anode and cathode, towards the anode. Near the anode, they combine with the dissolved ferrous ions and form ferrous hydroxide $Fe(OH)_2$

$$Fe^{2+} + 2OH^- \rightarrow Fe(OH)_2 \tag{2.5}$$

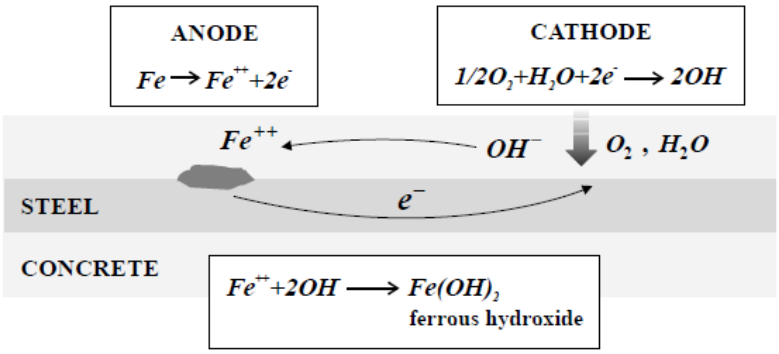

Figure 2-1: Corrosion cell in reinforced concrete

Given sufficient oxygen at the anodic sites, ferrous hydroxide can be further oxidized into other corrosion products, e.g., FeO(OH), $HFeO_2$, $Fe(OH)_3$, HFeOOH, $FeSO_3$, and especially black rust Fe_3O_4 as given in Eq.(2.6) [12]. The transformation of ferrous ions into higher oxidation states is accompanied by an increase in volume. Iron can expand as much as six times of its original volume, depending on the level of oxidation. The volume expanding leads to tensile stresses in the surrounding concrete, resulting in cracking and spalling of the cover concrete if the concrete tensile strength is exceeded.

$$\begin{aligned} &Fe^{2+} + 2(OH)^- \rightarrow Fe(OH)_2 \\ &4Fe(OH)_2 + 2H_2O + O_2 \rightarrow 4Fe(OH)_3 \\ &3Fe + 8(OH)^- \rightarrow Fe_3O_4 + 8e^- + 4H_2 \end{aligned} \tag{2.6}$$

Osterminski *et al* [13] summarized the conditions for corrosion to happen:

- "The dissolution of iron atoms must be possible – passive layer destroyed by aggressive substances like sulphates or chlorides or no passive layer existing;
- A sufficient potential difference between anode and cathode;
- The conductivity of electrons from anode to cathode;
- A supply of oxygen in the electrolyte surrounding the cathode;
- Conductivity in the electrolyte between anode and cathode."

If all these conditions are simultaneously fulfilled, corrosion may occur.

It is generally considered that two mechanisms are responsible for reinforcement corrosion in concrete structures which are distinguished by the location of anode and cathode: the micro-cell corrosion and the macro-cell corrosion, as shown in Figure 2-2, [14, 15, 16].

Micro-cell corrosion:

When the anodes and cathodes are extremely small and located closely side by side, micro-cell corrosion systems are formed. They externally appear to produce uniform removal of the steel. Micro-cell corrosion is generally induced by carbonation of the concrete and sometimes by very high and uniformly distributed chloride concentration on the steel surface [17, 18].

Macro-cell corrosion:

Macro-cell corrosion normally occurs in the case of chloride induced corrosion. Anodic and cathodic reactions have been observed to be spatially apart from each other, sometimes even up to few meters. The anodic reaction is confined to small zones where the chloride content exceeds the threshold value; the cathodic reaction takes place in areas that is adjacent to the anodes or sometimes quite far away [16]. In macro-cell corrosion mechanism, higher local corrosion rates are to be expected than in micro-cell corrosion mechanism, since the cathodic reacting area that involved could be much larger.

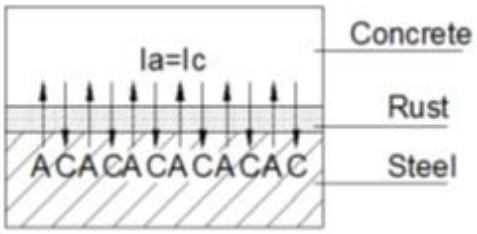

(a) Micro-cell (uniform iron removal)
A: Anode, C: Cathode

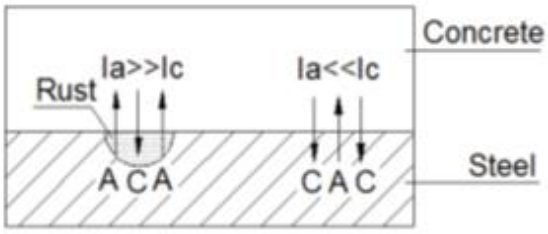

(b) Macro-cell (local iron removal, pitting)
A: Anode, C: Cathode

Figure 2-2 Two mechanisms of reinforcement corrosion

In most cases, micro-cell corrosion and macro-cell corrosion might co-exist.

Damage associated with uniform corrosion is usually in the form of cracking and spalling of the concrete cover before a significant reduction of the reinforcing bar cross-sectional area has taken place. However, when local corrosion occurs, the localized nature of the attack can result in an extreme loss of cross-sectional area of reinforcing bar before any other form of deterioration is detected, affecting significantly the tensile capacity of the corroded member. This is particularly critical for pre-stressed concrete structures.

2.1.3 Process of reinforcement corrosion

Tuutti [9] has presented a principal scheme which differentiated two distinct periods in the corrosion process of reinforcement in concrete: the initiation period, which involves the ingress of aggressive species (carbonation or chloride penetration) from environment into concrete; and the propagation period, which involves the metal dissolving which results from corrosion (see in Figure 2-3). Therefore, the service life of a structure can be determined as:

$$t_{service\ life} = t_{initiation} + t_{propagation} \tag{2.7}$$

where,

$t_{initiation}$ - the time until steel is depassivated by exceeding of the critical chloride content or carbonation of steel in concrete;

$t_{propagation}$ - the period with active reinforcement corrosion until limit states.

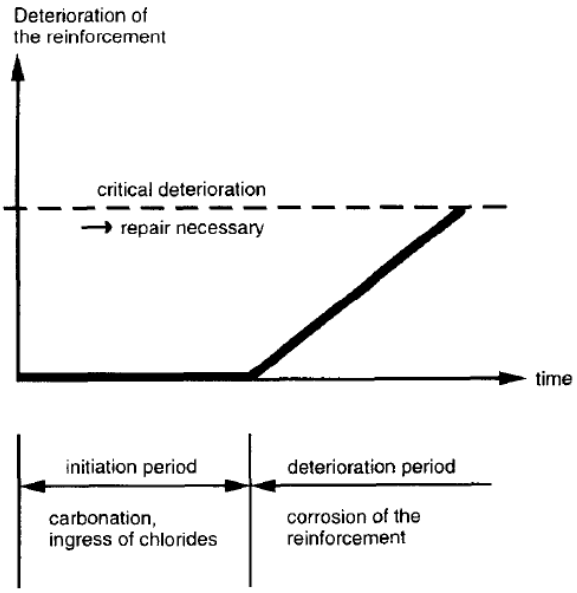

Figure 2-3: Deterioration scheme for reinforcement corrosion in concrete [9]

Based on Tuutti's model, Schießl and Osterminski [19] developed a complete picture of the entire service life design of reinforcement concrete structures, including all limit states, as shown in Figure 2-4.

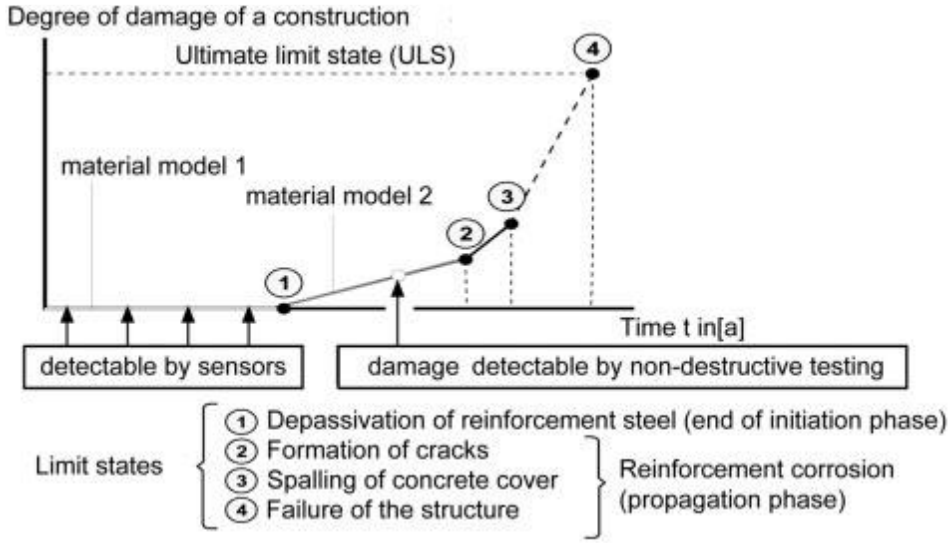

Figure 2-4: Time-dependent accumulation of corrosion induced damage and possible limit states according to [19]

The corrosion process not only lead to optically affected damage, but also structure failure. Corrosion of reinforcement may lead to a loss of the steel's cross section (mostly caused by chloride degradation) or cracking or spalling caused by a volume expansion of the corrosion products, as well as a loss of bond strength between steel and concrete. Therefore, before reaching the structure failure (limit state 4 in Figure 2-4, several other limit states may be

reached: the corrosion induced cracking (limit state 2 in Figure 2-4) and spalling of the concrete cover (limit state 3 in Figure 2-4). In some cases, reduction of steel cross section can also mean reaching the Ultimate Limit State. This is defined as the last Ultimate Limit State for the durability design [19].

Traditionally, the prediction of service life of reinforcement structures has been focused on the estimation of initiation period rather than to accurately predict the subsequent corrosion rates in propagation period [20]. However, ignoring the propagation period may lead to an underestimation of the service life, since the propagation period could add significantly to the service life. Therefore, it is important to model the corrosion process to get a better understanding of the probable time span of the propagation period.

A simplified electrical circuit model was introduced to represent the relationship between the driving voltage, the resistances of the corroding system and the electrolytic macro-cell current, [19]. As shown in Figure 2-5, anode and cathode were connected by a series of resistances: the anodic and cathodic polarization resistance and the resistance of electrolyte (in this case the concrete). According to Ohm's law, the galvanic corrosion current can be therefore obtained as the quotient of the driving potential between anode and cathode and the sum of all system resistances:

$$I_{corr} = I_{macro} + I_{micro} = \frac{\Delta E}{\frac{r_{p,a}}{A_a} + \frac{r_{p,c}}{A_c} + \rho_e \cdot k_e} + I_{micro} \tag{2.8}$$

where:

I_{corr}- corrosion current, which is the sum of macro-cell current and micro-cell current, [μA];

I_{macro}- macro-cell current between anode and cathode, in [μA];

I_{micro}- the current of self-corrosion, in [μA];

ΔE - driving potential, which is the difference between the cathodic and anodic rest potential ($\Delta E = E_{c,0} - E_{a,0}$), in [V];

$E_{0,a}$ - rest potential at the anode, in [V];

$E_{0,c}$ - rest potential at the cathode, in [V];

$r_{p,a}$ - specific anodic polarization resistance, in [Ωm];

$r_{p,c}$ - specific cathodic polarization resistance, in [Ωm];

A_a - anodically acting steel surface area, in [m^2];

A_c - cathodically acting steel surface area, in [m^2];

ρ_e - specific resistance of the electrolyte (concrete), in [Ωm];

k_e - cell constant of geometry, in [m^2/m].

The resistance for the electrons to transport through the steel is negligibly small compared to the other resistances and is consequently ignored in Eq.(2.8). Any one of these resistances can limit or control the rate of the corrosion reaction. Therefore, corrosion process in reinforcement structures could be under anodic, cathodic, ohmic or mixed control. In cement-based concrete which is lack of corrosion promoting substances and having adequate supply of oxygen, corrosion is generally under anodic control; conversely, the cathodic reaction can be restricted due to the lack of oxygen if concrete is submerged by water or soil. Corrosion in this case is therefore under cathodic control; in dry concrete with very high concrete resistivity, corrosion might be subjected to ohmic control.

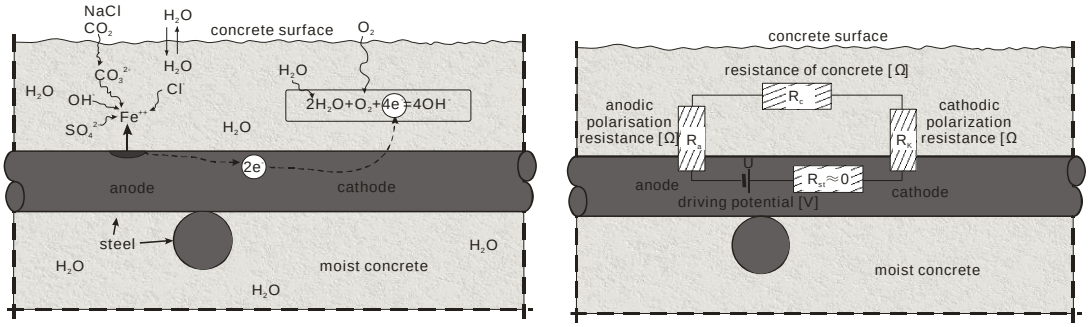

(a) (b)

Figure 2-5: (a) Electrochemical processes of the reinforcement corrosion, (b) Equivalent circuit diagram for the corrosion of steel in concrete including the model approach[13]

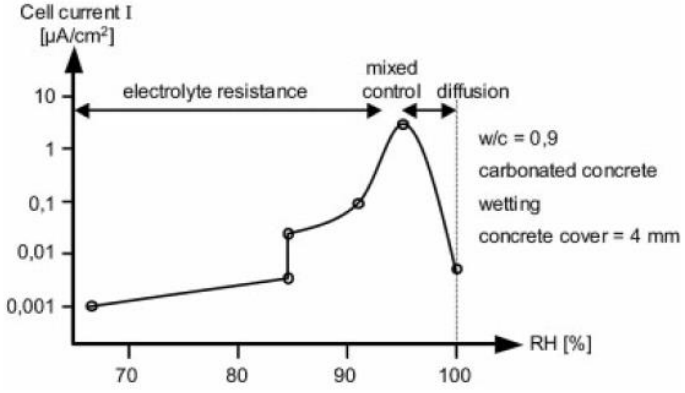

Figure 2-6: Influence of humidity on corrosion activity of reinforcement steel in carbonated concrete[9]

2.1.4 Factors that affect the corrosion rate of reinforcement in concrete

After depassivation, environmental-and-material-dependent reinforcement corrosion has to be taken into account. The prediction of the corrosion rate is a complex task when taking into account of the electrochemical nature of corrosion and the numerous parameters involved. Raupach [17] pointed out that the estimation of the macro-cell current is a challenging task due to the large amount of influencing parameters and the complex relationships among those parameters. He schematically presented the possible parameters as shown in Figure 2-7.

Plenty of contributions have been done to quantify the influence of the above mentioned factors on the corrosion rate. Actually those factors, either the concrete quality or the environmental conditions, influence the corrosion rate in the form of the electrolytic resistivity between the anode and cathode and the oxygen availability for the cathodic reaction, especially in the case of macro-cell corrosion with growing distance between anode and cathode.

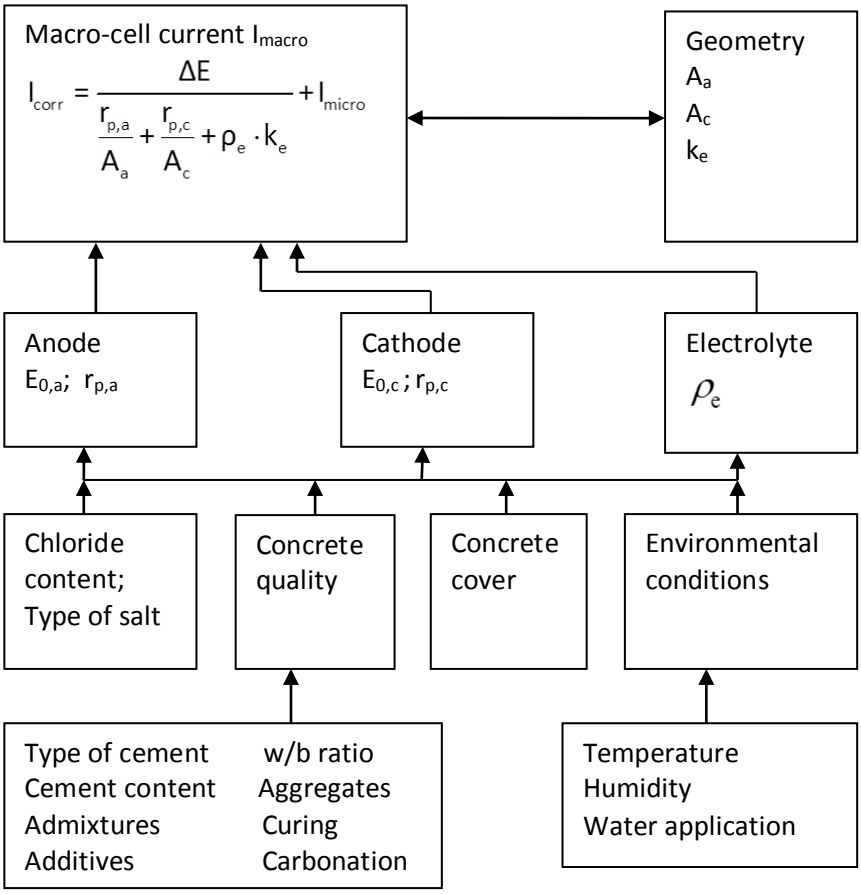

Figure 2-7: Influential factors for the corrosion rate of chloride induced macro-cells [17]

Influence of electrolytic resistivity of concrete

Corrosion can only occur when the pore solution of concrete is capable of conducting ionic current, which is carried by OH^- and F_e^{2+} ions. The resistance of concrete pore to conduct the flow of such a current is known as the electrolytic resistivity of the concrete [21, 22].

The effects of concrete resistivity on reinforcement corrosion involve in both the initiation and propagation period. For initiation period, concretes with low electrolytic resistivity are more vulnerable to chloride or carbon dioxide penetration, indicating the risk of an earlier depassivation. For propagation period, concrete resistivity directly relates to corrosion rate, especially in the case of macro-cell corrosion.

As material property, resistivity could be influenced by both microstructure properties of concrete and the environmental conditions. The magnitude of concrete resistivity varies in great range from 10^1 to 10^6 $\Omega \cdot m$, mainly depending on the factors as shown in Table 2-1.

Table 2-1: Influencing factors of concrete resistivity

Pore structure	Total porosity, pore size distribution and degree of continuity	Cement type, cement content, w/b ratio, supplementary cementitious materials, other additives, carbonation, casting quality, curing conditions, degree of hydration, etc.
Pore solution	Degree of saturation	Environmental conditions such as relative humidity, etc.
	Ionic concentration	Cement type, cement content, supplementary cementitious materials, temperature, chemical admixtures such as Cl^-, SO_4^{2-}, etc.
	Mobility of ion	Temperature, etc.

The mechanisms of those influencing factors are simply described as follow:

- Cement type: Cement type has an effect on both the pore structure and pore solution chemistry. Cements with high amounts of pozzolanic contents normally show higher resistivity than those without, e.g. Portland cement, due to a denser pore structure, [23, 24, 25].

- Cement content: Increasing the cement content leads to a decrease of resistivity at the rate of approximately 1% per 1% paste [26].

- w/c ratio: Concrete pore structure can be significantly influenced by water/cement ratio. As the w/c ratio increases, the pore structure becomes coarser and more continuous. Given

the same saturation degree, concrete with higher w/c ratio clearly delivers smaller resistivity [21, 26, 27].

- Temperature: Temperature has important effects on concrete resistivity. At higher temperatures, on one hand, more ions will dissolve into the pore solution; On the other hand, the viscosity of the pore fluid decreases, increasing the mobility of the ions. It is also found out that the temperature effect may vary with moisture content, with 3% for saturated and 5% for dry concrete for each degree K temperature change[28].

The general relationship between resistivity and temperature could be well expressed by the Arrhenius equation:

$$\rho_e(T) = \rho_0 e^{A(\frac{1}{T}-\frac{1}{T_0})} \tag{2.9}$$

where

ρ_e and ρ_0 -the resistivity at temperatures T and T_0 respectively in $[\Omega \cdot m]$;

A-the activation energy in [J].

- Moisture content: Of all the factors which have an influence on the electrical resistivity of concrete, moisture content is considered as the most significant one. When moisture content decreases, there is less pore solution to carry the current, leading to a decrease of concrete conductivity [29].

- Chloride content: Chloride admixture into concrete reduces concrete resistivity by enhancing the ion concentration. The influence of chlorides on concrete resistivity is related to the cementitious materials used in concrete. For concrete composition which is rich in C_3A, the influence of chlorides is relatively low.

- Carbonation: Carbonation affects concrete resistivity by creating a much denser pore structure.

- Curing: The effect of adequate curing is beneficial in order to create relatively more homogeneous material hence a less permeable concrete cover. Additionally, good curing ensures favourable conditions for the hydration process, which in turn increases the concrete cover quality.

Due to the electrochemical nature of the corrosion process, a relationship is expected between the concrete resistivity and the corrosion rate. Once the corrosion begins, its rate is mainly controlled by the electrolytic resistivity of concrete [1, 20, 30]. Electrolytic resistivity can be used as an indirect measure of the ability of concrete to resist corrosion. Based on an extensive research performed on mortar specimens which subjected to various exposure conditions, Alonso, *et al* [1] reported the great influence of concrete resistivity on the corrosion process. Corrosion current density i_{corr} is found to be inversely proportional to the concrete resistivity ρ_{con}. The relationship could be empirically expressed as:

$$i_{corr} = \frac{K}{\rho_{con}} \tag{2.10}$$

K- constant regression coefficient, [V/m], ≈ 1[V/m] [31, 32]

ρ_{con} - concrete resistivity, [$\Omega \cdot m$]

Page and Cunningham [30] reached the similar conclusion in their research, as shown in Figure 2-8.

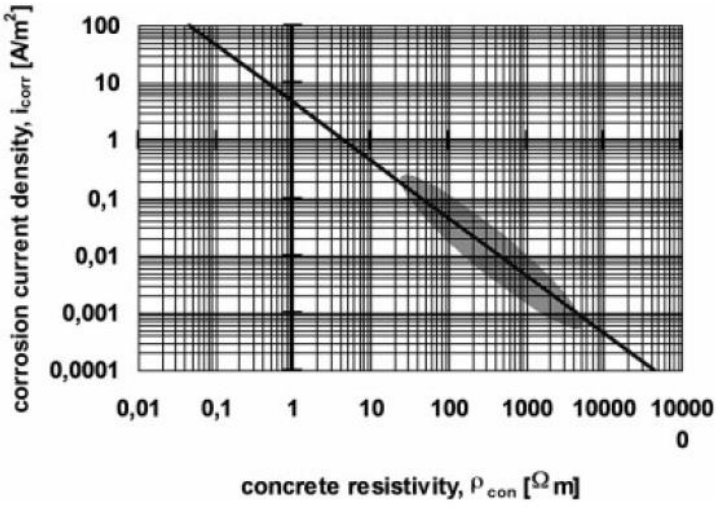

Figure 2-8: Dependence of corrosion current density i_{corr} on mortar resistivity for different types of cement and various exposure conditions[30].

However the above relationship is based on empirical results which is lack of sound theoretical basis. An empirical model has been introduced by Gulikers [20] to describe the relationship between concrete resistivity and corrosion rate in the case of carbonation induced micro-cell corrosion. An attempt was also made to provide a theoretical justification

for the empirical relationship presented by Eq.(2.11). It was found that $\log(R_{con})$ and $\log(i_{corr})$ can be approximated by an almost ideal linear relationship, Figure 2-9.

$$\log(i_{corr}) = -0.8125\log(R_{con}) - 1.0057 \qquad (2.11)$$

$$R^2 = 0.9945$$

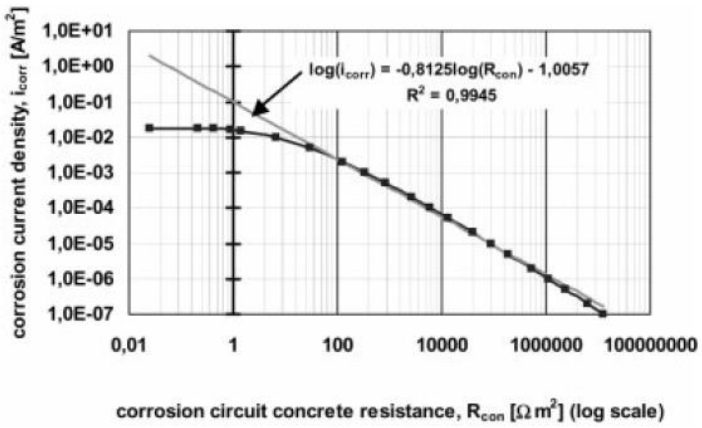

Figure 2-9: Relationship between concrete resistance R_{con} and corrosion current density i_{corr} [20]

The level of concrete resistivity needed to prevent corrosion has been studied in various researches. Whiting, *et al* [22] reported that moist concrete with resistivity of less than 50 $\Omega \cdot m$ could support very rapid corrosion; if the concrete in dry environment had a resistance as high as $200\,\Omega \cdot m$, ionic flow could not be supported. Suggested values are shown in Table 2-2.

Table 2-2: Relationship between concrete resistivity and corrosion rate[22]

Resistivity, [$\Omega \cdot m$]	Corrosion intensity
<50	Very high
50-100	High
100-200	Moderate to low
>200	Low

Influence of Oxygen availability

Oxygen availability is another factor which affects the corrosion intensity. It depends on several factors:

- **The cover concrete**

Uncracked concrete cover with enough thickness and good quality prolongs the oxygen penetration process and delays the oxygen from reaching the steel surface.

- **Permeability of concrete**

High quality concrete with low w/c ratio demonstrates finer microstructure which leads to low permeability and hence restricts the oxygen supply.

The effect of w/c ratio and cover thickness on the diffusion rate in water saturated concrete is shown in Figure 2-10. It can be seen that with given cover thickness, a decrease in w/c ratio of concrete will reduce the oxygen supply.

- **Moisture content or degree of water saturation of the concrete**

Oxygen could only be involved in cathodic reaction in dissolved state. The diffusion rate of oxygen through saturated concrete pores is extremely slow. According to Neville [25] the oxygen diffusion rate into liquid is 10^4 to 10^5 times lower than that into air. Tuutti [9] reported that supply of oxygen in OPC concrete was reduced when the degree of water saturation increased.

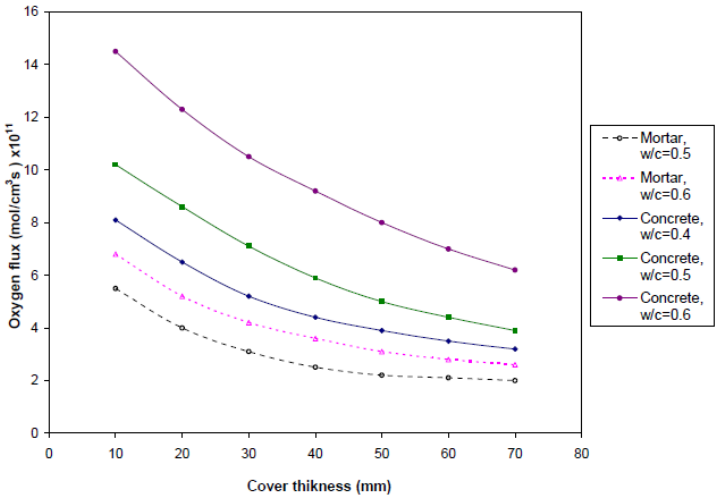

Figure 2-10: Effect of cover thickness and w/c ratio on oxygen flux [33]

In order to take into account of the various influences and to give proper prediction of the corrosion rate, a useful and practical model is quite essential. In recent years, probabilistic design models have been developed to simulate the initiation period, i.e. the carbonation process and the chloride penetration process into uncracked concrete. These models have already been successfully used in practice [34]. However, practical design models are quite rare for the propagation period. In order to quantify all material and environmental

influences on reinforcement corrosion and to develop a model of durability design, a probabilistic model was developed by a German research group [19]. All the influencing factors of the reinforcement corrosion were quantified probabilistically and integrated into the safety concept. The construction resistances as well as the stresses were quantified statistically. Therefore, "combine with the existing probabilistic design models for the initiation phase of uncracked concrete, a complete picture of the corrosion process can be given and an entire service life design of durability of reinforced concrete structures – including all limit states – was for the first time be possible" [19].

2.2 Corrosion in cracked concrete due to chloride degradation

The risk of corrosion of reinforcement should be minimal in a well-designed reinforced concrete structure which has a sufficient depth of good quality concrete cover and has been properly placed and compacted. Concrete cover provides both chemical and physical protection to embedded rebar thus the penetration of corrosive agents into concrete is controlled primarily by its cover, specifically its depth and properties. However, the presence of cover cracking would introduce an easier path for the corrosive agents to penetrate in and consequently leads to depassivation.

The mechanism and process of corrosion in uncracked concrete has been extensively studied during the last several decades. However, research on cracked concrete is rare. The influence of cracks on corrosion must be considered realistically for more reliable design of concrete structures. Otherwise, the performance and service life of concrete structures may be overestimated, leading to an unexpected premature failure of structures [35].

2.2.1 Cracks in concrete

Principal causes of cracking in concrete structures

In concrete structures, microcracks and macrocracks inevitably exist due to its unstable condition as a composite material or develop during its exposure to harsh environments or loads.

Cracks are classified into two types: microcracks and macrocracks, which are distinguished by either their morphology or means of formation. A commonly accepted definition is that cracks with a width less than $50\mu m$ [36, 37] or $100\mu m$ [38] is considered as microcrack, whereas cracks wider than this range are defined as macrocracks.

Cracks are often introduced in concrete structures due to the following specific causes:

Shrinkage: Shrinkage is the contraction of cement paste or concrete due to one of five causes: plastic shrinkage, drying shrinkage, autogenous shrinkage, thermal shrinkage and carbonation shrinkage [39], among which drying shrinkage is the most concerned one. Cracking due to drying shrinkage can never be eliminated in most structures. The main factors controlling drying shrinkage include relative humidity, cement/aggregate type and content, as well as w/c ratio. The rate of moisture loss and shrinkage of a given concrete is affected by the size of the concrete member, environmental conditions, distance from the exposed surface, and exposure time.

Chemical reactions: Chemical reactions, such as alkali-silica, alkali-carbonate and carbonation reactions might lead to the cracking of concrete. Normally, aggregates in concrete are stable during the whole exposure period until affected by deleterious reactions such as alkali-silica and alkali carbonate reactions. In alkali-silica reactions, the acid components of aggregates (silica and siliceous materials) react with the alkaline pore solution and produce the alkali- silicate gel which is expansive in volume, leading to cracking of the concrete. The resultants in the alkali-carbonate reaction (brucite $Mg(OH)_2$), calcium carbonate ($CaCO_3$) and alkali carbonates ($(K, Na)_2CO_3$) are also expansive in volume and enhance water pressure in pores. Carbonation of concrete causes decalcification of cement pastes and leads to the volume change of concrete as well [40, 41, 42].

Weathering processes: Harsh environmental conditions such as freeze-thaw cycles might depredate the concrete and cause cracking. The theory behind how concrete undergoes freeze-thaw cycles is that ice formation in water filled capillary pores causes volume expansion and hence exerted stresses in the surrounding cement paste, leading to the cracking of the paste. According to Beddoe [43], the freezing of pore solution of the cement paste is a function of the pores' surface area and the ion concentration of the solution. HPC has a better resistance to freeze-thaw degradation due to its low permeability and small moisture capacity which is endowed by its finer pore structure [44]. Jacobsen, *et al* [45] observed cracks up to 10μm widths in ordinary Portland concrete after subjected to seventy freeze-thaw cycles. However, cracks with such small width actually self-healed.

Loading: In reinforcement concrete structures, there are various types of load induced cracking, such as flexural cracks, torsion cracks, inclined shear cracks, and cracks due to dynamic and cyclic loading. Generally, when the tensile strength of concrete is exceeded,

microcracks are found to be formed at the aggregate-paste interface or at any defects in concrete [46]. Microcracks are also found in concrete members under compression due to the localized tensile stresses particularly in aggregate dense regions and at the paste-aggregate interface [47]. As the load increases, the microcracks increase in size and might finally form macrocracks, whereas a single major macrocrack might propagate into multiple microcracks at its tip. Cracking in concrete is strongly influenced by the properties of aggregate-cement-interfacial-zone. It is also found that more microcracks develop when concrete is subjected to cyclic loading than when it is under static loading. It is observed that high strength concrete has better resistance against load induced cracking than normal strength concrete due to its less interconnectivity of the pore structures [48].

Corrosion of reinforcement: Longitudinal cracking and spalling of concrete cover could be induced by the corrosion of embedded reinforcement, since the corrosion products is expansive in volume, which is shown in Figure 2-11. The unit volumes of the corrosion products presented in Figure 2-11 is based on theoretical assumptions. However, the actual volumes might be greater due to the inclusion of porous and water-filled spaces [39]. This volume expansion exerts radial pressure on the rebar-concrete interface and develops tensile stresses to the surrounding concrete, ultimately resulting in cracking or spalling of the concrete cover [49].

Permit cracks in design code

Almost every code and guidelines of concrete structural design contains provisions to control cracks and relates directly or indirectly permissible crack width to exposure conditions [11]. Codes and design regulations have dealt with durability not only by specifying limits to minimum concrete cover, minimum cement contents and/or maximum water cement ratios, but also include limits to crack width combined with formulas for calculating crack widths [50]. ACI 224.1 R-07[51] recommends 0.15 mm as maximum crack width for reinforced concrete structures which are submerged in seawater or exposed to sea water spray, and 0.4 mm for concrete structures exposed to dry air. BS 8110 [52] states that for appearance and corrosion, the maximum surface width of crack should not exceed 0.3 mm. The European design code, Comité Euro-International du Béton (CEB) (1989) limited the maximum crack width as 0.3 mm. The most common permissible crack width limits at present are 0.3mm in mild environments, 0.2 mm in moderate environments and 0.1 mm in severe environments[50]. Beeby [50] studied various national design codes concerning the design crack width obtained for a particular slab using the formulas, as shown in Figure 2-12.

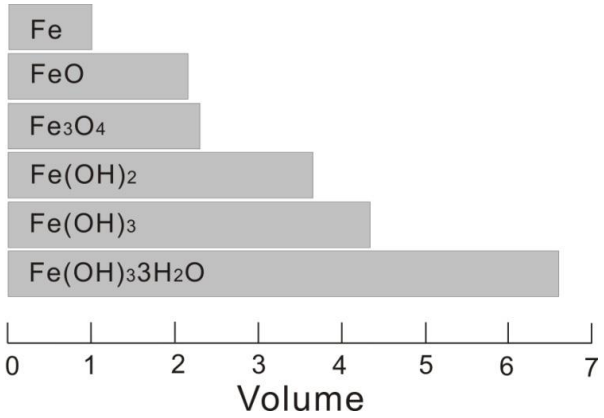

Figure 2-11: Volume expansion of corrosion products [12]

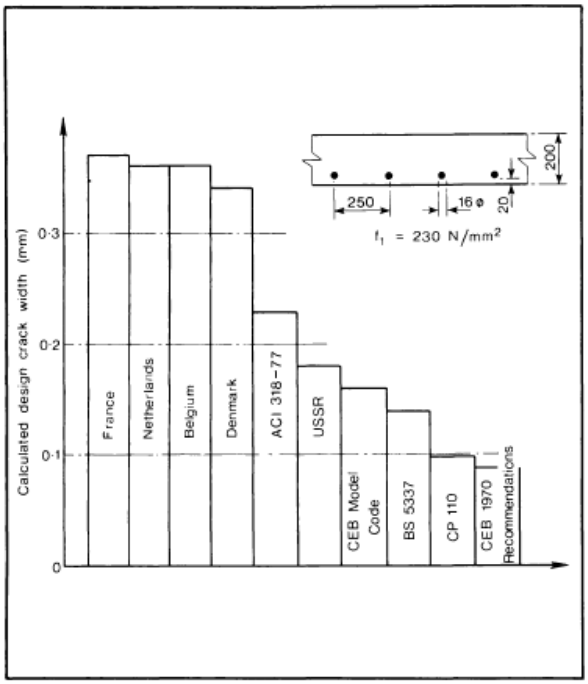

Figure 2-12: Design crack widths calculated using various regulations for the slab shown[50]

In recent years, maximum allowable crack widths are provided as a function of exposure conditions in some national codes such as the Canadian Highway Bridge Design Code [53] and ACI 224 [51].

2.2.2 Corrosion mechanism in cracked concrete

When cracks occur, an easier path for the corrosion promoting substances (chloride ions, carbon dioxide, etc.) is created. Therefore, in an aggressive environment, depassivation of the steel near the crack will take place before it happens in the uncracked areas [54, 55]. Similar with uncracked concrete, two different corrosion mechanisms are responsible for the corrosion in the crack region [3, 4, 14, 31, 56, 57, 58].

Mechanism 1 – Micro-cell corrosion

The anodic and cathodic processes take place both in the cracked zone. Anodes and cathodes are extremely small and cannot be separated. Oxygen supply to the cathodically-acting zones is mainly through the crack, as shown in Figure 2-13 (a).

Mechanism 2 – Macro-cell corrosion

Steel in the crack zone acts mainly as an anode, while the passive steel surface away from the cracks forms the cathode, as shown in Figure 2-13 (b). In this case, oxygen supply to the cathode is mainly from the uncracked concrete cover. Much higher corrosion rate is expected compared with micro-cell corrosion due to much larger cathodic acting area.

Many researchers have confirmed that in cracked concrete, which is with a small anode located at the crack area and large cathode away from the crack, macro-cell corrosion is the dominant corrosion mechanism [16, 56, 59]. Macro-cell corrosion has been identified as high corrosion current density, resulting in intense localized metal loss of the anode [60]. According to Bard and Faulkner [58]'s experiments on a series of reinforcing bars with intersecting flexural cracks, the macro-cell corrosion rate was up to 70 times higher than the corresponding corrosion rate from uniform corrosion. Sangoju, et al [61] also observed in his research that flexural/bending cracks can cause macro-cell corrosion of rebar within the concrete, resulting in very high charge.

Normally, macro-cell and micro-cell corrosion process might coexist to contribute to the total mass loss of the steel at the crack. However, the relative magnitudes of the micro-cell and macro-cell currents in such a system are neither theoretically nor technically clear. In recent years, researchers [59, 63] pointed out that when both micro-cell and macro-cell mechanisms contributed to metal loss at the crack, the Evans diagram representation indicated that an increase in the macro-cell current density resulted in a decreasing quotient of the micro-cell current.

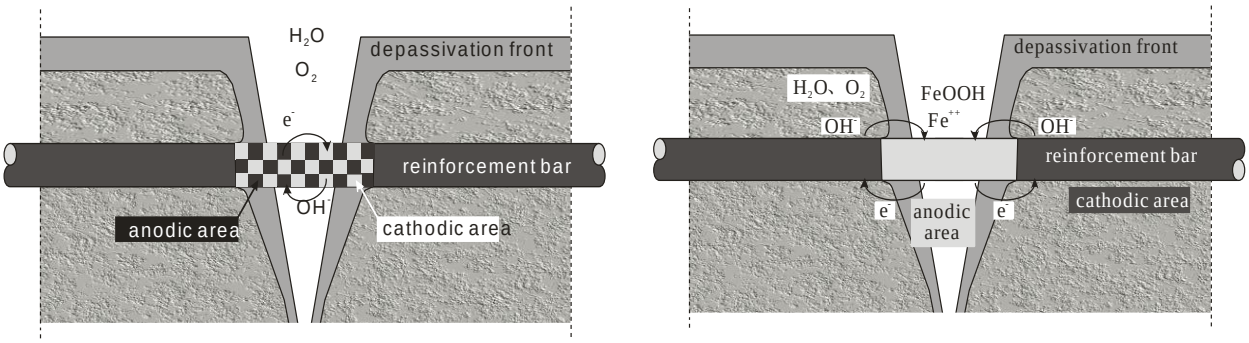

(a) Micro-cell corrosion mechanism (b) Macro-cell corrosion mechanism

Figure 2-13: Illustration of micro-cell & macro-cell corrosion mechanisms in cracked concrete[62]

2.2.3 Influence of cracks on reinforcement corrosion in concrete

Cracking of concrete cover not only reduces the overall strength and stiffness but also causes durability problems. It has been generally assumed that direct relationship exists between cracking of concrete and corrosion of reinforcement. Therefore, quantitative evaluation is needed to clearly understand the influence of cracks on reinforcement corrosion.

The role of cracks in corrosion initiation seems to be easy to comprehend. On one hand, the existence of crack results in spatial variation of physical and chemical environments along the length of steel surrounding and hence a difference in electrochemical potential, which promotes the formation of a corrosion cell; On the other hand, when cracks occur, a more preferable path for moisture and depassivating substances, e.g. chloride ions or carbon dioxide[15, 64, 65, 66], moisture and oxygen[67, 68], will be introduced. Therefore, early cracks due to service loading in reinforced concrete structural members exposed to an aggressive environment may open a direct path to the rebar and thus provide ideal conditions for the corrosion process to start. Once the carbonation front reaches the steel surface or a critical chloride content is exceeded, the passive film which formed by the high alkalinity of pore solution will be broken down, leading the steel to corrode. After depassivation, both anodic and cathodic reactions take place on the steel surface, provided that moisture and oxygen are available with sufficient concentration. Therefore initiation period can be greatly shortened by cracks. A nearly immediate intensive corrosion could be observed in cracked concrete, whereas the initiation period in uncracked concrete normally lasts for years.

The commonly questioned roles of the crack's influence on reinforcement corrosion focus on the propagation period. There have been two conflicting views: one view is that the presence of cracks only reduces the initiation period. The propagation period, however, is not significantly affected since the subsequent corrosion process is controlled either by the electrolytic resistivity of concrete or the oxygen availability in cathodic area. The other view is that concrete cover cracking not only shortens the initiation phase and promotes the depassivation, but also enhances the corrosion rate due to the reduction of barrier to diffusion of oxygen at least near the cracks themselves [55]. Some direct relationship can be found between the cracking and corrosion intensity. In consideration of the conflicting views, the knowledge on corrosion process in cracked concrete with continuous chloride/carbonation contamination is needed.

There have been a number of researches dedicating to find out the influence of cover cracking on the service life of reinforcement structures. For the initiation period, investigations were mostly focused on the crack induced changes in concrete permeability; whereas for the propagation period, more efforts were paid to the relationship between the corrosion rate and the crack, especially crack morphology such as crack width and crack frequency, etc..

Initiation period

It is believed that a well designed and manufactured concrete is originally water-tight, containing discontinuous pores and microcracks. When crack is present, the flow paths are interconnected and consequently the concrete permeability is increased [69].

In the case of chloride induced corrosion, initiation period in uncracked concrete is the time needed for the chloride to penetrate through the concrete cover t_{tran} and the time that needed for the chloride to accumulate on the steel surface to a critical content t_{accu}, as shown in Eq.(2.12).

$$t_{in} = t_{tran} + t_{accu} \tag{2.12}$$

Where

t_{in}- initiation period;

t_{tran}- time that needed for chloride ions to transport from exposed surface to steel surface;

t_{accu}- time that needed for chloride to accumulate on steel surface to threshold value.

It is generally believed that in the case of cracked concrete both t_{tran} and t_{accu} can be greatly shortened.

The main transport mechanism of chloride ions through a crack is convection due to capillary suction of water, which is much faster than the diffusion-based-mechanism through uncracked concrete cover[59]. In this case, it may take only a few hours for dissolved Cl^- to reach the steel through crack, whereas much longer time is needed through the uncracked concrete cover [70]. Researches based on laboratory study indicated that cracks lead to more rapid initiation of corrosion [3, 16, 60, 69, 71, 72, 73, 74, 75]. In situ observations also confirmed this point of view.

The effects of crack on transport properties have been studied by several researchers [69, 76, 77, 78, 79, 80, 81]. Mehta and Gerwick [82] specified that concrete contains discontinuous microcracks due to various kinds of loading and weathering effects under service conditions in marine environment. Once the surface cracks interconnect with the internal microcracks, the permeability of the concrete increases significantly. According to Gerard and Marchand [79], the presence of crack could contribute to the permeation (or absorption) coefficient of concrete by several orders of magnitude.

Djerbi, et al [83] further pointed out that the chloride diffusion coefficient through the crack, D_{cr}, is not dependent on material parameters of the concrete but becomes constant, and is equivalent to the diffusion coefficient in free solution when the crack width is higher than 80 µm. He conducted a steady state migration test on tensile cracked concrete disc with 110 mm diameter and 50 mm thickness, with its cracks ranging from 30 to 250 µm, Figure 2-14 and Figure 2-15. Results show that the transition period, which is the time needed for chloride ions to transport though the cracked concrete (both though concrete pore structure and crack) till the steady state is reached, was close to zero for crack widths above 80 µm,

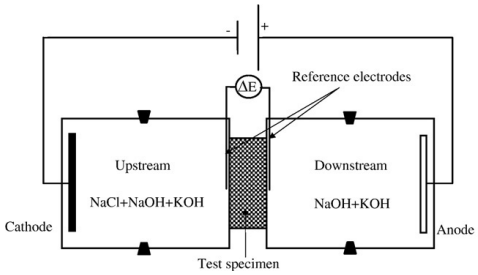

Figure 2-14: Migration cell

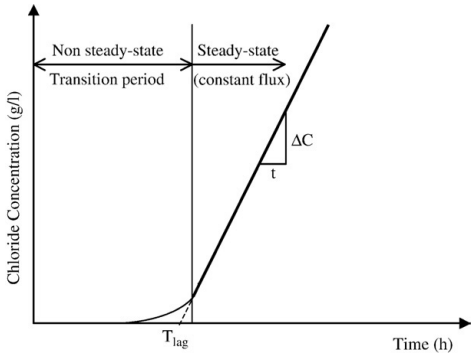

Figure 2-15: Schematic representation of non-steady state and steady state conditions of chloride migration[83].

It was generally believed that the permeability of cracked concrete increases with crack width [69, 76, 79, 84]. Several researchers noted that there is a certain value of crack width that the crack become first connected, i.e. the 'threshold crack width' [35, 69, 80, 81]. The permeability of concrete doesn't increase with increasing crack width until the crack width exceeds the so-called "threshold crack width". Below the threshold crack width, cracks have little influence on the permeability. However, the value of threshold crack width reported by different researchers varied. Wang, *et al* [69] reported that a crack opening displacement (COD) smaller than 50 μm under loading ($\approx 50 \mu m$ after unloading) rarely affected the permeability. However, when the COD (crack opening displacement) was increased from 50 to 200 μm under loading (≈ 15 to 65 μm after unloading), the permeability increased rapidly. Over 200 μm (65 μm after unloading), the permeability showed a steady increase. Aldea, *et al* [85] also reported similar results. Jacobsen, *et al* [80] and Gagné, *et al* [81] reported that crack can act as a continuous channel when the crack width exceeds 55 μm . Djerbi, *et al* [83] found that the diffusion coefficient of cracked concrete started to increase with the increasing crack width for cracks wider than $80 \mu m$. Similar findings were reported by Ismail, *et al* [86]. He reported that for cracks smaller than 30 μm , no diffusion occurred along the crack path regardless the age at which the crack was generated. Yoon and Schlange [87] identified that in short term test cracks narrower than 12 μm had no influence on chloride penetration depth; however, in a long-term test, the threshold width was found to be $50 \mu m$. Jang, *et al* [35] reported that the threshold crack width was around 80 μm based on steady state migration test data. He developed a parallel composite model to identify the permeability of cracked concrete. In this model 'crack geometry factor' was introduced, ranging from 0.067 to 0.206. The diffusion coefficient is found to be linearly correlated with the crack width, as shown in Figure 2-16.

The equivalent diffusion coefficients of cracked zone can be evaluated as:

$$\frac{D_{eq}}{D} = 1 + \frac{(w_{cr} - w_{cr,t})\beta_{cr}}{l_{cr}} \frac{D_0}{D} \tag{2.13}$$

in which,

β_{cr} - crack geometry factor, accounting for tortuousness, connectivity and constrictively of the crack pass perpendicular to the flow direction

D_0- the diffusion coefficients of chloride ions in free solution [m^2/s]

D_{eq}- the equivalent diffusion coefficient of cracked concrete [m^2/s]

D- diffusion coefficient of uncracked concrete [m^2/s]

W_{cr} and $W_{cr,t}$- crack width and threshold crack width [μm]

l_{cr}- length of crack [μm]

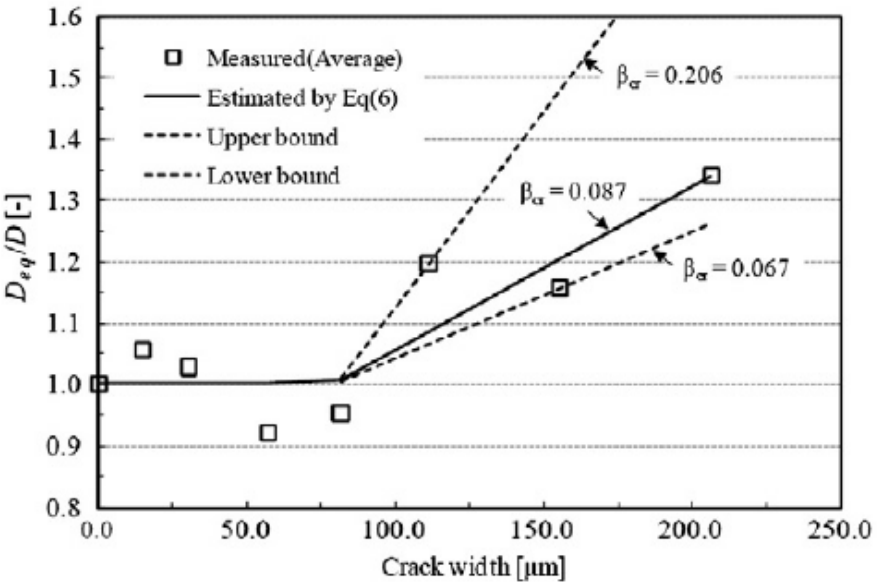

Figure 2-16: Relationship between relative diffusion coefficients and crack widths according to crack geometry factor.

The existence of the threshold crack width could be attributed to the so called autogeneous healing or self-healing effect. Autogeneous healing is a process that concrete undergoes a modification of its pore structure and consequently an increasing of concrete permeability due to continuous hydration the deposition of corrosion products in crack regions during its service life [88]. It is most likely that fine cracks in concrete autogenously healed and therefore were subjected to little chloride penetration. According to Schieβl and Raupach [89], the maximum crack width that can undergo autogenous healing was estimated to be

between 0.1 and 0.2 mm. Jacobsen, et al [80] reported that cracked concrete specimens which were subjected to self-healing for three months experienced a significant reduction in chloride permeability: 28-35%, compared to migration in newly cracked specimens. Additionally, Mohammed, et al [90] reported that in marine environment the fine cracks were healed due to the deposition of corrosion products in the crack regions, baffling further ingress of aggressive agents. Marcotte and Hansson [91] also observed the crack blocking by corrosion products.

Some researchers believed that the effect of crack width on permeability also has an upper limit. Concrete permeability doesn't increase with crack width when cracks are wider than this upper limit. Ismail, *et al* [92] reported that the diffusion of chloride ion in the solution was not a limiting factor controlling the diffusion process when crack width exceeds 200 µm. However, Wang, *et al* [69] reported that after the crack opening displacement reached 200 µm, the rate of water permeability kept on increasing steadily.

Researchers also dedicated efforts to investigate the influences of other factors such as w/b ratio, binder content, binder type, concrete strength and etc. on the permeability of cracked concrete. Win, *et al* [70] studied the influence of w/c ratios on chloride penetration in cracked ordinary Portland cement concrete. They observed that specimens with lower w/c ratio (0.25) showed lower chloride profile and penetration depth either from exposed surface or around the crack (compared with w/c ratios of 0.45 and 0.65). Audenaert, *et al* [93] concluded that increasing the amount of cement led to a reduction in chloride penetration depths. It was reported that when using blended cements or supplementary cementitious materials (slag, flyash, silica fume, etc.) a decrease in penetration depths can be found. Savija, *et al* [94] attributed all of these effects to the increased chloride binding capacity under these conditions. In a low-pressure water permeability test, Aldea, *et al* [77] concluded that for cracks above 100 µm, normal strength concrete showed higher permeability coefficient than high strength concrete, which is opposite to the situation of uncracked concrete.

Akhavan, *et al* [95] quantified the moisture permeability of localized cracks as a function of crack geometry (i.e., width, tortuosity, and surface roughness) on tension split plain and fibre reinforced mortar disk specimens. Results showed that crack tortuosity and roughness reduced the moisture permeability by a factor of 4 to 6 compared to what was theoretically predicted for smooth parallel plate cracks.

It is important to take into account the situation under loads since that in reality all of the structural members are mechanically loaded. Gowripalan, *et al* [65] found that the permeability was lower in the compression zone than in the tension zone of the beam element. This might be attributed to the damage at the aggregate-paste interface in the tension zone. Additionally, the reduction of porosity in the compression zone led to lower permeability. He also pointed out that crack width/cover ratio can be a more suitable parameter to estimate the permeability of cracked concrete. Küter, *et al* [96] quantified the effect of cyclic loading on chloride ingress into single crack of saturated mortar specimens, and concluded that the opening and closing of crack led to more severe chloride ingression than in the case of static loading conditions especially in the crack tip and compressive zone. It is, therefore, important to take realistic loading conditions into account when assessing the service life of a structure.

Most of the above mentioned contributions were based on experimental investigations. In recent years, numerical methods were adopted to develop a numerical algorithm in order to estimate the chloride penetration. Tang [97] used a mathematical model which was based on finite difference method to simulate the chloride ingress into saturated concrete under pure diffusion mechanism, taking into account of a nonlinear chloride binding isotherm. Martín-Pérez, *et al* [98] proposed an algorithm using a numerical formulation of the associated mass transport partial differential equations based on modified Fick's second law. This numerical model included the simulation of transport of chlorides, moisture, oxygen and heat convection through concrete which was resulted from seasonal variations in the surface conditions of the RC member. Wang, *et al* [99] developed a mathematical model to predict the ionic mass transport associated with chloride ingress into concrete or hydrated cement paste from a saline environment by incorporating the convection of pore solution. Compared with the results obtained from the models using Fick's second law, the model proposed by Wang was more detailed and accurate and can be applied to various different cases with unified ionic diffusivities. Xi, *et al* [100, 101, 102, 103] studied the chloride and moisture ingression into non-saturated concrete with the finite element methods. In his study, a material and environmental dependent diffusion coefficient was calculated by a factorial approach.

Up to now experiences on numerical simulations performed to determine the chloride penetration process into cracked concrete are not abundant. Marsavina, *et al* [104] conducted both experimental and numerical investigations on the influence of cracks on

chloride penetration in concrete structures. The experimental results were obtained with non-steady state migration test, using an electrical field and artificial cracks with varying depth and width. The numerical simulation results were obtained using a transient finite element analysis. Higher chloride penetration was observed at the crack tip compared with the uncracked part. The penetration depth was found to increase with increasing crack depth, whereas no effect of crack width was observed. A good agreement between experimental and the numerical chloride penetration results was obtained.

To summarize, the initiation period of cracked concrete can be greatly shortened by the presence of cracks due to the high permeability of cracks. The permeability of cracked concrete can be influenced by factors such as the quality and thickness of concrete cover, and especially the crack width. When exceeds a threshold crack width, the permeability of cracked concrete increases with crack width. Cracks which are narrower than the threshold crack width may be subjected to little chloride ingress due to the autogenous healing or the deposition of corrosion products.

Propagation period

The effects of cover cracking on the corrosion initiation phase have been specified in the previous section. When the carbonation front reaches the steel surface or the chloride concentration on the steel surface exceed the critical value the embedded rebar is depassivated and corrosion will take place. Schießl and Raupach [16] pointed out that the chloride-induced reinforcement corrosion in the crack zone involved the formation of a macro-cell. The rebar in crack zone acted as the anode, while the rebar away from cracks, sometimes up to a distance of several decimetres from the cracks, formed the cathode. There have been a number of investigations specifically dedicated to study the influence of cracking on the propagation phase of reinforcement corrosion.

Corrosion rate of steel in the crack zone was shown to be considerably influenced by a great number of parameters which could be sorted as crack geometry [105], concrete quality, and exposure conditions, etc..

Crack width

Published literatures show that there is some controversy regarding the effect of crack width on corrosion rate. Some researchers consider there is certain relationship between the crack width and corrosion whereas various observations from both outdoor and laboratory tests

have shown the fact that crack width has only a little influence on the corrosion intensity, no matter if the depassivation is caused by carbonation or chloride contamination [16, 39, 106].

Some researchers agree that there is a relationship between crack width and corrosion rate [39, 107, 108]. It is to some extent considered that wider crack causes higher corrosion rate in permeable concrete. Arya and Ofori-Darko [3] studied the macro-cell corrosion in cracked beam specimens subjected to alternate wetting-drying cycles. It was found that the macro-cell corrosion current increased with the crack width. However, the influence decreased with time. Burdall and Sharp [109] also found the risk of corrosion increased with increasing crack width; whereas the risk of corrosion was negligible in concrete with smaller crack width (0.1 to 0.3 mm). Mohammed used pre-cracked prism specimens with crack widths varied from 0.1 to 5 mm and observed that for the specimens with narrower cracks (< 0.5 mm), no distinct differences in chloride profiles were found between cracked and uncracked concretes; for wider cracks (>1.5 mm), however, significant loss of steel area was observed. Okada, *et al* [110] and Raharinaivo*, et al* [111] also reported that there was a relationship between crack width and corrosion rate of reinforcing steel in concrete, particularly for wider cracks.

Many other researchers supported the opinion that once corrosion initiated, the influence of the crack width on the corrosion rate is very limited [3, 16, 31, 73, 112, 113]. Beeby [56] reported that there were considerable influences of the crack width on the corrosion intensity, but only in the short term (1 to 2 years); this influence of the crack width decreased and would be negligible in the long term period. In a later publication [112], he pointed out that although cracks caused depassivation of steel at the cracked zone thus be responsible for corrosion initiation, however, in order the corrosion process to persist, continuous supply of oxygen at cathodic sites was required. Considering that cathodic sites were in crack-free zones, corrosion rate was also limited by the permeability of the uncracked cover, which was the same with uncracked concrete. Some other researchers [73, 90, 114] supported this point of view. Additionally, they pointed out that for long term process aggressive agents penetrate the concrete through uncracked concrete cover as well, lead to the same corrosion in the crack zones or uncracked zones. Jacobsen, *et al* [115] also concluded that narrow cracks (width <0.4 mm) do not affect the corrosion intensity of steel, compared to uncracked concrete. Other factors such as the quality and thickness of the concrete cover as well as environmental conditions were more important.

In order to clarify the corrosion mechanism and the dominant influencing variables, especially the influence of crack width, Schießl and Raupach [16] conducted a series of laboratory tests on cracked concrete beams, with the crack width ranging from 0.1 mm to 0.5 mm. The specimens were subjected to cyclic wetting (24h/1 week) by 1% chloride solution. Twelve chloride wetting periods were followed by two water wetting period, which again were followed by drying period in 80% RH chamber. Results showed that during early exposures, an increase of corrosion rate with increasing crack width could be found, Figure 2-17; however, this effect declined with test duration that no further systematic crack width influence was detectable after 2 years, as shown in Figure 2-18. Therefore, he concluded that the corrosion rate in the crack zone was influenced considerably by the conditions between the cracks. Concrete cover and composition have much greater influences than crack width.

Bentur, *et al* [55] presented a diagram to illustrate the influence of cracking on both the corrosion initiation period and propagation period, as shown in Figure 2-19. It can be seen that crack width significantly influenced the time for corrosion to take place. The initiation phase of reinforcement in concrete with greater cracks was shorter than that with smaller cracks. However after depassivation the influence of crack width decreases with time. For example, a distinct difference in corrosion rate between reinforcement with wider cracks and narrower cracks can be found; whereas at time t_3, the difference was much smaller.

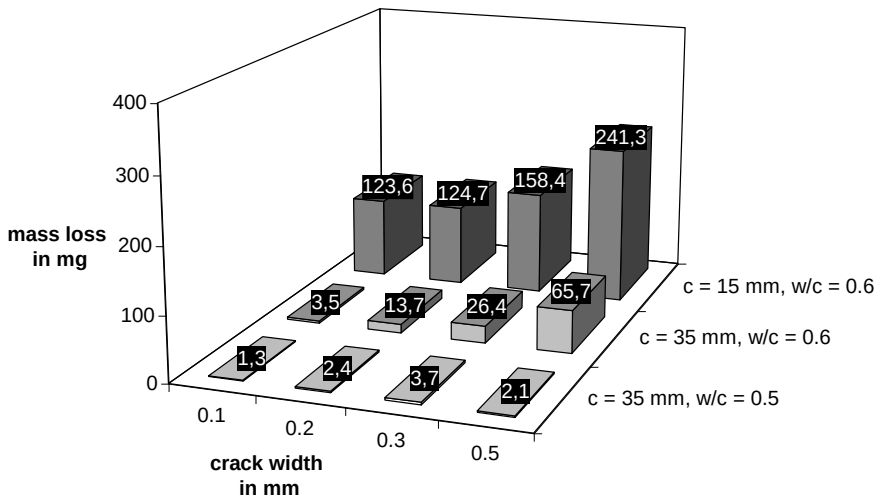

Figure 2-17: Calculated losses in mass of steel in crack zone due to macro-cell corrosion after test period of 24 weeks.

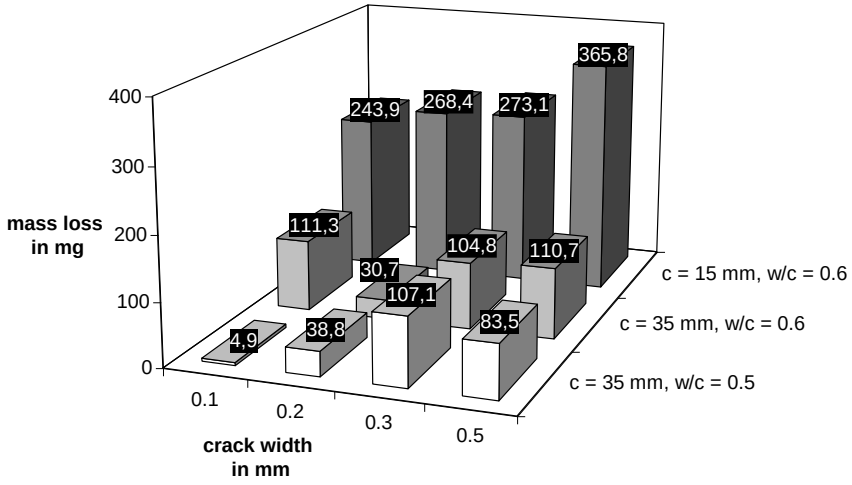

Figure 2-18: Calculated losses in mass of steel in crack zone due to macro-cell corrosion after test period of 2 years.

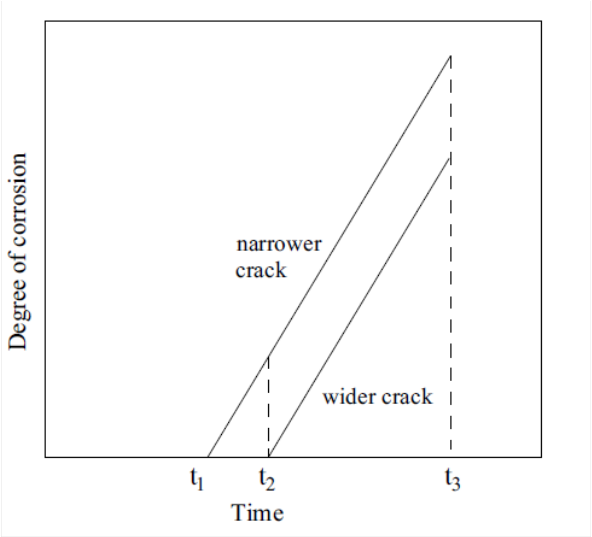

Figure 2-19: Influence of different crack width to degree of corrosion [55]

In light of the discussion above, it can be summarized that to a certain degree, researchers agree that embedded steels are subjected to little corrosion when the crack is fine enough; there is a certain influence of crack width on corrosion rate, however, this influence declines with exposure time.

Crack frequency

Crack frequency is another parameter which attracts researcher's interest. Very few studies have examined the influence of crack frequency on corrosion process. Suzuki, *et al* [11] compared the effect of single crack versus multiple cracks on the corrosion of steel in

concrete. Based on half-cell potential measurements and optical observation of rust stains on concrete, they concluded that the steel at the crack-steel intersection depassivated earlier than that at uncracked sections, and in specimens with multiple cracks, corrosion initiated earlier at the major (wider) cracks than the secondary cracks. This difference was attributed to the low availability of moisture and oxygen in the latter cracks.

In another work, Arya and Ofori-Darko [3] studied the relationship between crack frequency and reinforcement corrosion based on laboratory investigations on samples with artificial cracks which were generated by inserting plastic shims when casting. They found that decreasing the crack frequency led to a decrease in cumulative weight loss of embedded steel providing the total crack width is kept constant. A conclusion was made that an effective method against corrosion is to limit the frequency of intersecting cracking by increasing the cover thickness rather than by controlling crack widths.

Raupach [6, 7] observed a significant reduction of local corrosion rate at the crack when crack intervals were smaller. He attributed this phenomenon to a smaller cathode surface for each crack.

Concrete cover

The risk of corrosion of reinforcing steel should be minimal in a well-designed reinforced concrete structure containing a sufficient depth of good quality concrete cover which have been properly placed and compacted. In the case of cracked concrete, similar conclusion has been confirmed by some researchers that the thickness and quality of concrete cover have a much greater influence upon the corrosion process compared to crack width, especially for long term corrosion. Only through an adequately thick concrete cover the development of a macro-cell corrosion element in certain areas can occur. In addition, only though the concrete cover the transportation of oxygen for cathodic reaction could be persisted. Houston, *et al* [116]'s results showed the beneficial effects of an increase in cover thickness and in concrete quality, by means of reducing the w/c ratio, as shown in Table 2-3.

Table 2-3: Relative corrosion versus concrete cover and w/c ratio crack [116]

Cover thickness [mm]	w/c = 0.49	w/c = 0.55	w/c = 0.62
20	49	88	100
25	44	60	100
38	22	-	98
50	0	-	75

Houston, *et al* [116] further pointed out that ratio of cover to bar diameter was a more appropriate variable related to corrosion rate. Their results for all members exposed for 2 years with a w/c ratio of 0.55 are shown in Figure 2-20.

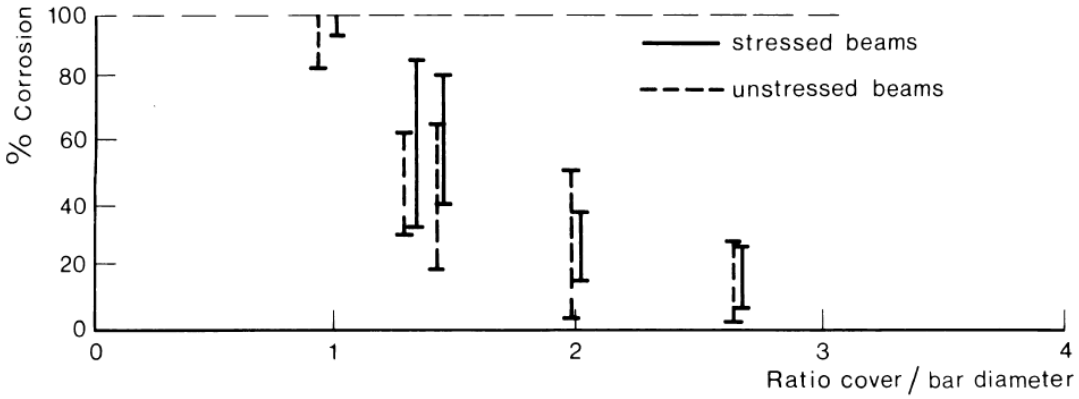

Figure 2-20: Influence of cover/ bar diameter ratio on corroded area, w/c ratio=0.55

A number of investigations have similar conclusions as Houston's. Bird and Callaghan [117] concluded that the logarithm of the relative weight loss by corrosion is inversely proportional to the square of the cover thickness. Hartl and Lukas [118] found that specimens (cover=35mm; crack width=0.4mm) with a w/c ratio of 0.7 exhibited an extreme pitting corrosion in crack zones; whereas the specimens with w/c ratio 0.5 only showed surface rust in the vicinity of cracks. Schießl and Raupach [16] also confirmed the effects of cover thickness and concrete quality on corrosion intensity, which has been shown in Figure 2-17and Figure 2-18.

Concrete composition

Mineral and chemical admixtures such as flyash, blast furnace slag and silica fume are widely used as partial replacement to blend with Portland cement to improve the concrete durability and enhance the corrosion resistance. Pozzolana Portland cements (PPC) and flyash replaced concrete (OPC+FA) has shown better corrosion resistance properties than Ordinary Portland Cement Concrete (OPCC). The order of performance is found to be OPC + FA> PPC> OPC. However, not very many results have been reported on the corrosion resistance of such concretes exposed to severe chloride environments under cracked conditions.

Weiermair, *et al* [119] investigated the influence of cracks in different types of concrete mixes which were subjected to tidal conditions in seawater. Active corrosion was observed in rebar at the cracks in HPC, however, the steel was repassivated after three months; while

corrosion rates of steel in other types of concrete increased over time. Hansson and Okulaja [120] found that cracked HPC offered better corrosion protection to embedded steel than cracked OPCC. However, the difference was less distinct than that in uncracked concrete. Sangoju, *et al* [61] reached similar conclusions based on electrochemical measurements such as half-cell potential and resistivity on both the uncracked/cracked PPC (Portland pozzolana cement) and OPCC. He found that when subjected to chloride deterioration, it was evident that concretes with PPC performed significantly better than concretes with OPC. The chloride permeability of PPC was nearly three times lower than that of the corresponding OPC, indicating better performance in chloride environment. The overall gravimetric weight loss of the rebar within OPC was 2.6 to 2.7 times of that in PPC in the case of uncracked concretes and about 1.5 to 2.0 in the case of cracked concretes. In addition, rebar corrosion was lower in concrete with lower w/c ratios. This can be attributed to higher resistance to the corrosion current and lower penetrability due to pore refinement.

2.3 Numerical simulation of reinforcement corrosion in propagation phase

Normally the prediction of service life of steel reinforced concrete structures has been focused on the assessment of the initiation period rather than to estimate the subsequent corrosion rates. However, the propagation period may add significantly to the service life. Consequently, ignoring the propagation period may lead to underestimation of the service life of reinforcement structures[20].

Most of the previous contributions have been focused on laboratory study; studies dealing with computer assistant calculations are not abundant. However, laboratory study is quite time-consuming and lab-condensed that it is challenging to deal with plenty of boundary conditions and various material properties. However, with numerical simulation those difficulties could be easily conquered.

In order to find out the distribution of electrical current density and potential at the surface of anodes and cathodes, it has to simulate the electrical field in the concrete domain around the electrodes. Theoretically, the electrical potential distribution in the concrete domain follows the Laplace's equation:

$$\nabla^2\phi = \frac{\partial^2\phi}{\partial x^2} + \frac{\partial^2\phi}{\partial y^2} + \frac{\partial^2\phi}{\partial z^2} = 0 \qquad (2.14)$$

At concrete surface, there is no electrical flow in or flow out, hence, $\partial\phi/\partial n = 0$; while at the interface of reinforcement and concrete, the relationship between electric and potential should follow the polarization curves of the electrodes, that is $i_a = f(\phi_a)$ or $i_c = f(\phi_c)$.

It's quite difficult to solve Eq.(2.14) directly. Therefore numerical methods are adopted, e.g. finite difference method (FDM), finite element method (FEM) and boundary element method (BEM).

2.3.1 Finite difference method (FDM)

This method is the most widespread method of approximation because it is easy to understand and simple to program. In finite difference method, the spatial discretization of the simulated domain is done by a regular, orthogonal grid. For each node of the grid an algebraic equation is created, in which the states of the neighbouring nodes by differential quotients are taken into account. It is to use central difference approximation to replace the differential items in Eq.(2.14) and produces the finite difference equation as

$$\frac{\phi_{i-1,j,k}-2\phi_{i,j,k}+\phi_{i+1,j,k}}{(\Delta x)^2}+\frac{\phi_{i,j-1,k}-2\phi_{i,j,k}+\phi_{i,j+1,k}}{(\Delta y)^2}+\frac{\phi_{i,j,k-1}-2\phi_{i,j,k}+\phi_{i,j,k+1}}{(\Delta z)^2}=0 \qquad (2.15)$$

The whole concrete domain could be discretized into small intervals and Eq.(2.15) is applied to each point and assembled as matrix form:

$$[A]\{\phi\}=\{F\} \qquad (2.16)$$

Combined with boundary conditions, the electrical potential at all discretized points could be solved [see in 121, 122, 123].

Based on cylinder symmetry assumption, Koretsky *et al* [122] used a two-dimensional grid to simulate a cylinder concrete with a small anodic and a large cathodic along the axial, to investigate macro-cell current distribution and the applicability of electrochemical impedance to the measurement of corrosion currents in reinforced concrete structures. They found that the distribution of the alternating current excitation emphasized the impedance contribution of the cathodic reaction to the overall impedance spectrum. Later, Kranc and Sagüés [124] used similar model to simulate reinforced concrete column in marine environment and found that total corrosion current varied from being almost equal to the total macro-cell current to being several times greater, depending on the values of concrete resistivity and oxygen diffusivity ranges assumed. Kranc and Sagüés [121]

developed a computational strategy to treat complex rebar configurations within typical structural shapes. They devised a procedure to represent the rebar surface with a minimum of additional computational burden. Both free corrosion and cathodic potential were simulated and it was found that the potential of the rebar with cathodic protection is more active than that without cathodic protection.

Besides, Muehlenkamp [123] also developed a two-dimensional finite difference simulation to study the behaviour of cathodic protection systems and actively corroding reinforced concrete structural elements. The potential and current distributions in a simplified rectangular geometry were determined. The simulation indicated that environmental conditions, particularly the degree to which concrete pores are saturated with water, greatly affected system performance.

One disadvantage of finite difference method is the condition of the orthogonal and regular lattice. Hence, irregular geometries are poorly recorded and the refinement of the lattice in the range of singularities is not possible.

2.3.2 Boundary element method (BEM)

Boundary element method is to use Coulomb's law as the fundamental solution for Eq.(2.14)

$$U(P,Q)=\frac{1}{4\pi rk} \tag{2.17}$$

Where $r=\sqrt{\left(x_p-x_Q\right)^2+\left(y_p-y_Q\right)^2+\left(z_p-z_Q\right)^2}$ is the distance between source point P and field point Q. And the electrical current from point P to point Q is

$$T(P,Q)=-k\frac{\partial U}{\partial n}=-k\left(n_x\frac{\partial U}{\partial x}+n_y\frac{\partial U}{\partial y}+n_z\frac{\partial U}{\partial z}\right) \tag{2.18}$$

Based on the theorem of Bette, the differential equation Eq.(2.14) in the whole domain could be transferred as a set of integral equations along the entire boundary surface:

$$u(P)=\int_S t(Q)U(P,Q)dS(Q)-\int_S u(Q)T(P,Q)dS(Q) \tag{2.19}$$

where $u(Q)$ and $t(Q)$ are the potential and the normal derivative respectively at point Q on surface S. It's still difficult to integrate along the whole surface. Therefore the whole

surface is discrete as small boundary elements. Then the integrals can be evaluated over each element separately and the contributions added:

$$\frac{1}{2}u^e + \sum_{e=1}^{nel}\int_{S_e} T(P,Q)dS_e(Q)\cdot u^e = \sum_{e=1}^{nel}\int_{S_e} U(P,Q)dS_e(Q)\cdot t^e \qquad (2.20)$$

Using matrix notation, it could be written as:

$$[\Delta T]\{u\} = [\Delta U]\{t\} \qquad (2.21)$$

Combined with boundary conditions, Eq.(2.21) could be solved for the electrical potential and current at boundary, and then any internal point also could be calculated with Eq.(2.19). More details about the methodology and solution could be referred to book 'the Boundary Element Method with Programming' by Beer *et al* [125]

In boundary element method, the simulated domain is discretized only on the edge, which offers significant advantages that the number of elements is much smaller than that with other methods. It is also possible, with the boundary element method to model unbounded domains, mainly in applications in the earth or in the sea water [126]. However, the disadvantage of BEM is the restriction that within model domain only constant conductivity of the electrolyte could be modelled. The only way to achieve varying conductivity is by the introduction of a series of sub-domains.

Zamani and Chuang [127] developed a boundary element program with constant element to simulate the corrosion of a storage tank. The influence of design weighting factor and polarization curve slope on the overall optimal control problem was studied. Plots of the type generated by BEM enabled a corrosion engineer to design more efficient cathodic protection systems through a systematic procedure based on optimal control theory.

The problems of actual structural corrosion are often too complicated to solve directly. In order to overcome the difficulty, several simplified method were developed, such as macroscopic polarization curve method, zooming method, Fourier series method, equivalent boundary condition method and fast multi-pole boundary element method. Amaya and Aoki [126] summarized the five methods and developed an effective optimization of cathodic protection design method to reduce the calculation time.

Computational Mechanics in Southampton, UK, developed the boundary element method as a general software, BEASY, which is widely used in cathodic protection. Brem [128] used

BEASY to simulate the corrosion in a reinforced concrete slab and quantified the influences of environmental conditions (temperature and relative humidity) and specimen geometry. The results showed that the anodic polarization curve is strongly affected by the concrete temperature, RH and exposure time. A good agreement between the field test results and numerical calculated results was achieved, indicating the promising possibility of simulating the large structural elements with relatively simple models. Warkus *et al* [129] used two practical problems to verify the usage of BEASY in reinforced concrete corrosion and concluded that simulations of corrosion processes in concrete members are possible. Warkus and Raupach [130] compared different structural members and diverse geometrical arrangements of anodically and cathodically acting reinforcement bars, and confirmed the strong influence of the geometry on the resulting macro-cell current.

Kyung *et al* [131] developed a 2-D boundary element program and analyzed electric fields around single and double reinforcing steel bars. It was found that the polarized area was related to the current density in steel bars, current ratio for the steel bar, and current ratio from the counter electrode. It was evident that the distribution of currents on the steel surface was suppressed by using double-disk electrodes instead of only using central electrodes.

Abootalebi *et al* [132] built a 2-D model to simulate a sacrificial anode cathodic protection problem of steel storage tank using BEM. The study showed that boundary element method was beneficial in modelling and analyzing cathodic protection systems.

2.3.3 Finite element method (FEM)

In this method, the simulated domain is divided into simple sub regions (elements) where the differential Eq.(2.14) is replaced as a weaker form based on Galerkin's integration method

$$\int_{v^e} N\left(\frac{\partial^2\phi}{\partial x^2}+\frac{\partial^2\phi}{\partial y^2}+\frac{\partial^2\phi}{\partial z^2}\right)dV=0 \tag{2.22}$$

Using Gauss's Divergence theorem, Eq.(2.22) could be transferred as

$$\int_{v^e}\frac{\partial\phi}{\partial x}\frac{\partial N}{\partial x}+\frac{\partial\phi}{\partial y}\frac{\partial N}{\partial y}+\frac{\partial\phi}{\partial y}\frac{\partial N}{\partial y}dV=\iint_S N\frac{\partial\phi}{\partial x}dS \tag{2.23}$$

Then, applying to all elements and getting summation, the finite element discretization process reduces the differential Eq.(2.14) to a set of equilibrium type matrix equations of the form

$$[K]\{\phi\} = \{I\} \tag{2.24}$$

Where $[K] = \sum_{nel} \int_{Ve} \left(k \frac{\partial N_i}{\partial x} \frac{\partial N_j}{\partial x} + k \frac{\partial N_i}{\partial y} \frac{\partial N_j}{\partial y} + k \frac{\partial N_i}{\partial z} \frac{\partial N_j}{\partial z} \right) dV$ is the symmetrical conductivity matrix, $\{\phi\}$ is a vector of nodal electrical potential values, and $\{I\}$ is a vector of nodal inflow/outflow electrical current.

Hassanein *et al* [133] modelled macro-cell corrosion with FEM and concluded that an increase in the concrete resistivity and concrete cover as well as a decrease in the cathode to anode area ratio (when anodic current density is constant) would increase the voltage drop in the concrete. It is important to consider these factors in the selection of the design current density.

Redaelli *et al* [134] pointed out the advantage of this method lied in the use of irregular elements which enabled the discretization of any domain forms. Another advantage is that with finite element model, location-dependent resistivity field of the electrolyte could be achieved. One disadvantage of this method is the large number of elements needed in order to obtain accurate results. This results in the limitation of the model size, especially for 2-D models.

Chapter 3 Laboratory Study on Corrosion of Reinforcement in Cracked Concrete

3.1 Introduction

As the most commonly used building material, concrete has superior properties in load bearing capacity and durability. However, its tensile strength and strain capacity are modest. Therefore even small imposed tensile strain due to hygral or thermal shrinkage or by mechanical loads or a combination thereof leads to crack formation [135, 136].

Cracks up to a critical width are directly or indirectly allowed in most concrete structural design codes, which indicates the agreement of the possibility of crack-induced corrosion. Up to the present day, researchers have questioned if the approaches of corrosion control suggested and required in the existing codes are enough. To answer this question, information such as the corrosion mechanism in cracked concrete and the relationship between the crack and corrosion rate should be clarified. Factors which probably influence the corrosion process in cracked concrete should be investigated as well.

Although there are plenty of recent reports and studies describing reinforcement corrosion in crack zones, a systematic investigation to access the corrosion process is still important and required. The aim of the research in this chapter is to clarify the corrosion mechanism in cracked concrete and to figure out which parameters influence and to what extent they influence the corrosion process.

In order to achieve these motivations, laboratory tests were carried out on central cracked concrete beams, in which a corrosion system with single anode and multiple cathodes were arranged. The beams were subjected to both 1h/week wetting-drying cycles of chloride solution or tap water, and natural unsheltered exposures. Macro-cell corrosion current and potential were selected as the basic research parameters. The corresponding data from 3 years' daily measurement have been collected and analysed. Then the beams were broken out step by step for destructive measurements. Chloride profiles in the crack zone as well as corroded area and depth were measured. Based on the test results, effects of the influential factors, such as concrete composition, exposure conditions and crack geometry, were investigated.

It is necessary to clarify here that only macro-cell corrosion is discussed in this study. This is because that on one hand, macro-cell corrosion is considered to be the major corrosion mechanism when the anode is wet and small while the cathodes are large and in a relatively dry condition [17, 137, 138]; on the other hand, only the macro-cell corrosion current could be measured by the corrosion system designed in this study. Theoretically, the contribution of micro-cell corrosion to the steel mass loss could be calculated by subtracting the quotient of macro-cell corrosion induced mass loss from the total steel mass loss. Unfortunately, the total steel mass loss could not be obtained due to the lack of original steel weight.

3.2 Experimental Setup

3.2.1 Specimens

Investigations were made on beams with the dimension of $500\times200\times150mm^3$. A predefined single crack (width=0.30mm) was produced right in the middle of the beam [19], as shown in Figure 3-1 and Figure 3-2.

Figure 3-1: Cracked beam in the frame

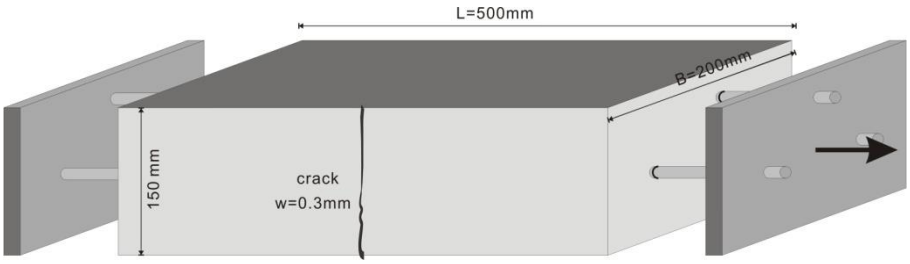

Figure 3-2: Geometry of cracked concrete beam

Each specimen contains three sets of corrosion cells each of which are composed of one anode and 4 cathodes. In each corrosion cell, a mild steel bar (d = 12 mm) which reaches from one end of the beam to the other, is coated with epoxy resin except a small area of 4 cm of length ($A_a = \pi dl = \pi \times 1.2 \times 4 = 15.08cm^2$) in the crack area, as shown in Figure 3-3. This area is supposed to be the anode. In parallel to each anode bar three short pieces (length = 5 cm) and one longer piece (length = 15 cm) of the same steel are arranged without any electrical contact between them and the anodes, serving as cathodes, as shown in Figure 3-4. It should be noticed that, a Cu/$CuSO_4$ reference electrode is fixed close to each anode to measure the anodic potential.

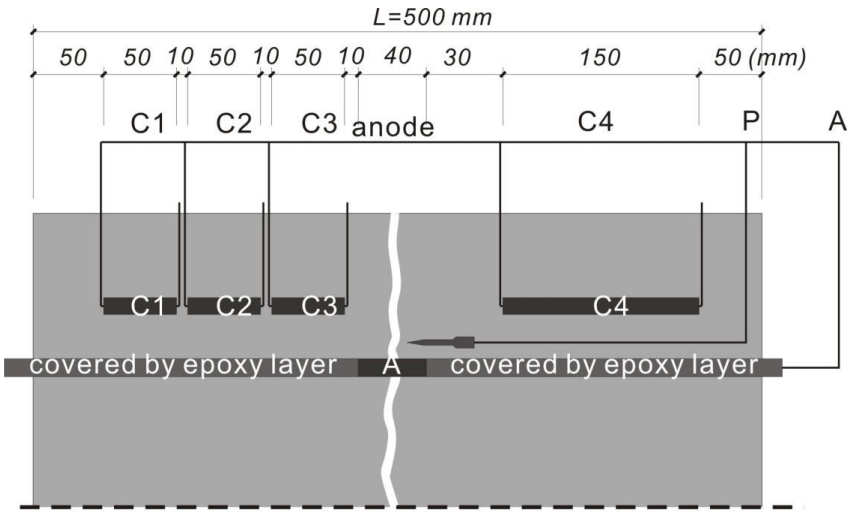

Figure 3-3: Profile of corrosion system (anode with 4 cm length in the center cracked area, and cathodes C1-C3 with 5 cm length, C4 with 15cm length)

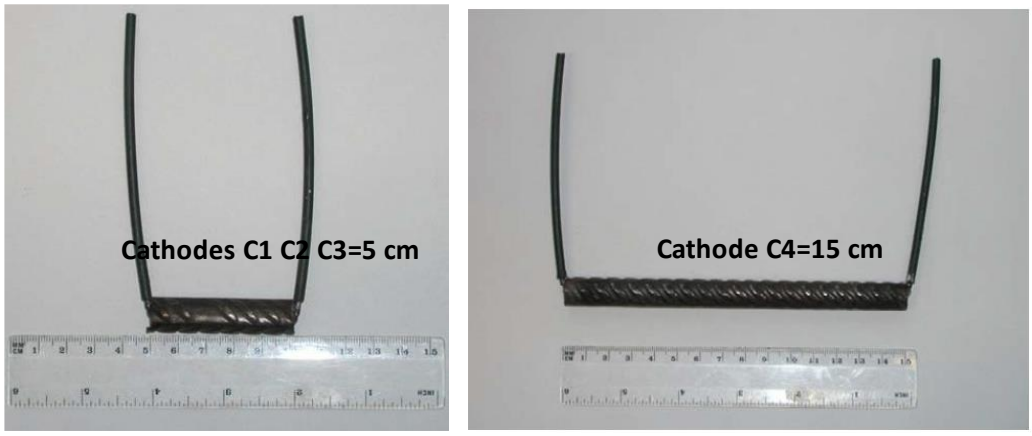

Figure 3-4: Dimension of the cathodes

To investigate the effect of concrete cover on corrosion, anodes are embedded with three different (2 cm, 3.5 cm and 5 cm, Type I) or three constant (5 cm, Type II) cover depths, as shown in Figure 3-5. The concrete surface without exposure was coated by epoxy resin. The

coating was necessary to comply with the aim of one dimensional influence on the cover of each anode and their corresponding cathodes.

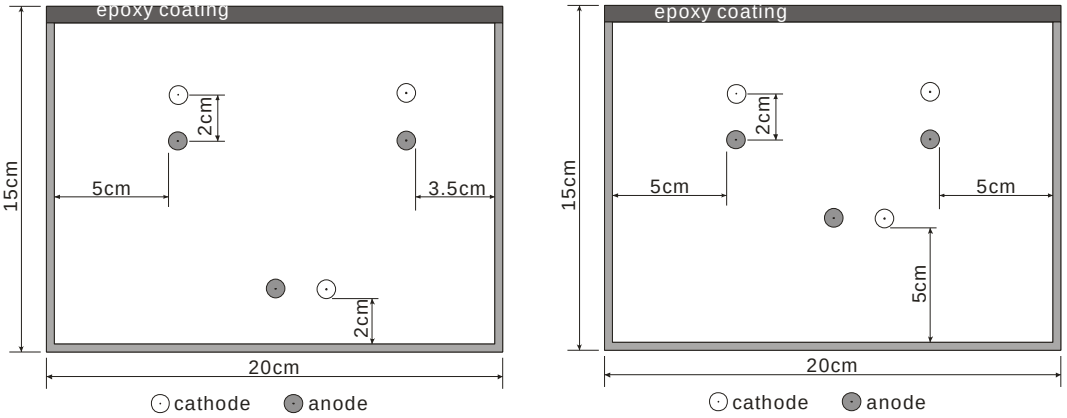

(a) Type I: with different cover depths (b) Type II: with constant cover depths

Figure 3-5: Cross section of cracked beams

The method of defining cracks

To be able to create a crack with fixed crack width as well as in the predefined position, double layered thin metal foils with 0.30 mm's thickness are prearranged in the middle of the beam before casting, Figure 3-6. A weak cross section is consequently created and single crack can be produced at the expected position during the tension test.

In tension test (Figure 3-7), the crack width was first adjusted to about 0.32 mm. Then metal foils of 0.30 mm thickness were inserted between the two embedded foils and the load was reduced again activating the spring force of the reinforcement Figure 3-8. Hence, the crack width could be set precisely to 0.30 mm, having it crossing exactly through the anodic area of the reinforcement. Afterwards, both steel plates were cut off. The details of the insert foils are shown in Figure 3-8 and Figure 3-9.

Concrete Composition

As cement type a Portland cement (CEM I 32.5 R) and a blast furnace slag cement (CEM III/A 32.5 N-LH) with a content of 360 kg/m³ were used. Furthermore limestone sand, gravel with a maximum aggregate size of 16 mm, tap water and water reducing agent at a w/c ratio of 0.5 and 0.4 respectively complete the concrete mixture. Concrete mixture is shown in Table 3-1. Mean values of the cube compressive strength at an age of 28 days are shown in Table 3-2.

Figure 3-6: Stainless foils are prepositioned in

Figure 3-7: Creating cracks with tension tests

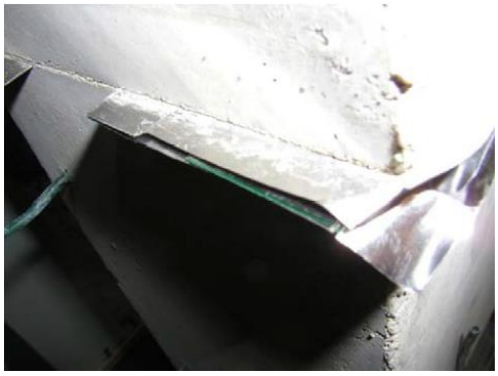

Figure 3-8: Foils in the crack zone.

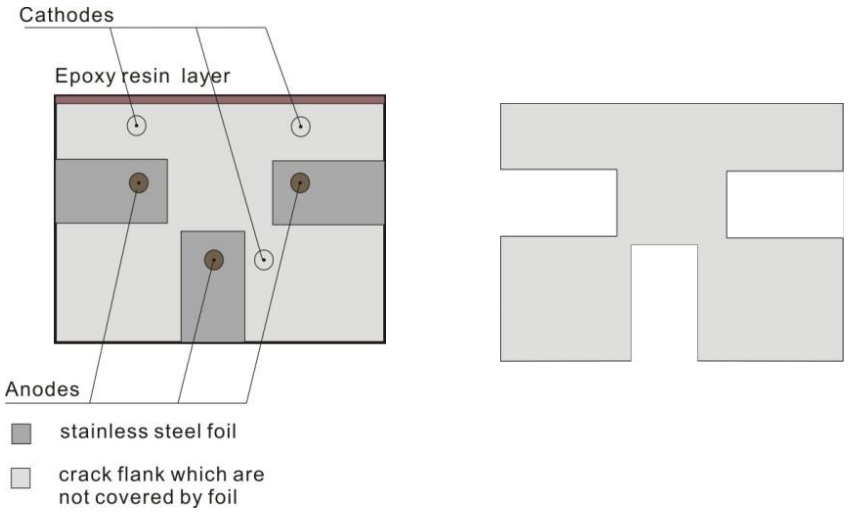

(a) Crack cross section (b) Shape of the stainless steel foil

Figure 3-9: Crack cross section

Table 3-1: Concrete composition of beams

Series A	Series B	Series C

0-4 cm	880	0-4 cm	877	0-4 cm	920
4-8 cm	475	4-8 cm	473	4-8 cm	496
8-16 cm	526	8-16 cm	525	8-16 cm	550
CEM I 32.5 R	360	CEM III/A 32.5	360	CEM III/A 32.5	360
water	180	water	180	water	144
plasticizer	1.08	Plasticizer	2.52	plasticizer	12.6

Table 3-2: 28 day compressive strength

	Series A	Series B	Series C
	CEM I 32.5 R, w/c ratio 0.5	CEM III/A 32.5, w/c ratio 0.5	CEM III/A 32.5, w/c ratio 0.4
Compressive strength [N/mm²]	54	55	58

3.2.2 Curing and exposure conditions

Curing

For curing, the specimens were left in mould at 20°C and 85% relative humidity (RH) for 7 to 14 days. Then the cracks were produced by tensile test. To simulate the situation of old structures or structures in industrial environments, at an age of 28 days a group of specimens are carbonated by being stored in the carbonation chamber of 1 Vol.-% carbon dioxide for 28 days. After these preparations the specimens were stored again in 20°C/85% RH until hydration was proceeded to an age of about 180 days. Then the specimens were divided into three groups and stored in three different exposure conditions respectively.

Exposure conditions

Among the various exposure conditions, cyclic wetting and drying in chloride rich environment is considered as the most aggressive one. The cyclic action enhances corrosion rate and aggravates durability problems as a result of two actions: on one hand, during the wetting period chloride ions diffuse or are sucked into the non-saturated concrete. The effect of capillary suction highly accelerates the chloride penetration rate; on the other hand, during the drying period the chloride concentration in the pore structure is condensed due to the moisture evaporation and furthermore, oxygen could penetrate quickly during the dry period to support the cathodic reaction. Unlike the submerged conditions (cathodicaly controlled corrosion) or the dry atmosphere-exposed conditions (anodically controlled or ohmic controlled), all the requirements needed for both the anodic and cathodic reactions

(moisture, oxygen, corrosion promoting substances, high conductivity electrolyte, etc.) could be fulfilled in cyclic chloride wetting conditions.

Cyclic wetting and drying of chloride rich environment can be commonly found in:

- Marine structures, particularly in the splash and tidal zones;
- Parking garages, in areas exposed to de-icing salts; and
- Highway structures, such as bridges and other elevated roadways.

Therefore, in the design of this research, a chloride wetting-drying cycle is selected as the main exposure conditions; additionally, a wetting-drying cycle with tap water is also applied to a group of specimens; natural unsheltered exposure is chosen as well to simulate the atmosphere-exposed situations.

The three different exposure conditions are given in detail as follow:

- Chloride cycle: stored in laboratory (approximately 20°C and 40-50% RH) and sprayed with 1% chloride solution (1.0 m.-% Cl^- by $NaCl:CaCl_2 = 9:1$, which simulates the conditions such as deicing salts applied in German roads) in the crack area, 1 hour per week;
- Water cycle: similar to chloride cycle but wetted with tap water;
- Natural exposure: subjected to normal weather conditions (direct rain, wind, sunshine etc.) in Munich, Germany, typical temperate continental climate;

In the two cyclic exposures, chloride solution or tap water are sprayed directly into crack via a hose with drilled holes. A gutter is positioned to hold the hose and meanwhile prevent the leakage of chloride solution or water outside of crack area, as shown in Figure 3-10.

Except the 1 hour's wetting time, the specimens are subjected to 167 hours drying period in laboratory climate per week. The laboratory climate is shown in Figure 3-11.

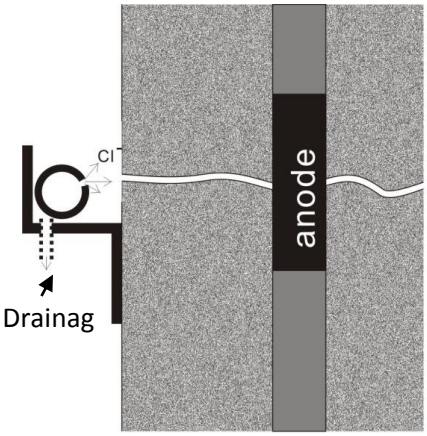

Figure 3-10: Setup of watering system

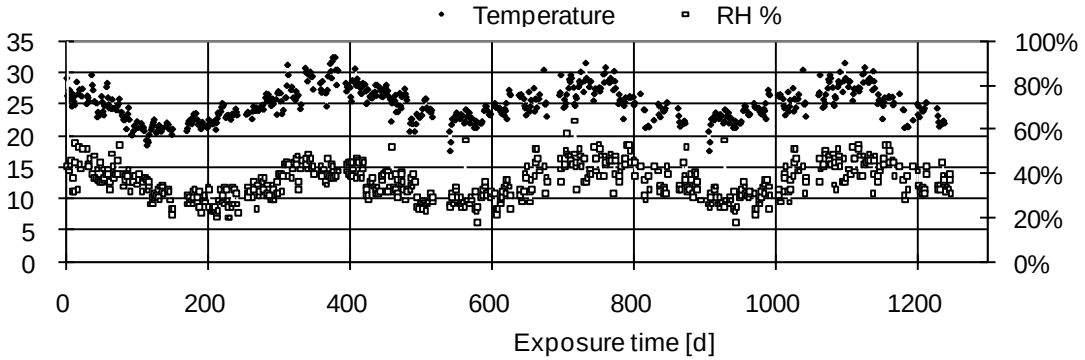

Figure 3-11: Laboratory climate

3.2.3 Specimens with Multi-Ring-Electrodes

Additionally to the corrosion specimens, specimens for measuring resistivity of the concrete beams by Multi-Ring-Electrodes were also produced.

The Multi-Ring-Electrode was originally designed to monitor the moisture conditions inside concrete in an indirect way: by monitoring the concrete's electrolytic resistivity. This is based on the principle that moisture content is somehow inversely related to the concrete resistivity. The electrolytic charge in porous material is carried by dissolved anions and cations. Therefore when moisture content increases, the amount of ion-carrying pore liquid increases accordingly, leading to a drop of electrolytic resistivity.

Multi-Ring-Electrode is a sensor which could measure the electrolytic resistivity at different depths and over a long period of time. The sensor consists of nine rings of stainless steel, which are isolated from each other by keeping a predefined distance by means of polymer rings, as shown in Figure 3-12. The electrolytic resistance is measured between the adjacent two rings, which are positioned above one another, by means of the two electrodes method

[139]. Then the resistance could be transferred to electrolytic resistivity by a known cell constant (k=0.1m).

Two Multi-Ring-Electrodes are embedded in each specimen, with one on the top of the beam while the other close to the crack area, Figure 3-13. In this case, the resistivity and moisture field in both top area and crack area could be monitored. Multi-Ring-Electrode measurements are conducted monthly to examine the resistivity and moisture change over exposure time.

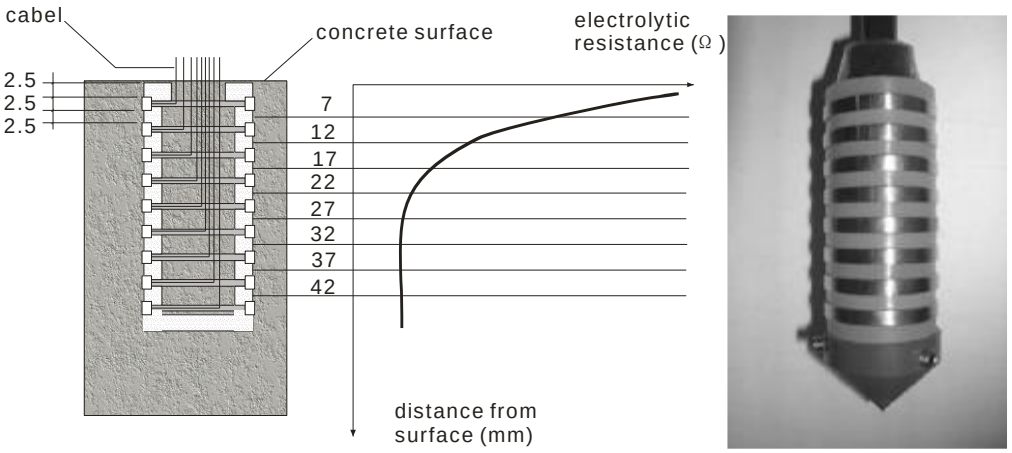

Figure 3-12: Multi-Ring-Electrode

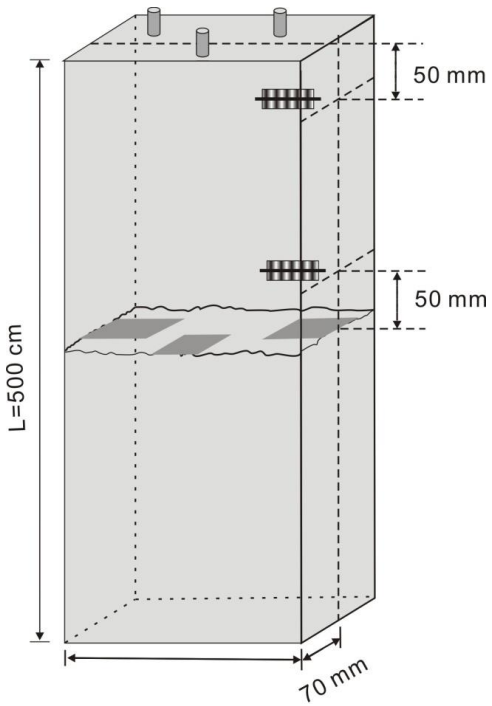

Figure 3-13: Setup of Multi-Ring-Electrode specimen

3.2.4 Measuring technique

In the range of this study, only macro-cell corrosion is taken into account. Macro-cell corrosion current is defined as an electron current flow between the anode and cathode. In order to carry out current measurements, the connection between the anode and the four cathodes are short circuited by a four-pole switch. The reference voltage is measured by an amplifier with 100 MΩ input resistance via $Cu/CuSO_4$ reference electrode. The corrosion currents and anode potential are measured once daily.

The measurement of micro-cell corrosion current due to local element development at the assumed anode is not possible in this experimental arrangement.

Destructive tests

The cracked beams in three different exposures are opened step by step in three batches. In each batch, nearly 1/3 of the specimens in each climate were opened. Exposure duration for specimens in different batches varies and hence the time development of corrosion product could be examined.

Before the specimen opening, epoxy resin was injected into the crack to check if the crack is still thoroughly open after the long exposure period.

Chloride profile was obtained by drilling holes progressively into the crack. The diameter of the drilled hole was approximately 1 cm. Drilling position was right into the crack and perpendicular to the concrete casting surface. Drilled powder was collected in 1 cm step. For each depth, three samples were collected and mixed for the later analysis, as shown in Figure 3-14. The total chloride content relative to cement content could be determined by analysing the drilled powder with titrating method with AgCl.

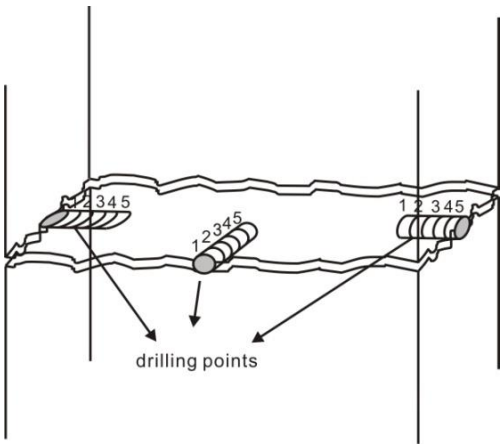

Figure 3-14: Drill positions in cracked area

In order to obtain the chloride profile perpendicular to crack flanks, blocks which contain both crack flank and concrete casting surface were collected. As shown in Figure 3-15, the crack plane, which was not covered by the foil, was divided into five strips in 1 cm step (relative to concrete surface). Concrete powder was collected by grinding in each strip for a layer of 1.5-2 mm depth (relative to crack flank). Only 3 layers were ground off since it is difficult to keep the whole layer in the same depth (relative to the crack flank). Then the grinded powders were collected for chloride concentration analysis.

Specimens were opened with split test, as shown in Figure 3-16. After the beams were split up, concrete cover was removed; anodes, cathodes, as well as $Cu/CuSO_4$ reference electrodes were taken out. Reference electrodes were carefully examined to see if any dry-out or leakage had happened during the exposure. The potential of the reference electrodes were then calibrated to make sure that they functioned well. If the values have deviated from -325 mV, the anodic potential has to be corrected accordingly.

Visual inspections of the rebar surface were carried out after the removal of cover concrete. Actual anode area and pitting depth were measured.

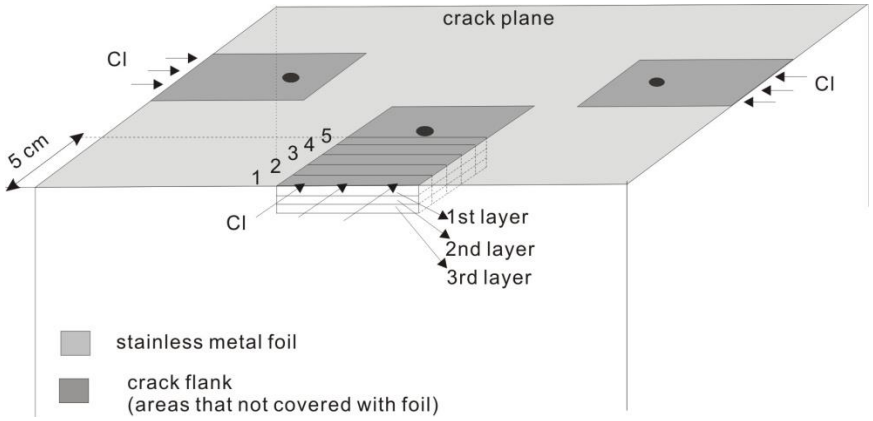

Figure 3-15: Chloride content analysis by grinding test

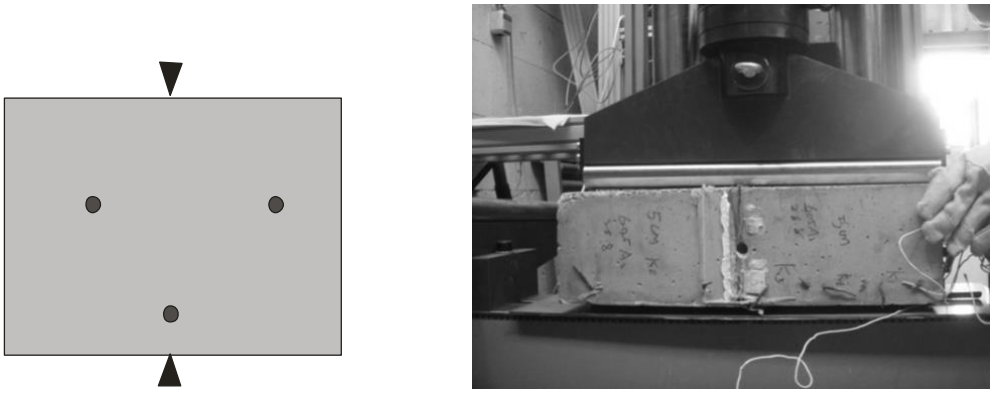

Figure 3-16: Open specimen with split test

As have been clarified in Section 3.1, micro-cell corrosion could not be measured due to the experimental setup in this research. The quotation of micro-cell corrosion could only possibly obtained by subtracting the calculated macro-cell corrosion induced mass loss from the measured total steel mass loss. However, this could not be achieved due to the following reason:

- the original weight of the reinforcement is missing.
- errors between the calculated value of macro-cell corrosion induced mass loss and the actual value exists.
- the epoxy layer could not be removed exhaustively, which adds errors to the result.
- the weight of corrosion product is too small compared to the total weight of the reinforcement. A very small deviation in the measurement will interfere the final results.

Above all the enumerated reasons, it is nearly impossible to get the micro-cell corrosion rate.

3.2.5 Experiment matrix

To give a clear overview, the investigated parameters are summarized in Table 3-3.

In order to have the possibility to process a statistical analysis of the results, an adequate amount of specimens were produced, see Table 3-4 and Figure 3-17.

Table 3-3: Experimental matrix

Parameter	Influence	Variation
1	2	3
Crack geometry	crack width	0.30 mm
	concrete cover depth	2 cm, 3.5 cm, 5 cm
	others	single & transverse crack

Concrete quality	cement type	CEM I 32.5R, CEM III/A 32.5
	w/c ratio	0.4, 0.5
Environments	exposures	1% Cl^- solution 1h/week tap water 1h/week natural unsheltered exposures
	carbonated (only in crack cross section)	yes /no

Table 3-4: Numbers of specimens in the three exposures

	Chloride cycle		Water cycle		Outside unsheltered	
	Type I (different cover depth)	Type II (constant cover depth depth)	Type I (different cover depth)	Type II (constant cover depth depth)	Type I (different cover depth)	Type II (constant cover depth depth)
CEM I 32.5R (w/c=0.5), non-carbon	3	2	3	0	3	
CEM I 32.5R (w/c=0.5), carbon	0	1	0	1	0	1
CEM III/A 32.5 (w/c=0.5), non-carbon	3	0	3	0	4	
CEM III/A 32.5 (w/c=0.5), carbon	0	1	0	0	0	0
CEM III/A 32.5 (w/c=0.4), non-carbon	0	1	0	0	0	0

(a) In laboratory

(b) In natural unsheltered exposure

Figure 3-17: Specimens stored in different environments

3.3 Results

To make it easier for understanding, brief notations are adopted to describe the concrete mixture, as shown in Figure 3-18. For example, concrete mixture with CEM I cement with w/c ratio of 0.5 and a cement content of 360 kg/m^3 is denoted as I05360.

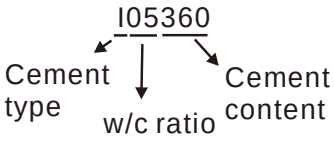

Figure 3-18: Simplified notation of concrete mixture

3.3.1 Initiation period

Depassivation could be judged in several ways: the observation of potential drop; decrease in polarization resistance; increase in corrosion current density; or by the visual observation of corrosion products. Alonso, *et al* [1] have suggested $1\mu A / cm^2$ as the threshold corrosion rate for active corrosion. However it is not realistic to follow this criterion in this research since the data being recorded is not in the form of current density, but current. The corrosion area remains unknown until the destructive tests. Therefore, in the range of this research, depassivation is judged by the observation of a sudden drop in anodic potential and the simultaneous drastic increase in corrosion current, as shown in Figure 3-19. Since the anodic potential and macro-cell current are monitored every day, the depassivation could be determined precisely.

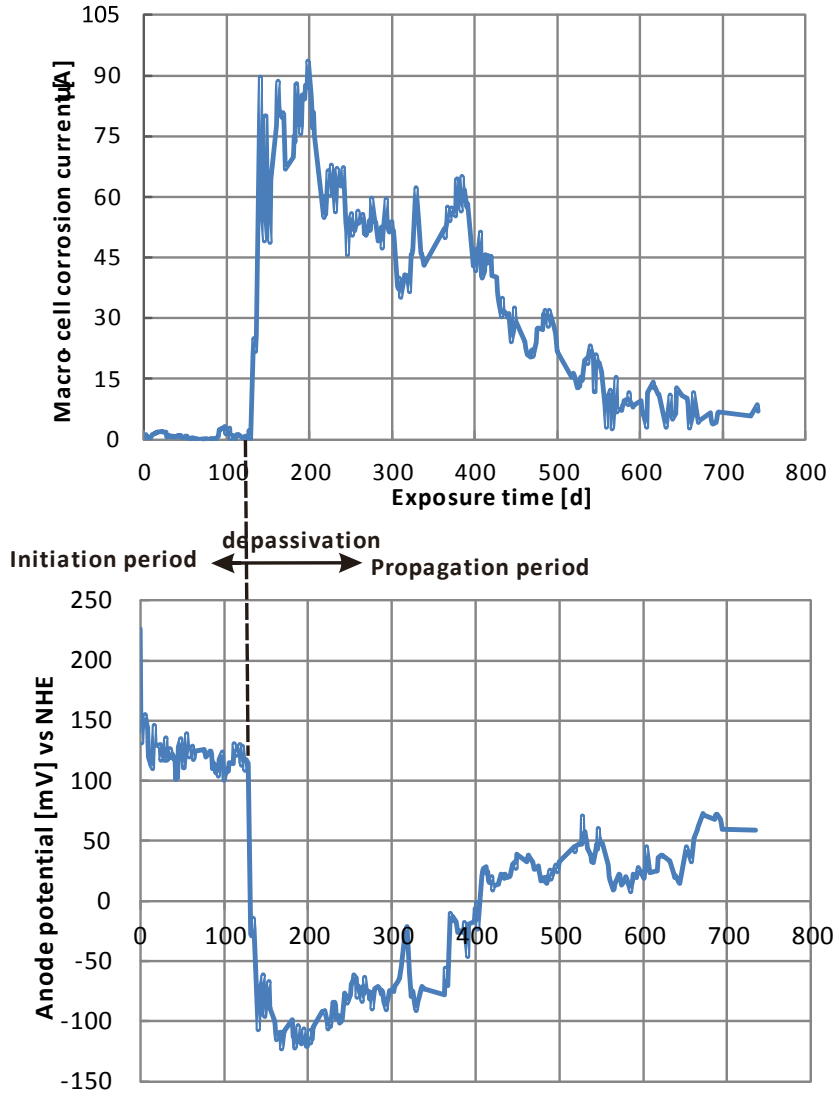

Figure 3-19: An example for determining depassivation

The crack width in this study is 0.30 mm and crosses the reinforcement, indicating that the time needed for chloride solution or tap water to reach the steel surface via crack can be extremely short. Additionally, the applied chloride concentration is 1%, which is high enough to depassivate the rebar. Therefore, the initiation period is expected to be very short.

It is observed that nearly all specimens in chloride cycle started to show active corrosion after a short time of exposure, while most specimens in water cycle and natural unsheltered exposure remain passive over the whole exposure period. Therefore, the following discussion is mostly focused on the specimens which are exposed to chloride cycle.

Figure 3-20 contains information about initiation periods of both I05360 and III05360 specimens in chloride cycle. The results are average values from several samples with the

same mixture and cover depth. In Figure 3-20 (a), a trend of longer initiation period with increasing cover depth could be observed. Anodes depassivated with an average duration of 68, 92 and 131 days for 2 cm, 3.5 cm and 5 cm cover depth respectively. For III05360 concrete (Figure 3-20 (b)), anodes with 2 cm cover depth depassivated almost immediately when the chloride solution is applied; while anodes with 3.5 cm and 5 cm cover depth depassivated after 70-80 days wetting. To some extent thicker concrete cover shows a superior resistance to depassivation. This is because that corrosion of steel also depends on the availability of oxygen, not through the crack, but through the uncracked concrete cover next to the cathodic area.

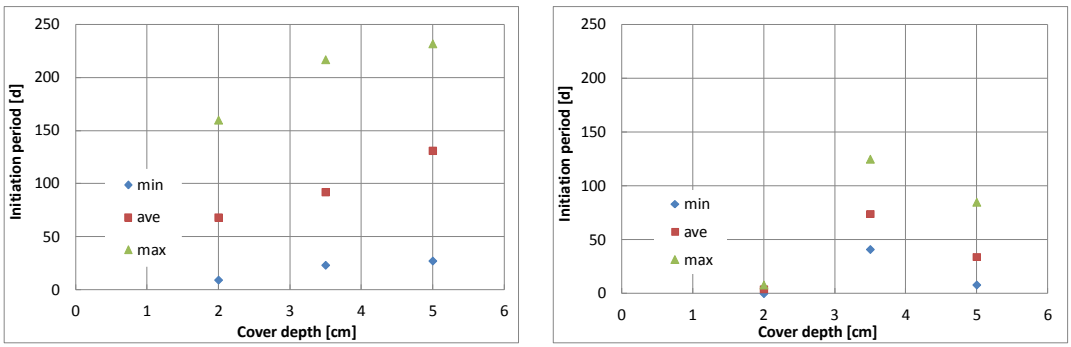

(a) I05360 (b) III05360

Figure 3-20: Initiation periods of specimens in chloride cycle

Comparing the two diagrams in Figure 3-20, it is found that initiation period of CEM I concrete lasts longer than CEM III concrete. In earlier studies, researchers have investigated the influence of cement type on the depassivation of chloride induced corrosion. Gouda and Halaka [140] found lower chloride threshold values for slag containing concrete specimens compared to OPC specimens, whereas Schieβl and Breit [141] reported the opposite trend. The effect of addition of GGBS on critical chloride content is double edged. On one hand, GGBS increases the chloride binding capacity due to improved chemical reaction and physically adsorption and consequently enhances the critical chloride content (if total chloride content is defined as critical chloride content); on the other hand, however, it decreases the pH of the pore solution: a pH of 12.4 in case of 60% replacement of OPC by GGBS was reported [142]. This means a lower critical chloride content in CEM III concrete.

Therefore, in this research the longer initiation period in CEM I concrete could be attributed to its higher OH^- content. Although CEM III concrete has a better chloride binding capacity, it seems that in the case of cracked concrete with direct chloride supply via the crack, free chloride content around the anode is always sufficient to break down the passive layer.

The large deviation of initiation period (from 0 days to around 200 days) could be due to the tortuous conditions of the crack flank and the inhomogeneity of the concrete microstructure of the passive film on the steel of individual specimens.

w/c ratio seems to play a crucial role in resisting depassivation as well. During three years exposure, all the three corrosion cells of III04360 (with lower w/c ratio 0.4) in chloride cycle behave inactively, except that only one of them shows a sudden increase in corrosion current at 205 days exposure, as shown in Figure 3-21. This increase is in such a small range that could nearly be neglected. However, the small rust spot observed in later-conducted destructive measurements indicates that this anode indeed slightly corroded.

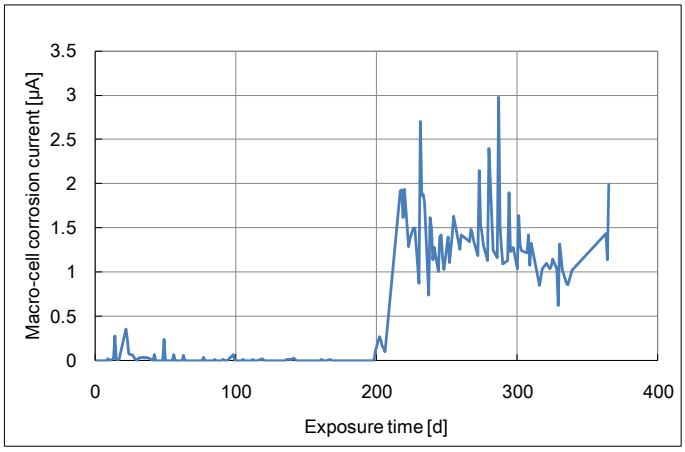

Figure 3-21: Macro-cell corrosion current, III04360, Cl cycle

No great increase of macro-cell corrosion current was observed in those specimens subjected to water cycle and natural unsheltered exposure. Most of them kept passive during the whole exposure period, with only several of them showed an increase of corrosion current in a small range.

Initiation periods of the specimens in chloride cycle are in the range of 1 year, which is as expected. It is a rather short period if compared to the relatively long service life of concrete structures. So a conclusion could be drawn that in the case of cracked concrete in chloride rich environment, an intensive corrosion could occur immediately.

3.3.2 Corrosion currents and potential- propagation period

As mentioned in the last section, nearly all the corrosion cells in chloride cycle with w/c ratio of 0.5 showed active corrosion. Specimens in water cycle and natural unsheltered exposure remain passive, or strictly speaking, did not show obvious active corrosion. So the following discussions are mostly focused on the specimens in chloride cycle.

Figure 3-22 contains results of macro-cell corrosion currents (above) and anodic potentials (below) of selected active anodes from chloride cycle. The three curves belong respectively to corrosion systems from:

- Series 1: I05360, i.e., CEM I concrete, w/c ratio 0.5 , chloride cycle
- Series 2: III05360, i.e., CEM III concrete, w/c ratio 0.5, chloride cycle
- Series 3: III04360, i.e., CEM III concrete, w/c ratio 0.4, chloride cycle

Each curve represents typical behaviour of its category. At the beginning of the chloride wetting-drying cycle, corrosion currents are around zero which indicates passive state. After a few days of exposure, the corrosion current in I05360 concrete increases steeply, which clearly announces the beginning of corrosion. It keeps on increasing till a peak of 119 µA is reached and then decreases gradually. Compared with I05360 concrete, corrosion in III05360 concrete is not so intensive. After depassivation corrosion current increases to the maximum value and then decreases smoothly. Both corrosion current curves show strong periodical vibration due to the weekly wetting and drying cycle with chloride solution. The vibration amplitude decreases with time which indicates that the moisture condition inside the concrete approaches an equilibrium state.

Meanwhile, as can be seen in Figure 3-22 (below), the variation of potential curves shows perfect agreement with current curves. A significant drop of anodic potential can be found exactly at the same moment when the steep increase of corrosion current is observed. This potential drop ΔU is 200mV for I05360 sample and 250 mV for the chosen III05360 sample. The order of anode potential over the exposure time is typically I05360 < III05360< III04360, which is opposite to the order of corrosion current.

Compared to I05360 and III05360 samples, the macro-cell corrosion current of III04360 sample remains around zero (red line), with its potential remaining high during the whole exposure time.

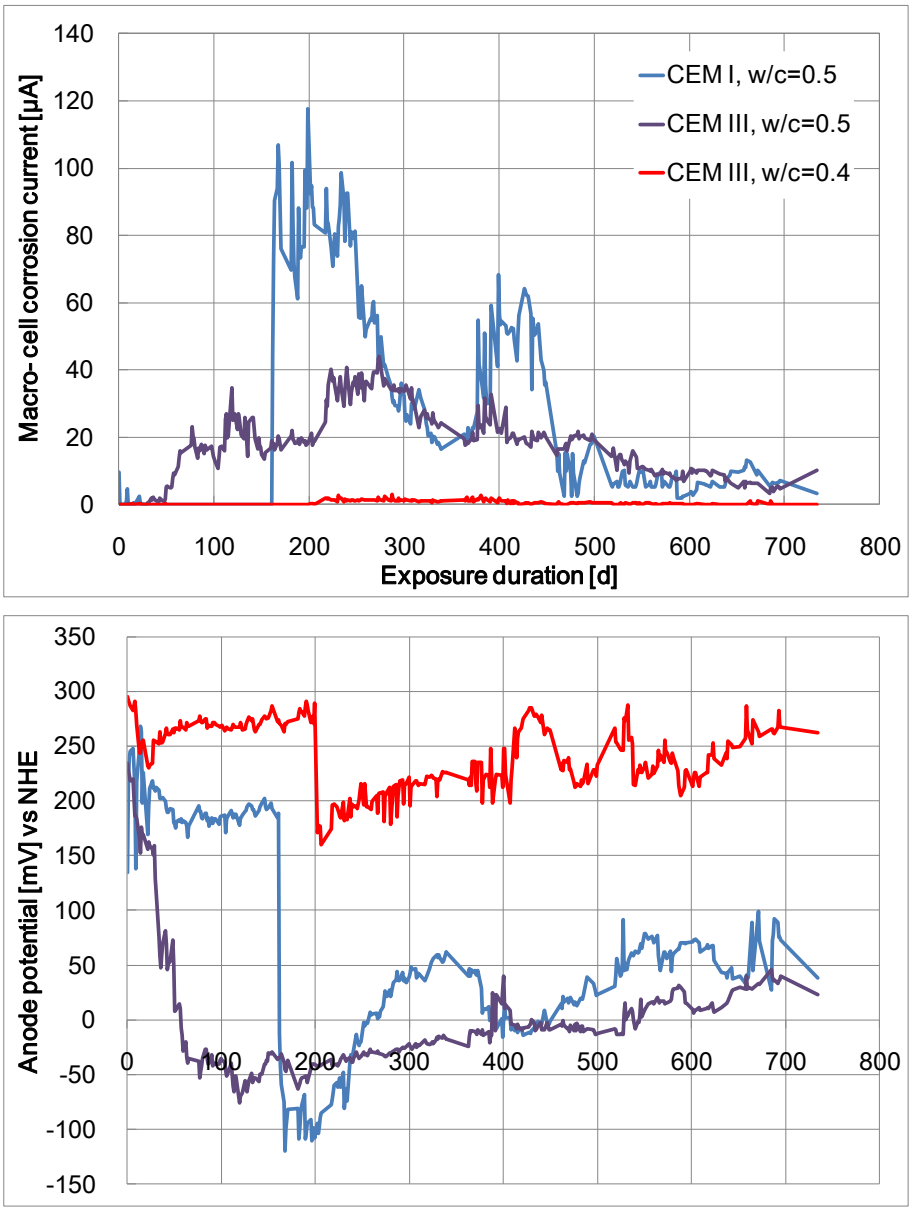

Figure 3-22: Corrosion current (above) and potential (below) of specimens in chloride cycle

Time variant process of corrosion current in cracked concrete

Corrosion is a dynamic process which is influenced by the environmental conditions over the exposure duration. As the initiation period being extremely short in cracked concrete, it is of great importance to build a model to describe the time-dependence of corrosion intensity since the residual service life depends greatly on the propagation period.

After examining the time variation of macro-cell corrosion current of all the depassivated anodes in chloride cycle, some common trends are found. The propagation period could be divided into three phases: the ascending phase, descending phase, and the equilibrium

phase. As shown in Figure 3-23, trend lines are added to characterize each phase. k_i represents the slope of trend lines.

Before P1: Initiation phase. Embedded reinforcement is still passive. This period is quite short for steels in cracked concrete subjected to cyclic chloride attack.

P1: Ascending phase. Critical chloride content at steel surface has been reached; the passive layer is broken down. Corrosion current increases steeply due to the continuous and sufficient supply of chloride ions and moisture.

P2: Descending phase. Corrosion current decreases gradually in this period. The decrease might be because of: 1) the pore structure became denser and denser due to the hydration process, leading to higher concrete resistivity and lower oxygen/moisture permeability; 2) more and more corrosion products accumulated on the surface of anode hence baffled further anodic oxidation, leading to partly repassivation again;

P3: Equilibrium phase. When the corrosion current density decreases to a certain level, the equilibrium between moisture/oxygen consumption and supply is built; the hydration process of concrete is almost completed. The increase of concrete resistivity slows down at this age which means the main corrosion resistance is also approaching equilibrium. Therefore corrosion rate tends to become steady.

The time span and the slope of each period might differ, depending on the concrete micro-structure, crack geometry and environmental conditions. Based on the model described in Figure 3-23, corrosion rate during the whole propagation period could be predicted.

Phase 3 might last for a long period till corrosion induced cracks are generated. The corrosion induced cracks will create new transportation paths for corrosion promoting substances, moisture and oxygen, leading to the re-arrangement of corrosive conditions. Actually, no corrosion induced crack was observed in the scope of this research.

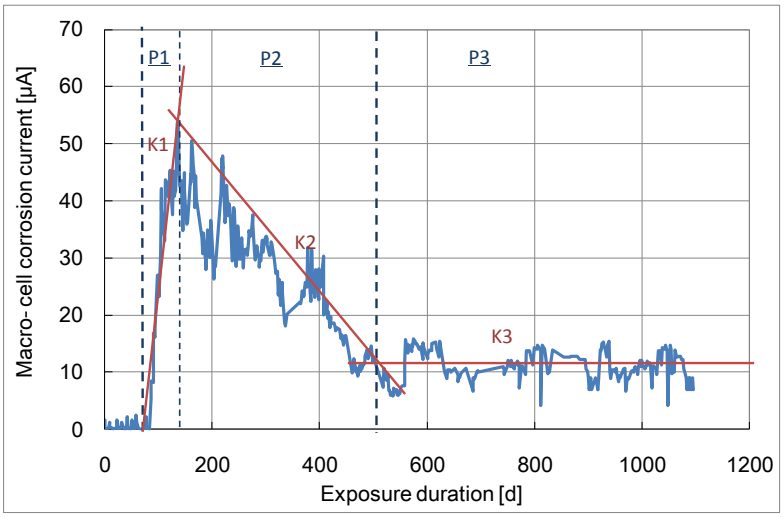

Figure 3-23: An example for time dependence of corrosion current, III05360, cover= 5 cm, chloride cycle

Figure 3-24 shows the average corrosion current of the first year, second year and third year of all the individual corroded anodes. It is the main trend that the annual average I_{macro} decreases with exposure duration. The difference between the second year and third year are much smaller than that between the first two years, which indicates that the corrosion intensity is approaching equilibrium.

The notation 'AEC' in Figure 3-24 refers to 'Average Equilibrium Current', which is the averaged corrosion current of all individual samples at equilibrium state. AEC for I05360 and III05360 are 16.22 µA and 6.96 µA respectively.

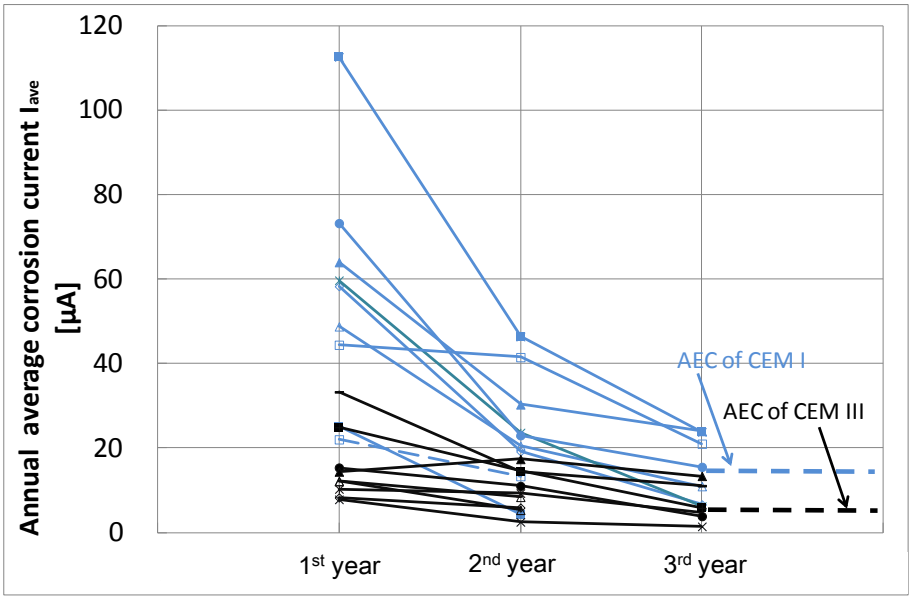

Figure 3-24: Annual average macro-cell corrosion current density over the exposure period, (A_a= 15.07cm^2)

3.3.3 Factors influencing corrosion in cracked concrete

Cement type

Cement type is one of the main factors which influence the corrosion intensity of reinforcement. Table 3-5 illustrates an average value of total electric charge that transported in the corrosion system in one year's duration after depassivation, for both CEM I and CEM III concrete. The total electrical charge is obtained by integrating the daily measured corrosion current with exposure duration:

$$Q_{acc} = \int I_{macro} dt \tag{3.1}$$

Q_{acc}- Accumulated macro-cell corrosion current, in [C]

If a comparison is made between I05360 and III05360 concrete, one can find out that Q_{acc} in I05360 concrete beams during the entire exposure time is approximately 1.54, 1.71 and 3.36 times larger than that in III05360 for 2 cm, 3.5 cm and 5 cm cover depths respectively. The ratio increases with cover depth.

The better corrosion resistance of CEM III concrete could be attributed to its denser microstructure induced by slag content. The benefits of denser microstructure are that: Firstly, moisture and oxygen penetration into concrete is retarded; Secondly, the concrete resistivity with denser microstructure is much higher than those without. The high concrete resistivity of CEM III has been proved by the parallelly conducted resistivity measurement on prism samples. Results show that resistivity of III05360 concrete could be two to three times of I05360 concrete, given the same w/c ratio and moisture content. The addition of ground blast furnace slag in CEM III cement increases the chloride binding capacity since these mineral additives form additional calcium aluminate hydrates in their reaction, which retards the penetration of chloride ions and reduces the free chloride content in pore solution.

Table 3-5: Averaged accumulated macro-cell corrosion current (Q_{acc}), one year exposure

Cover depth [cm]	CEM I, w/c=0.5 [A·s]	CEM III, w/c=0.5 [A·s]	Ratio between I05360/III05360
2	427	277	1.54
3.5	578	338	1.71
5	1191	354	3.36

It has been also observed that the pattern of corrosion current is different for steels embedded in CEM I and CEM III concrete. Generally, steels in CEM I concrete exhibit a rather

steep increase in corrosion current after depassivation. The peak of I_{macro} could reach as high as 270 µA. Then I_{macro} also decreases fast and finally reaches its equilibrium current. The ascending and descending phases (P1 and P2) in CEM III concrete are relatively smooth and last longer. There is no steep peak appeared; the maximum I_{macro} observed are all under 50 µA. The typical corrosion current patterns of both concrete are shown in Figure 3-25. The maximum I_{macro} observed in the entire exposure duration are shown in Figure 3-26.

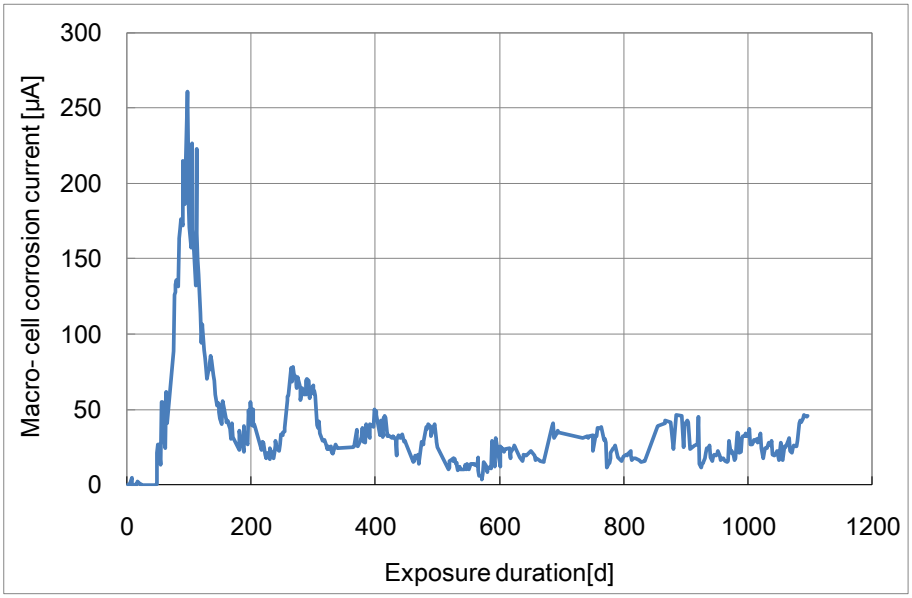

(a)I05360, cover= 5 cm, Cl cycle

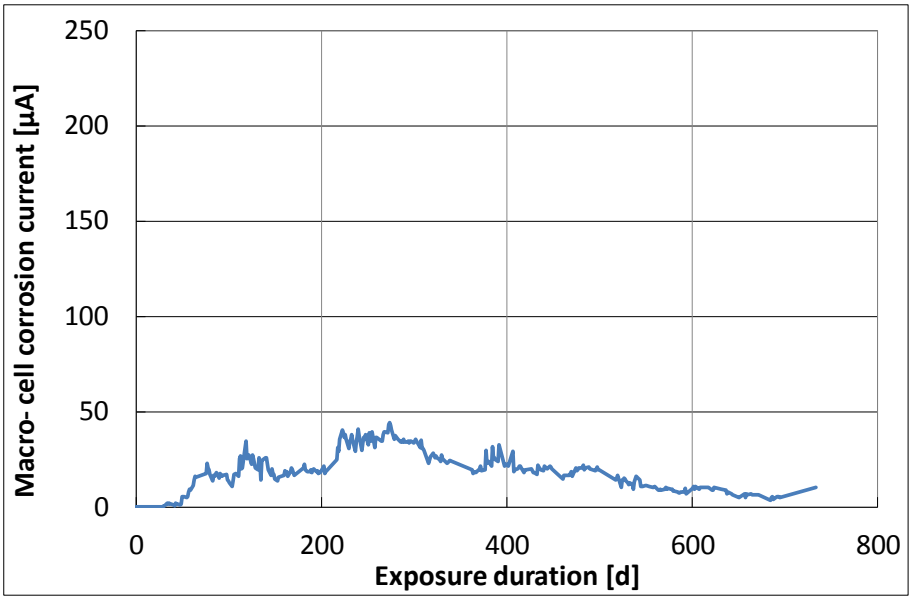

(b) III05360, cover= 5 cm, Cl cycle

Figure 3-25: Examples for time dependence of corrosion current, I05360 and III05360

The above discussions are all based on the corrosion currents I_{macro}, not the corrosion current densities i_{macro} since the anode areas are not known before the specimens are

destructed. Results obtained from destructive tests revealed that corrosion area of reinforcement embedded in III05360 concrete are generally larger than that in I05360 concrete. This indicates that if i_{macro} or the annual cross section loss is taken into account, corrosion intensity in CEM I concrete is even more serious.

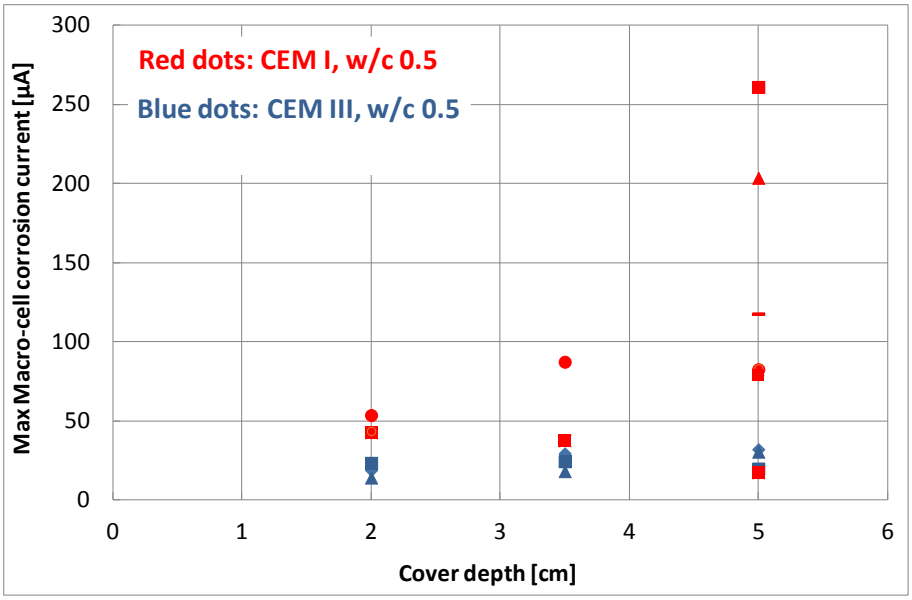

Figure 3-26: Maximum corrosion current during exposure, I05360 & III05360

w/c ratio

Compared to the sample with I05360 and III05360 concrete, the macro-cell corrosion currents of III04360 sample kept around zero. Their anodic potentials remained at high level during the whole exposure time. However, if enlarged, as shown in Figure 3-27, an increase in corrosion current and a simultaneous drop in anode potential could be observed, which indicate a possible depassivation. The maximum I_{macro} for III04360 is only 2.93 µA.

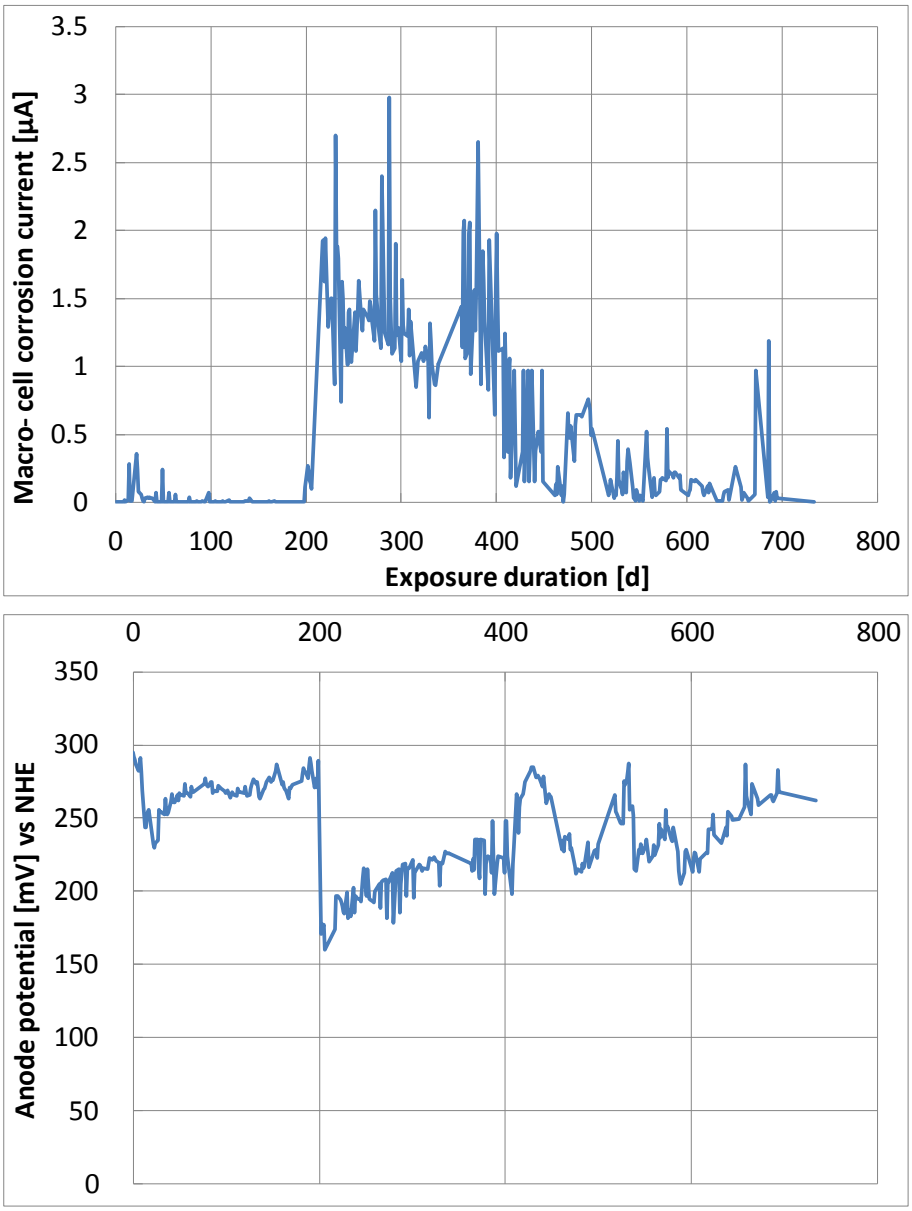

Figure 3-27: Corrosion current (above) and potential (below), III04360, cover=5 cm, Cl cycle

Macro-cell current distribution among cathodes- influence of cathode size and distance between anode and cathode

In order to investigate the effect of cathode size and distance between anode and cathode on the corrosion process, the four cathodes are arranged with different distances to the anode. Besides, the length of C4 is 15 cm, which is 3 times larger than the other three (C1, C2, C3= 5 cm).

In Figure 3-28, the separately measured corrosion currents for all corresponding cathodes are related to the sum of all cathodic currents. Data are collected from corrosion systems with 5 cm cover depth and are presented as averaged values. One can find out that, current

quotient of the three small cathodes, i.e. C1, C2 and C3, increase with the distance between them and the anode. The distant cathodes, C1 and C2, only seize a quite small proportion of the total corrosion currents. Their sum proportion is 25% for I05360 concrete and 19% for III05360 concrete. C3, which is the closest to the anode (3 cm from the anode), shares 25-30% of the entire current. C4 cathode shares more than half of the total I_{macro}, which is approximately the sum of the other three cathodes. Compared with C3, C4 possesses twice of the I_{macro} as C3 although it is further to the anode. This could be attributed to the relatively larger size of C4.

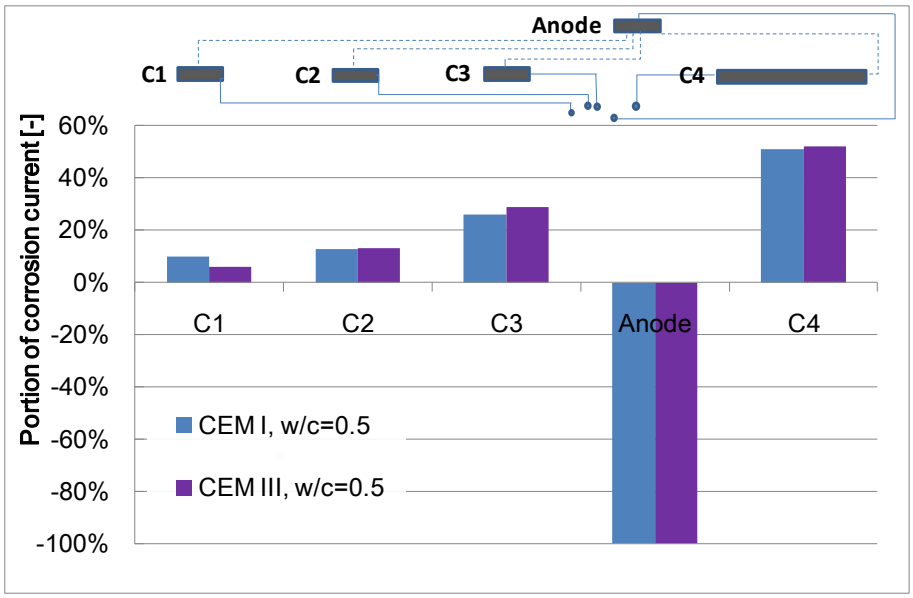

Figure 3-28: Proportion of corrosion currents for each cathode, I05360 & III05360, cover=5 cm, Cl cycle

From Figure 3-28, it can be concluded that the distribution of corrosion current among the cathodes is highly influenced by the concrete resistance between each cathode and the anode. To confirm this effect, resistance between anode and cathodes are measured by LCR-Bridge instrument. LCR-Bridge is a hand-held digital instrument which enables accurate measurements of resistance, capacitance, inductance, and dissipation factor. By directly connecting its two electrodes to the two ends of interested anode and cathode, a presented 50 mV potential is applied and then the resistance between the electrodes could be read. The age of the concrete beams is approximately 4 years when the measurements were carried out. Results are illustrated in Table 3-6.

To give a clearer overview, measured resistance data are converted into conductance, Figure 3-29. It is quite clear that the conductance between anode and cathodes in I05360 concrete

is much higher than that in III05360 concrete. For both concretes, the conductance increases from C1-A to C4-A.

Table 3-6: Resistance between anode and corresponding cathodes

	Cover depth[cm]	Resistance between electrodes [Ω]		
		I05360	III05360	III04360
A-C1	2	6267	39390	-
A-C2	2	3024	23110	-
A-C3	2	1967	15780	-
A-C4	2	1481	11992	-
A-C1	3.5	5076	25190	-
A-C2	3.5	2458	16250	-
A-C3	3.5	1675	13310	-
A-C4	3.5	1242	9754	-
A-C1	5	3639	21680	35670
A-C2	5	2367	13270	19200
A-C3	5	1358	10090	15950
A-C4	5	1139	7577	10090

* A for anode, C1-C4 for cathodes.

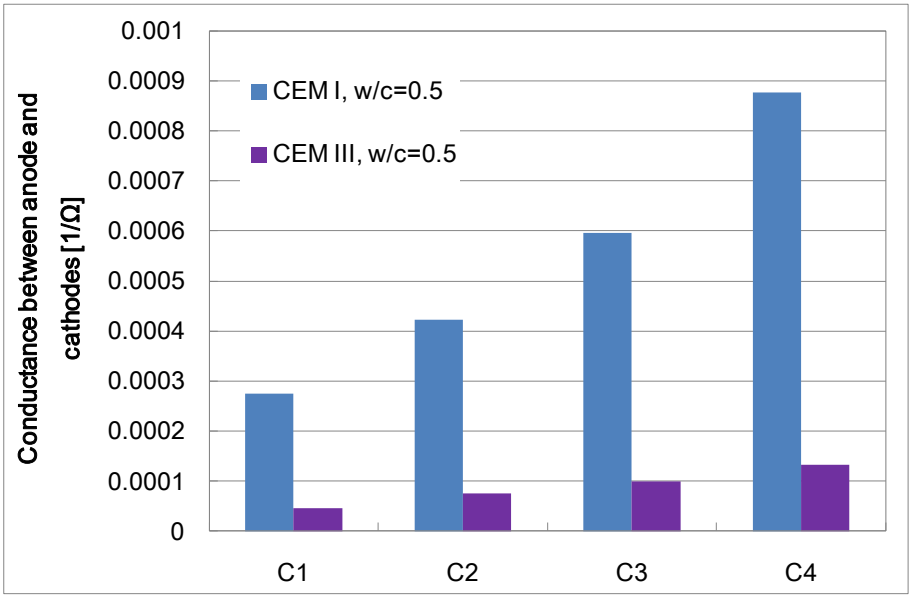

Figure 3-29: Conductance between anode and cathodes, I05360 & III05360

Figure 3-30 is the conductance portion of each cathode of the total conductance of the corrosion cell, which is calculated by:

$$P_i = \frac{C_i}{\sum_{i=1}^{4} C_i} = \frac{\frac{1}{R_i}}{\sum_{i=1}^{4} \frac{1}{R_i}} \tag{3.2}$$

where,

R_i - the resistance between anode and each cathode;

C_i - the conductance between anode and each cathode;

P_i - the conductance proportion of each cathode.

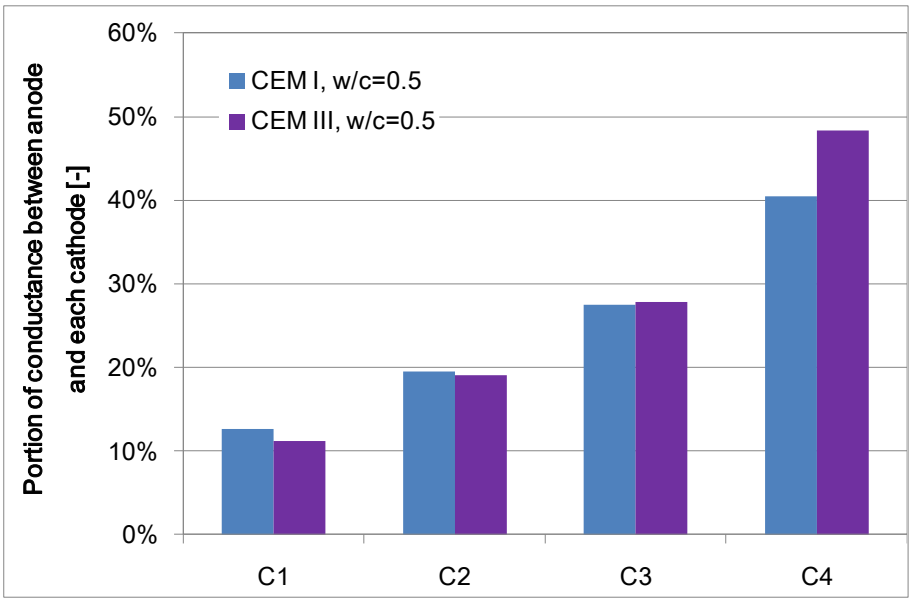

Figure 3-30: Proportion of conductance between anode and each cathode, I05360 & III05360

If a comparison is made between Figure 3-28 and Figure 3-30, it could be found that the distribution of macro-cell current and conductance agree very well with each other.

Considering the equivalent circuit model of macro-cell corrosion in Figure 2-5(b), macro-cell corrosion current could be determined by:

$$I_{macro} = \frac{\Delta U}{R_{p,a} + R_{p,c} + \mathrm{R_e}} \tag{3.3}$$

For the one anode with four cathodes corrosion system in this research, the total anodic corrosion current equals the sum of the four branch cathodic corrosion currents:

$$I_{macro} = \sum_{i=1}^{4} I_{macro,i} = \sum_{i=1}^{4} \frac{\Delta U_i}{R_{p,c}^i + R_{p,c}^i + \mathrm{R_e^i}} \tag{3.4}$$

Therefore, one could conclude that the corrosion current distribution is significantly dependent on the concrete resistance of the branch circuits. The impact of the polarization resistance is relatively not evident. It could also be observed that, the corrosion currents and conductance of III05360 specimen are more accordant compared to I05360, leading to the impression that corrosion systems in III05360 concrete, which has higher concrete resistivity, are more influenced by R_e.

Influence of carbonation

As mentioned in section 3.2.2, a group of specimens were carbonated to simulate the situation of old structures or structures in industrial environments. Results suggest that the carbonated specimens seem to be more susceptible to chloride induced corrosion than non-carbonated ones. Although there is no influence of carbonation on initiation period, the difference of propagation period between the carbonated and non-carbonated specimens is notable. Figure 3-31 illustrates the accumulated corrosion currents Q_{acc} in one year's exposure. An average magnification factor of 1.4 can be found between the carbonated and non-carbonated specimens for both I05360 and III05360 specimens. The combined effect of carbonation and chloride degradation causes more serious corrosion than a single effect. This might because that carbonation could dramatically reduce the chloride binding to almost zero [9].

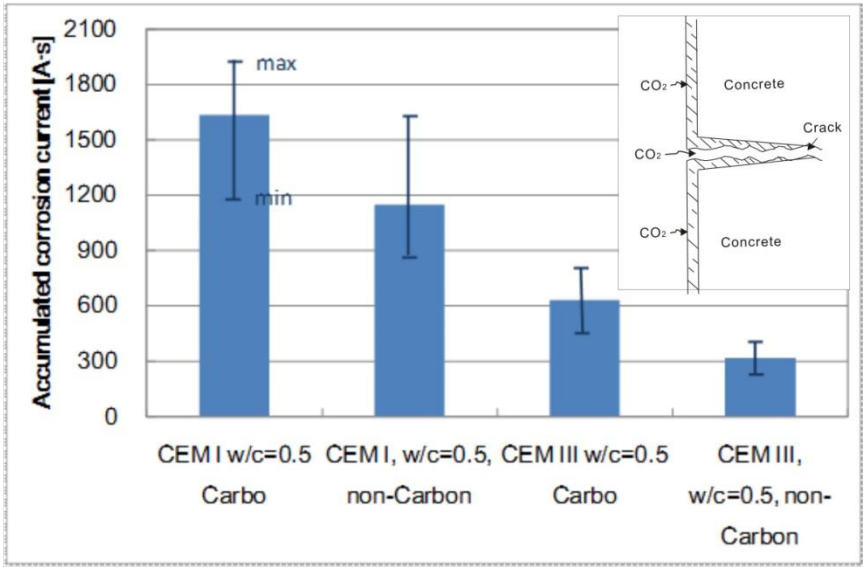

Figure 3-31: Comparison between carbonated specimens and normal specimens, I05360 &III05360, cover=5 cm, Cl cycle, one year exposure.

Environmental exposure conditions

Figure 3-32 illustrates time development of corrosion currents of two selected specimens in water cycle. Compared to the samples in chloride cycle, corrosion currents remained in a relatively low range. The maximum corrosion current observed is 15.5 µA for I05360 concrete and 7.39 µA for III05360 concrete. However, steep increase of current curve can be observed. Therefore, the current density might be not so low considering that the depassivated area might be also very small. Actually the very small corrosion spots that observed on the rebar surface in the later-conducted destructive test proved this hypothesis.

Figure 3-33 shows two chosen corrosion systems from natural unsheltered exposure. Both are I05360 concrete with 5 cm cover depth. The only difference between the two selected corrosion cells is that one is carbonated in the cracked zone, while the other is not. The macro-cell corrosion current of the carbonated sample showed a steep increase at around 400 days exposure and reached a peak value of 32 µA. The non-carbonated one kept passive during the whole exposure duration, which was mostly the case of the specimens in natural exposure.

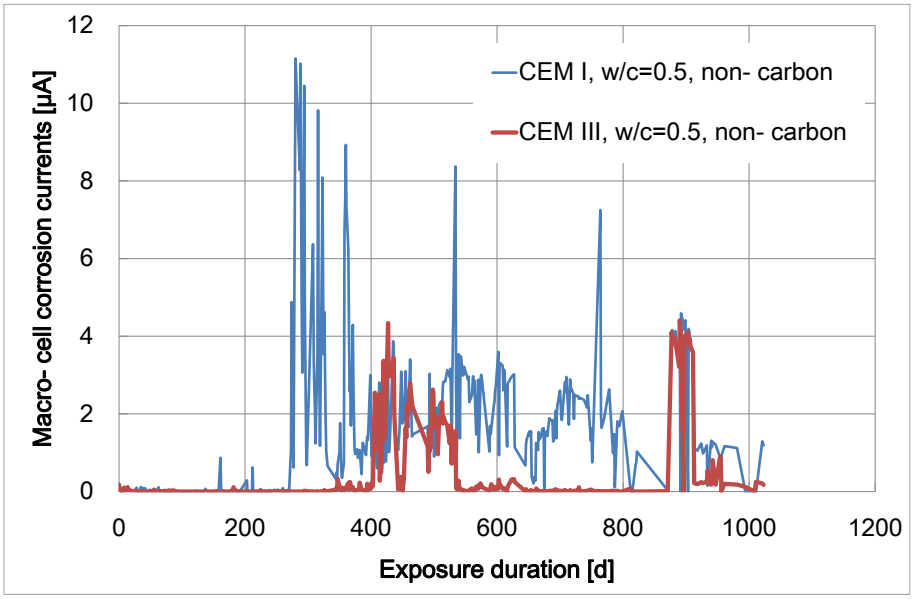

Figure 3-32: Time development of corrosion currents, I05360 &III05360, cover = 2 cm, water cycle

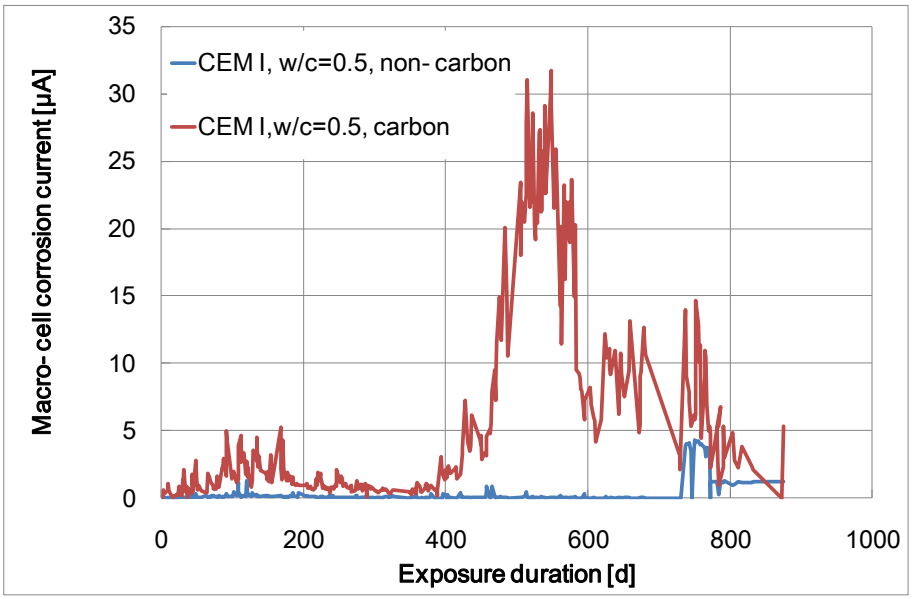

Figure 3-33: Time development of corrosion currents of I05360, cover = 5 cm, natural unsheltered exposure

3.3.4 Results from destructive measurement

General

According to the research plan, specimens in each environment are opened in three batches. In each batch, approximately 1/3 specimens in each exposure were destructed.

Carbonation depth

Being stored in laboratory climates and natural unsheltered exposure for different exposure durations, the concrete beams are carbonated to different extent. During specimen opening, carbonation depth was measured by spraying phenolphthalein solution onto the fresh-exposed concrete surface, as shown in Figure 3-34. Results were obtained by the average value of ten measuring points along the margin. When choosing the measuring points, areas with big aggregates were avoided.

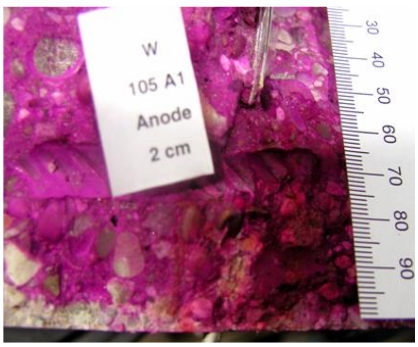

Figure 3-34: Carbonation tests, I05360, 1 year exposure

Figure 3-35 illustrated measured carbonation depth of both I05360 and III05360 concrete beams in laboratory climate and outside unsheltered climates, with the exposure duration of 1.5 years, 2.5 years, and 3.5 years. It is clearly shown that III05360 concrete has a much higher carbonation depth than I05360 concrete. The average carbonation depth after 3.5 years exposure for III05360 concrete is around 7 mm; while only 3-4 mm for the I05360 concrete. This is because that carbonation reaction in CEM III concrete leads to a coarsening of the pore structure which allows CO_2 to penetrate more easily into the concrete [143]. Moreover, the pH of CEM III concrete is slightly lower than CEM I concrete, suggesting a more vulnerable environment to carbonation.

Specimens in outside unsheltered climates did not show much carbonation.

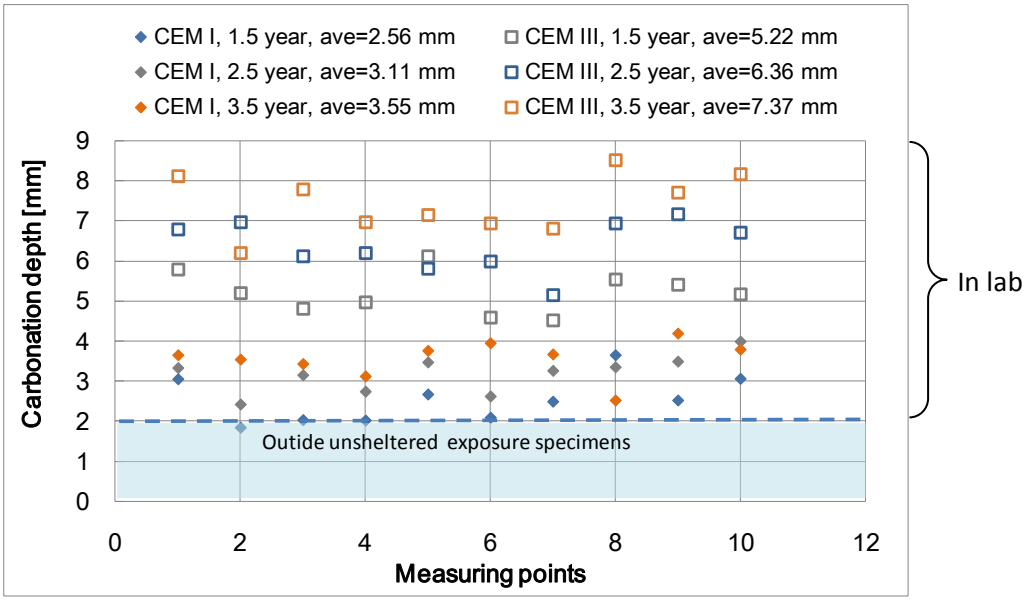

Figure 3-35: Carbonation depth of both I05360 & III05360 concrete in different exposure duration and climates

Chloride profile

As mentioned in Section 3.2.4, chloride profiles were obtained by drilling powders progressively in 1 cm step. The diameter of the drilled hole is approximately 1 cm. Drilling position is right into the crack and perpendicular to the concrete surface, Figure 3-14.

Chloride profiles for 2 years and 3 years exposure of both I05360 and III05360 concrete are illustrated in Figure 3-36. It is interesting that chloride content show an increase with increasing cover depth. Especially in the range of 0-3 cm, a strong increase of chloride content could be observed.

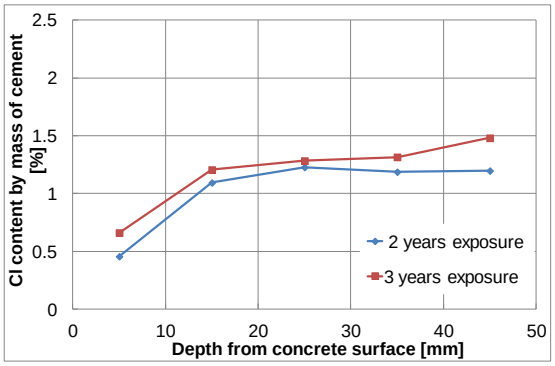

(a) I05360 concrete

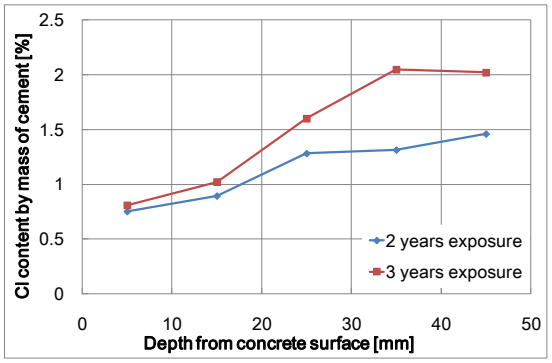

(b) III05360 concrete

Figure 3-36: Chloride profiles along crack depth

This trend is somehow controversial to the common sense. Existing studies have suggested that the total chloride content 'should' decrease with cover depth, either theoretically calculated by Fick's laws or by laboratory and field tests. However, it has to be noticed that most of the existed results are focused on the uncracked concrete, which means that the concrete casting surface is the exposed surface for chlorides to penetrate in. All the boundary conditions, i.e. relative humidity, temperature, and surface chloride content are identical along the exposed surface. Or more strictly, even though the above mentioned boundary conditions are time-dependent, they are not locally varying.

In the case of this study, the cracked concrete beams are subjected to cyclic wetting by chloride solution directly into the crack. Unlike the uniform boundary conditions in the case of uncracked concrete, the boundary conditions here are locally varied. Moisture condition in the crack differs along the crack depth due to the effect of water evaporation and refilling. It is evident that more moisture is kept in deeper crack depths, which implies lower resistivity level of the surrounding concrete and longer duration for chloride and water penetration. Therefore higher chloride content in deeper crack depths could be expected.

In order to obtain the chloride profile perpendicular to crack flanks, blocks which contain both crack flank and concrete casting surface are collected, as has been shown in Figure 3-15, Page 56. Results are shown in Figure 3-37 (a) and (b). By comparing the results of three layers, total chloride content decreases with depth (relative to crack flank) as expected. It has to be noticed that, results in Figure 3-37 only reflects the chloride profiles qualitatively, not quantitatively. This is because that the thickness of each layer is hard to control when powders were being ground.

From Figure 3-36 and Figure 3-37, one could also get the impression that CEM III concrete has higher total chloride content than CEM I concrete. Chloride penetration into concrete is a complex process which is influenced by numerous factors. It is known that the diffusivity of CEM III concrete is smaller than CEM I concrete due to its denser pore structure caused by the addition of slag. The chloride diffusion process is hence retarded. However, the better chloride binding capacity of CEM III concrete implies a higher bound chloride content. Therefore, CEM III concrete demonstrates higher total chloride content in the areas which are closed to the exposed surface.

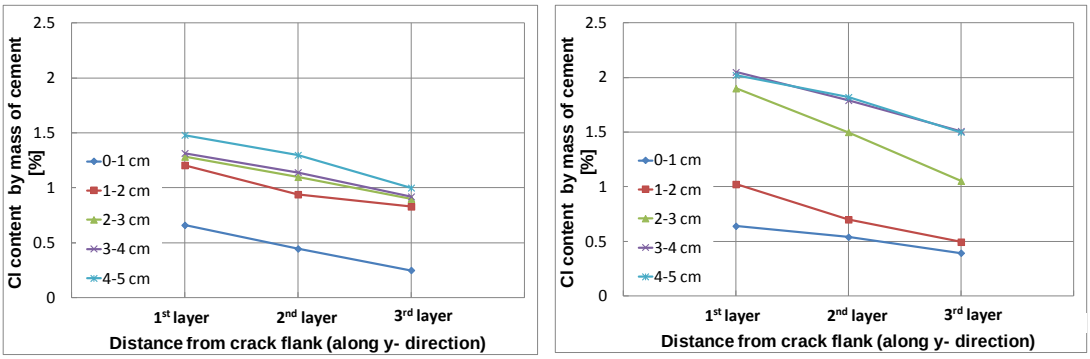

(a) I05360 (b) III05360

Figure 3-37: Chloride profile perpendicular to crack flank, 3 years exposure

Summary

Based on the measured results, the total chloride profiles along crack depth and perpendicular to the crack could be estimated. It increases along crack depth and decreases with depth in penetration direction, as shown in Figure 3-38.

The tendency that total chloride content increases along crack depth is controversial to the existed data in literatures (mostly uncracked concrete). However, it agrees well with the interesting phenomenon observed in corrosion current measurements that anodes embedded in a deeper cover concrete demonstrate higher corrosion intensity. This observation suggests that the micro-climate in cracks may play an important role. To validate the test results and figure out the corrosion mechanism in cracked concrete, further research was carried out and will be presented in chapter 4 and chapter 5.

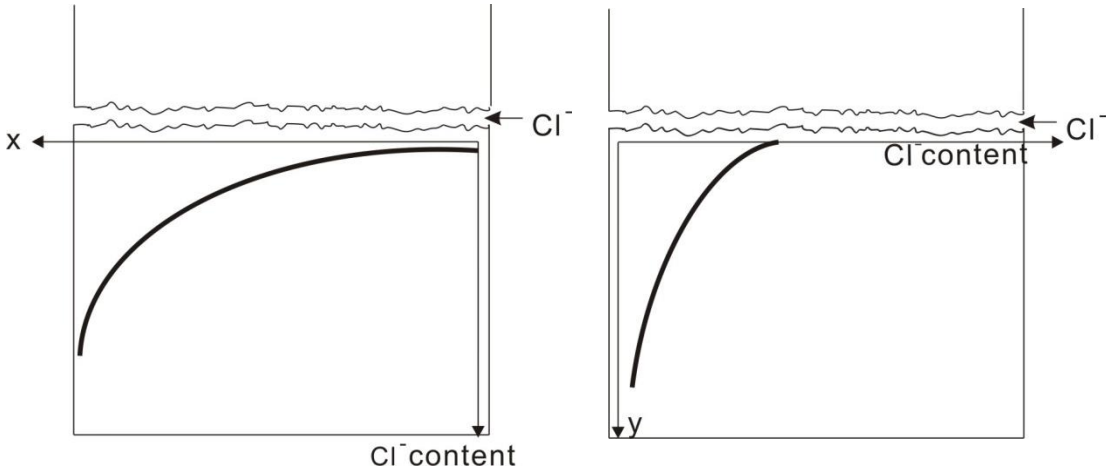

(a) Chloride profile along crack depth (b) Chloride profile perpendicular to crack

Figure 3-38: An assumption of chloride profile in cracked concrete

Anode area

Corrosion current density i_{macro} is of more interest to researchers and engineers than corrosion current I_{macro} since it represents corrosion intensity more directly. However, data collected during the three years' daily measurement in this study are I_{macro}, not the i_{macro}. In the experimental setup of this research, the 4 cm area in the middle of the rebar which is not covered by the epoxy resin is supposed to be the anode. Therefore the nominal anode area is 15.7 cm^2 ($\pi dl = \pi ? .2 ? = 15.07 cm^2$). However, the actual corroded areas might be either smaller or larger than the nominal anode area. This deviation will lead to overestimation or underestimation of corrosion intensity. Therefore it is necessary to measure the actual corrosion area.

After the cracked beams were opened, the cover concrete was removed from the steel. The corrosion area was measured as follows:

The steel bar was divided into 6.28×5 mm^2 grids (with 5mm interval along the longitudinal direction and six-bisectrix in the radius direction), Figure 3-39 (a). Then photos of each grid were taken under a microscope with 5 times magnification, Figure 3-39 (b).

Those photos were then analyzed on computer by AnalySIS, a software which is capable to measure the area with arbitrary shapes and boundaries, Figure 3-39 (c). With the corrosion product covered area marked, the area enclosed was automatically displayed.

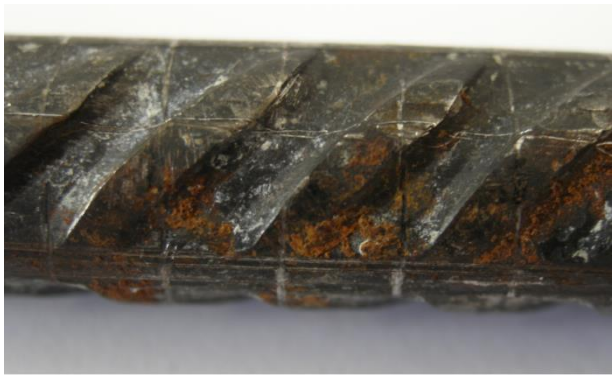

(a) Anode area divided into meshes

(b) Taking photographs for each mesh with microscope

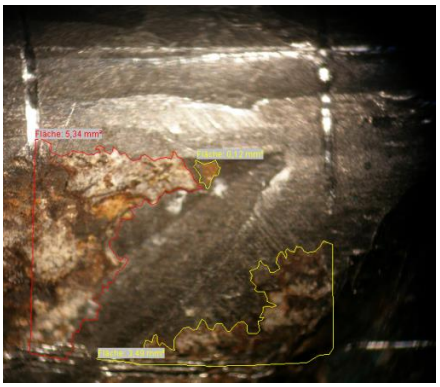

(c) Measurement of corrosion area in each mesh by AnalySIS

Figure 3-39: Measurement of corrosion area

The microscope takes photo in a flat plane while the steel surface, however, is curved. Therefore, it is necessary to introduce a 'bow factor' β_{curv} to convert measured plat area into the actual curved area, as shown in Figure 3-40.

$$\beta_{curv} = \text{bow} / \text{bowstring} = 1.05 \tag{3.5}$$

$$A_{i,j} = A_{measured\ i,j} \times \beta_{curv} \tag{3.6}$$

$A_{measured\ i,j}$- measured corrosion area in each grid;

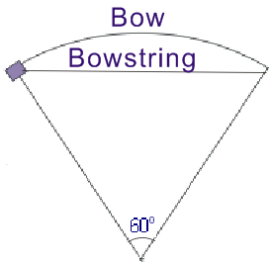

Figure 3-40: Scheme of bow effect

Thereafter, corrosion area of each steel bar was obtained by summing the measured area of all individual mesh.

$$A = \sum_{i=1}^{6} \sum_{j=1}^{n} A_{i,j} \tag{3.7}$$

where:

A -- total corrosion area of a single steel bar;

$A_{i,j}$- corrosion area in each grid;

n - number of intervals along longitudinal direction.

Anode area of specimens in chloride cycle

Figure 3-41 illustrates two typical corroded anodes of both I05360 and III05360 specimens, in chloride cycle. Based on the visual inspection and measurement, it is found that the distribution of corrosion products in the two types of concretes differs from each other:

1) The corroded area is generally larger in CEM III concrete than in CEM I concrete. On some of the anodes of CEM III specimens, corrosion areas are even larger than the nominal anode area (15.07 cm^2).
2) Corrosion in CEM III concrete is more superficial; while corrosion in CEM I concrete is deeper and more intensive.
3) Corrosion products in CEM III concrete tend to spread along steel-concrete interface. In some cases even penetrate under the coated epoxy resin and therefore caused the spalling of epoxy layer. Crevice corrosion might have taken place after the epoxy layer is destroyed; corrosion products in CEM I concrete prefer to remain in the vicinity of the crack and penetrate into adjacent concrete pore structure, Figure 3-42.
4) Pits can be clearly observed on steel surface, especially on CEM I concrete.
5) Corrosion product was observed to deposit in crack.
6) No corrosion induced crack was observed.

The above aspects could be explained both physically and chemically. Physically speaking, CEM III has a denser pore structure which indicates less space available for the corrosion products to deposit. Therefore the corrosion products are kept away from adjacent concrete and are confined to the steel-concrete interface; while CEM I concrete is more porous for corrosion products to diffuse into; chemically, the passivation degree of steel in CEM III concrete is lower in comparison with CEM I concrete. In other words, the growth rate of the passive layer is slow in CEM III in comparison to that in CEM I, which leads to a larger depassivated area.

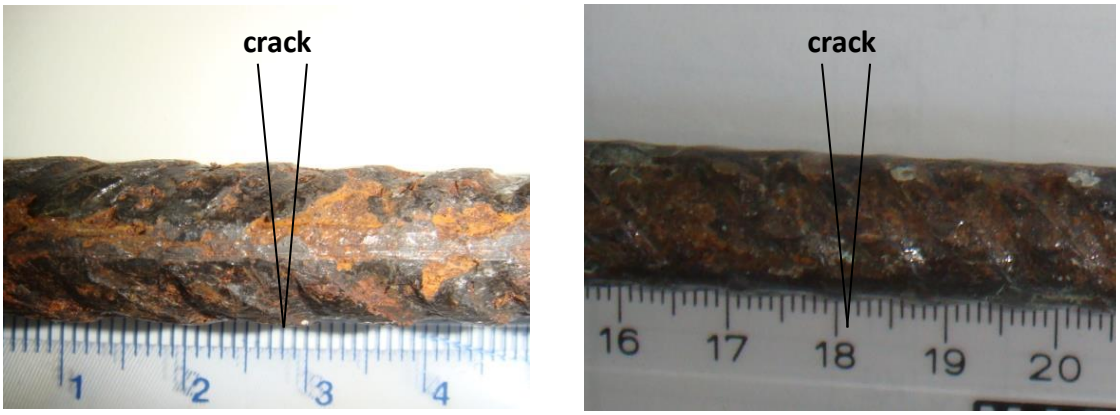

(a)I05360 (b) III05360

Figure 3-41: The distribution of corrosion products on the rebar surface, Cl cycle

Figure 3-42: Corrosion products in concrete pore structure, I05360, cover=5cm, Cl cycle

Results of measured anode areas are illustrated in Table 3-8 for CEM I, and Table 3-9 for CEM III, in Column 5. The average corrosion product covered area is 18.2 cm^2 for III05360 concrete and 12 cm^2 for I05360 concrete. Column 4 shows the accumulated corrosion currents Q_{acc}, i.e. total charge that transferred during the entire exposure duration, which is directly related to the total mass loss of rebar. By comparing Column 4 and 5, one could find

that the Q_{acc} is much higher in I05360 than that III05360 concrete. Considering the smaller corrosion area in CEM I concrete, corrosion intensity is much larger in CEM I than that in CEM III concrete. Column 7, 8 and 9 illustrate the annual average corrosion current density i_{annu} calculated by the measured corrosion area; while data in Column 10, 11and 12 are correspondingly calculated by the nominal area, 15.07 cm^2. Calculations with nominal anode area lead to underestimation for CEM I and over estimation for CEM III concrete.

Corrosion area did not show obvious increase with increasing accumulated corrosion current as expected. This could be attributed to the confine effect of epoxy layer. Addittionally, Q_{acc} is related to both corrosion area and corrosion depth.

Column 13, 14 and 15 are the calculated corrosion penetration depth P_{ave}, which is defined as the annual radius loss of the rebar cross section, assuming that the corrosion is uniformly distributed:

$$P_{ave} = \frac{1}{11.6} i_{corr} \tag{3.8}$$

where,P_{ave} is in μm/year, i_{corr} is in $\mu A / cm^2$.

As expected, P_{ave} decreases with exposure duration and approaches equilibrium; P_{ave} of CEM I is much higher than CEM III.

It has to be clarified that: Firstly, the corrosion area measured is the “corrosion product covered area”. The measured data might be larger than the real corrosion area due to the accumulation and dispersion of corrosion products on the noble steel surface; secondly, corrosion area increases with exposure duration. The measured result is the final state of corrosion area which is generally the largest. Third, the measured corrosion product covered area is not only caused by macro-cell corrosion, but also micro-cell corrosion. Therefore the actual corrosion current density is, in fact, higher than that calculated by measured corrosion product covered area [39].

Pitting corrosion

Pitting corrosion was observed, especially in the specimens which are subjected to the combined effect of chloride contamination and carbonation. A maximum pitting depth of 1.5 mm has been found in I05360 concrete with 5 cm cover depth, in chloride cycle, as shown in Figure 3-43.

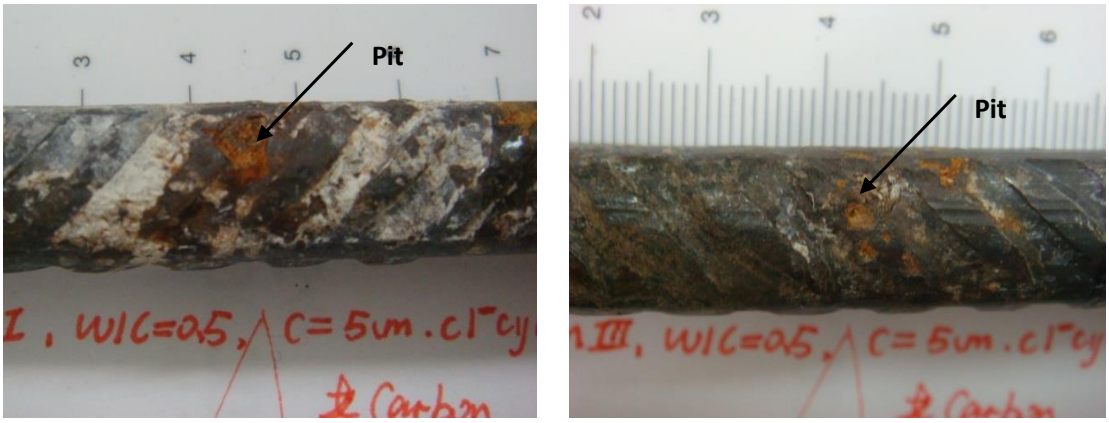

(a) I05360 (b) III05360

Figure 3-43: Pits on concrete, cover= 5 cm, chloride cycle

The P_{ave} in Table 3-8 and Table 3-9 is calculated based on the assumption of uniform corrosion which only gives a general view of the steel cross section loss. However, corrosion attack is practically uneven. When pitting corrosion takes place, the cross section at the pits becomes the weak cross section of the rebar. González, *et al* [144] defines the ratio between maximum penetration of the deepest pits and average penetration depth as pitting factor α, Eq.(3.9). The α value reported by him is between 4 and 8.

$$\alpha = \frac{P_{max}}{P_{ave}} \tag{3.9}$$

Table 3-7 shows the observed maximum pit depth and calculated α ratio. Only several anodes in chloride cycle have obvious pitting corrosion. None of the specimens in water cycle and outside unsheltered exposure exhibits pitting corrosion. Obtained α ratios are in the range of 6-15 for CEM I concrete and 28 for CEM III concrete, which is higher than results in literature.

Table 3-7: α ratio

Specimen	Exposure duration	Average penetration depth after 3 years	Maximum pit depth	α ratio
[-]	[year]	[mm]	[mm]	[-]
I05360, non-carbon	1	0.082	1.2	14.6
I05360, non-carbon	3	0.092	0.6	6.5
I05360, carbon	3	0.139	1.5	10.8
III05360, carbon	3	0.025	0.7	28

Table 3-8: Measured anode area and calculated results of CEM I

Concrete	Cover depth	Exposure duration	Integrated corrosion current	Measured anode area A_{mea}	Nominal anode area A_{nom}	Average annual i_{annu} [calculated by A_{mea}]			Average annual i_{annu} [calculated by A_{nom}]			Annual corrosion penetration depth P_{ave} [calculated by A_{mea}]		
	[cm]	[month]	[A·s]	[cm^2]	[cm^2]	[$\mu A/cm^2$]			[$\mu A/cm^2$]			[μm/year]		
						1st year	2nd year	3rd year	1st year	2nd year	3rd year	1st year	2nd year	3rd year
1	2	3	4	5	6	7	8	9	10	11	12	13	14	15
CEM I, w/c=0.5 Non-carbon	2	12	513	9.46	15.07	1.82			1.14			21.11		
	2	12	966	10.23	15.07	3.42			2.32			39.66		
	5	12	467	6.65	15.07	5.22			2.30			60.59		
	5	12	3574	20.3	15.07	7.12			9.58			82.54		
	5	24	576	13.59	15.07	1.85	0.32		1.67	0.28		21.44	3.66	
	3.5	24	688	9.44	15.07	2.34	1.41		1.46	0.88		27.09	16.39	
	2	36	1649	8.46	15.07	3.65	1.91	1.28	2.05	1.07	0.72	42.34	22.21	14.9
	3.5	36	3044	12.23	15.07	4.30	1.90	1.72	3.49	1.54	1.39	49.93	22.06	19.94
	5	36	2757	15.58	15.07	2.85	2.67	1.35	2.95	2.75	1.39	33	31	16
	5	36	1695	9.75	15.07	5.98	1.97	0.68	3.87	1.27	0.44	69.35	22.84	7.90
	5	36	1605	11.52	15.07	4.23	1.78	0.95	3.24	1.36	0.73	49.12	20.68	11.04
	5	36	3278	14.34	15.07	4.46	2.11	1.67	4.25	2.01	1.59	51.76	24.52	19.41
CEM I, w/c=0.5 Carbon	5	36	4153	15.23	15.07	7.39	3.04	1.56	7.47	3.08	3.08	85.74	35.32	18.13
	5	36	2044	9.96	15.07	5.99	2.38	0.63	3.96	1.57	0.42	69	28	7
	5	36	3161	13.37	15.07	5.48	1.72	1.16	4.86	1.53	1.03	63.54	19.96	13.47

Table 3-9: Measured anode area and calculated results of CEM III

Concrete	Cover depth	Exposure duration	Integrated corrosion current	Measured anode area A_{mea}	Nominal anode area A_{nom}	Average annual I_{macro} [calculated by A_{mea}]			Average annual I_{macro} [calculated by A_{nom}]			Annual corrosion penetration depth P_{ave} [calculated by A_{mea}]		
	[cm]	[month]	[A • s]	[cm^2]	[cm^2]	[$\mu A/cm^2$]			[$\mu A/cm^2$]			[μm/year]		
						1st year	2nd year	3rd year	1st year	2nd year	3rd year	1st year	2nd year	3rd year
1	2	3	4	5	6	7	8	9	10	11	12	13	14	15
CEM III, w/c=0.5 Non-carbon	3.5	12	186	17.2	15.07	0.5			0.57			5.80		
	5	12	372	13.95	15.07	1.16			1.07			13.40		
	2	24	409	9.75	15.07	0.85	0.61		0.55	0.39		9.86	7.02	
	3.5	24	439	28	15.07	0.44	0.19		0.81	0.35		5.05	2.22	
	5	24	605	12.3	15.07	0.99	0.66		0.81	0.56		11.45	7.93	
	2	36	749	22.4	15.07	0.46	0.42	0.21	0.68	0.62	0.32	5.33	4.83	2.47
	3.5	36	843	21.2	15.07	0.72	0.52	0.18	1.02	0.73	0.26	8.41	6.02	2.12
	5	36	349	15.6	15.07	0.50	0.16	0.09	0.52	0.17	0.10	5.83	1.87	1.08
CEM III, w/c=0.5 Carbon	5	36	1268	19.29	15.07	1.29	0.75	0.30	1.65	0.96	0.39	14.97	8.73	3.5
	5	36	1410	13.69	15.07	1.05	1.27	0.98	0.96	1.15	0.89	12.21	14.72	11.34
	5	36	1577	27.12	15.07	1.23	0.53	0.41	2.21	0.95	0.74	14.24	6.14	4.74

Anode area: CEM III, w/c=0.4

The III04360 specimen in chloride cycle did not show intensive corrosion. Only small surface corrosion area could be observed on the steel surface, Figure 3-44.

Figure 3-44: Corrosion area of III04360, Cl cycle, cover=5 cm, 3 years exposure

Anode area: Water cycle

No intensive corrosion was found in weekly wetting-drying cycle of tap water exposure. Only tiny corrosion spots could be observed on several anodes. Some of the supposed anode steel bars are without any hint of corrosion at all. The maximum corrosion area observed is 0.29 cm^2, Figure 3-45.

Anode area: Natural unsheltered exposure

Similar to specimens in water cycle, no intensive corrosion was found in natural unsheltered exposure, including the carbonated specimen. Only some steel bars are slightly corroded with rather small and superficial corrosion area. The maximum corrosion area observed is 0.17cm^2, Figure 3-46.

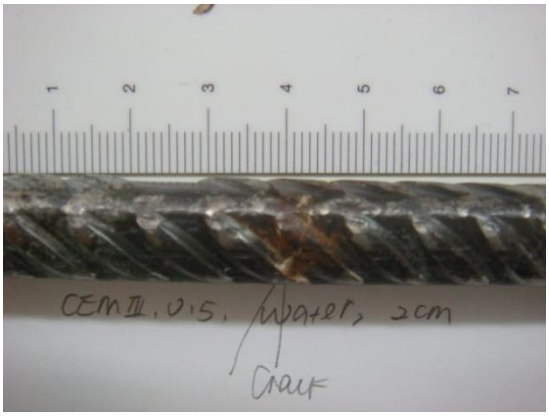

Figure 3-45: Corrosion area of specimens in water cycle, III05360, cover =2 cm, 3 years exposure

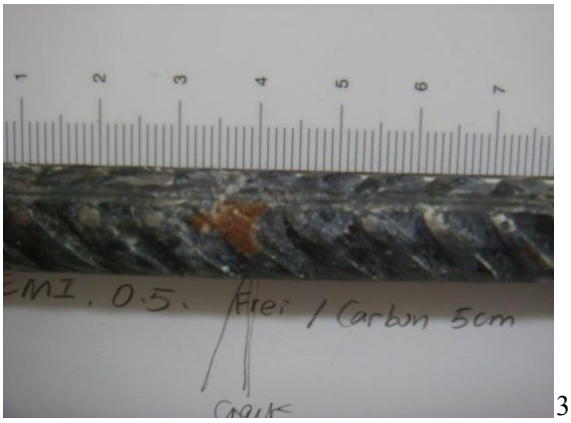

Figure 3-46: Corrosion area of specimens in natural unsheltered exposure, III05360, cover =2 cm, carbonated, 3 years exposure

3.4 Discussion

3.4.1 Influence of cover depth on corrosion in cracked concrete

Sound and dense concrete cover provides good protection by keeping the deteriorating substances, such as carbon dioxide and chlorides, away from the embedded reinforcement. In uncracked concrete, the deeper the cover depth, the better protection it offers. Researchers have confirmed the positive effect of thicker concrete cover on durability.

However, when cracks exist, the situation is somehow different. Cracks are more preferable path for carbon dioxides and chloride ions to penetrate in. It is found in this study that the advantage of thicker cover concrete is negligible. Figure 3-47 illustrates the accumulated corrosion current Q_{acc} over 1 year's exposure after depassivation, for both I05360 concrete and III05360 concrete. For CEM I specimens, Q_{acc} increase with cover depth; For CEM III specimens, Q_{acc} of anodes with 3.5 cm and 5 cm cover depth are approximately equal and are both higher than the ones with 2 cm cover. In short, more intensive corrosion has been observed on the rebar with thicker concrete cover.

The tendency shown in Figure 3-47 is controversial to the practice experience so far. Therefore it is important to find out the mechanisms behind the irregular observations. The followings are some possible explanations:

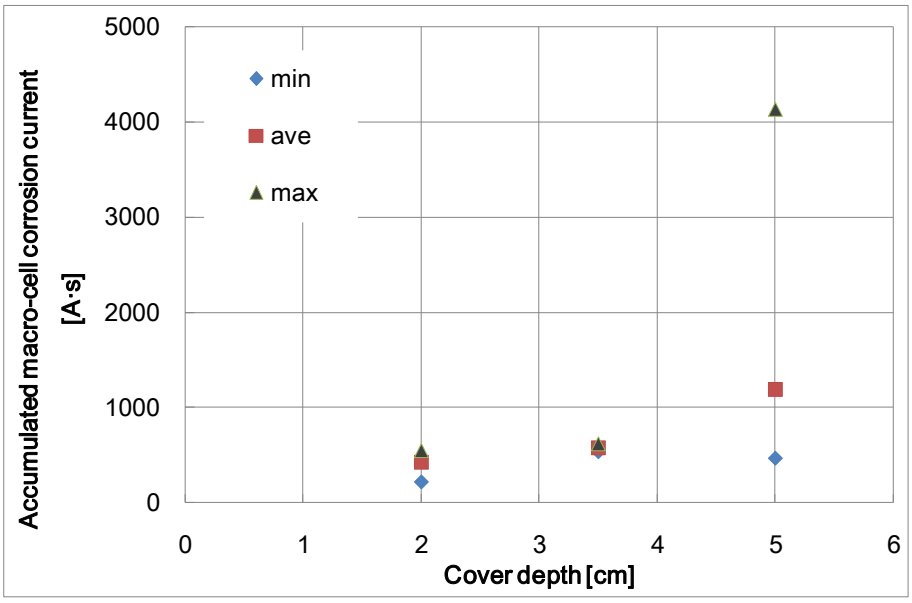

(a) I05360

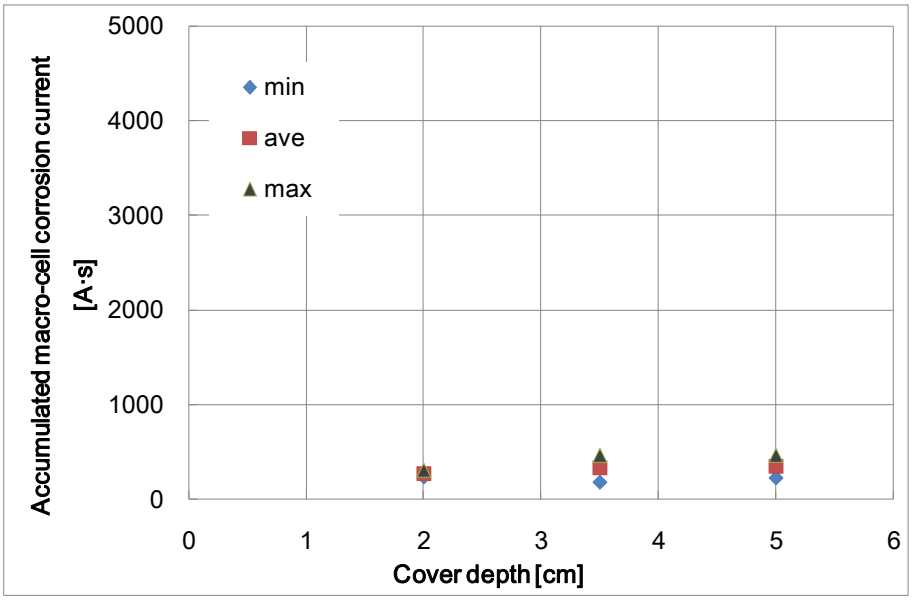

(b) III05360

Figure 3-47: Accumulated corrosion currents Q_{acc}, one year after depassivation

First of all, thicker concrete cover has no advantage for initiation period in the case of cracked concrete. We have to keep in mind that the contribution of thick concrete cover on the service life in case of uncracked concrete mainly refers to the initiation period. Initiation primarily depends on the time needed for chloride ions to diffuse from the concrete surface to the embedded steel plus the time needed for chloride content to reach the threshold value. According to Fick's law, for a certain mix of concrete and boundary conditions this duration primarily depends on the length of diffusion path, i.e. the concrete cover depth. However, when crack occurs, the crack would be a more preferable path for the chloride

ions to penetrate in. The chloride diffusion coefficient can be several orders higher through crack than through uncracked concrete cover. Initiation period is greatly shortened or even reduced to zero by the presence of cracks. Therefore, the positive effect of cover thickness on preventing corrosion initiation is eliminated.

Secondly, concrete resistivity is lower in deep concrete than in outer concrete due to the moisture gradient, especially in the case of cracked concrete with chloride solution sprayed into the crack. Therefore, the corrosion intensity is more severe for rebar embedded in thicker cover during the propagation period. To prove this explanation, resistance between anode and cathodes with different cover depth are examined. Results are shown in Figure 3-48 and Figure 3-49. It could be clearly seen that for both CEM I concrete and CEM III concrete, the resistances between anode and cathodes decreases with increasing cover depth. Resistances between anode and cathodes in corrosion systems with 2 cm cover depth are 1.68 and 1.44 times higher than those with 5 cm cover depth for CEM I and CEM III concrete respectively.

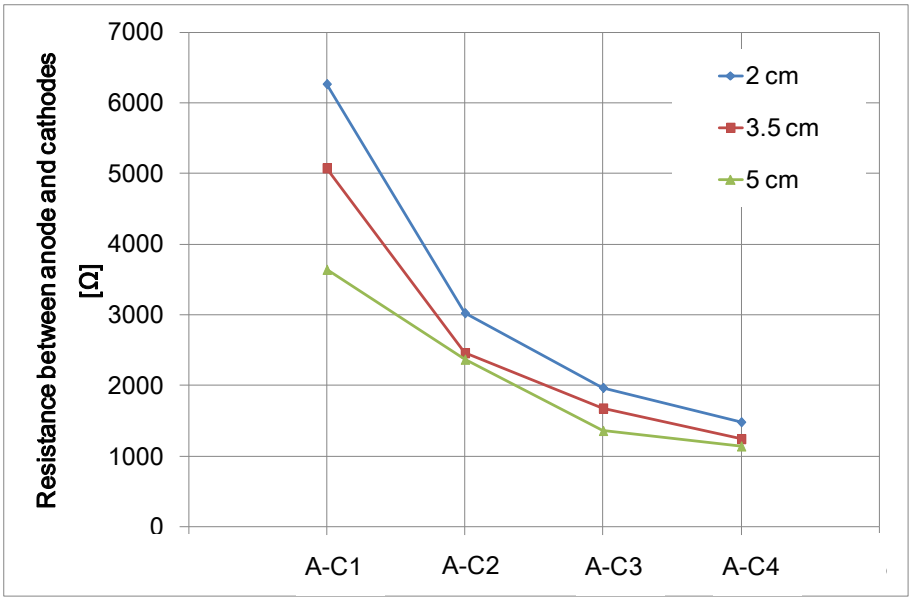

Figure 3-48: Resistance between anode and cathodes, I05360, Cl cycle, 2 years exposure

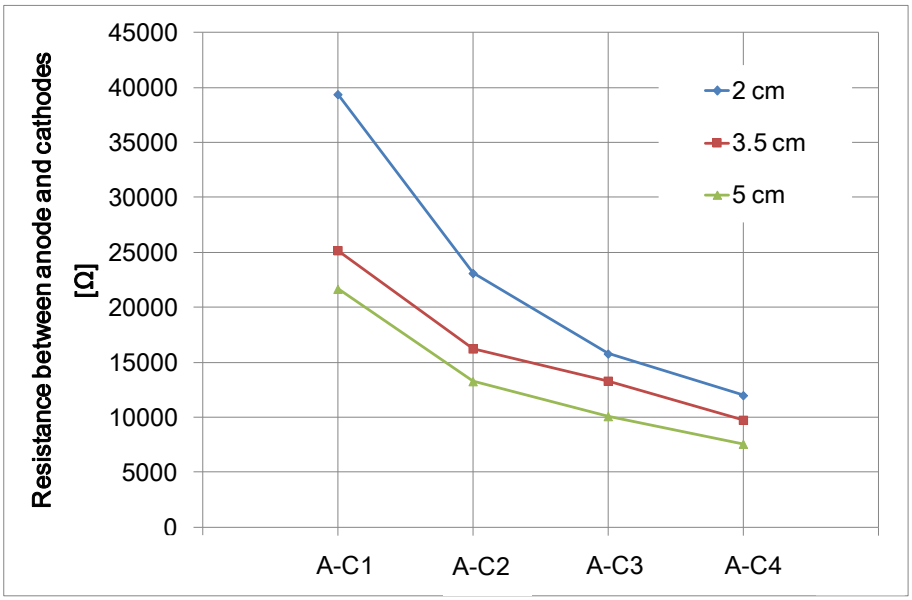

Figure 3-49: Resistance between anode and cathodes, III05360, Cl cycle, 2 years exposure

Additionally, the chloride penetration process from crack flank into the inner concrete lasts longer in deeper concrete than in outer concrete. In the experimental set up of this study, cracked beams are subjected to cyclic wetting of chloride solution which is directly sprayed into the crack. Except for the 1 hour wetting period, specimens are exposed to dry laboratory environment for the rest of the week during which the solution in crack evaporates gradually. The water evaporation rate is much slower than the rate it is filled in. Therefore deeper zones in the crack are filled with chloride solution for longer period, leading to more chloride penetration into the concrete from the crack flank. Therefore the chloride attack is much more intensive for the anodes in deeper cracks (e.g. with 3.5 cm and 5 cm cover depth) than in outer cracks (e.g. with 2 cm cover depth). This hypothesis is schematically described in Figure 3-50.

To prove this explanation, further research on evaporation rate of crack solution is carried out; the chloride penetration process from crack flank into concrete is studied. Details are given in chapter 4.

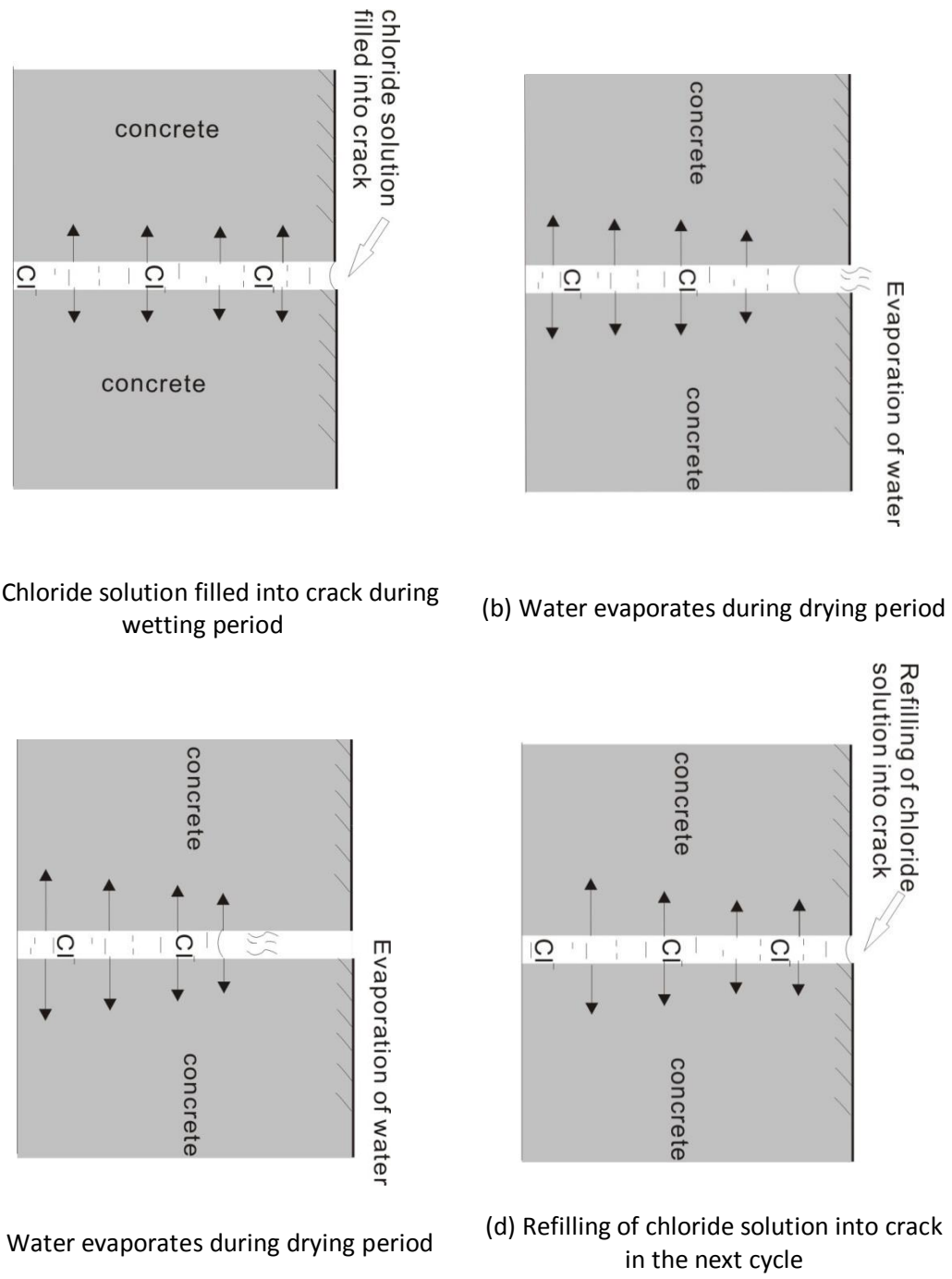

Figure 3-50: Variation of water level in crack due to evaporation and refilling.

3.4.2 Effect of concrete resistivity on reinforcement corrosion in cracked concrete

Electrolytic resistivity of concrete ranges from 10 to $10^{15}\,\Omega\cdot m$, mainly depending on its pore structure and moisture content. It is an important material property which characterizes the quality of concrete in durability respect. In corrosion science, it indirectly reflects the concrete's ability of resisting the penetration of corrosive substances into the concrete and directly describes how easy the dissolved ions can be transported from anode to cathode.

Therefore, the concrete resistivity plays an important role in both initiation period and propagation period.

Initiation period: As has been mentioned in Section 2.2.3 (Page 24), the initiation period in the case of chloride induced corrosion could be subdivided into two periods: the time that needed for the chloride ions to transport from exposed surface to the steel surface (t_{tran}) and the period for chloride concentration on the steel surface to reach the threshold value (t_{accu}):

$$t_{in} = t_{tran} + t_{accu} \tag{3.10}$$

Concrete resistivity plays an important role in both t_{tran} and t_{accu}.

Andrade, *et al* [145] proposed a model to correlate concrete resistivity with chloride diffusion coefficient based on Einstein law.

$$D_{cl} = \frac{k_{cl}}{\rho_e \cdot r_{cl}} \tag{3.11}$$

where

D_{cl} - the effective diffusion coefficient considering linear binding of concrete;

ρ_{es} - the concrete resistivity in saturated conditions;

k_{cl} - factor which depends on the external ionic concentration;

r_{cl} - the binding factor.

Combining Eq.(3.11) and Fick's law, the duration of t_{tran} can be estimated.

Morris and Vázquez [146] related the electrolytic resistivity of concrete with chloride threshold value. He pointed out that when electrolytic resistivity increases from 2 to 100 $k\Omega \cdot cm$, the chloride threshold value Cl_{TH} increases from 0.44% to 2.32% relative to the weight of cement. The best line fit can be expressed by the following expression:

$$Cl_{TH}(\%) = 0.019\rho + 0.401 \tag{3.12}$$

Combining Eq.(3.12) and Fick's law, t_{accu} could be calculated. Therefore, the initiation period t_{in} can be decided.

However, in cracked concrete the effects of concrete resistivity are mainly focused on the propagation period, since the initiation period in this case can be extremely short.

Propagation period

The relationship between concrete resistivity and the reinforcement corrosion rate in the case of uncracked concrete has been studied exclusively (detailed introduction refer to literature review, Section 2.2.3). A linear relationship between inverse resistivity and corrosion rate was found for different types of cement [1, 147, 148]. Gulikers [20] stated that for a wide range of corrosion current densities the relationship between $\log(I_{macro})$, and concrete resistance, $\log(R_{el})$ can be approximated by an linear relationship. Morris, *et al* [146] derived the same correlation and gave an empirical expression based on fitted experimental data:

$$i_{corr} = 55000\rho^{-1.3} \tag{3.13}$$

The above researches are mainly focused on the uncracked concrete; the contributions on the influence of concrete resistivity on corrosion in cracked concrete, however, are not abundant.

It has also been observed in this research that for the reinforcement embedded in cracked concrete beams, the corrosion intensity is highly influenced by concrete resistivity. As has been stated in Table 3-5, the accumulated corrosion current Q_{acc} of I05360 concrete is 1.54-3.16 times higher than III05360 concrete, depending on the cover depth. The III04360 specimens did not show intensive corrosion at all. The main difference between these concretes could be attributed to the difference in their charge transfer capacity, i.e., conductivity. It is well known that the concrete resistivity depends on its composition. Cements with high amounts of pozzolanic or latent hydraulic compounds (such as fly ash or slag) provide higher resistivity than those without. The use of blast furnace slag cement instead of ordinary Portland cement can increase the resistivity of concrete by a factor of three. Those binding agents lead to denser pore structure and therefore to an increase in resistivity. The pore structure can also be influenced by varying water/cement ratios. Higher w/c ratio forms a coarser pore structure and thus, larger capillary pore diameters leading to a quicker ingress of water into the concrete. Provided constant moisture content in concrete, an increase of w/c ratio results in a decrease of concrete resistivity [135].

By comparing the resistance between corresponding anode and cathodes, one could find out that the resistance of III05360 and III04360 are 6.4 and 9.6 times of that in I05360 specimens, Figure 3-51. These ratios are much higher than in uncracked concrete. In a parallel conducted project, concrete resistivity of different composition has been investigated. Results show that in uncracked concrete samples, resistivity of III05360 and III04360 are only 2.47 times and 3.24 times as that in I05360 concrete, Table 3-10. The reason for such a high ratio in cracked concrete might be attributed to the combined effect of wetting cycle and the concrete pore structure. After each wetting period, the moisture content in CEM I concrete is much higher due to its relatively coarser pore structure.

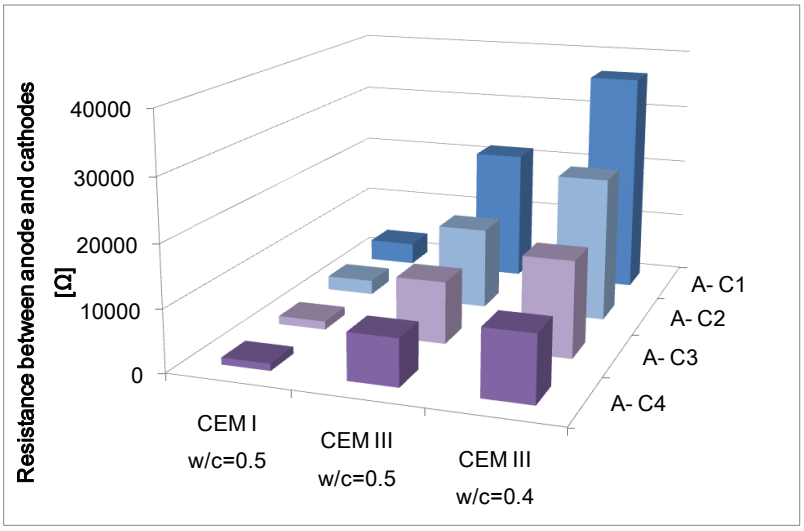

Figure 3-51: Resistance between anode and cathodes for different concrete compositions, with cover depth =5 cm, Cl cycle

Table 3-10: The ratio of concrete resistivity between different concrete compositions in uncracked concrete and cracked concrete, in saturated condition

	Uncracked concrete	Cracked beam
III05360 / I05360	2.47	6.41
III04360 / I05360	3.24	9.63

It can also clearly be observed in Figure 3-51 that the resistances between anode and different cathodes increase with the distance between them. The corresponding distribution of corrosion currents among the cathodes have already been illustrated in Figure 3-28. One could see the effect of concrete resistivity by combining the two figures. To illustrate the correlation more clearly, resistance between anode and cathodes and corresponding corrosion current density is plot together in Figure 3-52. A linear logarithmic relationship between i_{macro} and resistance between electrodes was found:

$$\ln i_{corr} = 3.14 - 0.97 \ln R_{el} \tag{3.14}$$

The parameter -0.97 indicates the nearly inverse linear correlation between electrolytic resistance and corrosion current density. Therefore, the macro-cell corrosion in cracked concrete is mainly under resistance control.

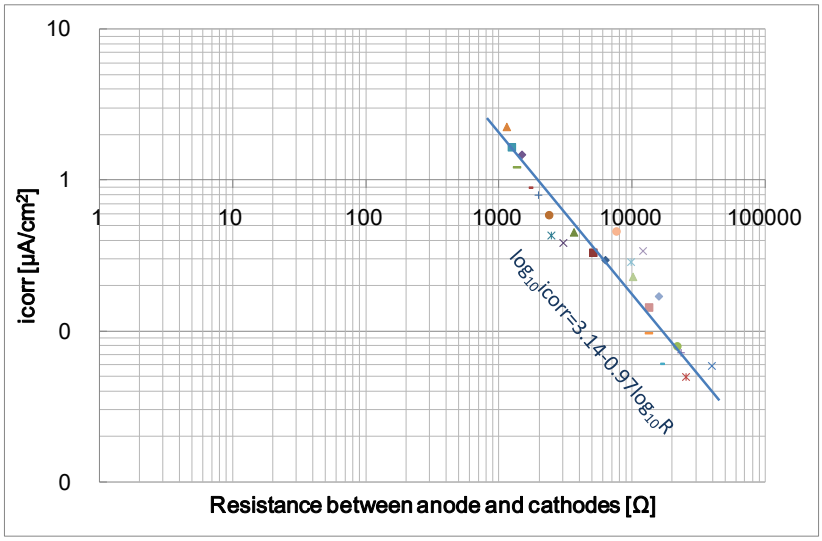

Figure 3-52: Correlation between corrosion current density (i_{macro}) and electrolytic resistance of concrete between anode and cathodes.

3.5 Summary

Concrete is commonly used building material, however, is not crack free. When cracks occur, a preferable path for corrosion promoting substances (CO_2, Cl ions, etc.) is created and depassivation will happen. In order to investigate the corrosion mechanisms and processes in cracked concrete, laboratory tests were carried out on centrally cracked concrete beams, in which 3 corrosion cells with single anode and multiple cathodes with different cover depth were arranged. The beams are subjected to both chloride/water wetting-drying cycle and natural exposures. Based on the experimental results from three years measurement and destructive tests, the following conclusions can be drawn:

Initiation period

Penetration of chloride solution though crack is rather fast. The initiation period of reinforcement in cracked concrete which is subjected to cyclic chloride contamination is extremely short, ranging from less than one week to around 200 days. Therefore, compared to the relatively long service life of concrete structure in harsh environments (i.e. cyclic

chloride loading) the embedded steel could be considered as “immediately” depassivated once the crack arises.

Propagation period

The mechanism of reinforcement corrosion in cracked concrete is macro-cell corrosion which is greatly influenced by concrete resistivity. According to the test results, corrosion intensity depends on environmental exposure conditions, concrete composition (cement type, w/c ratio), and specimen geometry (concrete cover, cathode area and distance between anode and cathode, etc.).

With the chloride solution directly sprayed into the cracks, chlorides and moisture reach the anode quickly. With atmospheric exposure and moderate concrete cover, the oxygen supply to cathode is adequate as well. Experimental results in this research reveal that the logarithm anode-to-cathode resistance and corrosion intensity is nearly inversely proportional. This indicates that the corrosion system in cracked concrete is under electrolytic resistance control.

Influence of environmental conditions

Most of the specimens subjected to water wetting-drying cycle and natural unsheltered exposure remained passive over the entire exposure duration. Only several of them corroded slightly. Intensive corrosion was only observed in specimens subjected to wetting-drying cycle of chloride solution, which indicates that an alternatively wetting chloride environment is the most dangerous condition for cracked concrete. The water cycle and natural unsheltered exposure without chloride attack is relatively less severe.

Influence of concrete composition

Three types of concrete composition have been studied in this research: CEM I cement with w/c ratio 0.5, CEM III cement with w/c ratio 0.5, and CEM III cement with w/c ratio 0.4. Specimens made by CEM III cement with w/c ratio 0.4 only show a quite slight corrosion, indicating the better corrosion resistance of concretes with lower w/c ratio. By comparing the corrosion process in the two cement types, it is found that corrosion in CEM I w/c 0.5 concrete is much more intensive than in CEM III w/c 0.5 concrete. Actually, the effects of cement type and w/c ratio could both be attributed to the influence of concrete pore structure. The addition of slag or a lower w/c ratio leads to denser pore structure, which results in a lower diffusivity and higher resistivity. In the case of chloride induced corrosion

in cracked concrete with macro-cell corrosion as the main corrosion mechanism, the resistivity of the concrete is a dominant parameter which determines the severity of corrosion.

Corrosion products distribution in CEM III concrete is more dispersive and spread along steel-concrete interface; while CEM I concrete is characterized with more localized corrosion.

Cover depth is found to be another influential factor. In this study, anodes embedded in thicker cover depth (5 cm) illustrated relatively more intensive corrosion. This is because that chloride penetration though crack is a rather quick process that the advantage of a thicker cover depth is consequently eliminated. In the experimental setup of this research, the crack is a 0.3 mm and parallel-shaped crack which is generated by tension test. With chloride solution directly sprayed into the crack 1 hour per week, it is probably that more moisture is kept in the deep crack; while the moisture in outside crack is dried out due to the effect of evaporation. The chloride penetration duration (from crack flank into concrete) is consequently longer in deeper crack. To prove these hypotheses, evaporation rate test and numerical simulation of chloride penetration in cracked concrete are performed in the next chapter.

Observations from both CEM I and CEM III concrete specimens suggest that there exists an equilibrium corrosion state after a certain exposure duration. The anodic and cathodic reactions remain in a static state if the environmental conditions remain unchanged. However, more data and longer exposure periods are needed to allow for a sufficiently realistic prediction.

Chapter 4 Numerical Study on Chloride and Moisture Penetration into Cracked Concrete

4.1 General

4.1.1 Motivation

Chloride contamination is one severe predisposing factor that may induce the deterioration of reinforcement structures. In durability design, one of the most important factors determining the service life of structures is the transport property of concrete. Researchers have dedicated to investigate the process of moisture and chloride transportation in concrete. Those achievements make the prediction of the initiation period possible. However, research interests are mostly focused on uncracked concrete. Contributions relate to cracked concrete are quite rare.

In Chapter 3, an unconventional trend has been observed that in cracked concrete beams thicker cover did not show its advantage in preventing reinforcement from chloride induced corrosion. It is deduced that the higher moisture and chloride content in deeper crack might be the reason. This conjecture needs to be proved. However, it is not appropriate to conduct a series of duplicated experiments due to the limitation of time and labour. Therefore, numerical method is a preferable choice to model the moisture and chloride penetration process into cracked concrete and to verify the laboratory observation.

The advantages of numerical modelling are obvious: It is less expensive and time-consuming than laboratory experiments. The number of cases and variations are not limited. Cases could be easily calculated with any environmental conditions and any material properties.

4.1.2 Main content of this chapter

At the beginning of this chapter, three mechanisms of chloride transportation in concrete are briefly introduced. The influence of cracks on chloride/moisture penetration into concrete and the difference of chloride penetration between uncracked concrete and cracked concrete are specified.

The problem to be solved in this chapter is the chloride penetration from the crack flank into non-saturated concrete, with varying chloride concentration and up-and-down water level. Therefore, the transportation mechanism is considered to be diffusion and convection

coupled with moisture diffusion. Two-dimensional basic equations have been built based on Fick's first law and mass conservation. Chloride binding is taken into account, obeying Freundlich binding isotherm and Langmuir binding isotherm at different concentration level. The chloride diffusivity and moisture diffusivity are estimated by a factorial approach.

In order to determine the varying chloride concentration in crack solution and the moisture condition in crack, experiments were conducted to find out the moisture evaporation rate in crack.

After the material properties and boundary conditions are determined, a two dimensional model was built to simulate the chloride penetration process from the crack flank into non-saturated concrete. The numerical simulation was conducted with the self-developing program "CPUCC", i.e. "Chloride Penetration in Unsaturated Cracked Concrete". CPUCC is written in FORTRAN in which ADI method (Alternating-Direction-Implicit finite difference method) is implemented to solve the two dimensional differential equations.

Numerical results are found to agree with the experimental results (Chapter 3) quite well. The influences of crack on chloride/moisture penetration are discussed.

4.2 Theoretical background

4.2.1 Description of the studied case

As has been stated in Chapter 3, concrete beams are cracked in the centre by tensile test. Crack goes through the whole cross section. Stainless foils are positioned in the crack to keep the crack width as constantly 0.3 mm (see in Figure 3-6, Figure 3-7, and Figure 3-8 in page 47). The cracked beams are subjected to three exposure conditions: 1h/week wetting-drying cycle of 1% chloride solution; 1h/week wetting-drying cycle of tap water; and natural unsheltered exposure. In the 1 hour wetting period, chloride solution/tap water is directly sprayed into cracked area. During the drying period, cracked beams are exposed to laboratory environment with an average temperature of 25^{o}C and RH 40-50%.

In order to make the discussion much easier to understand, three-dimensional coordinate system is introduced onto the interested domain, Figure 4-1.

x-direction: the direction from concrete surface into crack;

y-direction: the direction that from crack flank perpendicularly into concrete;

z-direction: the direction that perpendicular to the xy-plane.

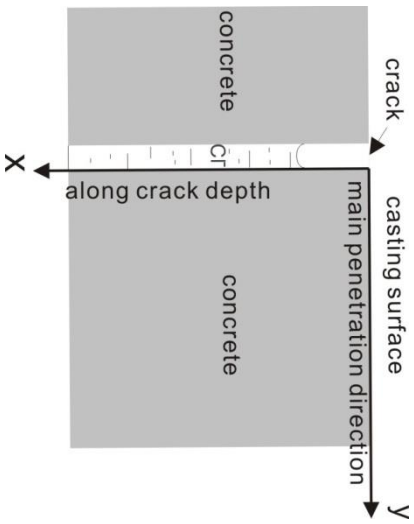

Figure 4-1: Specification for the directions.

Among all the specimens, the specimens in chloride cycle demonstrated the most severe corrosion and therefore are of most concern. In Chapter 3, it is observed that reinforcements embedded in deeper concrete cover exhibited more corrosion, which is disaccord to the existed knowledge. A possible explanation for this unconventional observation is that chloride and moisture penetration into concrete last much longer in deeper crack compared to the outer crack, due to the evaporation effect, as shown in Figure 4-2.

In this research, the only exposed surface for chloride penetration is the crack flank. The penetration from concrete casting surface is of less interest. At the beginning of one cycle, the crack is filled with chloride solution. Chloride ions penetrate from the crack flank perpendicularly into concrete, Figure 4-2 (a). After the one hour's wetting, the water level of the crack solution starts to drop due to the effect of evaporation, Figure 4-2 (b) and (c). At the beginning of the next cycle, the crack is refilled again with chloride solution, Figure 4-2 (d).

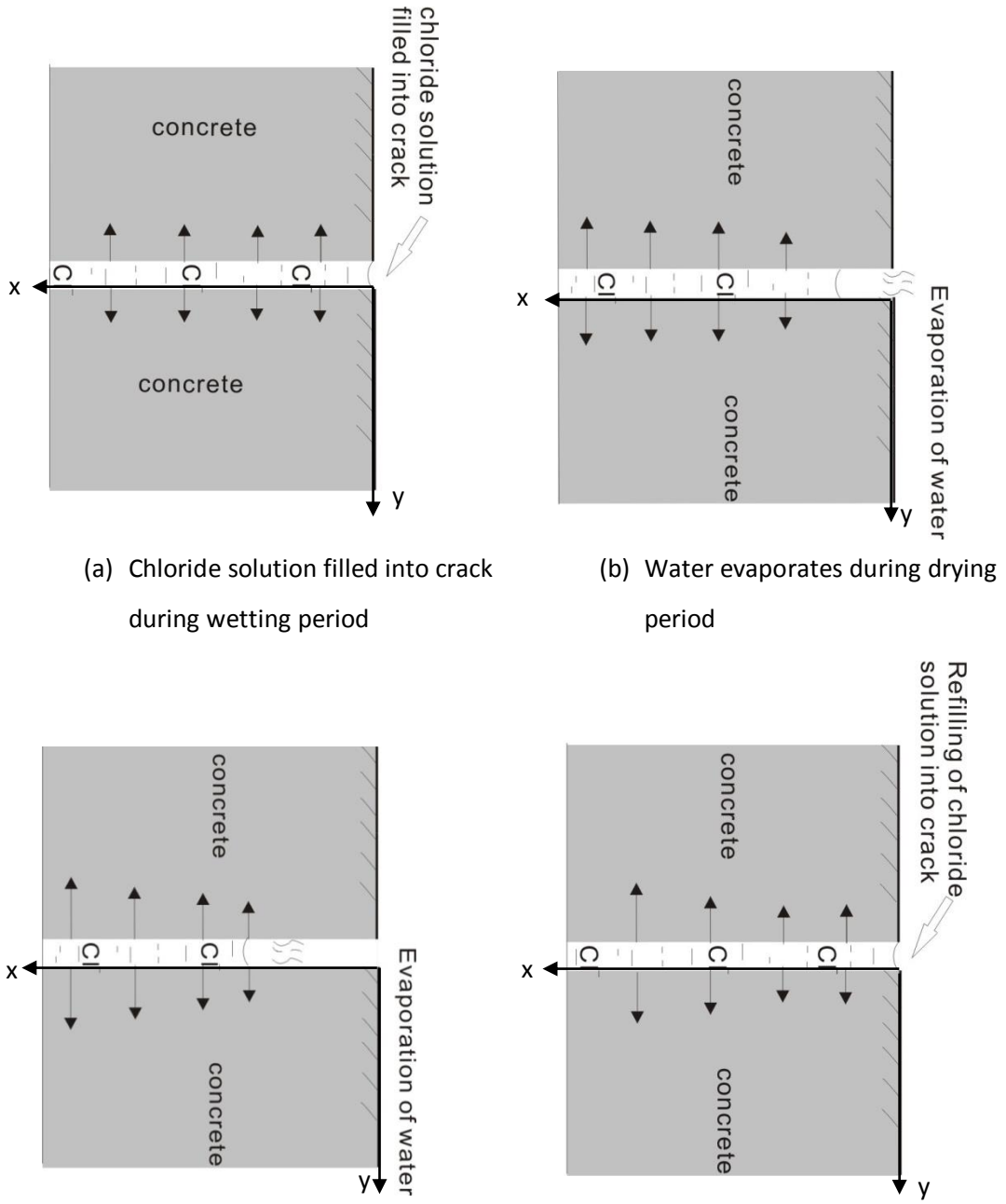

(a) Chloride solution filled into crack during wetting period

(b) Water evaporates during drying period

(c) Water evaporates during drying period

(d) Refilling of chloride solution into crack in the next cycle

Figure 4-2: Variation of water level in crack due to water evaporation and refilling.

The fowling are the basic assumptions and simplifications for the numerical calculation:

1. Concrete is considered to be homogenous material in which the pores, gaps and connectivity are uniformly distributed.
2. The chloride penetration along z-direction is much smaller than that along y-direction or x-direction that could be ignored in the numerical simulation. So a

simplified two-dimensional model is used instead of the complicated three-dimensional model in this study, which was also widely used in numerical simulations [e.g., 65, 149, 150, 151, 152].

3. The crack is considered as ideal parallel crack with constant width of 0.30 mm, no tortuosity and roughness are taken into account.
4. Chloride binding capacity of the concretes is assumed to obey Freundlich isotherm and Langmuir isotherm at different concentration level.
5. The chloride penetration rate through the crack is several orders higher than that in concrete [151]. Therefore the chloride penetration process through the crack is not discussed.
6. Chloride concentration in crack solution is simply considered as completely uniform; the refilled solution mixes immediately and homogeneously with the surplus solution during the wetting period.
7. The original RH in the concrete is assumed to be uniformly 50%. The boundaries are simply assumed to be closed boundary, opening boundary and symmetry boundary respectively. Details will be given in Section 4.3.2.
8. The environmental conditions are considered to be constantly 25°C and RH 50%.

4.2.2 Transporting mechanism of chloride in unsaturated cracked concrete

Chloride transport in concrete is a rather complex process which involves ion diffusion, capillary suction and convective flow with flowing water, accompanied by physical and chemical binding [153]. The mechanism of migration might also be involved if an external electrical potential is imposed. Eq.(4.1) describes the basic equation of chloride transportation under the three mechanisms:

$$J = -D\frac{\partial c_f}{\partial x} + u \cdot c_f + D\frac{zFU}{RTL} \cdot c_f \qquad (4.1)$$

The first term on the right hand side of Eq. (4.1) is diffusion, which is induced by the concentration gradient of chloride ions. Diffusion is important transport mechanism in both saturated and non-saturated concrete. The second term is convection, which is induced by non-uniform distribution of moisture. Moisture drives the solute chloride ions to move from a humid part to relatively dryer part. Convection is only considered in non-saturated concrete. The third term is migration, which is driven by an electric potential gradient. Migration is not discussed in this study.

In reality, concrete is normally in non-saturated condition. The cracked beams in this research, which are subjected to cyclic wetting, are also in non-saturated condition. Therefore, it is necessary to specify the transportation properties in such a condition.

Chloride transportation in saturated concrete vs non-saturated concrete

The main difference between chloride penetration into saturated concrete and non-saturated concrete is the transportation mechanism. In saturated concrete, the pore structure is considered to be constantly in a completely liquid state for the whole range of concrete. Therefore the predominant transport mechanism is considered to be pure diffusion, provided that no external electrical field is applied. Based on Fick's first law and mass conservation, the governing equation is:

$$\frac{\partial c_t}{\partial t} = \nabla^2 c_f \tag{4.2}$$

where

c_t - total chloride concentration relative to mass of cement, in [g/g] ;

c_f - free chloride concentration relative to volume of pore solution, in [g/l].

The equation could be numerically solved if initial and boundary conditions are known and the chloride binding isotherm is clarified.

For the case of chloride penetration into non-saturated concrete, the transportation mechanism is not pure diffusion, but combined with convective flow of flowing water. The problem becomes more complex since the coupled moisture transportation has to be taken into account. Details are discussed in the next section.

Chloride transportation in uncracked concrete vs. cracked concrete

As has been stated in Chapter 3, the cracked concrete beams are subjected to a wetting-drying cycle with 1% (in gram of Cl^- per gram of solution) chloride solution directly spayed into cracked area for 1 h/week. Except of the 1 hour's wetting, the beams are exposed in laboratory climate with an average temperature 25°C and RH 40%-50%. The chloride penetration process in this research is from crack flank instead of from uncracked concrete surface. The differences exist in the following aspects:

One main difference is the boundary condition, or more specific, the surface chloride concentration. For uncracked concrete, surface concentration could be directly determined by the environmental chloride concentration. Constant surface chloride concentration is commonly taken for submerged or atmospheric exposed concrete, while sinusoidal function is suggested for the concrete structures in splashed and tidal zone[154]:

$$c_0(t) = \frac{c_{0,\max} + c_{0,\min}}{2} + \frac{c_{0,\max} - c_{0,\min}}{2} \sin \lambda (t + \tau_c) \tag{4.3}$$

where

$c_{0,max}$ and $c_{0,min}$ - the maximum and minimum concentrations during each period;

λ - the periodic factor;

τ_c - the initial time.

Assuming a period of one year, $\lambda = 2\pi$.

In the case of cracked concrete, the determination of surface chloride concentration is rather complicated. Chlorides ions penetrate from crack flank into concrete. Therefore the surface concentration is actually the concentration of the 'crack solution', which is greatly influenced by the micro environment in the crack. With the moisture evaporation and the cyclic refilling of chloride solution, the 'water level' in the crack varies with time, resulting in the time-dependent Cl^- concentration of the crack solution. This time dependence will be explained in details in later sections.

Another difference is the depth dependence of chloride diffusion coefficient D_c (and moisture diffusion coefficient D_w in the case of non-saturated concrete). The local composition of the concrete is strongly heterogeneous and depth dependent. Compared to the inner concrete, the pore structure in surface zone is much denser due to more binder and less aggregate. Therefore, diffusivity is lower in the surface zone than in the inner zone. This is called the 'skin effect' or 'wall effect', Andrade *et al* [145]

Tang and Nilsson [154] studied this depth dependence with non-steady state tests and gave a simplified model as shown in Figure 4-3.

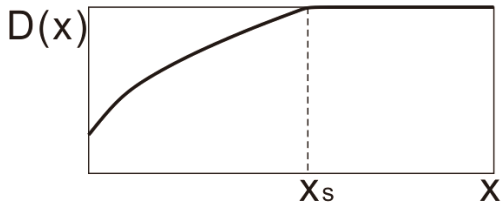

Figure 4-3: Example of depth dependent chloride diffusivity [154]

Based on the test results, an empirical relationship between the chloride diffusion coefficient and depth in both the surface zone and inner zone is given as [155]:

$$D_x = D_s \cdot f(x) = \begin{cases} \varphi + (1-\varphi)(x/x_s)^{\beta_x} & x < x_s \\ 1 & x \geq x_s \end{cases} \quad (4.4)$$

where

φ- the ratio of the diffusivity at the surface to that at the inner zone $(\varphi = D_{surface}/D_{inner})$;

x_s and β_x - constants. The value of β_x and x_s are given by Tang [155] as shown in Table 4-1.

Table 4-1: Typical coefficients for chloride diffusivity [155]

Binder type	w/b ratio	x_s [cm]	φ	β_x
Dagerhamn	0.35	0	0.53	0.68
Dagerhamn	0.4	0	0.53	0.68
Dagerhamn + 5% CSF	0.4	2	0.53	0.68
Dagerhamn	0.4	4	0.21	0.65
Bansk	0.52	3	0.48	0.878

When modelling the chloride penetration into uncracked concrete, it is important to consider the depth dependence of chloride diffusivity.

However, in the case of cracked concrete it is not necessary to take into account of this wall effect in the main chloride transportation direction (i.e. y-direction, Figure 4-1). This is because the concrete permeability along y-direction can be considered as identical.

A third aspect is the initiation period. For uncracked concrete, the distance between the casting surface and the embedded reinforcement, i.e. the cover depth, is the shortest chloride transportation path. When the chloride reaches the steel surface and accumulates to a critical content, corrosion is initiated. However, for the concrete with a crack crossed the reinforcement, initiation period is extremely short. Crack flank acts as a newly exposed surface and absorbs the solution into the concrete. Therefore, the research interest is not

focused on how long the initiation period lasts, but how large an area is depassivated and how deep the chloride penetrates into the concrete.

4.2.3 Basic Equations of chloride penetration into unsaturated cracked concrete

In non-saturated concrete, at any point, there exists an infinitesimal element whose centre located at the point, as shown in Figure 4-4.

According to the principle of mass conservation, we have:

$$\frac{\partial J_x}{\partial x}+\frac{\partial J_y}{\partial y}=-\frac{\partial c_t}{\partial t} \tag{4.5}$$

In which,

J_x and J_y - chloride penetration flux along x and y direction respectively, in (g of chloride iron per cm^2 per $second$).

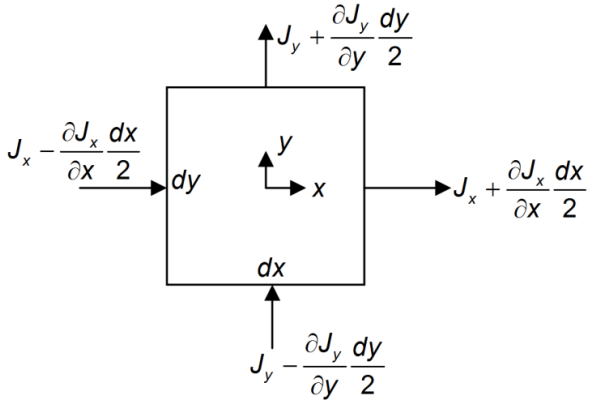

Figure 4-4: Chloride penetration flux on a typical element

Considering the two transportation mechanisms involved in unsaturated concrete, the flux are composed of two parts: chloride diffusion due to the gradient of chloride concentration, and the convection induced by moisture diffusion. Expressed as:

$$J_c=\begin{Bmatrix}J_x\\J_y\end{Bmatrix}=\begin{Bmatrix}-D_c\dfrac{\partial c_f}{\partial x}\\-D_c\dfrac{\partial c_f}{\partial y}\end{Bmatrix}+\mu\begin{Bmatrix}c_f\cdot J_x'\\c_f\cdot J_y'\end{Bmatrix} \tag{4.6}$$

In which

D_c- chloride diffusion coefficient, in (cm^2/s);

μ - pore solution content, i.e., mass ratio of concrete to pore solution, in (g of concrete/g of pore solution).

J_x' and J_y' - moisture flux along x and y direction (g of pore water per cm^2 per $second$).

Similar to Eq(4.5), moisture conservation could be written as:

$$\frac{\partial J_x'}{\partial x} + \frac{\partial J_y'}{\partial y} = -\frac{\partial w}{\partial t} \tag{4.7}$$

In which, w- the moisture content (g of solution/g of concrete), including both evaporable water and non-evaporable water.

Eq.(4.5) and Eq.(4.7) are the basic equations for moisture and chloride transportation, by which the main required variables h and c_f could be solved, once the boundary and initial conditions are known.

To solve the basic equations, parameters have to be determined, e.g. the diffusivity of chloride and moisture, and the chloride binding capacity of concrete, as well as the moisture capacity. In this study, the diffusivity is obtained by a factorial approach, taking into account of the influence of concrete composition and environmental conditions. Freundlich binding isotherm and Langmuir binding isotherm are adopted for chloride concentration in different levels.

The details on calculation process and the determination of parameters are given in Appendix B.

4.3 Numerical model of the chloride/moisture penetration into cracked concrete

4.3.1 Geometry of the model

Figure 4-5 shows half of the cracked beam. The rectangular area 'MNPQ' is the crack flank. Chloride solution is filled in this domain during wetting cycle and then penetrates into concrete perpendicularly from the crack flank. Therefore, the geometric domain for the numerical modelling is a rectangular area "ABCD", with the dimension of $8 \times 10\mathrm{cm}^2$. This geometry is so selected that the real conditions of the cracked beam could be represented and unnecessary domains are neglected for simplification. Considering the stainless foil in the crack cross section, the length along crack (i.e. A->D, x-direction) is set as 8 cm; after a

trial calculation and rough survey into related literatures, the chloride penetration depth is expected to be less than 5 cm for the concrete. However, in order to minimize the influence of cutting calculation domain, the length along main penetration direction (A->B, y-direction) of the models is set as 10 cm.

Although there are three corrosion cells in one cracked beam, it is not necessary to build them all.

4.3.2 Initial condition and boundary conditions

Initial conditions

As has been shown in Figure 4-6, the relative humidity in laboratory mainly ranges from 40% to 50%. Therefore it is simply assumed that the RH in pore structure of whole specimen is uniformly 50%, which is used as the initial condition for moisture diffusion simulation:

$$h^0 = 0.5 \quad \text{for all points} \tag{4.8}$$

Strictly speaking, the original specimens might contain a bit of chloride ion from its components, but the amount of the chloride ion in this study is very small and will be ignored. So the initial condition for chloride is:

$$c_f^0 = 0.0 \quad \textit{and} \quad c_t^0 = 0.0 \quad \text{for all points} \tag{4.9}$$

Boundary conditions

The right edge (AB side) of the model is the concrete casting surface which is exposed to the air. Boundary condition on this side could be assumed the same as environmental condition:

$$RH = 50\% \quad \textit{and} \quad c_f = 0.0 \quad \text{at line AB, always} \tag{4.10}$$

The left edge (CD side) of this model is a symmetric boundary since the specimen at the left side of CD is the same as the right part of the model. Therefore the boundary condition at the left edge could be assumed as symmetric condition. A column of virtual points are located outside the left edge and mirrored with points $i = N_x - 1$ (N_x is the column number of the meshed points)

$$h_{N_x+1,j} = h_{N_x-1,j} \quad \textit{and} \quad (c_f)_{N_x+1,j} = (c_f)_{N_x-1,j} \quad \text{,always} \tag{4.11}$$

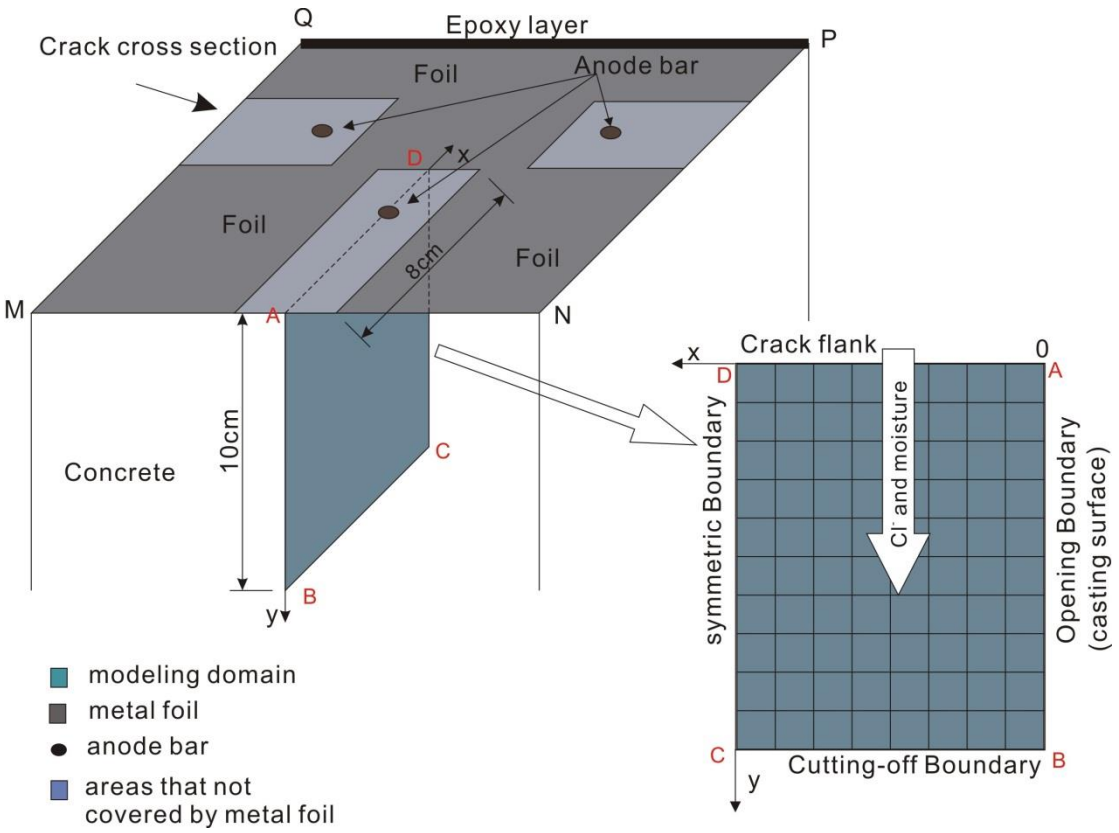

Figure 4-5: Geometry of modeling domain

The bottom edge (BC side) is also assumed to be symmetric condition that neither chloride ions nor moisture could pass through this edge. Boundary conditions on bottom edge (BC) are expressed similarly as the left edge (CD):

$$h_{i,N_y+1} = h_{i,N_y-1} \quad and \quad (c_f)_{i,N_y+1} = (c_f)_{i,N_y-1} \quad \text{always} \tag{4.12}$$

In which N_y is the row number of the meshed points.

The top edge (AD side) is the crack flank which is exposed to the wetting-drying cycle of chloride solution. Consequently, the A->B direction is the main penetration direction for the moisture and chloride ions. The boundary condition on AD side is rather complicated. The water level and chloride concentration vary with time due to the effect of moisture evaporation and cyclically refilling of chloride solution. Therefore, the crack flank boundary is divided into three zones:

Zone D->E: Point E represents the water level at a certain moment. Then boundary DE is under submerged condition with its surface concentration varies with time:

$$C_s = C_s(t), \text{ when } x \in \left(x_{E(t)}, x_D\right) \text{ and y=0} \tag{4.13}$$

where $C_s(t)$ is the time dependent chloride concentration in crack solution, $X_{E(t)}$ is the time dependent water level in the crack which could be estimated by water evaporation rate test. Both $C_s(t)$ and $X_{E(t)}$ would be discussed in detail in section 4.4.

Zone E->F: A small area (5 mm) above point E is considered as the transition zone. It is a semi-saturated zone with RH linearly varies from 100% to 50%;

Zone F->A: This area is above the transition zone. In this zone, RH is set as 50%.

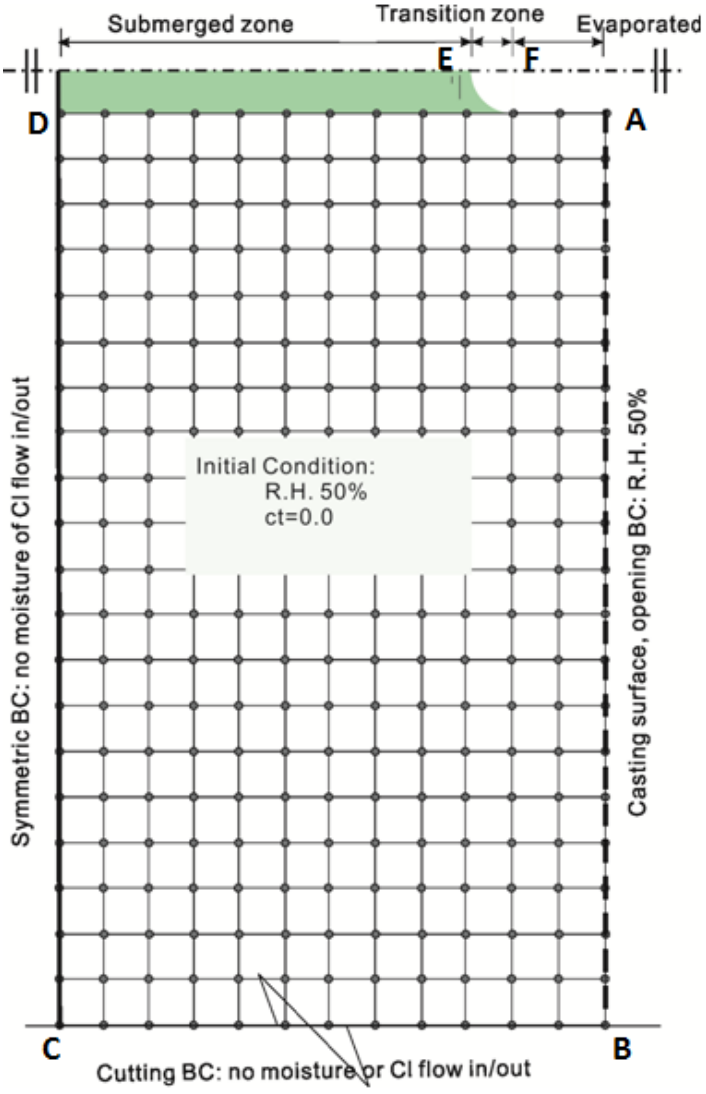

Figure 4-6: Boundary conditions and finite-difference mesh in numerical analysis

4.4 Experimental study on water evaporation rate in crack

To solve the basic equations in Eq.(4.5) and Eq.(4.7), certain boundary conditions have to be figured out. As stated in Section 4.3.2, all the boundary conditions are already known except

those on the crack flank (boundary AD). It has been assumed that a certain 'water level' exists in the crack, as shown in Figure 4-7. Above this level, chloride solution has dried out due to evaporation and consequently stopped penetrating into the concrete. Only under this level chloride and moisture keep penetrating into concrete. The location of the water level is indispensable in determining the chloride concentration in crack solution. It is essential input data for the numerical calculation.

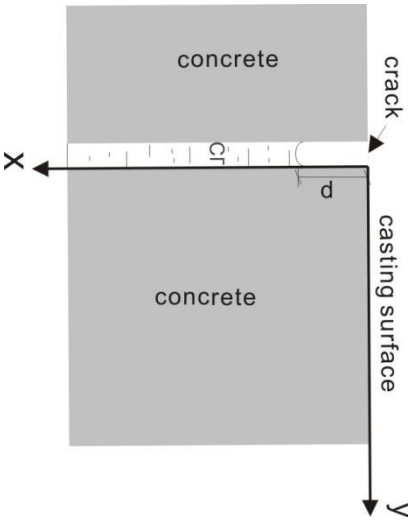

Figure 4-7: Scenario of water evaporation in crack

4.4.1 Measuring principle

To determine the moisture condition in crack, water evaporation rate test has been conducted on centrally cracked concrete slabs. Wire probes were arranged in the crack at different depth in order to measure the resistance of the crack. Resistivity could serve as an indicator of moisture condition or the water level in crack. The method of determining the moisture condition by measuring the electrolytic resistivity is based on the principle that the resistivity is reversely related to moisture content to a certain extent. When the electrolytic resistance between two probes increases drastically, the concrete there might be experiencing drying out.

4.4.2 Experimental setup

Water evaporation rate tests were conducted on concrete slabs with the dimension of $30 \times 30 \times 10cm^3$, on both CEM I and CEM III concrete with w/c ratio of 0.5. Concrete age was three years which is approximately the same age as the cracked beams studied in Chapter 3. The slabs were originally stored in chamber with temperature 0-5°C and RH 75% and then

were stored in normal laboratory climate (20°C and RH 50%) for two months till they were cracked.

A single crack was generated by applying a compressive force along the intermediate line of the slab through two triangular steel prisms. A group of wires were arranged parallelly in the crack plane with stepwise depths, Figure 4-8. The diameter of the wires is approximately 0.30 mm. The wires are isolated with rubber cover except 1 mm o n the tip, which work as probes for the resistivity measurement. Then the two halves of the slab were anchored together again.

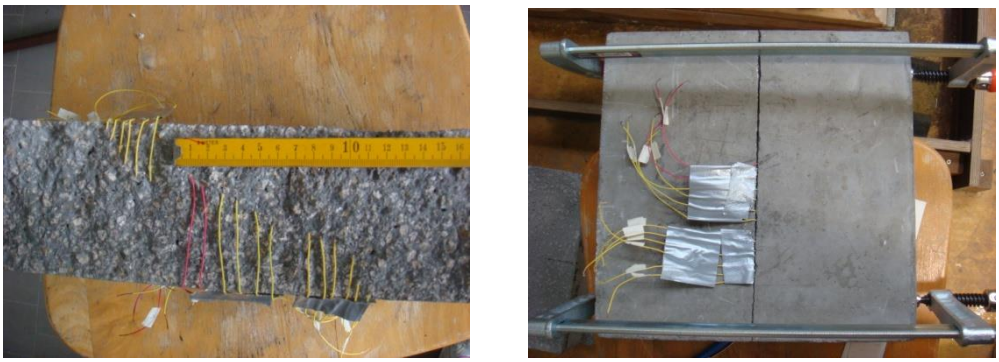

Figure 4-8: Wire arrangement in crack

Electrolytic resistances of the cracks at different depths were measured via a LCR-Bridge instrument by connecting two adjacent wire probes, as shown in Figure 4-9. The electrolytic resistivity of saturated concrete is in the range of hundreds $\Omega \cdot m$, depending on its composition and age; while dry air is nearly ideally isolating. So it is reasonable to assume that if a drastic increase of resistance between two probes is observed, water level has dropped to this level at this moment.

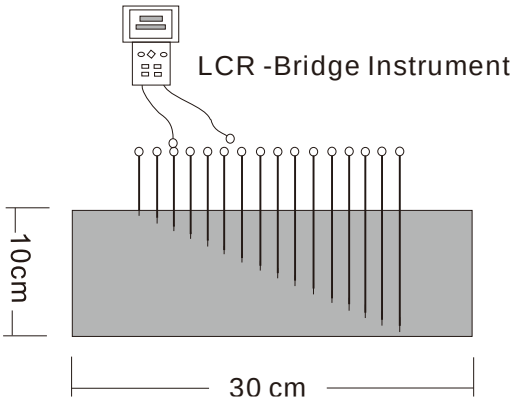

Figure 4-9: Measurement of electrolytic resistance between adjacent wires

In order to get stable results, the samples were pre-moisturized for one month by spraying water into crack for 30 min each day. By doing this, the vicinity concrete of the crack could be considered in a relatively stable moisture condition.

After all the preparations, slabs are subjected to weekly wetting-drying cycle with tap water sprayed into crack area for 30 minutes per week. Electrolytic resistances were measured and recorded at certain time intervals till the next cycle. The watering cycle was repeated for 8 weeks so that more accurate and stable results could be obtained.

4.4.3 Results

It was observed that the moisture condition at a certain crack depth d_i can be differentiated in three phases, Figure 4-10:

Phase 1- Saturated Phase. Measured electrolytic resistance in this phase is very low, indicating that depth d_i is still under water.

Phase 2- Evaporating Phase. Electrolytic resistance in this phase shows a drastic increase, indicating that d_i is currently experiencing evaporation. Surrounding concrete at d_i is partially saturated. This transition phase lasts from less than 1 hour to hundred hours, depending on how deep d_i is.

Phase 3- Dried out Phase. Electrolytic resistance in this phase is very high and shows no further increase. Readings from LCR-Bridge instrument is quite unstable due to the high resistance. This phase lasts from the end of evaporation phase till the crack is refilled by Cl solution again.

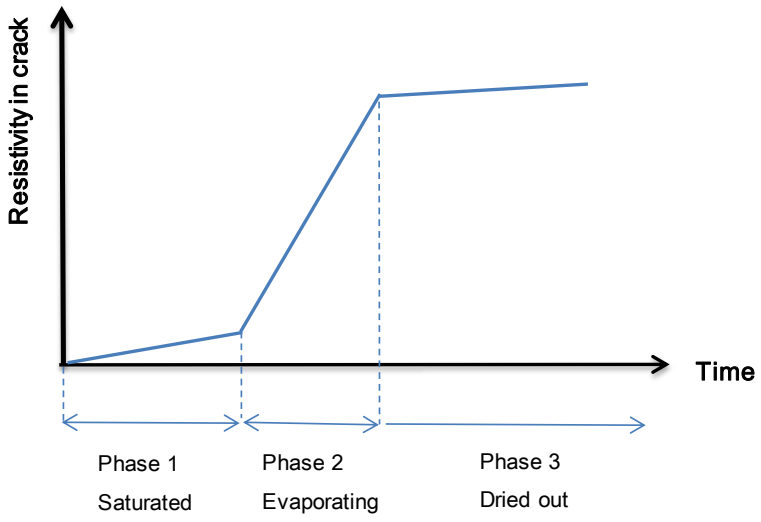

Figure 4-10: 3-phase model of moisture condition at d_i in crack

It's also noticed that crack has the opportunity to experience all the three phases only when d_i is above a certain depth d_{lm}. There is no phase 3 or even phase 2 if d_i is deep enough because one week is a rather a short exposure time. This means that the crack under this certain depth d_{lm} is always saturated. This critical depth d_{lm} depends on crack width and environmental conditions such as temperature and RH, etc.

Actually, if related to Figure 4-6, points between D-E are in phase 1; points between E-F are in phase 2; points between F-A are in phase 3.

The relationship between the water level and the exposure time is illustrated in Figure 4-11 (a) and (b). The two curves in (a) are time developments of resistances at two different crack depth, d_m and d_n. From the drastic increase of resistance, the moments when evaporation begins could be determined. For d_m=0.66 cm, the evaporation begins at t_m= 2h, while for d_n= 1.98 cm, evaporation begins at 24h; The two curves in (b) are electrolytic resistances at different crack depth measured at 24 h and 48 h respectively. Judging by the huge difference of measured resistance between the adjacent depths, the water level could be determined. At t_p= 24h, water level d_p is at 1.98 cm; while at t_p= 48h, water level dropped to 2.66 cm. Combining the two judgments in Figure 4-11, the time dependent water level in crack can be determined.

Since no difference between CEM I and CEM III concrete was found, the following results are based on the experimental data averaged from the four specimens in 8 cycles. A logarithm relationship between water level and exposure time t was obtained by data fitting with minimum square method, Figure 4-12 and equation (4.14)

$$d(t) = a \cdot \log(t) + b \tag{4.14}$$

Where in this experimental set up, $a = 1.283$, $b = 0.334$.

The two constants a and b in Eq.(4.14) are simply mathematically estimated without any physical meaning. For example, the water level drop should be zero at the very beginning of the test (t=0), however, according to Eq. (4.14), $\lim_{t\to 0} d(t) = -\infty$.

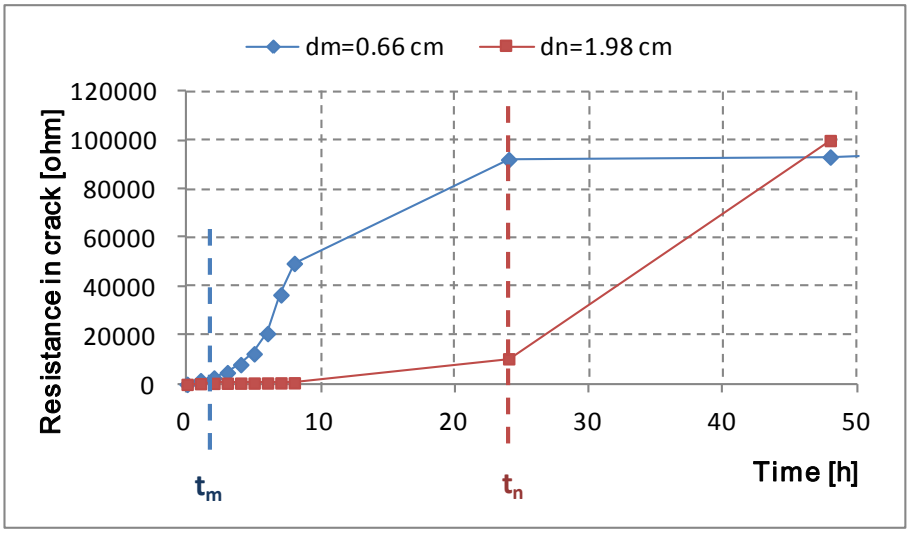

(a) The variation of electrolytic resistance with time, at two depths.

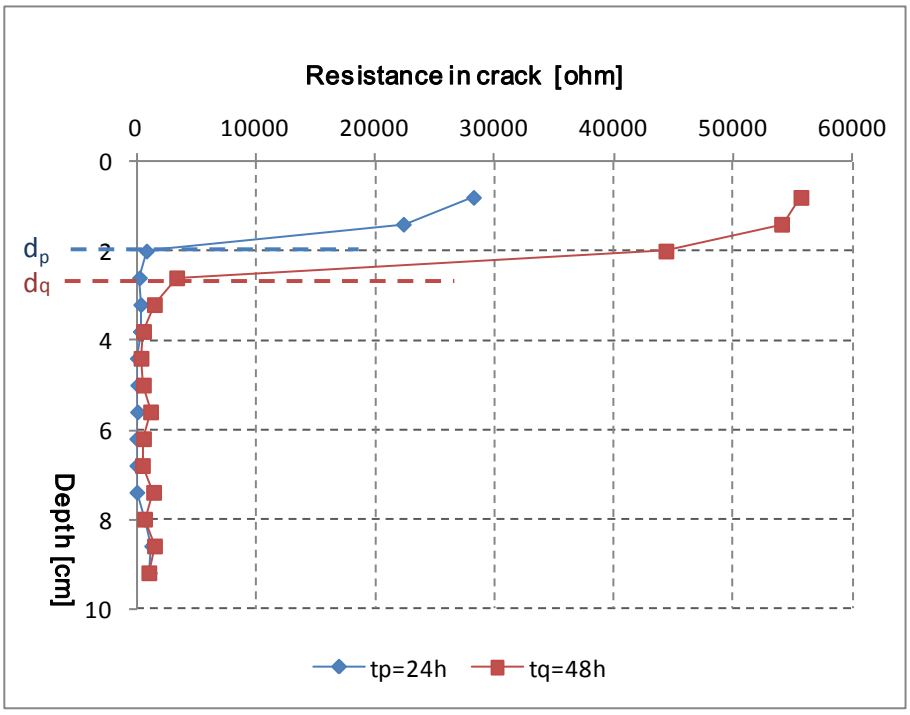

(b) The variation of electrolytic resistance with crack depth, at two moments

Figure 4-11: Determination of the relation between the water level and evaporation time

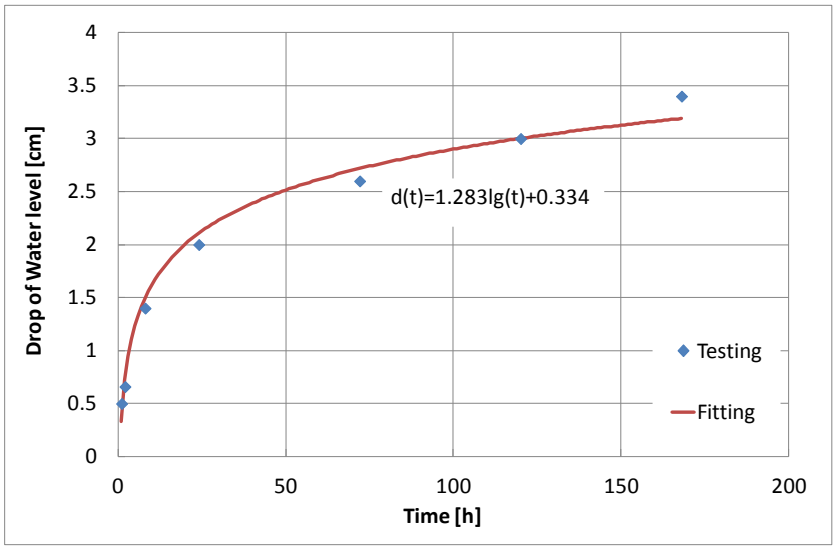

Figure 4-12: Drop of water level with exposure time

4.4.4 Summary for the water evaporation test

A brief summary for the water evaporation test:

1) It is a feasible method to use electrolytic resistance as an indicator for the moisture measurements in the crack.
2) Water level in a crack has found to be logarithmically related to exposure time. A formula has been given based on experimental data. Consequently an estimation of the time dependent chloride concentration in the crack solution is possible in the later numerical calculation.
3) No influence of cement type on water evaporation rate in cracks has been found.
4) Although the water evaporation test has been so designed to simulate the cracked beams mentioned in Chapter 3 as close as possible, there are still disparities. The differences exist in crack width and wetting duration.
5) In addition to the investigated parameter, it can be expected that factors such as crack width and environmental temperature and relative humility etc., fundamentally influence the water evaporation rate in crack. Further research on those factors is necessary if time and finance permitted.

All in all, this experimental setup is rough but feasible; its accuracy needs further validation.

4.5 Results of numerical calculation

Chloride penetration into non-saturated cracked concrete is a complex process with different transport mechanisms included: diffusion and convection, coupled with humidity diffusion.

The penetration of moisture and chlorides is influenced by both the material properties of concrete and the environmental boundary conditions. For concrete material properties, factors such as cement type, w/c ratio, cement content (aggregate fraction) and curing time, play a crucial role; for environmental boundary conditions, temperature and relative humidity, as well as chloride concentration at the exposed surface are the most important influencing factors.

This study deals with the chloride penetration into concrete from crack flanks. It is an even more complex case since the chloride concentration at the exposed surface varies with time due to the mixed effect of evaporation and wetting-drying cycles. The determination of chloride concentration at the exposed surface (i.e. the crack flank) is quite difficult since it is related to the crack geometry, the evaporating and cyclic refilling of chloride solution and the consumption rate of chloride ions by the concrete. The chloride consumption rate is again affected by surface concentration and concrete properties. Therefore, due to the particularity of this study, the surface chloride concentration and the chloride/moisture penetration mutually influence each other.

4.5.1 Water level and chloride concentration at the exposed surface

Figure 4-13 shows the variation of water level with the exposure time in crack. As has been stated in Section 4.4.3, water level could be reduced by 3.1 cm in one wetting-drying cycle due to the effect of evaporation and then rise back to surface when the next cycle begins.

The variation of the chloride concentration in the crack solution with exposure time is also shown in Figure 4-13. Chloride concentration is 1% at the beginning of the wetting cycle, then decreases gradually and finally reaches minimum value of about 0.01% at the end of the first drying period. The chloride ions in the crack solution are almost consumed by the concrete. At the beginning of the second cycle, the concentration is raised to 0.4% due to the refilling of chloride solution. After the 1 hour wetting period, solution density increased within a short period. This is because that water level drops very fast at the beginning of

drying period. After this short period, the water evaporation slows down and the solution density in crack begins to decrease again.

Figure 4-14 illustrates the variation of chloride concentration in crack solution during 3 years exposure, I05360. It is obvious that the chloride concentration increases with exposure time. This is because the consumption of chloride ions by the concrete decreases with exposure time. The maximum concentration value can reach to 2.41% after 3 years exposure.

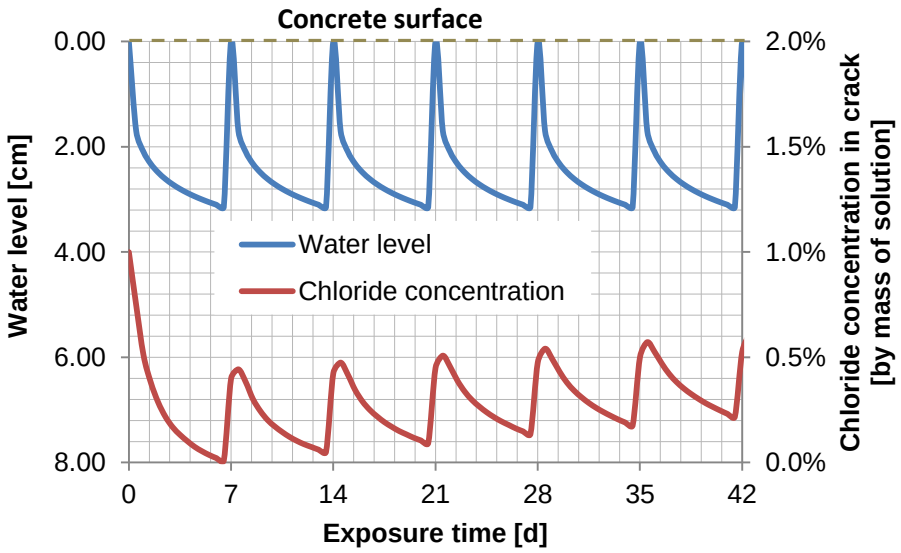

Figure 4-13: The variation of water level and the chloride concentration in crack solution with exposure time, I05360

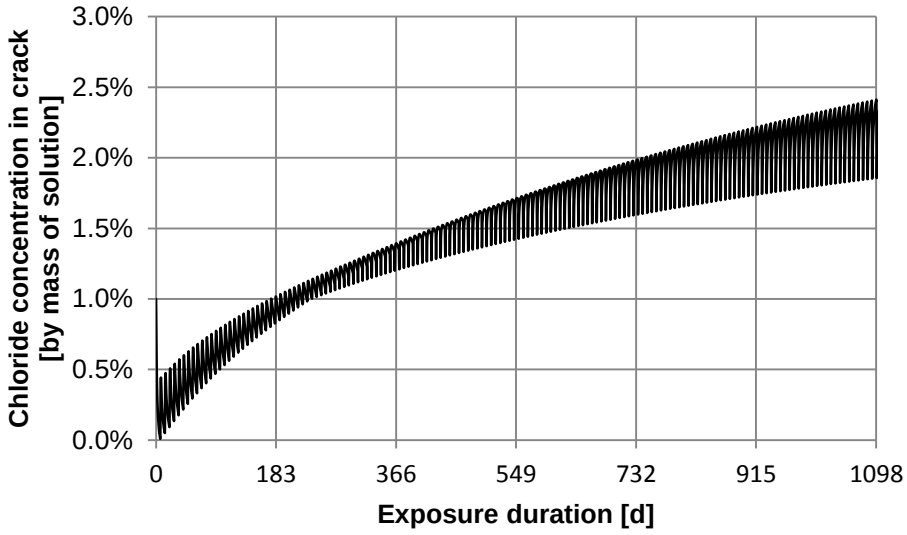

Figure 4-14: Variation of chloride concentration in crack solution with exposure duration, I05360

4.5.2 Moisture distribution in cracked concrete

As has been introduced in section 4.4.3 that the initial pore relative humidity inside the concrete is assumed to be 50%; crack flank is the only boundary that exposed to wetting-drying cycle of chloride solution. Therefore, moisture diffuses into the concrete from crack flank when the cycle starts, with a main diffusion direction along y-direction.

Figure 4-15 (a) to (d) illustrate the contour plots of relative humidity in concrete pore structure at different exposure duration. Here are some observations from these plots:

1) The moisture diffusion is rather fast in the early cycles and then slows down gradually after one year exposure. Moisture field reaches equilibrium after one and half year's exposure duration. This coincides well with the observed equilibrium state of corrosion current that has been reached after 1.5 years exposure in chapter 3. Therefore equilibrium of moisture field could be a main reason for the equilibrium of corrosion currents.
2) Moisture diffusion is uneven along crack depth (along x-direction). Pore RH increases with x value in the range of $x \in (0, 3.1)$ cm, with y value fixed. This is because that water level only dropped 3.1 cm in one drying cycle. The crack flank is exposed to chloride solution for different duration in the range of $x \in (0, 3.1)$, and is permanently submerged in the range of $x \in (3.1, 8)$. However, pore RH in the range of $x \in (3.1, 8)$ are not completely uniform. This is because that moisture diffusion along x-direction also takes place due to the moisture gradient in this direction.

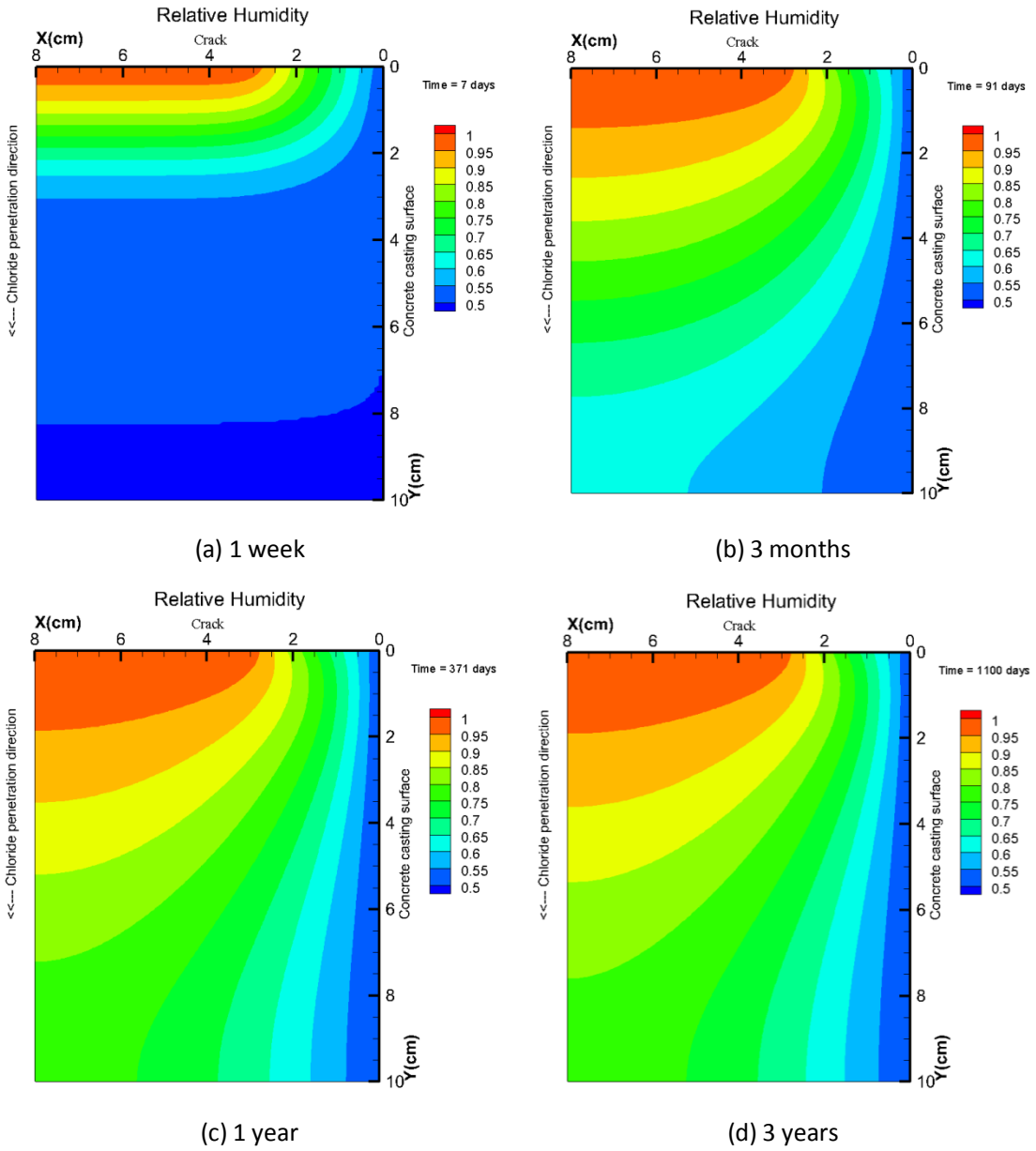

(a) 1 week

(b) 3 months

(c) 1 year

(d) 3 years

Figure 4-15: Contour plots of relative humidity in concrete, I05360.

Figure 4-16 is the profile of RH in concrete pore structures at x= 5 cm, at different exposure durations. It could be seen that at any fixed time, pore RH decreases from the exposed surface to the inner concrete. RH gradient decreases with the increasing of exposure duration. The curve with one year exposure is nearly overlapped with the 3 years' curve which indicates that the moisture field in concrete is approaching equilibrium after one year exposure.

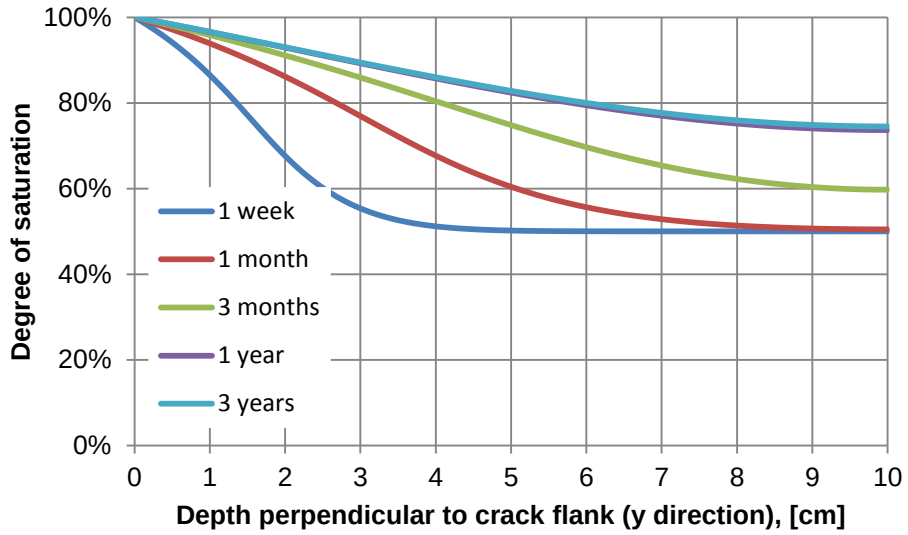

Figure 4-16: Profile of degree of saturation, at x=5 cm, I05360

4.5.3 Diffusivity coefficients D_h and D_c

As important material property, moisture diffusion coefficient D_h is not purely defined by concrete itself but also the RH conditions in concrete pore structure. D_h, in turn, also influences the moisture diffusion process and consequently the RH conditions in concrete. Figure 4-17 (a) to (d) illustrate contour plots of D_h at different exposure durations. D_h decreases with y value, with fixed X value; while increases along x-direction in the range of $x \in (0, 3.1)$ cm. Similar to RH, the variation of D_h tends to stop after about one and a half years' exposure. According to the results, D_h of I05360 concrete ranges from $1 \times 10^{-7}\ cm^2/s$ to $4.6 \times 10^{-7}\ cm^2/s$.

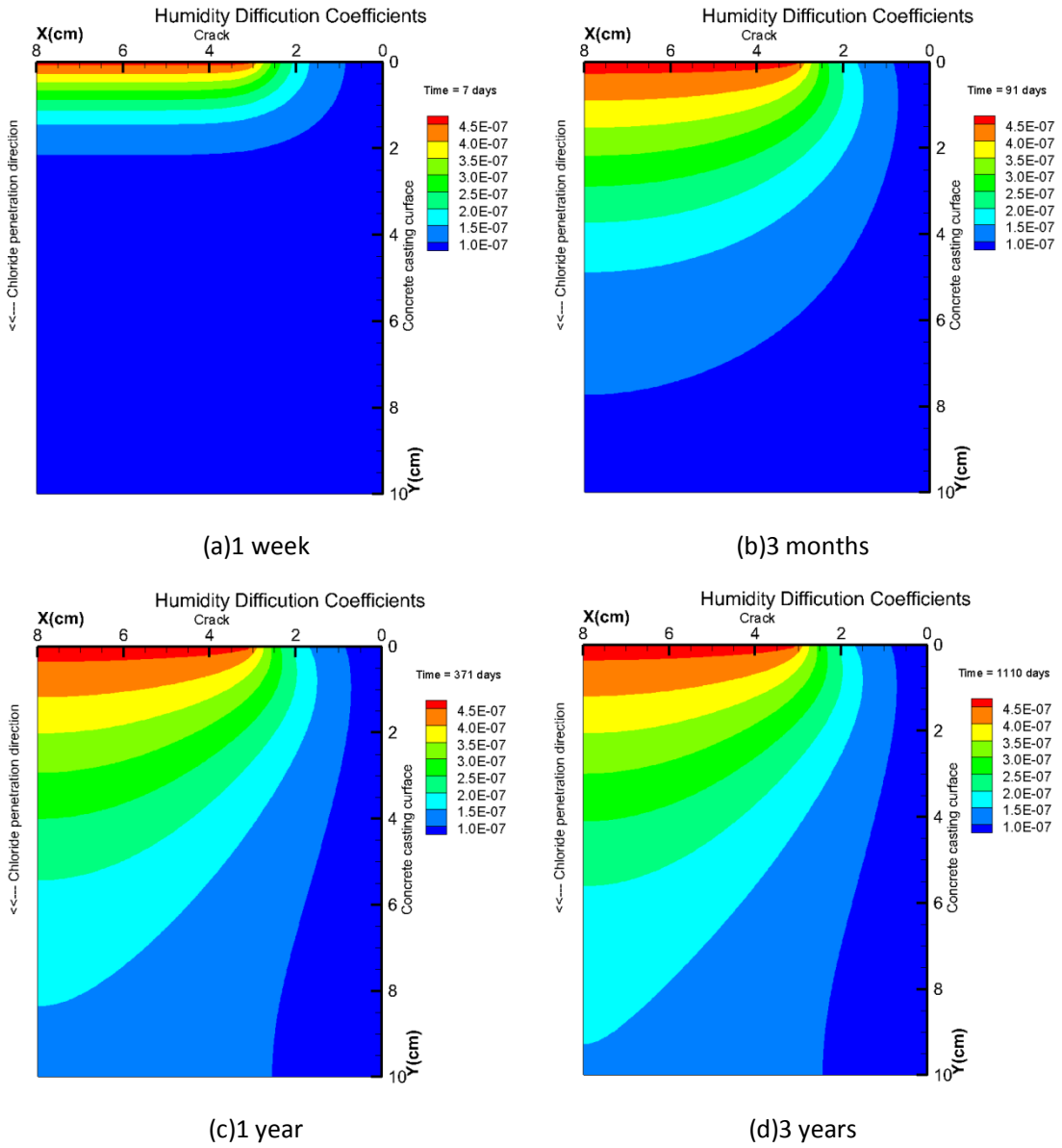

(a)1 week (b)3 months

(c)1 year (d)3 years

Figure 4-17: Contour plots for diffusion coefficient of RH, I05350, [cm^2/s],

Figure 4-18 (a) to (d) illustrate contour plots of chloride diffusion coefficient of I05360 concrete. D_c ranges from $5 \times 10^{-9} cm^2/s$ to $7 \times 10^{-8} cm^2/s$. Unlike D_h, D_c varies with exposure duration all the time that no equilibrium state has been observed within 3 years' exposure. This is because that D_c does not only depend on moisture content but also the free chloride content. Besides, D_c neither simply decreases with penetration depth (y value) nor increases with time.

It is known that the CEM III cement, which contains 36-65% of granulated blast furnace slag as replacement of cement has much finer pore structure than that of CEM I concrete. Therefore, it is expected that CEM III concrete has better resistance against chloride

penetration than CEM I concrete. The diffusion coefficient of III05360 is in the range of 5×10^{-10} to 1×10^{-8} cm^2/s which is approximately one order lower than that of I05360. Results of III05360 are attached in the appendix D.

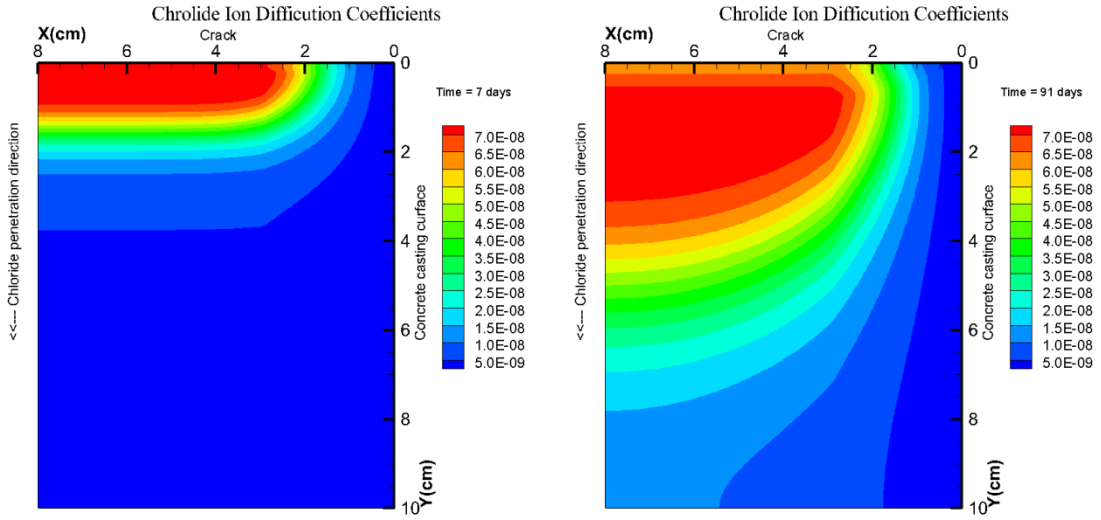

(a) 1 week

(b) 3 months

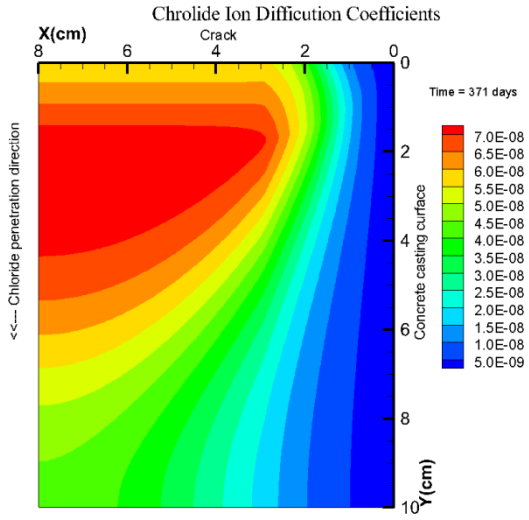

(c) 1 year

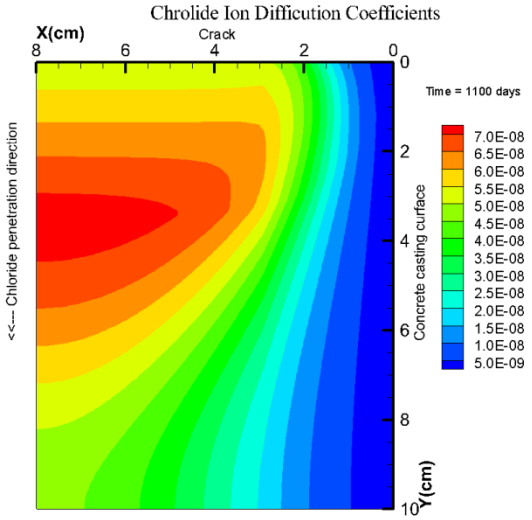

(d) 3 years

Figure 4-18: Contour plots of chloride diffusion coefficient D_c of I05360, [cm^2/s].

4.5.4 Total chloride content C_t and free chloride content C_f

Figure 4-19 (a) to (d) are contour plots of total chloride content C_t at different exposure durations of I05360. Initial chloride content in concrete is zero. Chloride ions penetrate from crack flank into concrete due to the propulsion of diffusion and convection. The different colours in contour plots denote the levels of total chloride concentration by mass of cement, in [g/g]. Total chloride content decreases from crack flank into inner concrete. Meanwhile, C_t

increases with x value in the range of $x \in (0,3.1)$, with y fixed. This is because that in this range the exposure duration also increases with x value due to the effect of moisture evaporation. With the contour plots, total chloride contents at any time and any location could be easily determined.

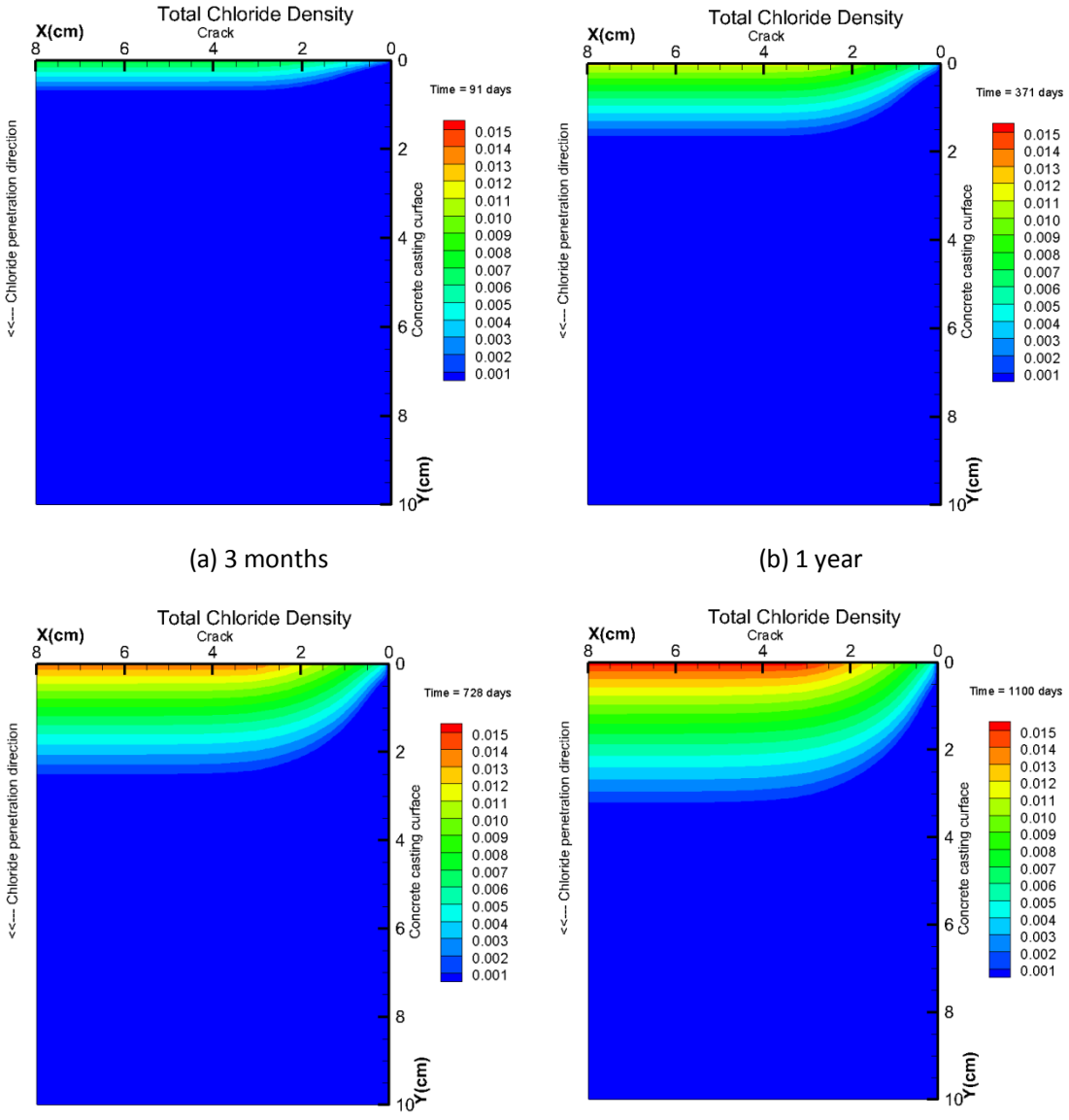

(a) 3 months

(b) 1 year

(c) 2 years

(d) 3 years

Figure 4-19: Contour plots of total chloride density C_t in concrete, I05360, [g of Cl^-/g of cement]

With the calculated C_t, the chloride penetration front in concrete can be determined. Penetration front is defined as the depth in the concrete where the total chloride concentration C_t equals a predetermined value. If this predetermined value is set as the chloride threshold value (C_{TH}), then the location of C_{TH} at this moment could be predicted. In

this study, C_{TH} is set as 0.5% by mass of cement for CEM I concrete and 1% for CEM III concrete[141]. In Figure 4-20, the location of the penetration front is plotted against the exposure time, I05360, at x=5 cm. It could be seen that, the penetration front reaches a depth of 2.15 cm after 3 years exposure.

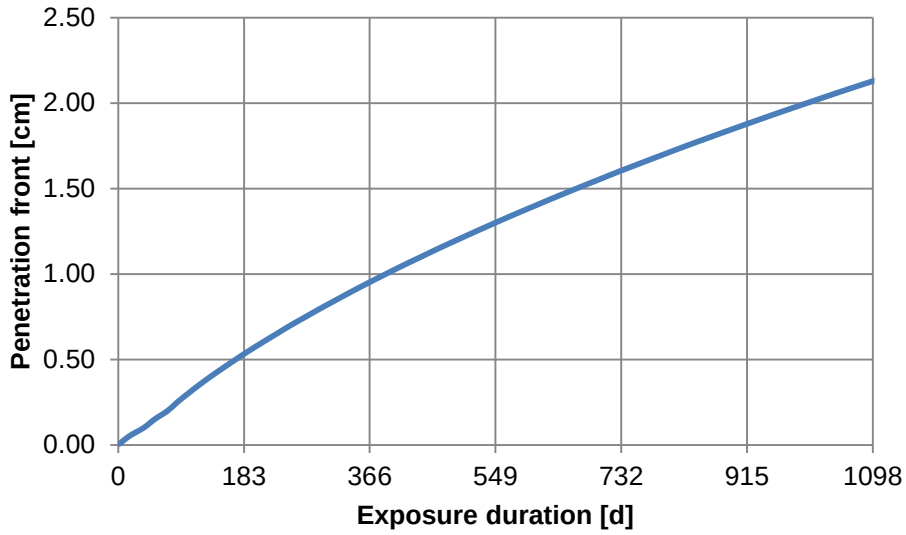

Figure 4-20: Development of penetration front with exposure duration, at x=5 cm, I05360

Figure 4-21 shows the location of penetration front at the exposure duration of 3 years. The penetration front is denoted as the interface of the red zone and blue zone in Figure 4-21. Therefore, either Figure 4-20 or Figure 4-22 can be used to predict the location of the penetration front for a fixed C_{TH} at any time and any location.

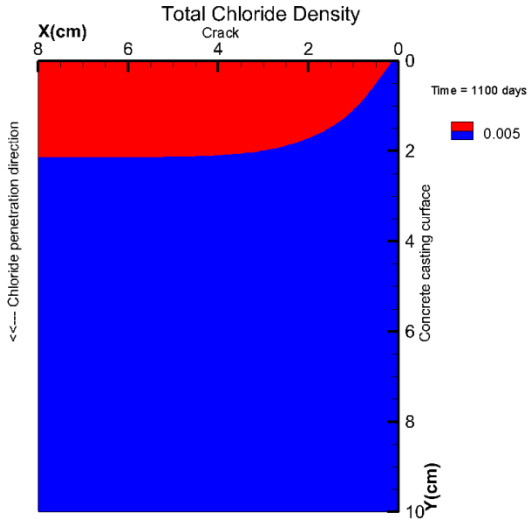

Figure 4-21: An example of determining the location of C_{TH} at 3 years, I05360.

Figure 4-22 illustrates the total chloride concentration C_t along the main penetration direction (y-direction) at different exposure durations. C_t close to the exposed surface (crack flank) ranges from 0.78% to 1.55% by mass of cement and then decreases with penetration depth. An almost linear relationship between C_t and penetration depth could be observed.

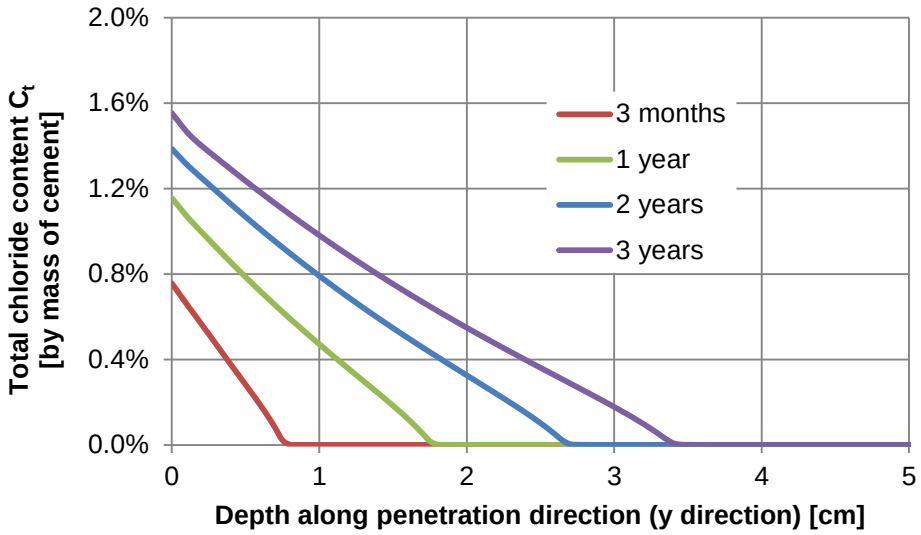

Figure 4-22: Total chloride concentration C_t along penetration direction (perpendicular to crack flank, i.e. y-direction), x=5 cm, I05360

Contour plots of free chloride contents at several selected exposure time are shown in Figure 4-23 (a) to (d). With those contour plots, free chloride content at any time and any location could be easily known. The distribution of C_f is similar with the contour plots of C_t.

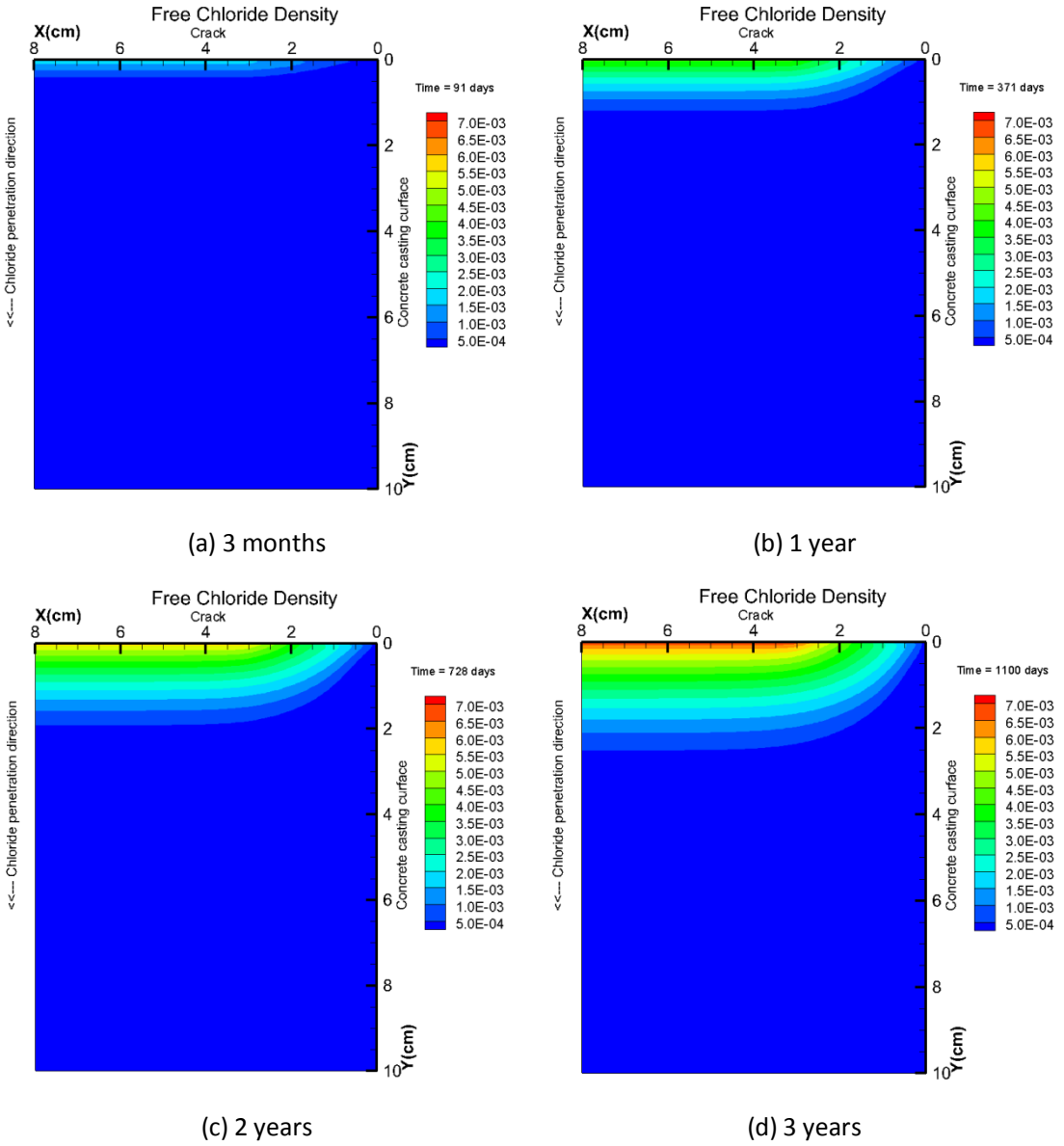

(a) 3 months (b) 1 year

(c) 2 years (d) 3 years

Figure 4-23: Contour plots of free chloride density C_f of I05360, [% by M. of cement].

Figure 4-24 illustrates the free chloride concentration C_f along main penetration direction (y-direction) at different exposure durations. C_f close to the exposed surface ranges from 0.19% to 0.69% by mass of cement and then decreases with penetration depth. Unlike the C_t curve, the curve of C_f against penetration depth is a concave line, indicating that the penetration of free chloride slows down in deep concrete. This is because that the binding isotherm is concentration dependent.

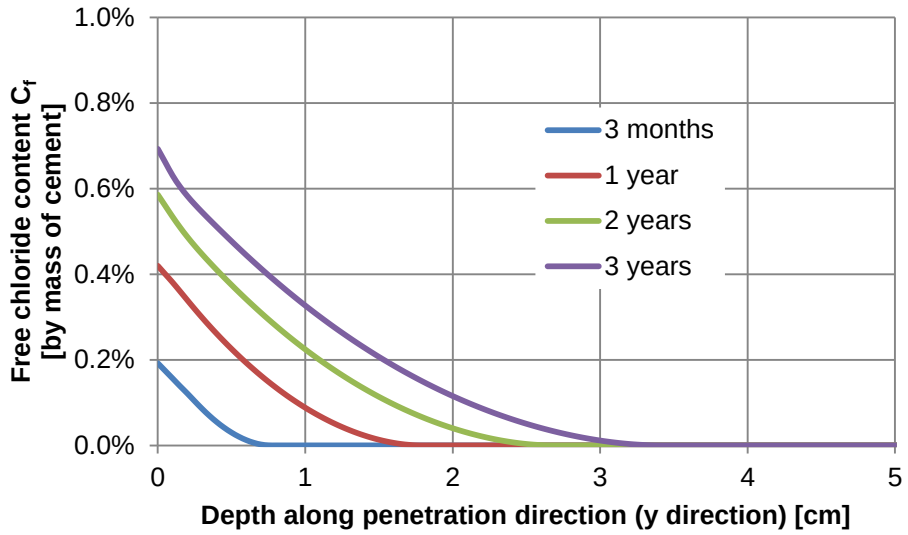

Figure 4-24: Free chloride concentration C_f along penetration direction (perpendicular to crack flank, i.e. y-direction), x=5 cm, I05360

The above discussed results are mostly from I05360. The corresponding calculated results for III05360 are given in Appendix D.

4.6 Discussion

4.6.1 Comparison with experimental results

One of the motivations of the numerical calculation of this chapter is to validate the experimental results of Chapter 3. In Chapter 3, total chloride profiles were obtained by taking sample in 1 cm steps from concrete surface perpendicularly into crack, i.e. along x-direction (see in Figure 3-14 in page 56 and Figure 3-36 in page 79). There were five steps. Therefore total chloride contents C_t from x= 0 to 5 cm were obtained.

The comparisons between experimental and numerical results of I05360 after two and three years' exposure are illustrated in Figure 4-25. Although there is some dispersion, the numerical results could generally match with the experimental results.

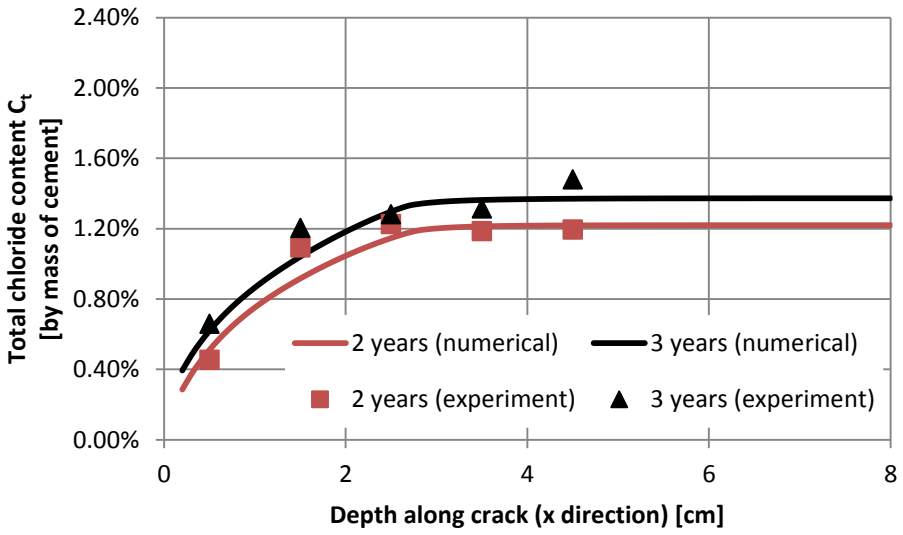

Figure 4-25: Comparison of total chloride profile along crack (x-direction), I05360

The comparisons between experimental and numerical results of III05360 are shown in Figure 4-26. Numerical data deviate from experimental data, however in acceptable range. The deviation can be attributed to the difference in crack geometry of individual cracks. The overall tendency is accordant.

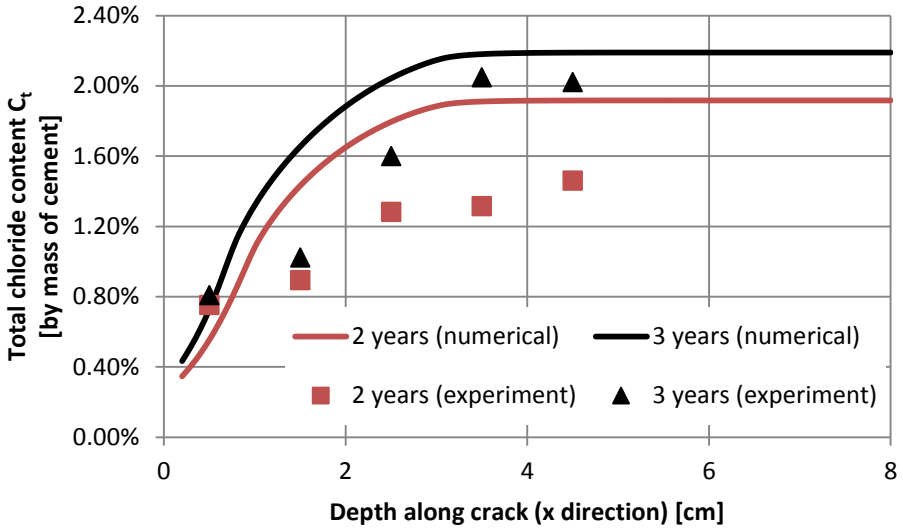

Figure 4-26: Comparison of chloride profile along crack (x-direction), III05360

Figure 4-27 illustrates the evolution of penetration front of I05360 and III05360 concrete at x=5 cm. It has to be noted that, the critical total chloride concentration C_{TH} for CEM I and CEM III concrete are considered as 0.5% and 1% respectively[141]. Chloride ions penetrate much further and faster in CEMI concrete than in CEM III concrete. For example, penetration

front reaches 2.15 cm in CEM I concrete after 3 years exposure, while for CEM III concrete, this value is only 0.98 cm. This result clearly indicates that CEM I concrete is more vulnerable to chloride attack.

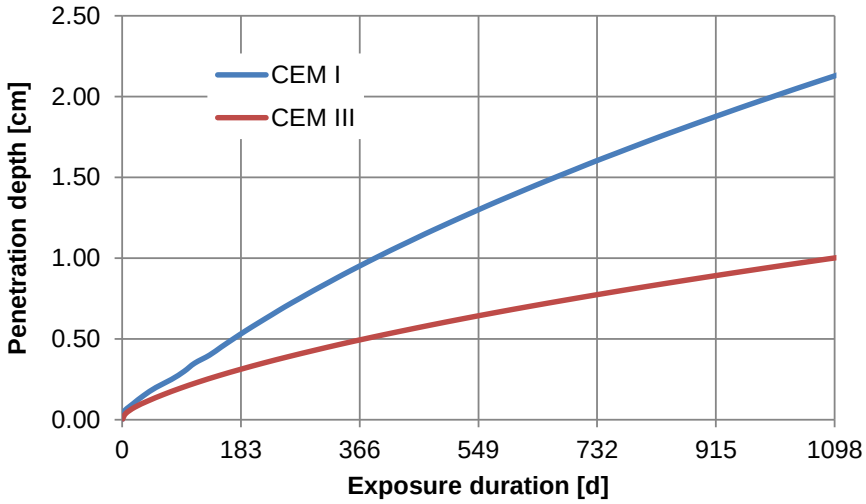

Figure 4-27: Comparison of penetration depth of different cement types (I05360 vs III05360, exposure duration=3 years, at x=5 cm)

Figure 4-28 illustrates the total chloride profiles of both I05360 and III05360 concrete at 3 years exposure duration. It could be seen that at 3 years exposure, C_t of III05360 close to the crack flank is as high as 2.8% by mass of cement, which is higher than that of I05360 concrete (approximately 1.55% by mass of cement). This is because that on one hand, the CEM III concrete has better chloride binding capacity; on another hand, the chloride concentration in the crack solution is higher for CEM III concrete than that of CEM I concrete. CEM I concrete consumes more chloride ions from crack solution than CEM III concrete due to the coarser pore structures, which leads to the lower chloride concentration in the crack solution, as shown in Figure 4-29. However, C_t of III05360 concrete decreases much faster over depth than I05360 concrete. C_t is nearly zero at depth 1.4cm after three years exposure, Figure 4-28.

Comparison of free chloride profiles of I05360 and III05360 concrete is shown in Figure 4-30. As expected, C_f of III05360 concrete also decreases with depth much faster than that of I05360.

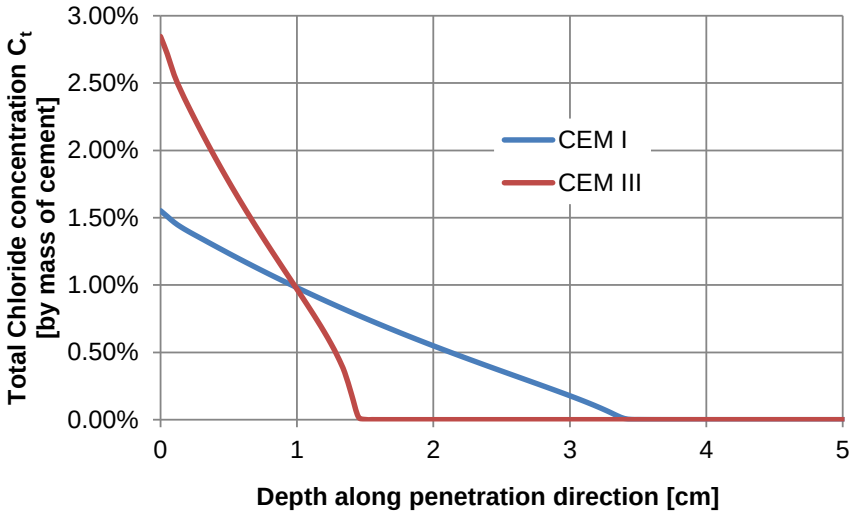

Figure 4-28: Comparison of total chloride C_t profiles with different cement types (I05360 vs III05360, exposure duration=3 years, at x=5 cm)

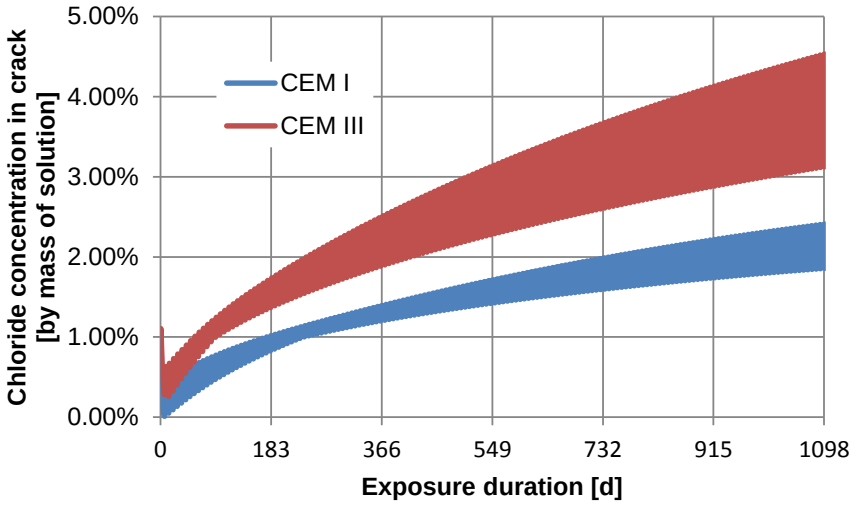

Figure 4-29: Variation of chloride density in crack solution with exposure time for different cement type.

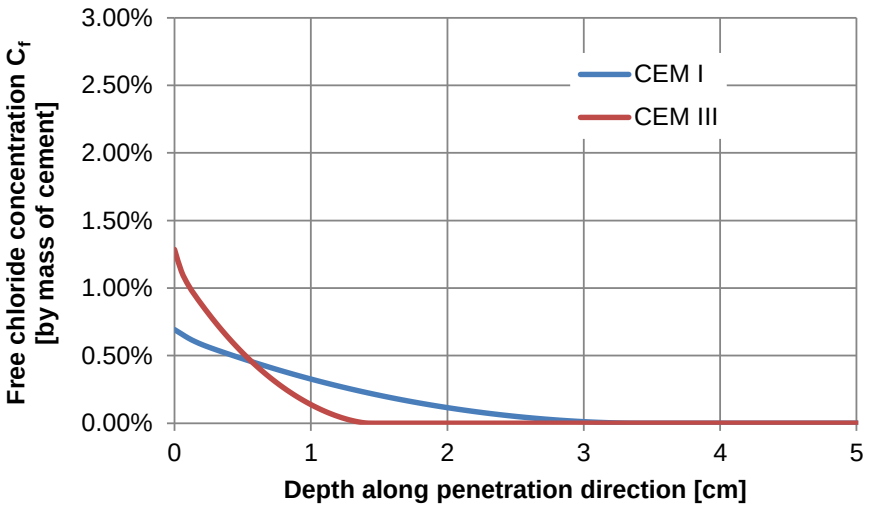

Figure 4-30: Comparison of free chloride C_f profiles with different cement types (I05360 vs III05360, exposure duration=3 years, at x=5 cm)

4.6.2 Influence of cracks on chloride penetration into concrete

In this section, a comparison between the chloride penetration process in the case of uncracked concrete and cracked concrete is presented. A discussion on the effect of concrete cover depth on chloride penetration is also presented in this section.

Chloride/moisture penetration into uncracked concrete

To investigate the influence of cracks on the chloride/moisture penetration into concrete, a 2-dimensional numerical model for uncracked concrete has also been built. The simulation was carried on a rectangular domain with a dimension of $8 \times 10 cm^2$, Figure 4-6. Only one side (i.e. side A->D) is subjected to a 1h/week wetting-drying cycle of 1% chloride solution. Boundary condition on this side could be assumed the same as environmental condition:

$$\text{chloride solution concentration} = 1\% \text{ at line AD, always} \tag{4.15}$$

The other three boundaries are closed, which means no moisture/chloride exchange on those boundaries.

$$h^0 = 0.5 \quad \text{when t=0, for all points} \tag{4.16}$$

$$c_f^0 = 0.0 \quad \textit{and} \quad c_t^0 = 0.0 \quad \text{when t=0, for all points} \tag{4.17}$$

When calculating, the depth dependency of diffusivity is taken into account. The diffusion coefficient along x-direction is kept constant; while the variation of diffusion coefficient along penetration direction (y-direction) is estimated by Eq. (4.4);

$$D_x = D_s \cdot f(x) = \begin{cases} \varphi + (1-\varphi)(x/x_s)^{\beta_x} & x < x_s \\ 1 & x \geq x_s \end{cases} \quad (4.18)$$

Figure 4-31 is an example of pore RH distribution in uncracked concrete at 7 days exposure. Differing from cracked concrete, the diffusion of moisture is evenly distributed.

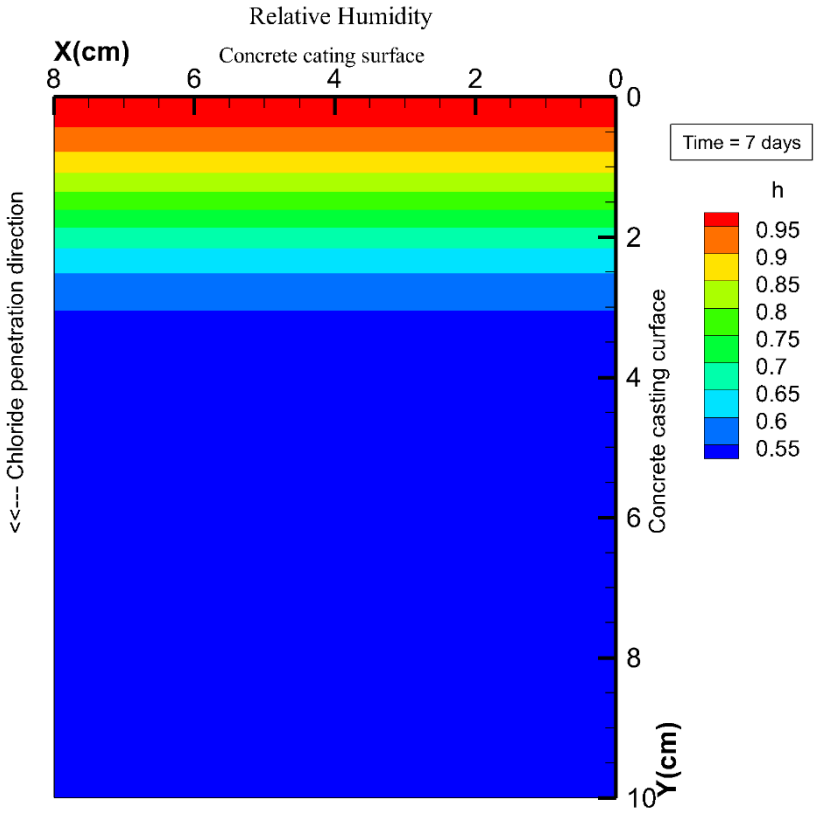

Figure 4-31: Contour plot of RH in uncracked concrete at 7 days' exposure, I05360.

Figure 4-32 illustrates the evolution of pore RH in concrete pore structure. The four curves belong to four selected points which are 0.5 cm, 3 cm, 5 cm and 10 cm from the exposed surface. The original relative humidity in concrete pore structure is 50%. Moisture penetrates inwards quickly that the whole calculated domain is completely saturated at the duration of two years, due to the close boundary.

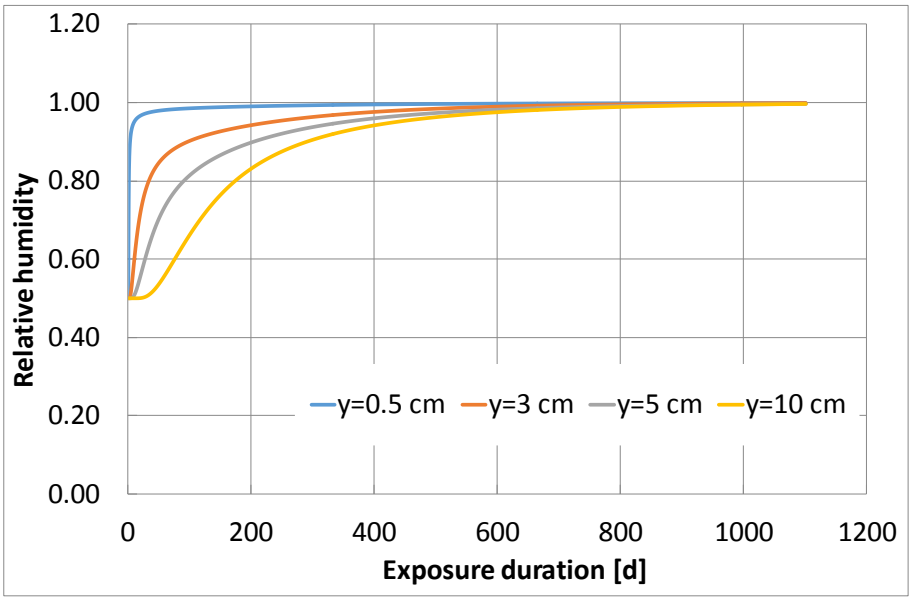

Figure 4-32: Evolution of RH in pore structures of uncracked concrete at different depth, I05360.

The contour plot of total chloride content C_t in uncracked concrete after 3 years exposure is shown in Figure 4-33. Chloride penetrates into inner concrete evenly.

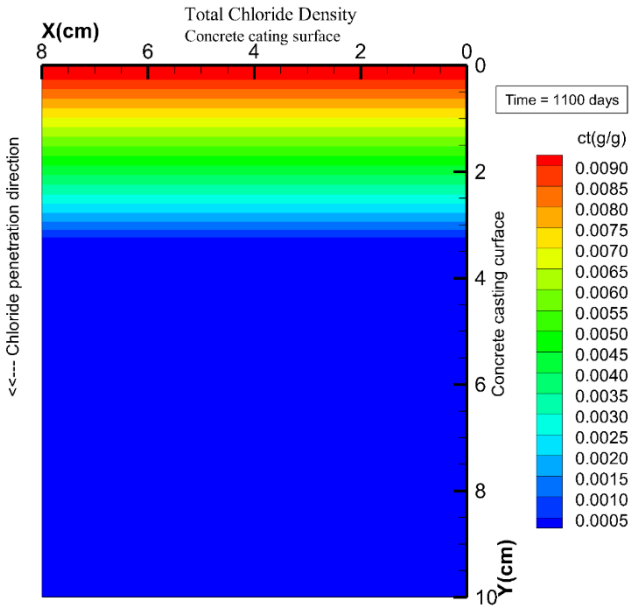

Figure 4-33: Contour plot of total chloride concentration C_t in uncracked concrete at 3 years' exposure, I05360.

Figure 4-38 and Figure 4-39 are the variation of total and free chloride content at different exposure durations. The total chloride concentration C_t close to the exposed surface is approximately 0.94%.

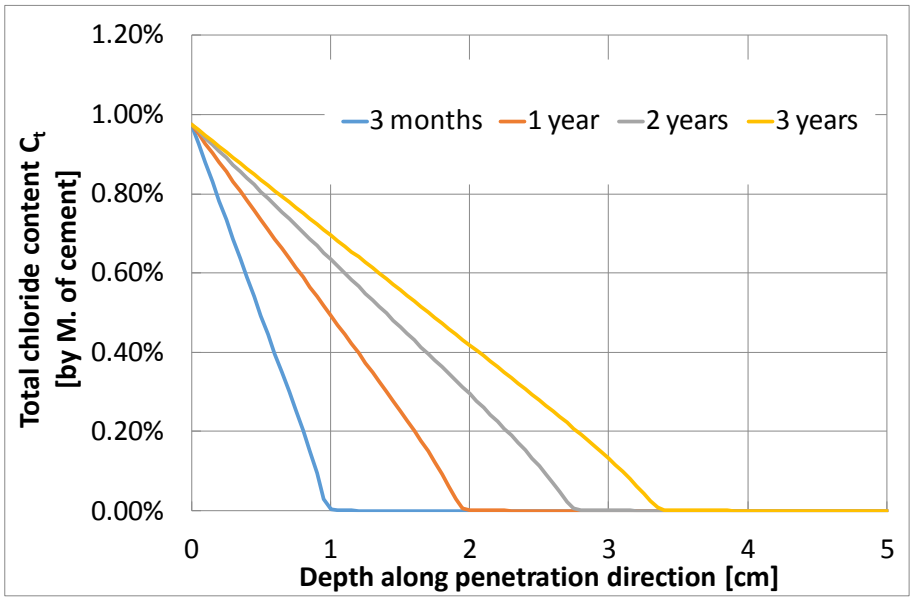

Figure 4-34: C_t profile along penetration direction of uncracked concrete (I05360)

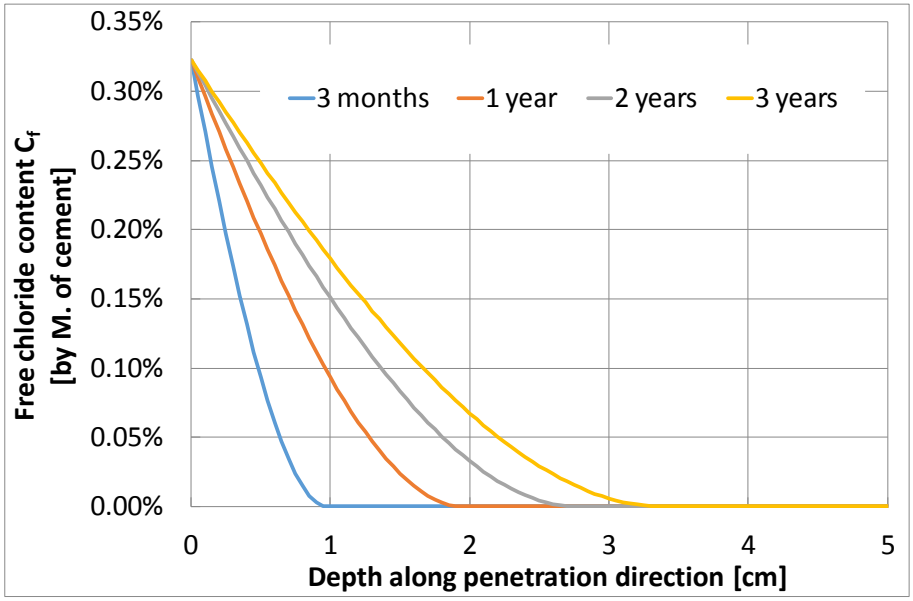

Figure 4-35: C_f profile along penetration direction of uncracked concrete (I05360)

Effect of cover depth on chloride/moisture penetration

As has been clarified above, the effect of cover depth on chloride/moisture penetration into uncracked concrete mainly focuses on the duration of initiation period. The thicker the concrete cover, the longer the initiation period.

Figure 4-36 illustrates the development of chloride penetration front with time in uncracked concrete. If a reinforcing steel bar is embedded at a certain depth, and a certain chloride concentration is the threshold chloride concentration that triggers the onset of steel

corrosion, then the relationship (among the penetration front, depth, time) can be used to predict the starting point of the steel corrosion and the development of the corrosion process. This relationship provides very useful information about the service life of a concrete structure and the time needed for rehabilitation. Therefore, if 0.5% (by mass of cement) is again set as chloride threshold value for I05360 concrete, penetration front reaches 1 cm and 1.5 cm depth after 366 days and 879 days exposure respectively.

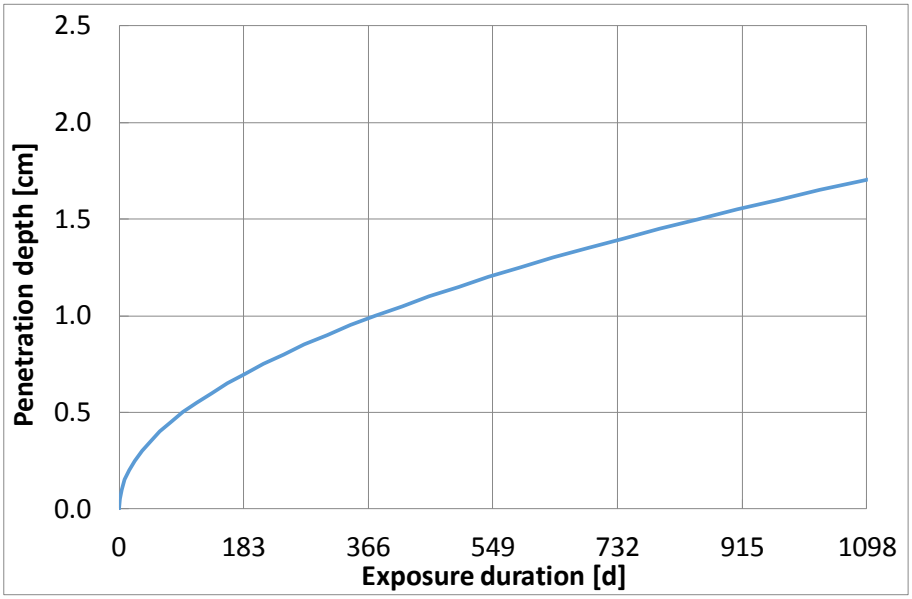

Figure 4-36: The evolution of penetration front in uncracked concrete (I05360)

However, in the case of cracked concrete, the crack is a preferable path for the chloride solution to penetrate in. The speed of chloride solution penetrating into cracks is so fast that the embedded reinforcement could be immediately depassivated if it is crossed by the crack. Therefore, the initiation period of reinforcements in cracked concrete is extremely short, no matter how thick the cover depth is. The effect of cover depth on the corrosion of embedded reinforcement in cracked concrete might be focused on the depth dependence of moisture and chloride penetration.

Figure 4-37 and Figure 4-38 are the variation of relative humidity with time at chosen points. The three curves belongs to points which are 1 cm away from the crack flank (y=1 cm) at different crack depths: x=2 cm, 3.5 cm, and 5 cm. Following are the observations:

1) With original pore RH set as 50%, the moisture content in concrete increases rapidly when wetting-drying cycle starts. The increasing rate slows down with exposure time and finally reaches an equilibrium value after about 1 year's exposure. The

equilibrium of moisture field in the concrete well explains the equilibrium of macro-cell corrosion currents that observed in Chapter 3.

2) A tendency could be observed that the deeper the crack depth (i.e. larger x-value), the higher the RH. Average RH in the equilibrium state at the depths of x= 2cm, 3.5 cm and 5 cm are 85.6%, 94.4% and 96.6% respectively. This is due to the periodically up-and-down variation of water level which is induced by the combined effect of evaporation in drying period and refilling of chloride solution during wetting period in crack.

   This tendency well explains the astonishing observation which was afore mentioned in Chapter 3: reinforcements embedded in deeper crack demonstrate more intensive corrosion. Moisture content in pore structure could greatly influence the electrolytic resistivity of concrete. Therefore, the higher moisture content in deeper crack could be an indirect cause for the more intensive corrosion of the deeper-embedded steel bars.

3) It is also observed that the 2 cm curve vibrates in great amplitude. The vibration is the combine effect of evaporation and chloride solution refilling: moisture penetrates inwards concrete when the crack is filled (re-filled) with chloride solution; moisture penetrates back to the crack flank again during the drying period. The vibration of 3.5 cm curve is not as large as 2 cm curve because that x=3.5 cm depth is permanently submerged. The slight vibration at this depth is actually caused by moisture movement in the secondary diffusion direction, i.e. x-direction. There is nearly no vibration at 5 cm's curve since the concrete is subjected to permanently submerged condition at this depth. To give a clearer view of the vibrated curves, another figure is given in Figure 4-38 with a smaller time scale.

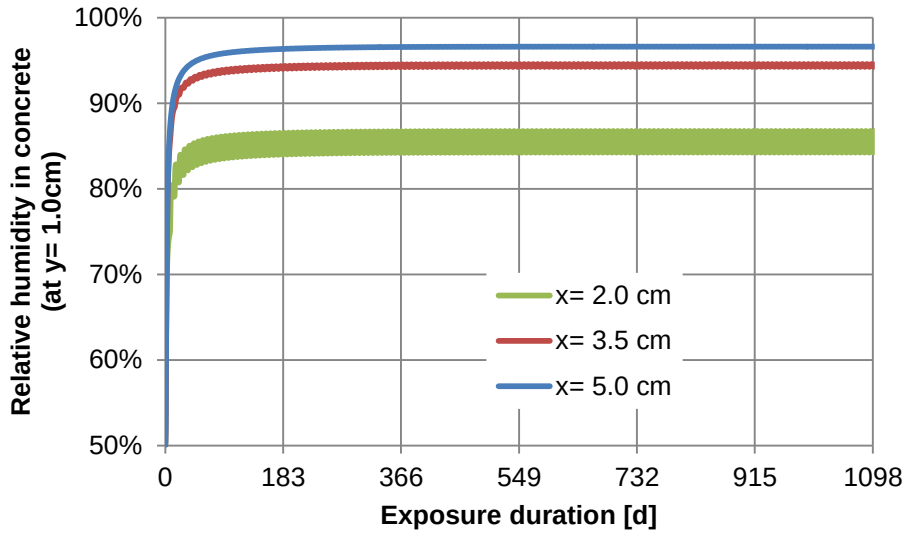

Figure 4-37: Time development of pore RH at selected points, in cracked I05360 concrete, y=1 cm

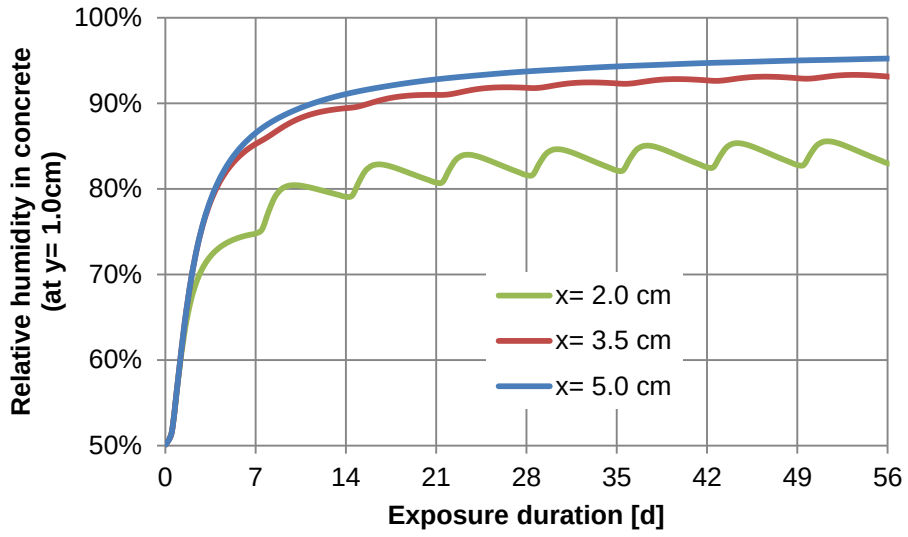

Figure 4-38: A clearer view of Figure 4-37 with smaller time scale.

Figure 4-39 illustrates total chloride profiles along main penetration direction (y-direction) of I05360. The three curves represent three different cover depths: x= 2 cm, 3.5 cm and 5 cm. Exposure duration is 3 years, which is same with the cracked beam samples in Chapter 3. It could be noticed that C_t is lowest at x=2 cm depth; C_t at x= 3.5 and 5 cm depth are nearly the same. This is because that crack flank at x=2 cm is exposed to longer drying period; while crack flank at deeper crack is subjected to longer wetting period. Meanwhile, D_c and D_h are also higher due to higher moisture content in deeper crack.

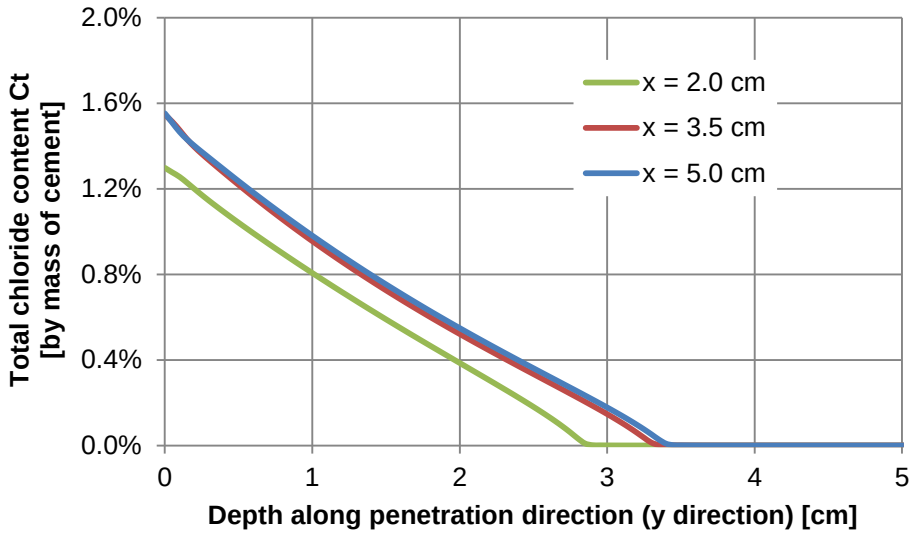

Figure 4-39: Total chloride profile C_t along penetration direction (y-direction) for 3 different concrete covers, with the exposure duration of 3 years, cracked concrete

Figure 4-40 illustrates the penetration front at different crack depth. It can be seen that the penetration front increases with crack depth (x value). This indicates that depassivated areas on deeper-embedded reinforcements (with larger x-values) are larger than those embedded in shallower crack depth.

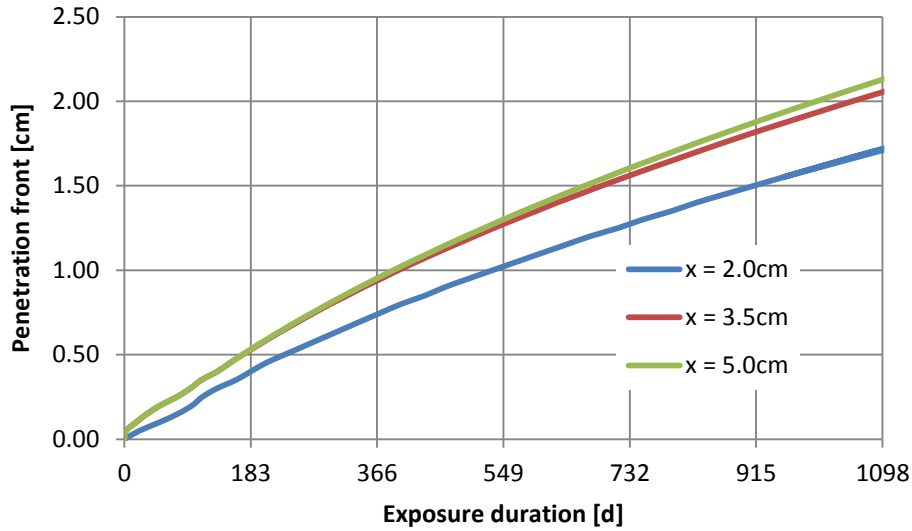

Figure 4-40: Chloride penetration front (along y-direction) at different crack depth (x-direction) of I05360.

To sum up, the regularity of 'thicker concrete cover provides better protection for its embedded reinforcement from corrosion' is only feasible for uncracked concrete. In the case of cracked concrete, thicker concrete cover loses its advantage since the crack is a direct and

much preferable path for chloride to penetrate in. The main reason for the more intensive corrosion observed on reinforcements with thicker concrete cover is the higher moisture and chloride content in deeper crack. Corrosion is greatly promoted by the higher RH and the consequently lower resistivity in deeper concrete as well.

4.7 Summary

In this Chapter, the penetration of moisture and chloride into unsaturated cracked concrete are numerically investigated. The transportation mechanisms are considered to be diffusion and convection. Based on the Fick's 1st law and mass conservation, two-dimensional differential equations of chloride penetration coupled with moisture diffusion were built, considering the chloride binding which obeys Freundlich and Langmuir binding isotherm. The diffusion coefficients of chloride and moisture are obtained by factorial approach.

In this study, ADI method (Alternating-direction Implicit finite element method) is implemented with self-developed FORTRAN program CPUCC (Chloride Penetration in Unsaturated Cracked Concrete) to solve the basic equations.

A series of laboratory tests were conducted to find out the moisture evaporation rate in crack under weekly wetting-drying cycle. Consequently, the water level and chloride concentration in crack solution were determined, which serve as boundary conditions to make the numerical calculation possible.

Based on the numerical model and boundary conditions, the chloride/moisture penetration process was studied. The following conclusions could be drawn:

1) With the self-developed program CPUCC, concrete pore RH, total chloride content C_t, free chloride content C_f, as well as moisture diffusion coefficient D_h and chloride diffusion coefficient D_c could be output as contour plot. In contour plot, the above mentioned terms can be easily determined at any time and any location.
2) Numerically calculated chloride profiles are compared with the experimental data in Chapter 3 and are found to agree well with each other. The tolerable deviations between them could be attributed to the difference of crack geometry of individual crack. Besides, the main parameters used in numerical calculation are roughly estimated from literature study, which might deviate from the real values. The correspondence of numerical results and experimental data proves the validity of

the experimental data in Chapter 3. Mutually, the reliability of the numerical model is testified.

3) The unconventional phenomenon that corrosion is more intensive in deeper crack has been explained. It concerns with the particular condition of the cracked beams:
   Firstly, due to the effect of moisture evaporation, the upper part of the crack are cyclically moisturized and dried out; while the deeper part are subjected to permanent submerged condition. Therefore the RH in pore structure in deeper (e.g. x=5 cm) concrete is about 10 % higher than that in shallower part (e.g. x=2 cm). Moisture content is proportionally related to concrete conductivity. Therefore, higher moisture content leads to high corrosion intensity since the macro-cell corrosion in cracked concrete is mainly under resistance control.
   Secondly, chloride ions penetrate further from deeper crack flank into concrete than shallower flank. Chloride concentration is also higher in deeper concrete. Higher chloride concentration in pore solution also leads to the reduction of concrete resistivity. Meanwhile, deeper diffusion depth means a larger area of steel being depassivated. Consequently, the corrosion current is larger with larger anode area, provided the same current density.
4) The penetration process of chloride/moisture into unsaturated uncracked concrete is also modeled. With a predetermined critical chloride value, initiation period could be predicted.
5) It could be believed that the CPUCC is a trustworthy numerical tool in predicting the moisture distribution and chloride penetration in both uncracked concrete and cracked concrete and in both saturate and non-saturate the conditions.

Practical significance

Both the test results in chapter 3 and the numerical results in this chapter indicate that in the case of cracked concrete which is subjected to cyclic chloride attack, the conventional view of a thicker concrete cover provides embedded reinforcement with better protection is not properly applicable.

Therefore in practice when cracks are onset, more attention should be paid to those reinforcements which are embedded with thick concrete covers, since they might be more vulnerable to chloride attack.

It also has to be noticed that, the chloride concentration in crack can be actually higher than the environmental chloride concentration. Ignoring this would lead to underestimation of the corrosion intensity.

(Blank page)

Chapter 5 Numerical Study on Corrosion in Cracked Concrete

5.1 General

Reinforcement in concrete is usually protected against corrosion by the alkalinity of the pore solution. However, as a result of chloride ingress or carbonation the reinforcing steel can be depassivated and corrosion can thereby be initiated. In this chapter, a numerical method was developed in order to build a model for the simulation of the corrosion process of reinforcement in propagation period.

5.1.1 Motivation

The aim of this chapter is to develop a generalized numerical tool for the modelling of reinforcement corrosion in active state and to evaluate the effect of the presence of crack on the corrosion intensity. Additionally it is used to validate the experimental results in Chapter 3.

Reinforcement corrosion is a dynamic process which is influenced by a number of factors such as the environmental conditions and the material properties of concrete and steel. Some of these factors vary with time, indicating the corrosion process is time dependent. However corrosion modelling based on solving Laplace equations gives a stationary solution for a constant set of input parameters. Therefore, the numerical calculation in this chapter only reflects the state at the moment when the boundary conditions were measured. Time dependence of corrosion process could not be revealed unless the simulation and the measurement of boundary conditions are performed periodically.

5.1.2 Main content

Numerical simulation is carried out with a self-developing FEM program named 'MCRC', i.e., the 'Macro-cell Corrosion of Reinforcement in Concrete'. This program is written in FORTRAN. Galerkin's method is employed to solve the Laplace equations [156]. A validation of the MCRC program is carried out by modelling the same case with Warkus, *et al* [129] and Redaelli, *et al* [134].

As boundary condition, polarization curves are measured on both I05360 and III05360 cracked concrete beams. The resistivity field in cracked concrete was estimated by combing

the numerically modelled moisture field that obtained in Chapter 4 and the resistivity data obtained in a parallel project [DFG-537].

With the geometrical model and boundary conditions, the corrosion state in cracked concrete beam was simulated. Based on the calculated results, the potential and corrosion current contour on both electrodes and concrete were determined. Then anodic and cathodic polarization resistance could be calculated. Controlling factors of anode, cathode and electrolyte could be thereby calculated as well.

Finally a numerical parametric study was carried out. The investigated parameters were concrete resistivity, driving potential and concrete cover depth.

5.2 Numerical calculation

5.2.1 Program implementation

As mentioned in previous section, a three-dimensional finite element program which was named as 'MCRC' (Macro-cell Corrosion in Reinforcement Concrete) was developed. MCRC could simulate corrosion of reinforcement with arbitrary geometry and/or arbitrary electrical resistance distribution. The self-developing program is more flexible than other commercial FEM software.

MCRC includes three functional parts: 1) Input of model information; 2) Main calculation procedure; and 3) Results output. Detailed information of the three function parts are given in Appendix F.

When modelling active corrosion, one of the main difficulties is how to deal with polarization curves. As boundary condition, polarization curve describes a non-linear relationship between the current and potential, instead of a simple fixed value or linear function. This is a problem which could not be solved by existing commercial FEM software. MARC succeeded to solve this challenging problem by introducing an interfacial layer. The details are also given in Appendix F.

5.2.2 Program validation

When a new numerical program is developed, it is crucial and necessary to prove its validity. Therefore, cases reported by Warkus, *et al* [129] and Redaelli, *et al* [134] were simulated to validate the feasibility of MCRC.

The proposed case is to predict the corrosion state of a horizontal reinforced concrete element which is subjected to chloride induced corrosion. The element has a flexural crack in the centre which is perpendicular to the exposed top surface and exposed to a wetting-drying cycle of chloride solution (de-icing salts during winter period and atmosphere during the remaining period). The concrete is ordinary Portland cement with w/c ratio 0.55. The reinforcement is with diameter of 16 mm and is embedded with 3.5 cm cover concrete. The depassivated steel surface, 10 mm length, forms a local anode while the rest of the reinforcement bar acts as cathode, as shown in Figure 5-1. More details about the model could be found in references [129, 134].

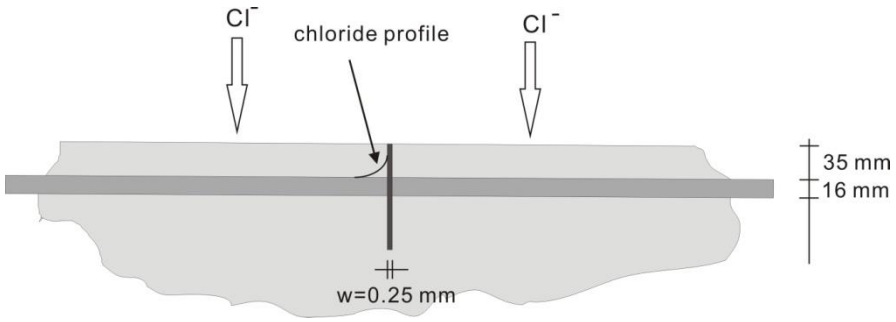

Figure 5-1: Schematic representation of the case [129, 134]

Due to the symmetry, only one eighth of the model is simulated, as shown in Figure 5-2. The zone around anode is meshed into finer elements due to the larger potential and current density gradient in this area. The interfacial layers for both anode and cathode are with 0.2mm thickness. There are 50 interfacial elements for anode and 400 for cathode. The concrete domain is meshed into 8740 elements. There leaves a small gap with 0.2mm thickness between anode interface element and cathode interface elements to avoid numerical error caused by those nodes which belong to both anode and cathode, as shown in Figure 5-2 and Figure 5-3.

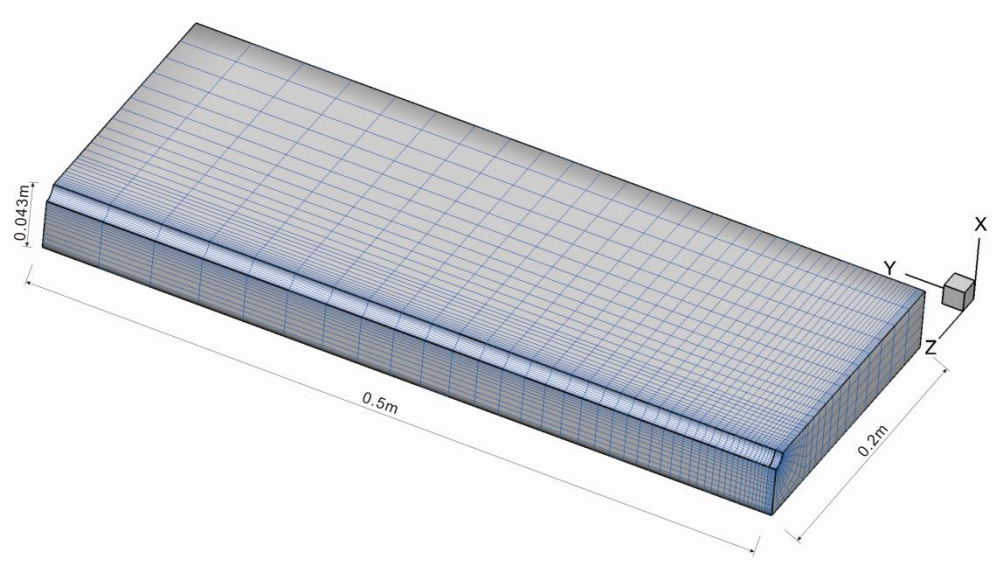

Figure 5-2: The studied model with FEM mesh

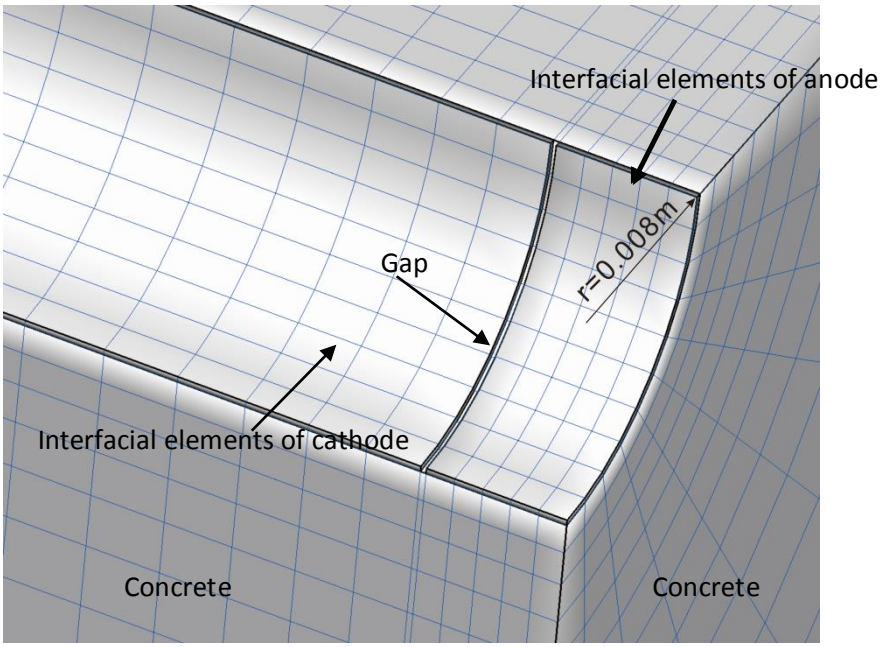

Figure 5-3: Detailed anode model with FEM mesh

Comparison with Warkus, et al [129]'s Results

Warkus, *et al* [129] adopted boundary element software BEASY CP to simulate this case. The anodic and cathodic polarization curves are illustrated in Figure 5-4, which follows the Butler-Vollmer equation. Due to the limitation of boundary element method (BEM), it's impossible to achieve a location-dependent concrete resistivity field except by dividing the model into several sub-domains. Therefore Warkus simply took a uniform concrete

resistivity field. To make the calculated results comparable with Warkus's, the same polarization curves and constant resistivity distribution were adopted in MCRC modelling.

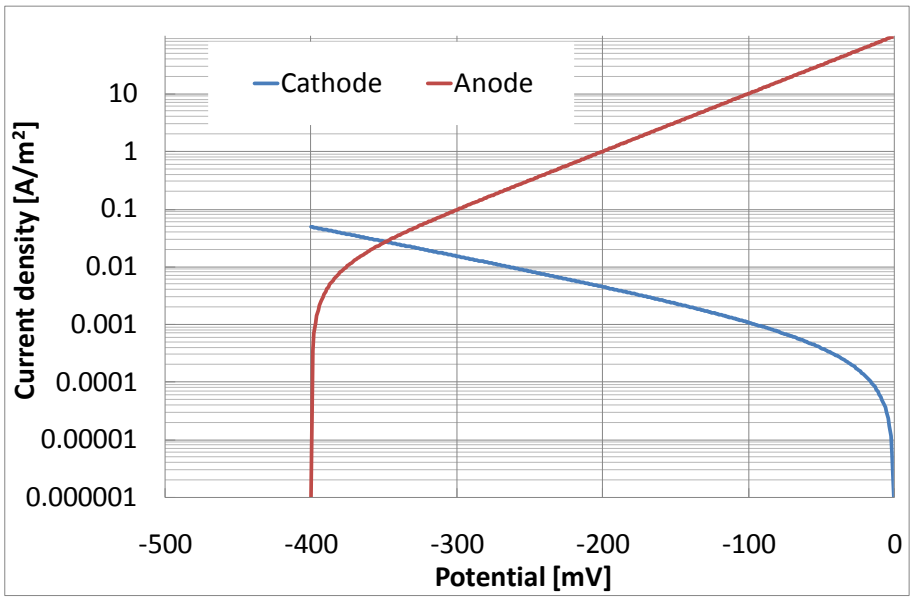

Figure 5-4: Polarization curves [129]

Figure 5-5 shows the calculated potential distribution in the concrete with uniform resistivity $500\,\Omega\cdot m$. The potential at the anode surface demonstrates the lowest values. The cathodic potential is quite close to its free corrosion potential at the left end, but drops to about -300mV at the right end. Figure 5-6 illustrates the potentials along the reinforcement calculated with three different concrete resistivity values. Comparing the three curves, one could find that the potential on the cathodic section increase with increasing concrete resistivity; while potential on the anode section appears oppositely. Both Figure 5-5 and Figure 5-6 obtained from MCRC agree perfectly well with the results presented in Warkus, *et al* [129]'s paper. Furthermore, the macro-cell currents, i.e. the total flowing out current from anode surface, are compared in Table 5-1. The consistence between MCRC's result and Warkus' result also validates the program MCRC.

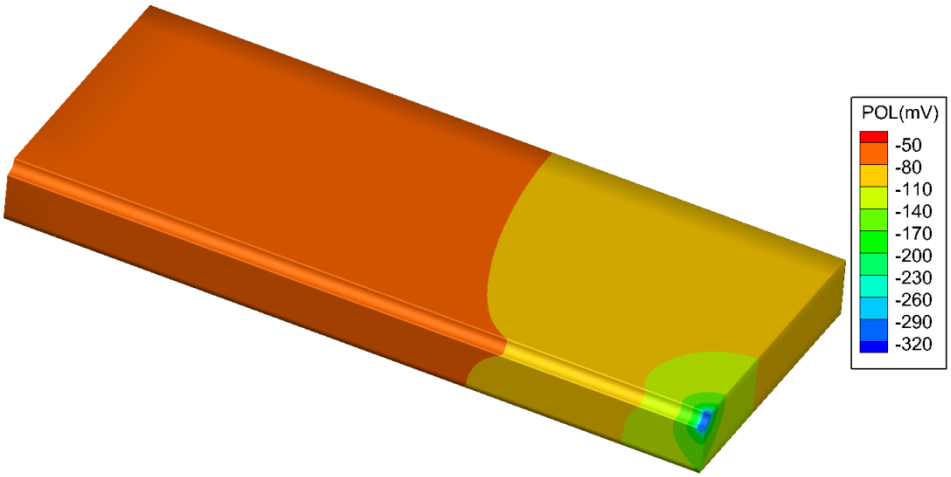

Figure 5-5: Calculated concrete potential distribution with uniform resistance $500\,\Omega\cdot m$

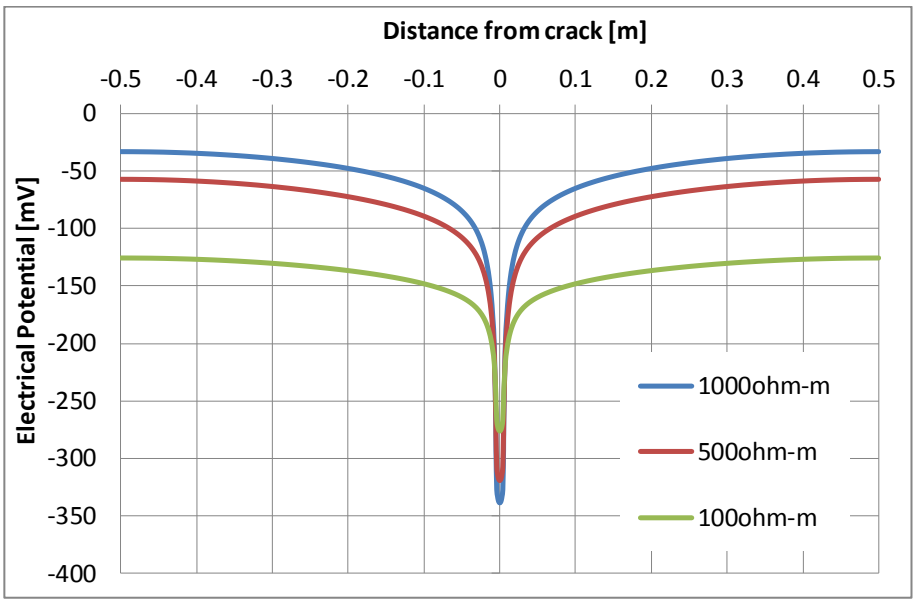

Figure 5-6: Calculated potential distribution at the surface of the reinforcement

Table 5-1: Comparison of corrosion current with Warkus, *et al* [129]'s result

Concrete Resistivity [$\Omega\cdot m$]	Corrosion current [μA] from Warkus, *et al* [129]	Corrosion current [μA] calculated by MCRC	Relative difference
100	99.76	99.36	-0.40%
500	37.75	38.06	0.83%
1000	23.37	23.74	1.60%

Comparison with Redaelli, et al [134]'s Calculation

Redaelli, *et al* [134] used finite element software COMSOL MULITIPHYSICS to simulate the same case as Warkus. Temperature dependence of polarization curves were particularly specified by him, as shown in Figure 5-7. Larger driving potential could be induced by higher temperature. Compared with BEM, one of the advantages of FEM is that a nonlinear location-dependent concrete resistivity could be simulated, Figure 5-8, which is closer to the real situation than the constant resistivity distribution which is assumed by Warkus.

By adopting the same polarization curves and concrete resistivity distribution as Redaelli, the output results that calculated by MCRC are shown in Table 5-2, which agree quite well with Redaelli's.

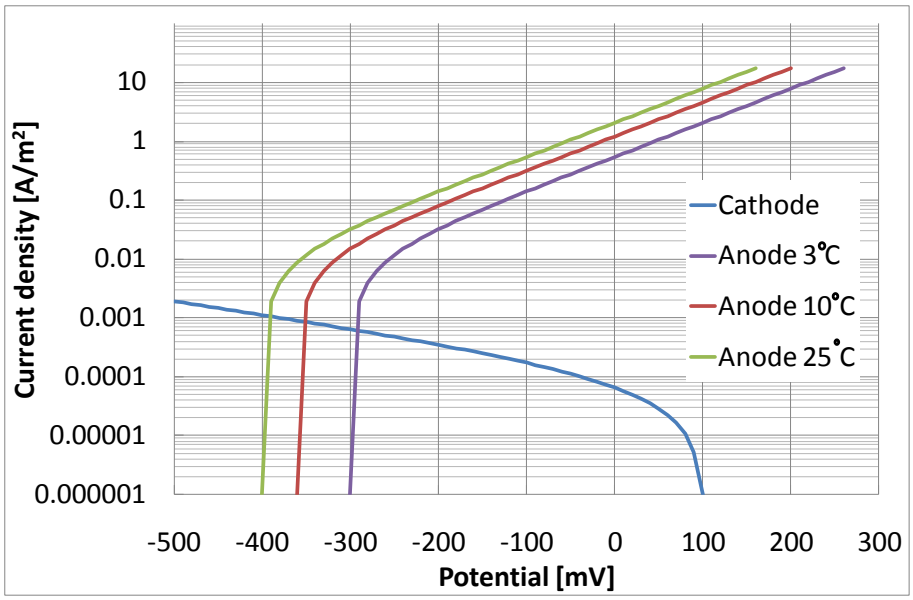

Figure 5-7: Polarization curves for anode & cathodes at different temperature [134]

The good agreement between the two case studies indicates that the self-developing program 'MCRC' is feasible to simulate the reinforcement in concrete, even with uneven electrical resistances. It will be used to simulate the corrosion state in cracked concrete in which the electrical resistance varies in all three directions.

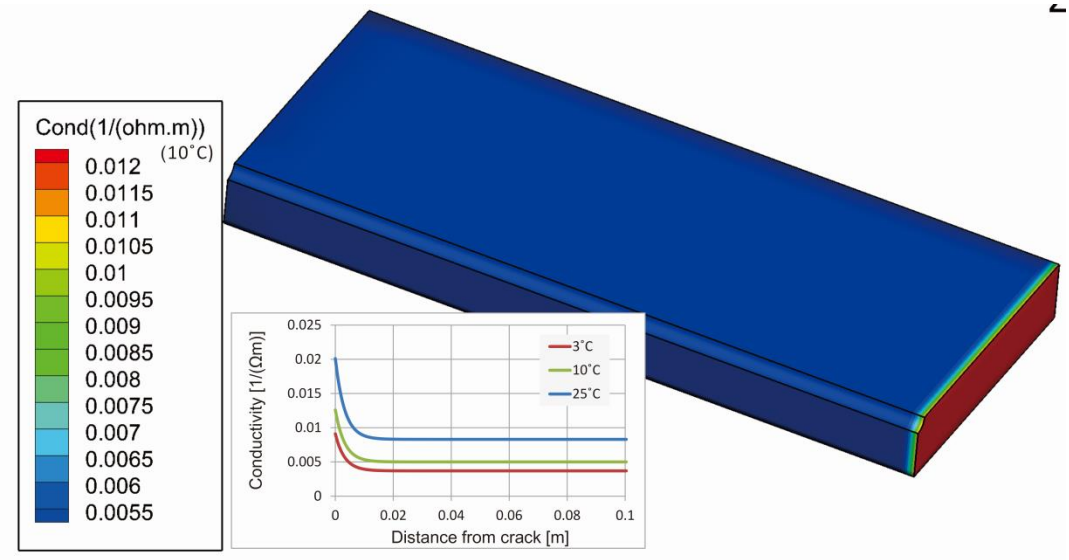

Figure 5-8: Distribution of concrete conductivity [134]

Table 5-2: Comparison of corrosion current with Redaelli, *et al* [134]'s results

Environmental Condition	I_{corr} [μA] reported by Redaelli, *et al* [134]	I_{corr}[μA] calculated by MCRC	Relative difference
Wet, 3°C	41.72	42.02	0.73%
Wet, 10°C	68.86	70.65	2.59%
Wet, 25°C	113.10	113.84	0.66%

5.2.3 FEM model of the cracked concrete beam

Assumptions and simplifications

In this research, efforts are mainly focused on the validation of experimental results of Chapter 3. Therefore, the numerical model is built to reflect the cracked beams as close as possible. First of all, some simplifications and assumptions should be made:

- The concrete is considered as homogeneous one-phase material. The pore structure and the two-phase cement-aggregate characteristics are not modeled.
- The anode and cathode are considered to be fully polarized, which means that the corrosion current density is calculated by the entire surface area of the anode and cathode.
- The influences of environmental conditions (e.g. temperature and relative humidity) are involved in the boundary conditions, i.e. the polarization curves and concrete resistivity.

- The influence of chloride wetting-drying cycle is also involved in the boundary conditions, i.e. the polarization curves and concrete resistivity.
- As cracked concrete, the crack is not geometrically modeled. The concrete beam is modeled as continuous domain without any crack/gap elements built in the model. This is because that the anode is in the center of the beam and is crossed by the crack. Therefore macro-cell current between the anode and the cathodes are theoretically not interrupted by the crack. The effect of the presence of the crack is involved in the polarization curves and concrete resistivity.
- Although there are three groups of corrosion systems embedded in each cracked beam, only one group is modeled.

It has to be clarified that, reinforcement corrosion is a dynamic process which is influenced by the external environments (temperature, RH, Cl or CO_2 conditions, etc.) and its internal characteristics (hydration process, the development of corrosion products etc.). However, the results from numerical modelling could only reflect the transient state when the boundary conditions are determined.

Geometry and mesh

The configuration of the numerical model is based on the specimen as discussed in Chapter 3. As has been mentioned, only one corrosion system was built in one beam for simplification, Figure 5-9.

The bulk concrete is meshed into 97,664 hexahedral elements as shown in Figure 5-10. The zone around anode with larger potential gradients and current density is meshed with finer elements in order to reach higher calculation precision; while the other zones which are close to the two ends with smaller potential gradients and current density are meshed with coarser and larger elements to reduce calculation time. As shown in Figure 5-11, the interfacial layer between the anode and the concrete are composed with a thin cylinder and two circular plates at each end (cylindrical hull). The interfacial layer is with a thickness of 0.2mm and is meshed into 896 thin hexahedral elements. Figure 5-11 is a diagram which cut off the interface layer into slices to illustrate the inner empty. Similarly, the four interfacial layers for the cathodes are meshed into 576, 768, 834, and 1056 hexahedral elements respectively.

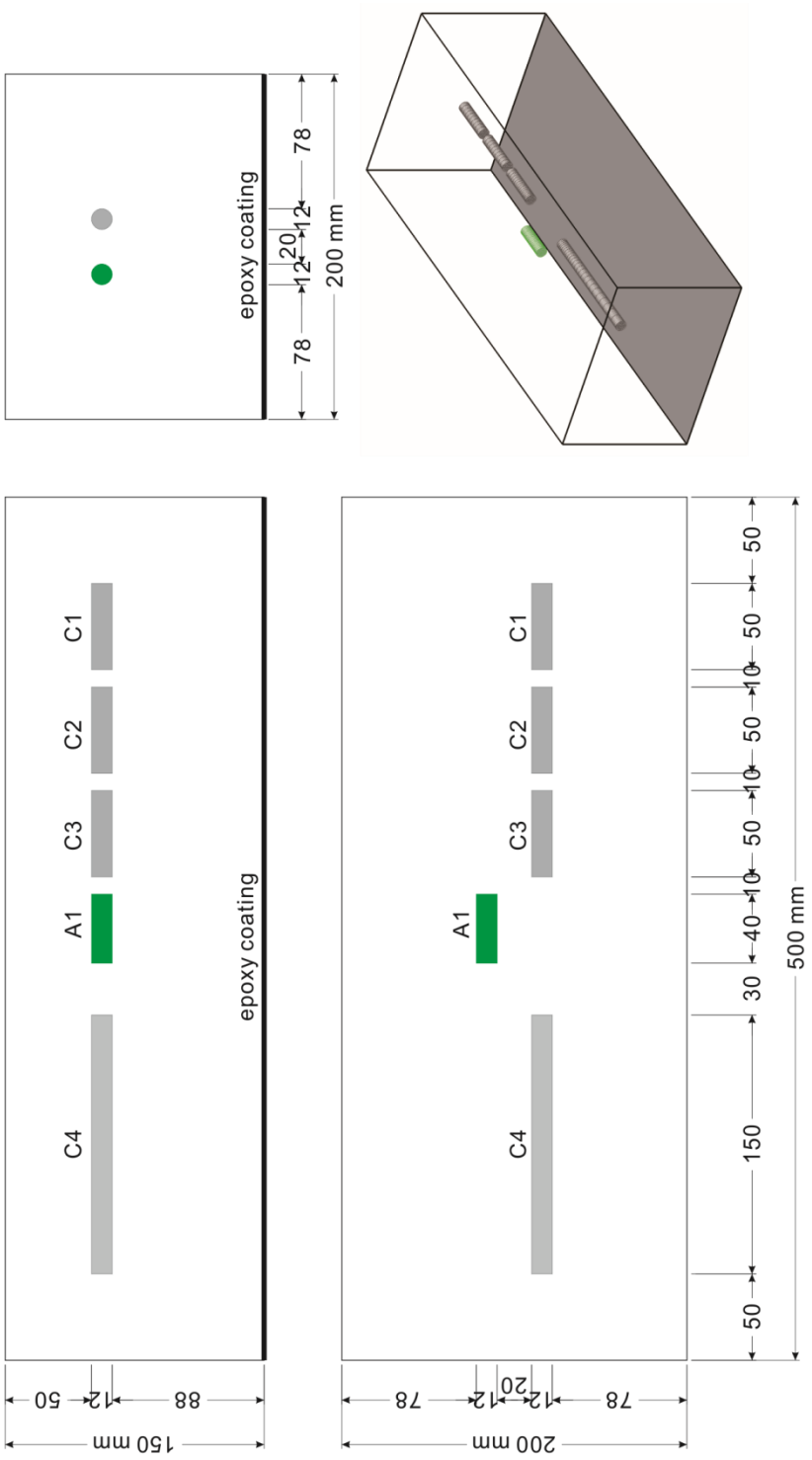

Figure 5-9: Geometry and dimension of the calculation model

In sum, the whole model is meshed into 101,536 hexahedral elements with 109,170 nodes. So there are 109,170 equations in the equation system Eq.(E.16) for this calculation, which is also named as total degree of freedom. Combining the measured concrete resistivity field and polarization curves, the model could be simulated by the program MCRC.

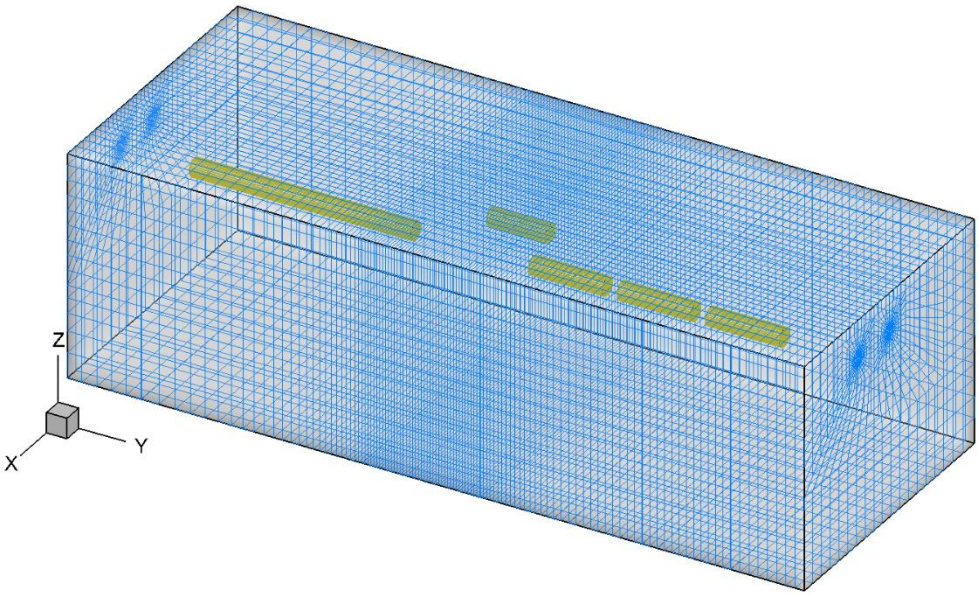

Figure 5-10: FEM mesh of the calculation

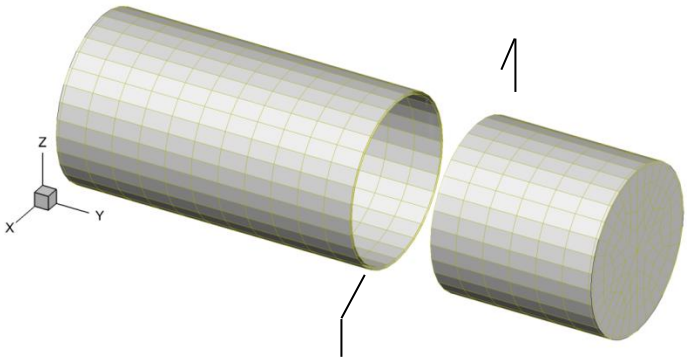

Figure 5-11: Interfacial elements of electrodes, (cut in the middle to show the hollow shape)

Input information

This part consists of reading the control information and boundary conditions. The control information includes the model geometry, detailed information of nodes and elements, the required precision of the calculation, the convergent tolerance and the maximum iteration number. The boundary conditions include the polarization curves and concrete resistivity. According to the program, polarization curves could be input either in the form of Butler-

Volmer equation, with the constants obtained [157] from data fitting or in the form of a series of discrete points which are taken from the actually measured polarization curves. In this study, the polarization curves and resistivity data are directly from laboratory measurements. For each corrosion system, one anodic polarization curve and four cathodic polarization curves, as well as a location-dependent resistivity field are adopted, which is given in details in section 5.3.

Calculation procedure

To give a better understanding of the iteration calculation process, a flow chart is given in Figure 5-12.

As shown in Figure 5-12, the electrical current density is initially assumed to be uniform and equal to i_0. Usually, this is not the real solution, but it could help to determine the electric conductivity for all anodic and cathodic interface elements, and compute the distribution of potential. A new electrical current density at each integration points could be calculated from the potential distribution. The newly obtained current density may not be the accurate solution, but it should be closer to the accurate solution than the old one, theoretically. Then the newly obtained current density is used to replace the old one, and a better one may be obtained by repeating the same procedure. In this way, the solved current density will be more and more close to the accurate solution which exists but usually is unknown. Actually, it could be incredibly close to the accurate solution, but not to fully equal to the accurate solution. Therefore criteria must be defined to terminate the iteration. In this study, the 2-norm of the difference between the new and old current density is used as the convergence criteria. In order to eliminate the influence of dimensions and units, it is normalized to divide the 2-norm of the newly obtained current density. The final terminate criteria is

$$\frac{\left\|\{i\}^{(j+1)}-\{i\}^{(j)}\right\|}{\left\|\{i\}^{(j+1)}\right\|}\leq\varepsilon \tag{5.1}$$

In which

$\|\cdot\|$ - the 2-norm of a vector;

ε - the specified convergence accuracy.

In this study, 0.1% is used for ε, which should be accurate enough for general engineering purpose.

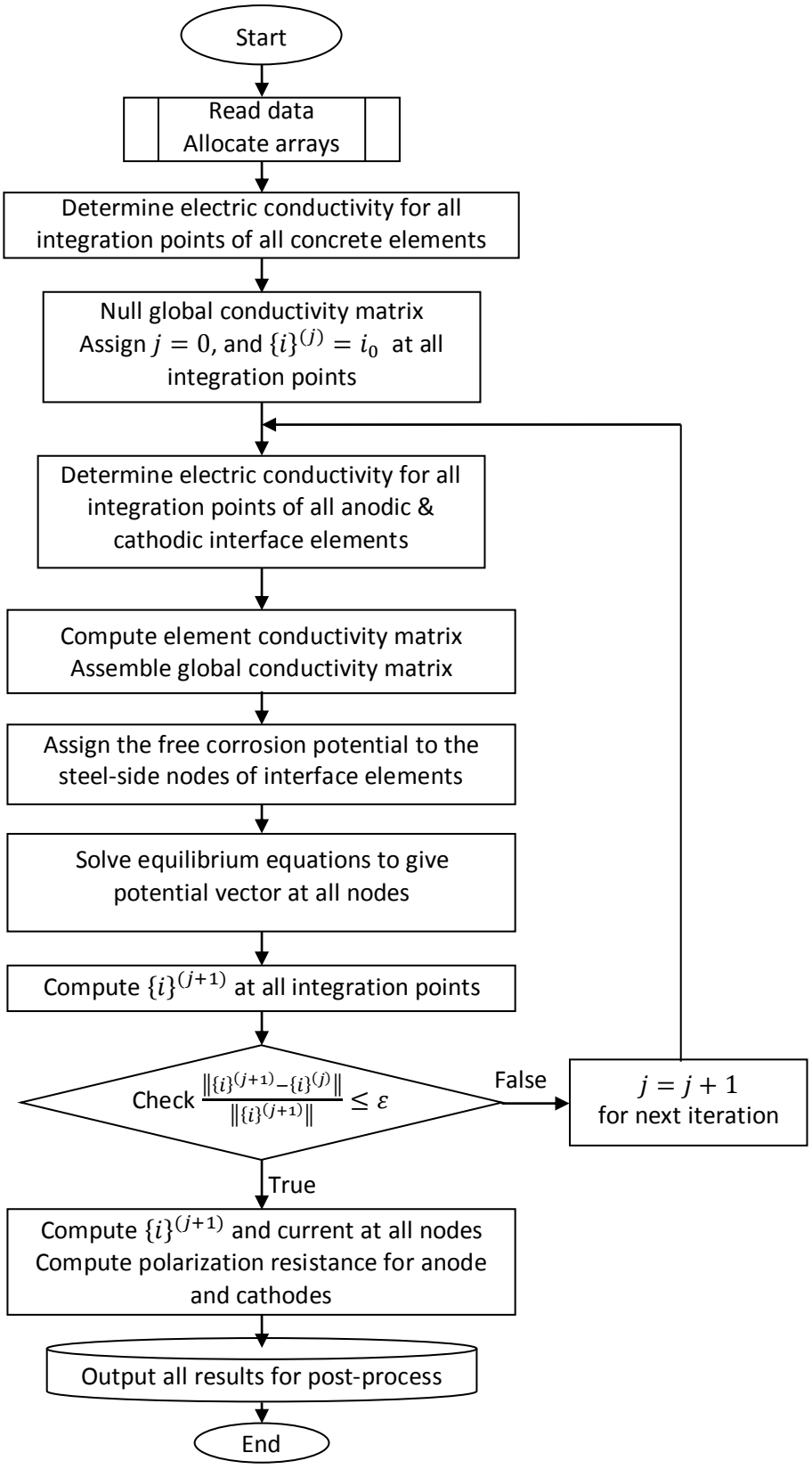

Figure 5-12: Flow chart of the calculation process

The iteration will be terminated when the criteria in Eq.(5.1) is satisfied. However, there may be something wrong and the criteria would not be always satisfied, e.g. inputting wrong data. In this case, the calculation will be forced to terminate after a certain number of iterations. In this study, this number is set as 50, which is large enough for all calculated cases.

It has to be noted that, in modelling active corrosion one of the main difficulties is that as boundary condition, the polarization curve describes a non-linear relationship between the current and potential, instead of a simple fixed value or linear function. This is a problem which could not achieve by existing commercial FEM software. The MCRC succeeded to solve this challenging problem by introducing an interfacial layer. The details are also given in Appendix F.

Results output

From the MCRC program, the potential, corrosion current, and current density of each node on the electrodes or in bulk concrete can be calculated. Based on these data the anodic and cathodic current could be obtained by summing the nodal currents, Eq.(5.2). Theoretically, the anodic current and cathodic current should be equal, Eq.(5.3). The difference between the two currents is a measure of the accuracy of calculations.

$$I_a = \sum_{e=1}^{n} I_{a,e} \quad \text{and} \quad I_c = \sum_{e=1}^{n} I_{c,e} \tag{5.2}$$

$$I_a = -I_c \tag{5.3}$$

where

I_a and I_c - the anodic and cathodic current, in [μA];

$I_{a,e}$ and $I_{c,e}$ - the anodic and cathodic element current, in [μA].

Based on the calculated data, the polarization resistance could be obtained:

$$R_{p,a} = \frac{E_a - E_{a,0}}{I_a} \quad \text{and} \quad R_{p,c} = \frac{E_{c,0} - E_c}{I_c} \tag{5.4}$$

where

$R_{p,a}$ and $R_{p,c}$ - the anodic and cathodic polarization resistance, in Ω ;

$E_{a,0}$ and $E_{c,0}$ - the anodic and cathodic resting potential, in [mV];

E_a and E_c - the calculated anodic and cathodic potential, in [mV].

However, it is not feasible to calculate the polarization resistances by considering the anode (or cathode) as an entirety because the potential and current on each node are different from each other. It is more reasonable to consider the electrode's polarization resistance as a series of parallel resistors comprised by each node. Hence the polarization resistance could be written as:

$$\frac{1}{R_{P,a}}=\sum_{N=1}^{n}\frac{1}{\left(E_{a,N}-E_{a,0}\right)/I_{a,N}} \quad \text{and} \quad \frac{1}{R_{P,c}}=\sum_{N=1}^{n}\frac{1}{\left(E_{c,N}-E_{c,0}\right)/I_{c,N}} \tag{5.5}$$

where

$E_{a,N}$ and $E_{c,N}$ - the node potential, for nodes on anode and cathode respectively, in [mV];

$I_{a,N}$ and $I_{c,N}$ - the current on nodes, for nodes on anode and cathode respectively, in [μA].

The system resistance of the corrosion cell is equal to the sum of polarization resistances and the resistance of electrolyte (i.e. concrete). It is the quotient of driving potential and macro-cell current:

$$R_{sys}=R_{p,a}+R_{p,c}+\mathrm{R}_{el}=\frac{\Delta U}{I_{corr}} \tag{5.6}$$

The concrete resistance between anode and cathode could be therefore determined. The controlling factor of every reaction can be calculated as the related fraction of the total resistance:

$$C_{p,a}=\frac{R_{p,a}}{R_{sys}}, \quad C_{p,c}=\frac{R_{p,c}}{R_{sys}}, \quad C_{el}=\frac{\mathrm{R}_{el}}{R_{sys}} \tag{5.7}$$

where,

$C_{p,a}$, $C_{p,c}$ and C_{el} - the controlling factor of anode, cathode and electrolytic resistance respectively.

5.3 Experimental study on the input parameters of numerical models

The solution of Laplace's equation requires that the values of a number of corrosion parameters can be pre-determined. In order to obtain the necessary input information for

the numerical modelling, measurements of the concrete resistivity and polarization curves have been carried out.

5.3.1 Resistivity field of cracked concrete beams

Concrete is anisotropic material. It contains more paste in the surface zone and more aggregate in the inner zone, leading to much denser pore structure in the surface zone than the inner zone. Even inside the concrete, the pore size and connectivity differs everywhere. Advanced casting technique and good curing conditions could diminish this non-homogeneity but not eliminate it; the moisture distribution in the concrete is also non-homogenous due to the effect of water evaporation. Therefore the local resistivity of concrete, which is greatly influenced by concrete pore structure and moisture content, varies with its location.

The resistivity field of the cracked concrete beams studied in this research is even more complicated due to the presence of the cyclic wetted central crack; the three corrosion cells are embedded at different cover depths and the distances from anode to cathodes differ from each other, which additionally increase the complexity. Therefore, the assumption of uniform resistivity in the whole cracked beam in numerical modelling is not realistic. It is important to figure out the location-dependence of concrete resistivity, i.e. the resistivity field.

To obtain the resistivity field of the cracked beam, the cross section is divided into two zones in the “radial direction”: the outer zone and the inner zone, as shown in Figure 5-13 (a). The outer zone is the area that within 3.1 cm to the concrete surface. At the crack cross section, concrete in outer zone is directly subjected to the 1h/week wetting-drying cycle of chloride solution; while concrete in inner zone is in submerge condition (water evaporation test results of chapter 4). Therefore concrete resistivity in the inner zone is considered to be constant at the same y-value.

To make it easier for analysis, the cracked beam is also divided into 3 zones along the longitudinal direction of the beam (y-direction), Figure 5-13 (b).

Zone 1 refers to an area within 12 cm to the crack. Concrete resistivity in Zone 1 could be estimated by data which were obtained on prism specimens with the similar composition and exposure conditions;

Zone 2 is an area from 12 to 20 cm relative to the crack. In Zone 2, it is considered that the influence of moisture diffusion from the crack has vanished. Meanwhile, it is not interfered by evaporation since it is 5 cm away from the casting surface. Resistivity in this area is assumed to be constant along the longitudinal direction (y-direction), which is equal to the areas with pore RH 65%.

Zone 3 refers to an area that within 5 cm to the casting surface. Resistivity in this area increases quickly due to evaporation. Concrete resistivity in zone 3 is estimated by the testing results of the Multi-Ring-Electrodes.

Consequently, the real resistivity field of the cracked beam can be assessed by the combination of the above approaches.

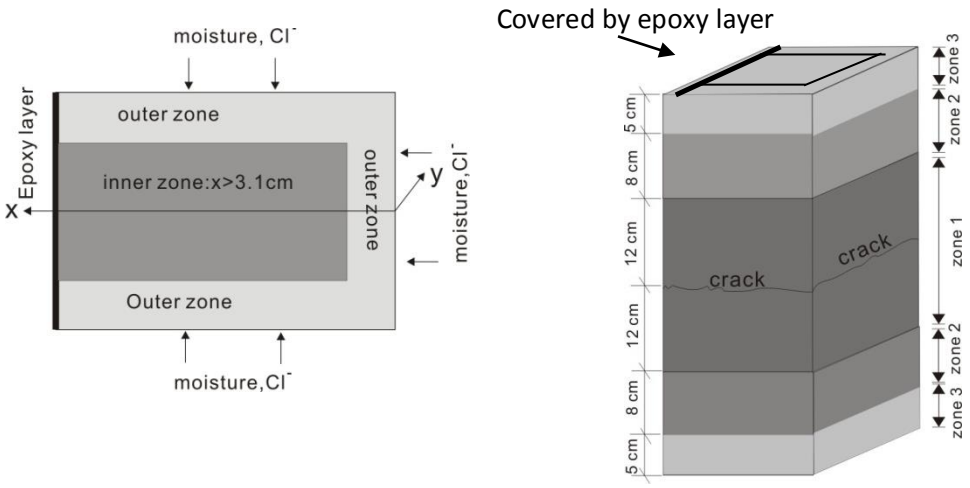

(a) Sub-zones in beam cross section (b) Sub-zones along the longitudinal direction

Figure 5-13: Zones for the estimation of concrete resistivity

Resistivity in cracked area (zone 1)- estimated by prism specimens

The crack area refers to an area within 12 cm above and below the crack. Within this area the moisture condition in pore structure is influenced by the wetting-drying cycle. The concrete resistivity in this area is directly related with the pore moisture content.

Concrete electrolytic resistivity is the material property which characterizes how far electrical charges could be transported. It depends on concrete composition (cement type, w/c ratio, mineral additives, etc.), environmental conditions, hydration degree, and etc. For specific concrete, pore moisture content is the most fundamental factor that influences the concrete resistivity. In a parallel proceeded project, influences of those factors, especially the pore moisture content and wetting-drying cycles, were quantified on prism specimens.

The dimension of the concrete prism is $30 \times 80 \times 240 mm^3$, with four embedded stainless steel meshes working as electrodes. They were submerged until they reached an age of 90 days. After that period, the specimens were dried in $40^{o}C$ and 70% RH to achieve a quicker cessation of the climates. Afterwards, they were rearranged in different climates: 1) in 20°C and RH 65%, 75%, 85%, and 95% chambers; 2) in 20°C, wetting-drying cycle of 1h/day, 1h/week, and 1h/2 weeks.

Concrete resistivity of specimens in different climates is measured intermittently every few months. Figure 5-14 and Figure 5-15 illustrate the results for I05360 and III05360 concrete in different moisture conditions respectively. Each data point was taken from an average value of 4-6 samples. It could be observed that resistivity kept on increasing with time even after 50 months exposure, indicating that hydration process did not cease yet at this age. Environmental RH has great influence on concrete resistivity. The resistivity of samples that stored in 65% RH is approximately 3.6 times of that in 95% RH for I05360 concrete, and 2.6 times for III05360 concrete. These data are used to assist the estimation of resistivity in inner zone&zone 1 of the cracked beam.

As the samples have been stored in their climate for several years, it could be assumed that the pore RH inside the concrete equals to the environmental RH. Based on this assumption, concrete resistivity could be related with the pore RH, which has been modelled in Chapter 4.

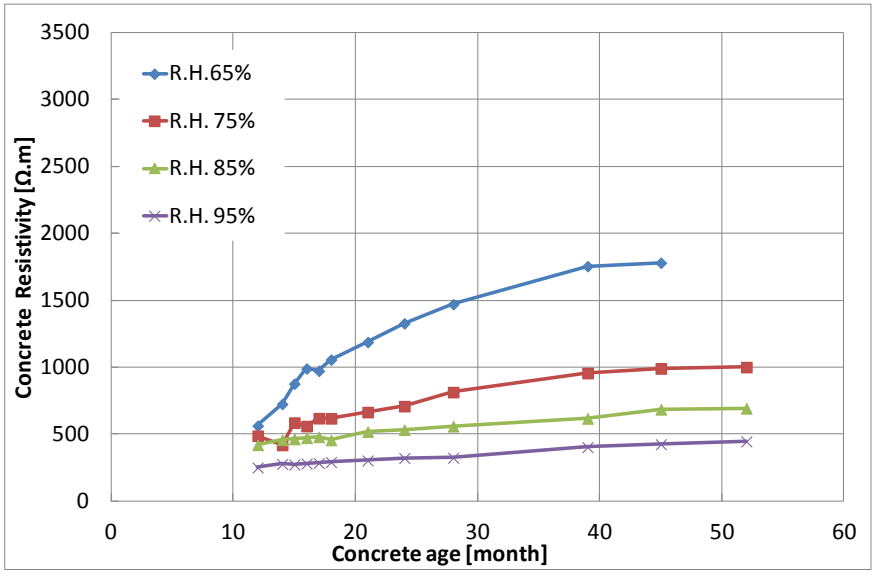

Figure 5-14: Resistivity of I05360 concrete stored in different RH

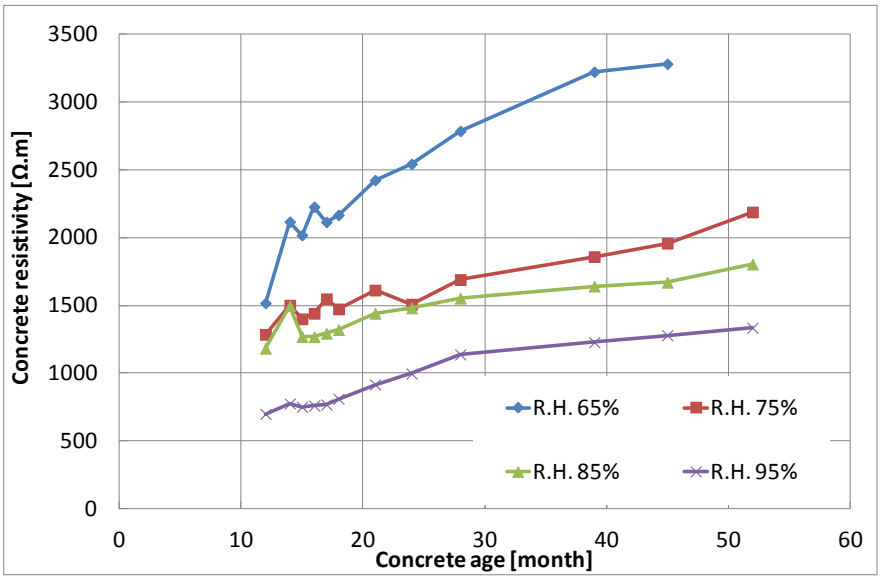

Figure 5-15: Resistivity of III05360 concrete stored in different RH

Resistivity of samples subjected to wetting-drying cycle is illustrated in Figure 5-16. Concrete resistivity shows vibration due to the wetting-drying cycle. These data are used to assist the estimation of the resistivity in outer zone &zone 1 of the cracked beam.

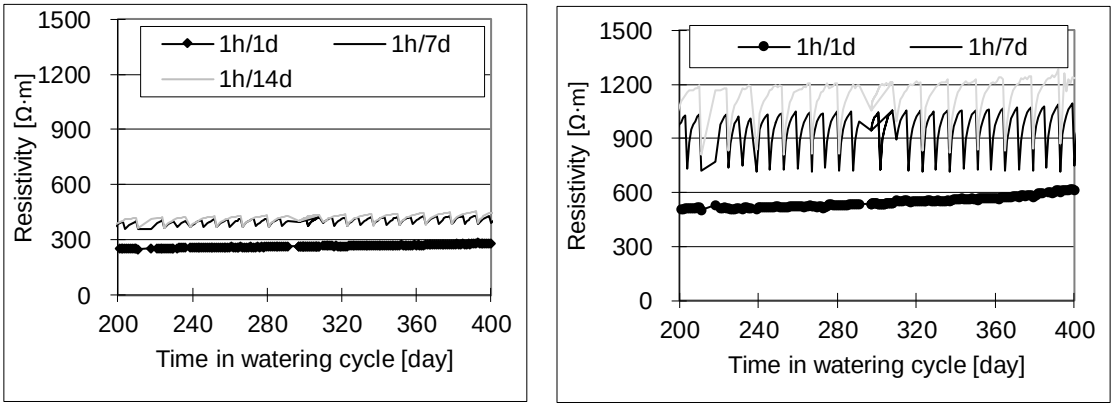

(a) I05360 (b) III05360

Figure 5-16: Concrete resistivity of samples subjected to wetting-drying cycle.

The moisture diffusion process from crack flank into concrete under wetting-drying cycle has been modelled in Chapter 4. Pore RH conditions at any time and any location of the concrete beam could be determined by the numerical model. Figure 5-17 illustrates the pore RH distribution of the cracked concrete after 1 year exposure, I05360. Only the bottom half of the cracked beam is modelled since the top half could be considered to be symmetry with the bottom half. Actually, moisture diffusion does not proceed much further after 1 year. As shown in Figure 5-17, pore RH decreases from crack flank to inner concrete. In a small area

close to crack flank, pore RH is as high as 100%; at the depth of y=12 cm, pore RH drops to 65%. Pore RH also varies along x-direction due to the effect of evaporation and wetting-drying cycle. Therefore, if Figure 5-14 and Figure 5-17 are correlated, resistivity in areas where RH is above 65% could be determined. Resistivity in the areas where RH is between (65%, 75%), (75%, 85%) (85%, 95%) is determined with linear interpolation method.

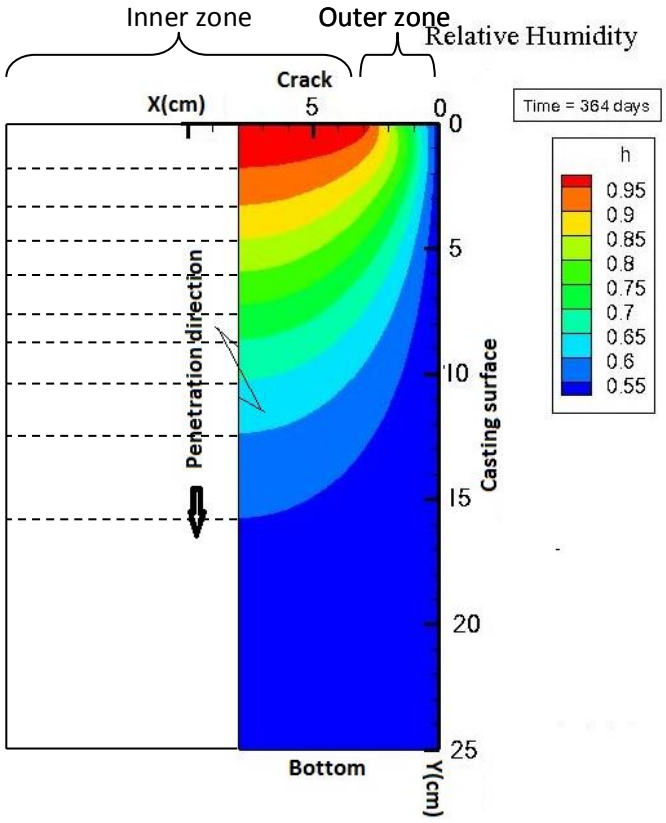

Figure 5-17: Contour plot of pore RH after one year's exposure calculated by CPUCC in Chapter 4, I05360

Resistivity in zone 2

As has been mentioned above, the resistivity in this area is considered as constant along the longitudinal direction (y-direction), which equals to the areas with pore RH 65%.

Resistivity in zones that away from crack (zone 3) estimated by Multi-Ring-Electrodes

As have been mentioned in Chapter 3, cracked beams embedded with Multi-Ring-Electrodes are also produced to monitor the moisture content and the resistivity change over the cover depth in both top side and the cracked area of the beams.

Figure 5-18 illustrates the concrete resistivity measured by Multi-Ring-Electrode. It reflects the variation of resistivity with depth due to moisture gradient. The four curves belong to I05360 and III05360 concrete respectively, on either top part or in crack vicinity. It clearly shows that a) the resistivity in crack area is much lower than in top part, due to the weekly wetting-drying cycle; b) resistivity of III05360 concrete is much higher than I05360 concrete in both positions.

Here, resistivity data that measured by top Multi-Ring-Electrodes are used to estimate the resistivity value in top and bottom part of the cracked beam (zone 3). Data that measured by the electrodes in cracked area are used to assist the determination of resistivity in zone 1.

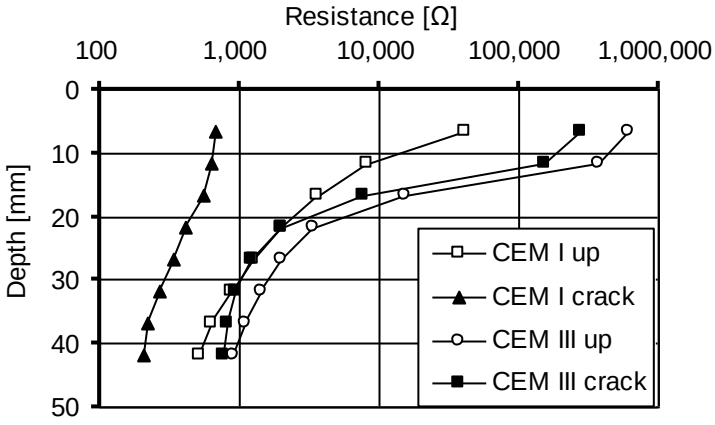

Figure 5-18: Concrete resistance measured by Multi-Ring-Electrode, 1 year exposure duration

Results

Figure 5-19 and Figure 5-20 illustrate the concrete resistivity along the longitudinal direction (y-direction) of the beam after one year, two years and three years exposure, for inner zone($x > 3.1$ cm). In inner zone, concrete resistivity varies with y-value when x-value is fixed; while it keeps constant when y-value is fixed and x-value varies in the range of $x > 3.1$ cm .

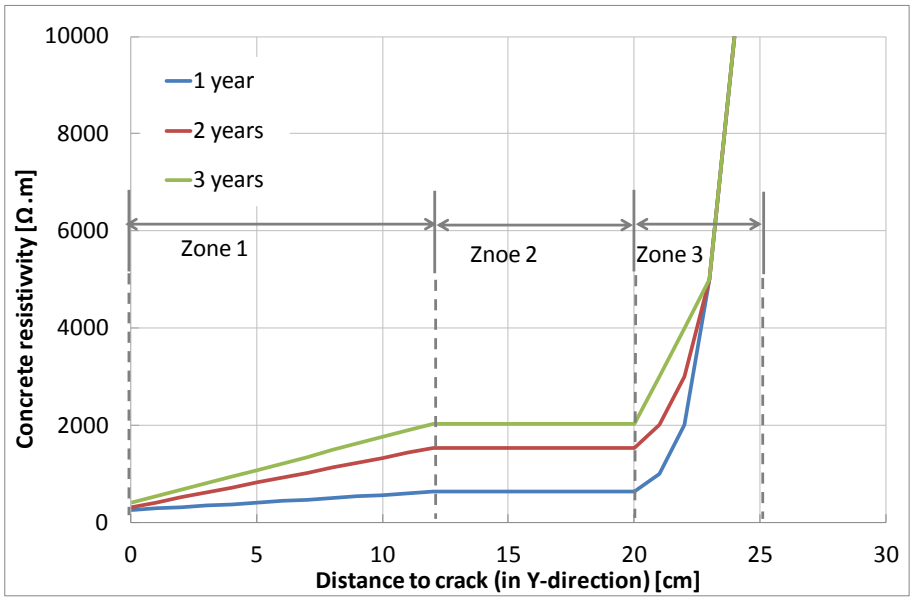

Figure 5-19: Concrete resistivity along y-direction, I05360， at x>3.1 cm, inner zone

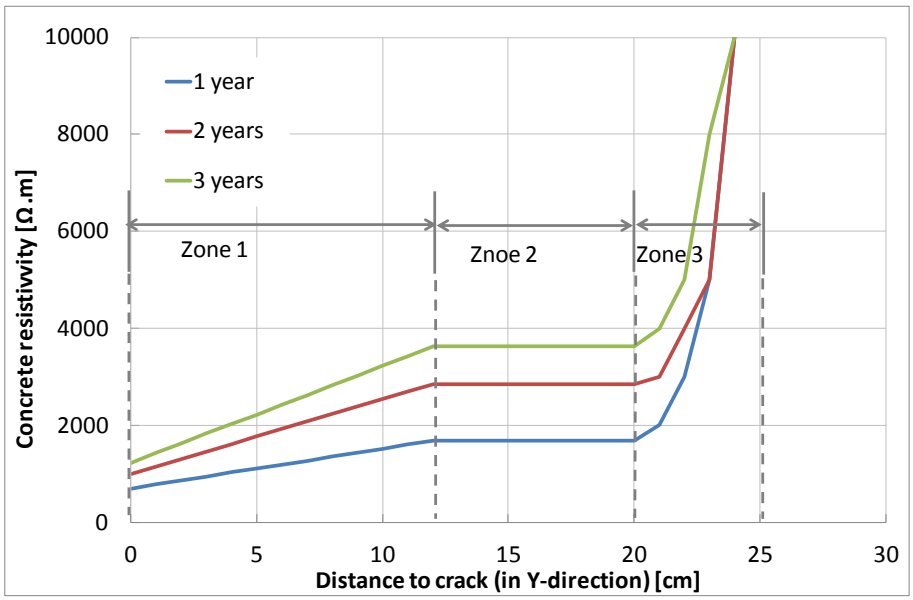

Figure 5-20: Concrete resistivity along y-direction, III05360, when x>3.1 cm, inner zone

However, in the outer zone resistivity varies with x-values (range of $x \in (0, 3.1)$) due to the wetting-drying cycle, which means that concrete resistivity on cross section is supposed to be concentrically varying.

Figure 5-21 shows the resistivity contour plot on the surface of the concrete beam. Resistivity is represented in the form of conductivity. It gives an over view of the resistivity distribution. Figure 5-22 shows the concentrically varying resistivity filed by cutting the beam model into slices. Figure 5-23 is the contour plot and sciagraghy of conductivity field in

cracked concrete, taken I05360 as an example. The cutting positions are marked with numbers and are shown in Figure 5-21.

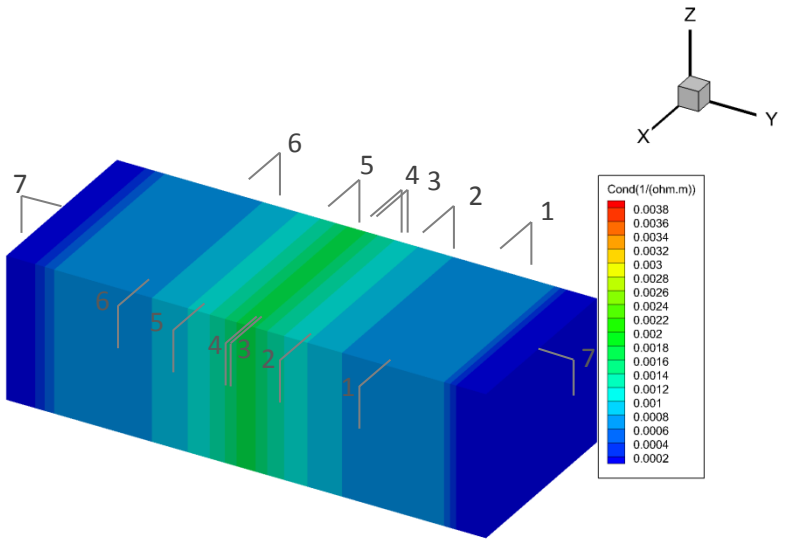

Figure 5-21: Contour plot of resistivity field of cracked concrete at surface, I05360, 1 year exposure

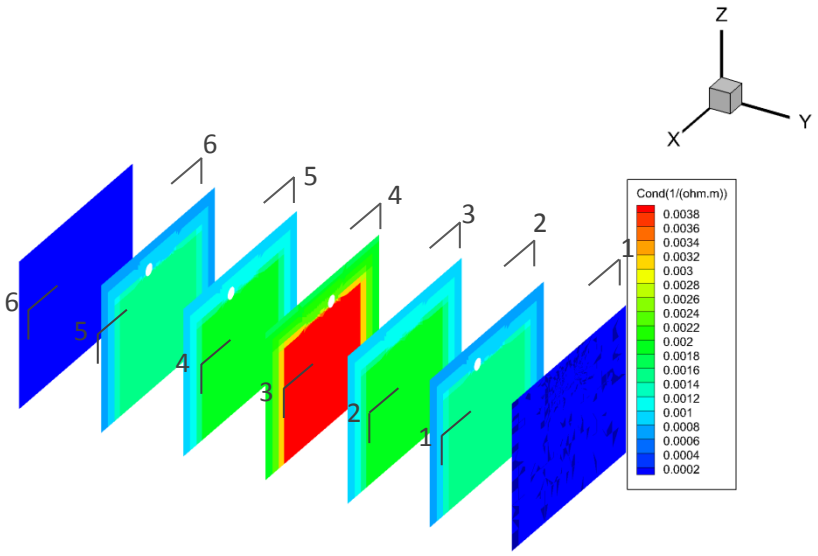

Figure 5-22: An example of concrete resistivity distribution in cross section, I05360, 1 year exposure, in term of conductivity,

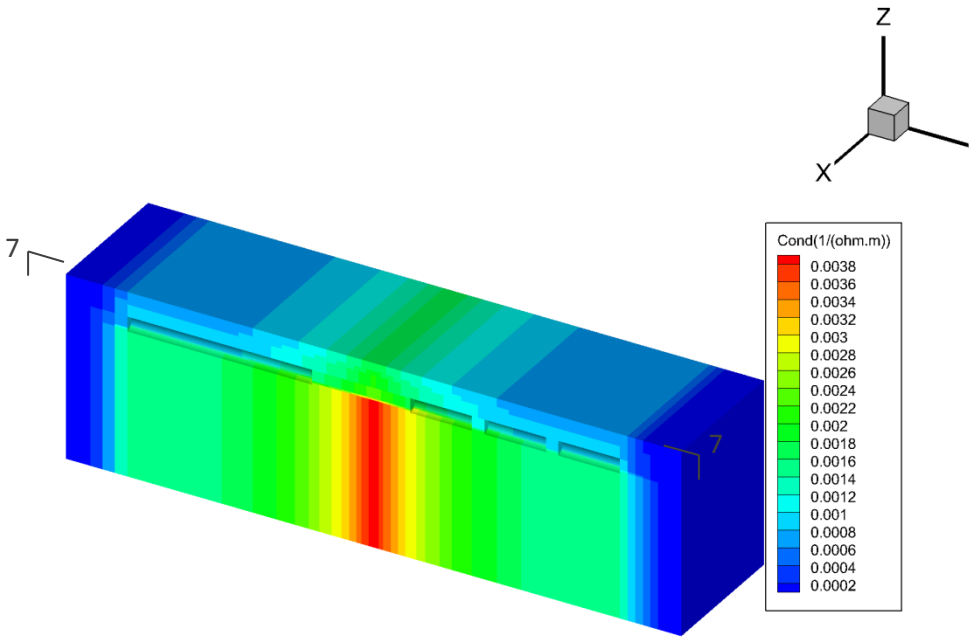

Figure 5-23: Sciagraphy of concrete resistivity filed in term of conductivity, I05360, 1 year exposure

In addition to the concrete resistivity contour which reveals the real resistivity distribution in the cracked concrete beams, other resistivity values are also discussed to study the influence of electrolytic resistivity on corrosion rate for scientific interests. Parametric study is carried out by varying resistivity from 150 $\Omega \cdot m$ to 10000 $\Omega \cdot m$, with uniform distribution.

5.3.2 Polarization curve measurement

Polarization curve describes the relationship between the current density and potential when the anode or cathode is polarized from its resting potential. Polarization curves are fundamental input parameters for the numerical calculation of MCRC. However, very few information about polarization properties of cracked concrete could be found in literature. Besides, it is not realistic to simply take data from literature, since polarization is material property which is determined not only by the nature of electrodes and surrounding concrete but also by the environmental conditions. Therefore it is necessary to determine the polarization properties of the individual reinforcements by experimental tests. This section describes how the polarization curves were measured and how the results were interpreted.

Experimental setup

Polarization curve measurements were carried out directly on the cracked beams. Two cracked beams from the chloride wetting-drying cycle were selected: one is from I05360 specimen with different cover depths (2 cm, 3.5 cm, and 5 cm); the other is from III05360 specimen with constant cover depth (5 cm). When being measured, the two cracked beams have been exposed in the chloride cycle for 3 years. Polarization curves in early exposure durations were unfortunately not measured.

Keep in mind that there are 3 groups of corrosion cells in each beam, embedded with either different or identical cover depths. In each corrosion cell, there are one anode and four cathodes. The numbers of polarization curves obtained are shown in Table 5-3.

Table 5-3: Sketch of the measurement

	I05360	III05360
No. of corrosion systems	3	3
No. of anodic polarization curves	3	3
No. of cathodic polarization curves	12	12

The cracked beams were four years old when the polarization curve measurements were performed. They were stored in 20°C and RH 85 % for the first half year and then exposed to laboratory climate for another half year. The laboratory climate could be found in Figure 3-11 (page 50), in Chapter 3. Then the specimens were subjected to a chloride wetting-drying cycle with 1% chloride solution sprayed into crack area 1 hour per week for three years.

Figure 5-24 (a) shows how anodic polarization curves were measured. The anode rebar served as the working electrode (WE); the stainless steel foil in the crack, which was used to keep the crack width constant, worked as the counter electrode (CE); the $Cu/CuSO_4$ reference electrode, which was embedded very close to the anode, served as reference electrode (RE).

Figure 5-24 (b) shows how the cathodic polarization curves were measured. One of the cathode rebar served as WE; A stainless steel mesh with 1 cm grid was tightly mounted around the beam surface to serve as CE; an external Ag/AgCl reference electrode was adopted as RE. In order to create an intimate electrical connection between the CE/RE and

the concrete surface, wet sponge was inserted between the concrete surface and the stainless steel mesh.

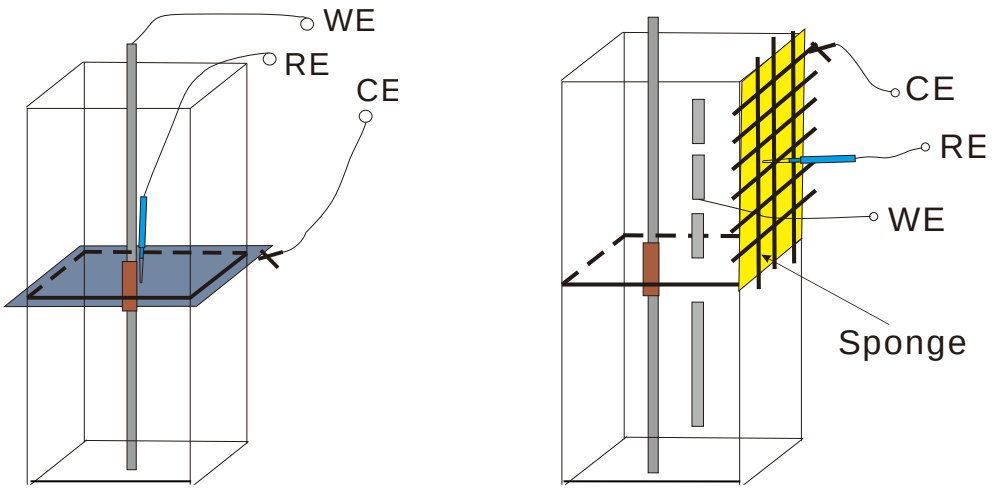

Figure 5-24: (a) Sketch of anodic polarization curve measurements
(b) Sketch of cathodic polarization curve measurements

The anodic and cathodic reactions were investigated by current-potential measurements. The measurements were carried out with the assistant of the Solartron potentiale instrument (S1 1255 HF Frequency Response Analyze, S1 1285 Electrochemical Interface, and 1281 Multiplexe). Before the anode or cathode was polarized, the anodic or cathodic resting potential was predetermined and the iR-drop between the WE and RE was measured. Subsequently the polarization of the anode (or cathode) started from the resting potential. The sweeping frequency was set as 0.167 mV/s. The anode was anodically polarized for 800 mV and the cathodes were cathodically polarized for 600 mV from their resting potential respectively. The measured potentials were corrected with the measured iR-drop.

Results

It has to be noted that the current density of the polarization curves corresponds to the entire anode or cathode area, although the actual anode or cathode area could be different. Both anodic and cathodic polarization curves for anodes and cathodes have been measured. However, only the anodic polarization curves of anode and cathodic polarization curves of cathode were of interest and analyzed.

Figure 5-25 illustrates the anodic polarization curve of anodes, for both I05360 and III05360 concrete beam. The anodic resting potentials range from -300 mV to -100 mV vs. NHE. In

order to make the slope of the curves comparable, the curves were slightly moved along x-axis to reach the same resting potential. However the original polarization curves were adopted when calculating. As shown in Figure 5-25, the corrosion current density increase steeply when the over-potential is within 100mV. Then it starts to show a linear course when the over-potential is around 100 mV. If a comparison is made between the anodes embedded in I05360 and III05360, it could be observed that the curves are steeper in I05360 than in III05360. Besides, the anodic polarization curve of the anode with 2 cm cover depth is less steep than the other two (3.5 cm and 5 cm cover depths), I05360.

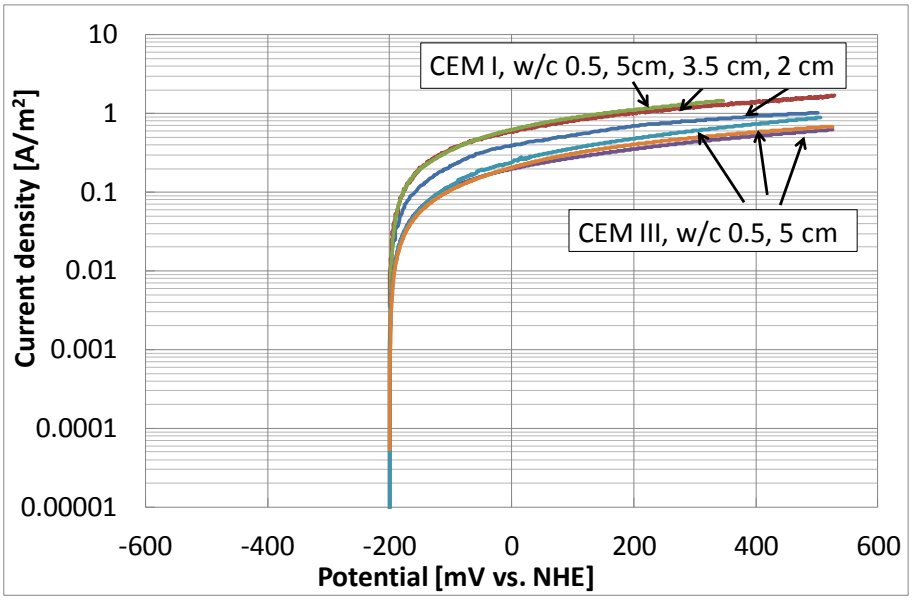

Figure 5-25: Anodic polarization curves of both I05360 concrete and III05360 concrete, 3 years exposure.

Figure 5-26 and Figure 5-27 illustrate examples of cathodic polarization curves for both I05360 and III05360 concrete beams. The resting potentials range from 100 mV to 200 mV. Similar with the anodic polarization curves, the cathodic polarization curves are also moved along the potential-axis to reach the same resting potential, so that the slopes of the curves could be compared. The slopes of cathodic polarization curves become less steep when the over-potential is around -100 mV. A tendency of the Tafel slope of the four cathodes is: C4>C3>C2>C1.

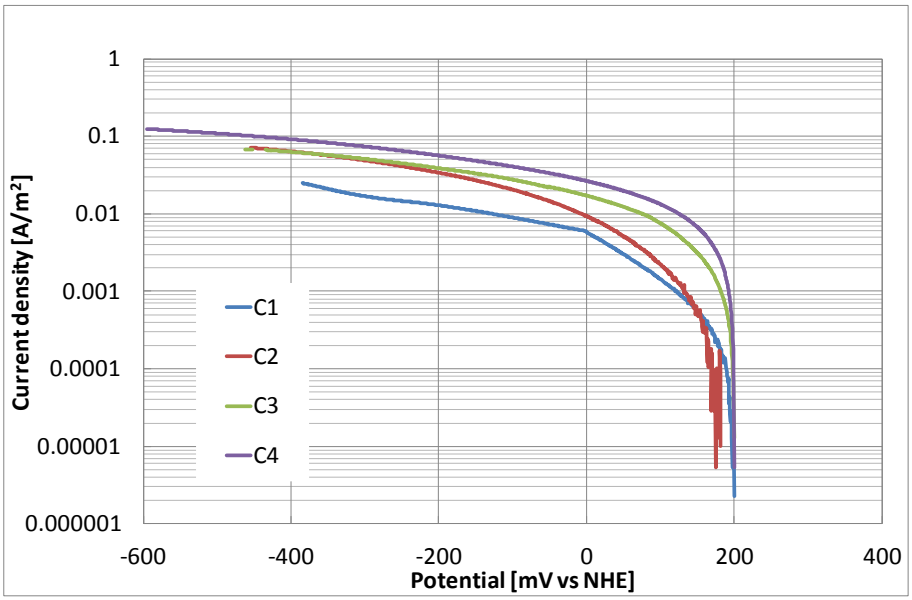

Figure 5-26: An example of cathodic polarization curves of cathodes, I05360, 3 years exposure

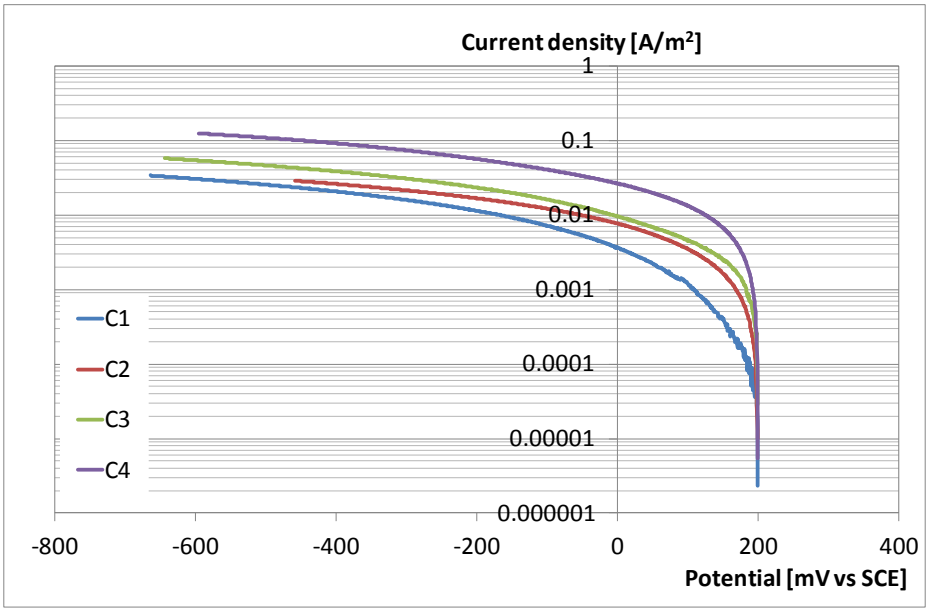

Figure 5-27: An example of cathodic polarization curves of cathodes, III05360, 3 years exposure

5.4 Results and discussions

It has been proved in section 5.2.2 that the self-developing FEM program MCRC is a valid and efficient tool for modelling macro-cell corrosion. Therefore, the corrosion state in

cracked concrete which is subjected to cyclic chloride attack could be simulated based on the laboratory measured resistivity and polarization curves.

The calculated results are analyzed and compared with experimental results of Chapter 3 in the following section. Additionally, a parametric study is conducted to investigate the effects of concrete resistivity, driving potential and concrete cover depth, etc.

5.4.1 Corrosion currents and potential distribution

As afore mentioned, polarization curves were only measured after three years exposure. Therefore resistivity distribution data that being adopted is also the value of the same age if not particularly annotated. Consequently, the calculated model reflects the corrosion state of the cracked beams after 3 years cyclic chloride exposure.

Figure 5-28 shows exemplarily the calculated potential distribution of I05360 concrete beam on both electrodes and concrete. This case is calculated with anodic resting potential -200mV (vs. NHE) and cathodic resting potential 100mV (vs. NHE). It could be observed that corrosion potential on the anode is as low as -190 mV, while potential on cathodes ranges from -78 mV to 20 mV. A clearer view of potential distribution on electrodes is given in Figure 5-29. The polarization of cathodes decreases with its distance to the anode. C3 has been polarized -175 mV at the close end to the anode, while C1 is only polarized -75 mV.

(a) overview

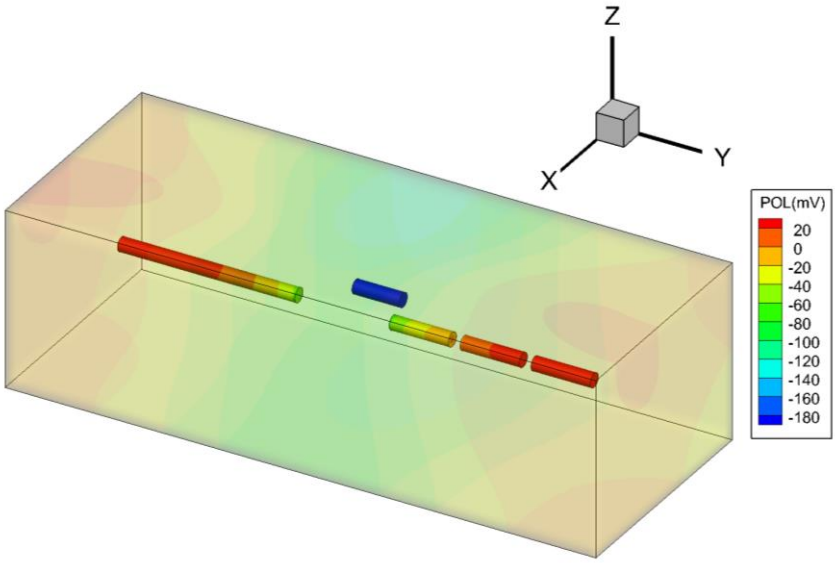

(b) cross section

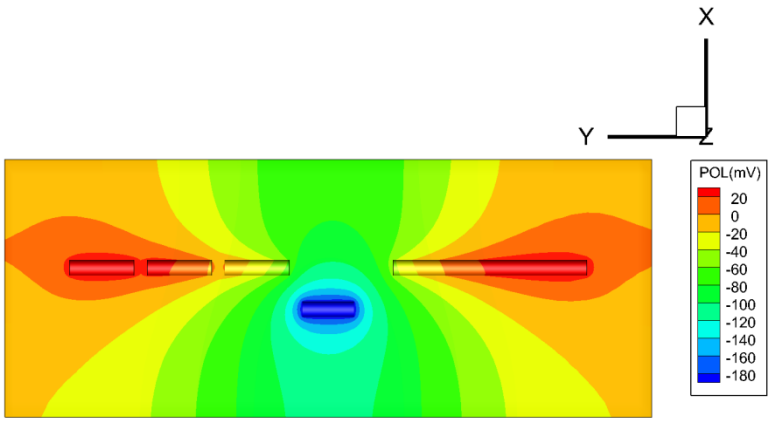

Figure 5-28: Contour plot of corrosion potential, I05360, cover depth=5 cm, 3 years exposure duration

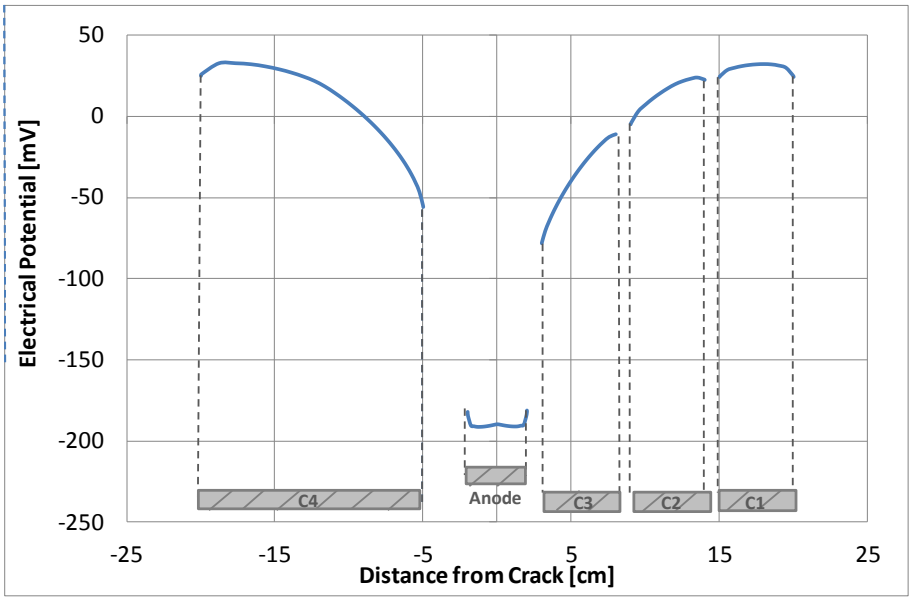

Figure 5-29: Calculated potential on electrodes, I05360, cover depth= 5 cm, 3 years exposure duration

Figure 5-30 shows the contour plot of calculated potential distribution on concrete surface, for I05360 concrete with reinforcement embedded with 5 cm cover depth. Potential contour shows a valley shape area right above the anode. The concrete surface potential far from the anode is approximately -5 mV; and is -116.5 mV right above the anode centre.

Figure 5-31 directly shows the varying concrete surface potential along the line right above the anode, for I05360 concrete. The three curves represent cases calculated with three different concrete cover: 2 cm, 3.5 cm and 5 cm respectively. In order to keep the results comparable, the three cases are calculated with the same concrete resistivity field and polarization curves. It could be seen in Figure 5-31 that the reduction of potential on concrete surface is less pronounced for those with thicker cover depth. This means when conducting the surface detecting technique, e.g. potential mapping, corroded rebar which is embedded under deeper concrete cover is less detectable. Therefore, more attention should be paid to those deep-embedded rebar even though the detected surface potential drop is not evident. The concrete surface potential contour plot is of practical significance in validating the field tested potential mapping results.

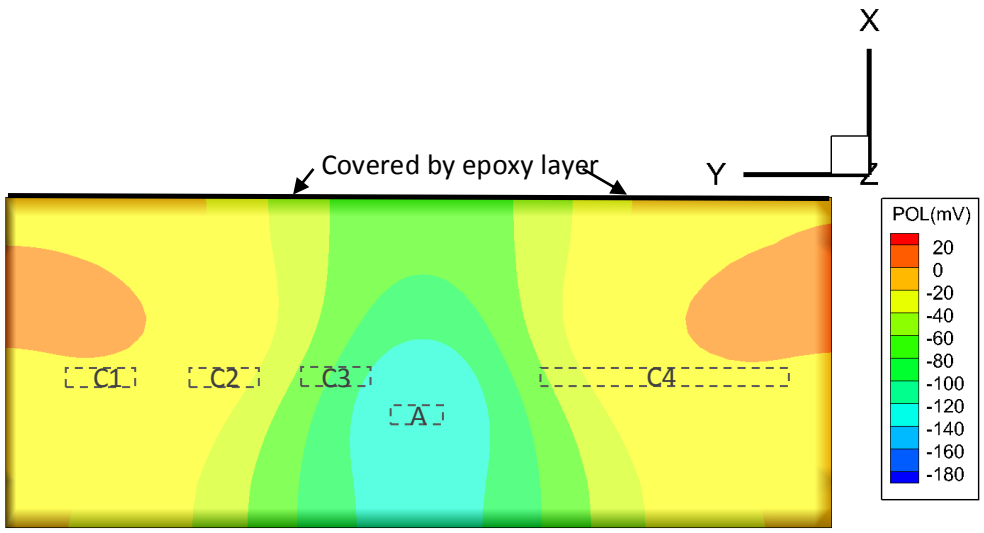

Figure 5-30: Contour plot of potential on concrete surface, I05350, anode embedded with cover depth= 5cm, 3 years exposure duration

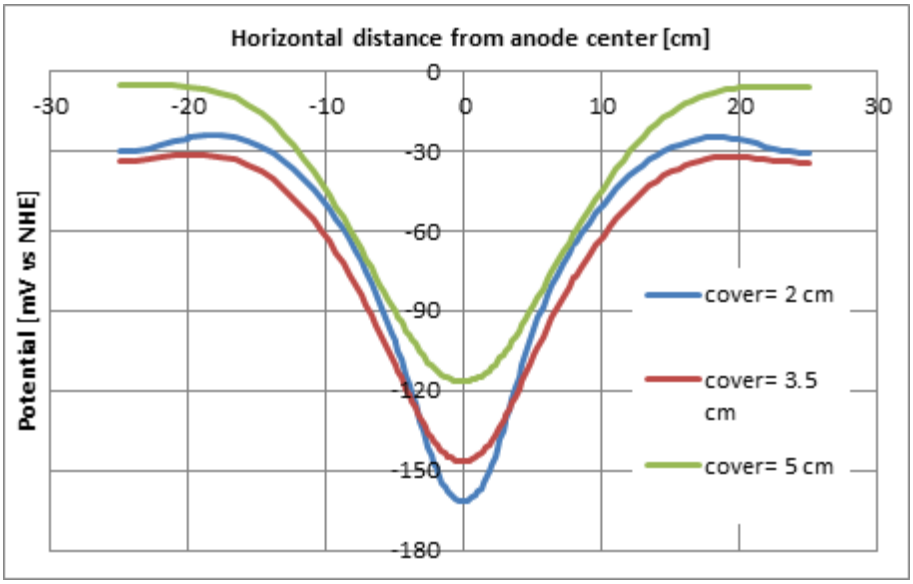

Figure 5-31: Potential on concrete surface along the line right above anode, I05360, 3 years exposure

Figure 5-32 shows the trace lines of electrolytic current, which denote the direction of flowing current.

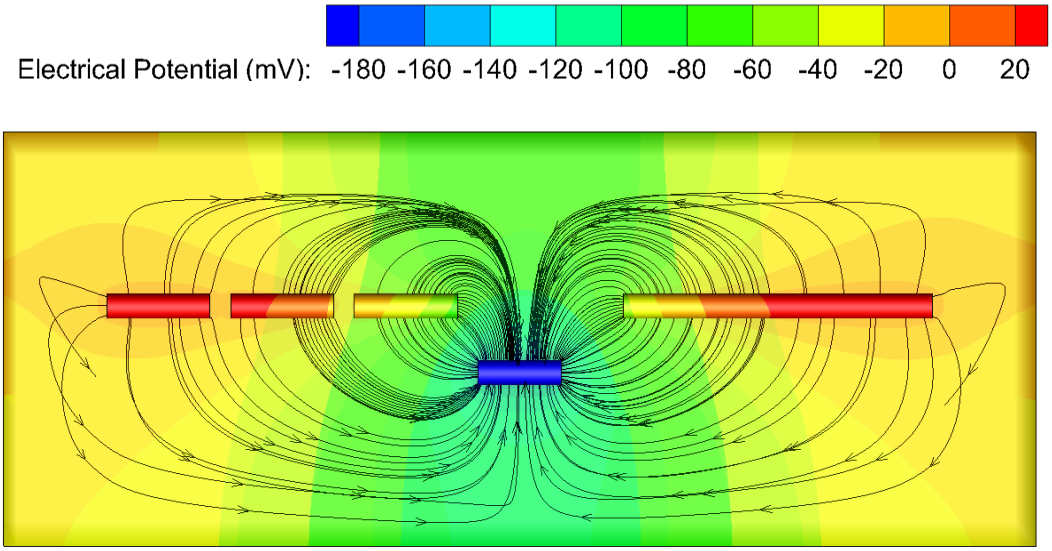

Figure 5-32: Trace line of electrolytic current, I05360, cover= 5cm, 3 years exposure duration

Figure 5-33 illustrates the current density on electrodes versus the distance to the centre of anode. Current density is as high as 3.4μA/cm^{2}at the two ends of the anode. The current density on cathodes decreases with the distance to anode centre.

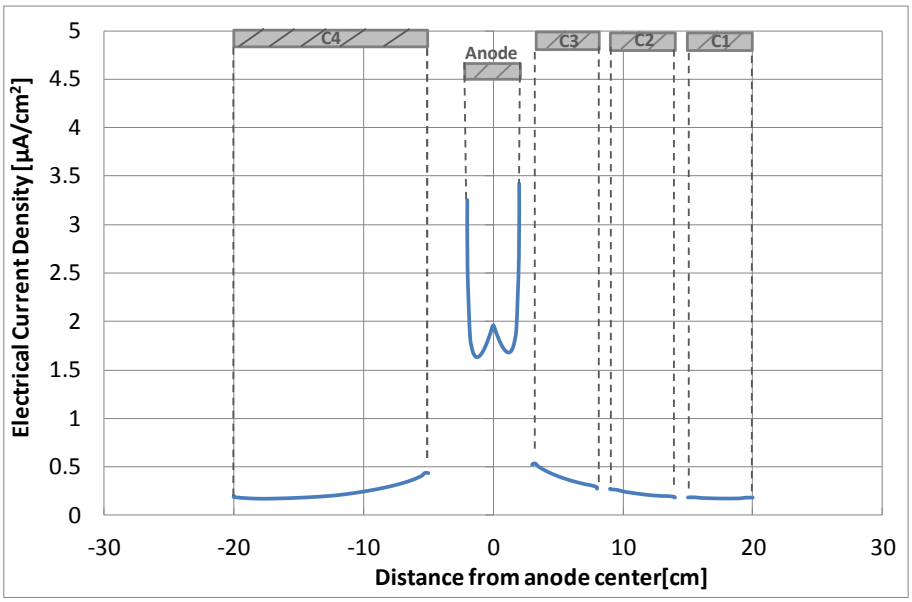

Figure 5-33: Distribution of current density on electrodes, I05360, cover= 5cm, 3 years exposure duration

It has been stated in Chapter 3 that the C4 cathode, which is with larger size (l=15 cm), possesses nearly half of the total macro-ell current; C3, which is with smaller size (l=5 cm) but close to the anode, holds approximately one quarter of the total current; while C1 and

C2, which are with small size (l=5 cm) and far from the anode, hold the rest one quarter of the total current (also shown in Figure 3-28 in page 68). The same phenomenon is also observed in the numerically calculated results, as shown in Figure 5-34, which validated the experimental results quite well.

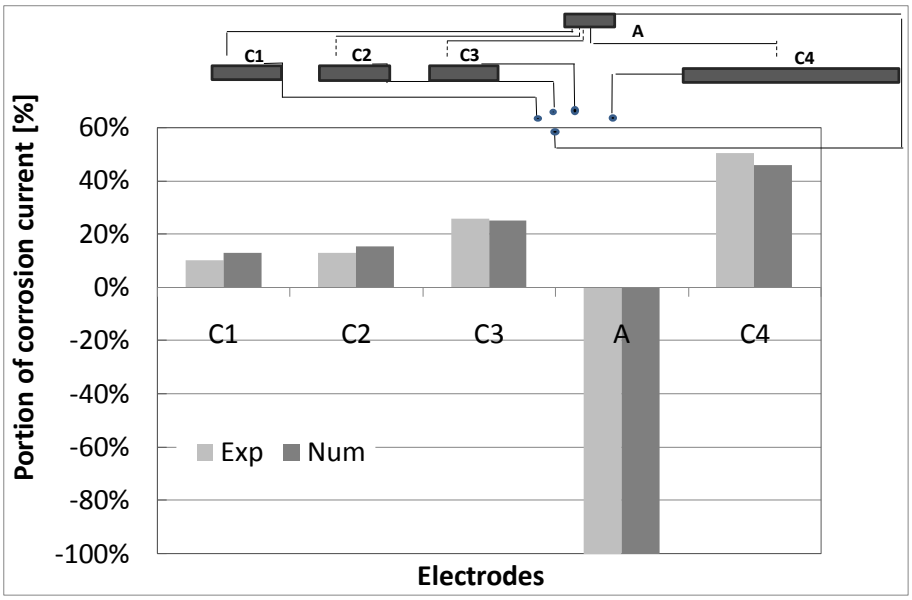

Figure 5-34: Distribution of corrosion currents among cathodes, num & exp, I05360, cover depth= 5cm, 3 years exposure

In Table 5-4, the numerical calculated results are compared with the experimental results of Chapter 3. All the six cases are calculated with its individual polarization curves and resistivity distribution which are measured at 3 years exposure. The experimental results are the averaged corrosion current measured in the same duration. The current data shown in Table 5-4 refers to the total macro-cell current, i.e. the anodic current. It can be seen that deviation between numerical and experimental results ranges from 5% to 45%. The deviation might be introduced by the polarization curve data. Before the polarization curve measurement, the concrete beams were shortly submerged in water to minimize the potential drop caused by cover concrete. By doing this, the moisture conditions in the concrete is changed which probably leads to a slight deviation of the polarization curves. Anyhow, the deviation is small enough that the numerical results can be considered as acceptable. The validity of the experimental results is also proved.

It could also be seen in Table 5-4 that for both numerical and experimental results, the corrosion current of I05360 is higher than that of III05360. From a numerical point of view, this is because the resistivity of I05360 is lower and the polarization curves are steeper. The

comparison of resistivity field and polarization curves between I053660 and III05360 concrete has been shown in earlier section (Figure 5-19, Figure 5-20, Figure 5-25, Figure 5-26 and Figure 5-27).

Table 5-4: Comparison between numerical and experimental results, 3 years exposure.

Concrete	Cover depth [cm]	Anodic current $[\mu A]$		
		Numerical	Experimental	Deviation
I05360 (3 years exposure)	2	21	17.68	16%
	3.5	24.88	19.82	20%
	5	26.7	21.20	21%
III05360 (3 years exposure)	5	13.57	14.28	5%
	5	11.27	6.21	45%
	5	12.92	11.03	15%

Corrosion process is a process which dynamically varies with time due to the changes of exposure conditions and hydration. However, the Laplace equations based corrosion modelling only gives a stationary solution for a constant set of input parameters. Therefore, the afore discussed results only represent the corrosion state after 3 years exposure.

To describe the dynamical corrosion process, frequent measurement of polarization curves and concrete resistivity should be carried out. However, the polarization curves for the earlier period are missing, although the time dependence of concrete resistivity field could be estimated. An attempt was made to partially estimate the corrosion state of the earlier period with concrete resistivity data that measured in earlier period but with the polarization curves that measured after the 3 year's exposure. This attempt is reasonable since it has been reported in Chapter 4 that the moisture content in the cracked beam reached an equilibrium state after approximately one year's exposure, which indicates that the polarization curves should not have changed much thereafter. Strictly speaking, this attempt is not completely accurate, but reflects the tendency to some extent.

The comparison of corrosion currents in early period's exposure is shown in Table 5-5. The deviation between experimental and numerical results ranges from 4% to 45%. The deviation could be attributed to the difference between the real resistivity and polarization data and the estimated/measured data which are used in numerical calculation. As expected, the deviation is not considerable large, which indicates that the polarization curve's

variation over time is not big. It also indicates that the dependence of corrosion rate over exposure time mainly relies on the variation of concrete resistivity.

Table 5-5: Comparison of numerical and experimental results of corrosion current at different exposure duration, cover depth =5 cm.

Concrete	First year			Second year			Third year		
	Num [μA]	Exp [μA]	Dev [%]	Num [μA]	Exp [μA]	Dev [%]	Num [μA]	Exp [μA]	Dev [%]
I05360	42.89	44.43	4%	30.87	41.5	34%	26.27	21.2	19%
III05360	19.95	20.96	5%	15.48	14.27	8%	11.27	6.21	45%

Based on the numerical results, the controlling factors for macro-cell corrosion could be calculated according to Eq(5.11). Results are shown in Figure 5-39. The $R_{p,a}$ varies from 200 Ω to 400Ω, remaining in a low level. Therefore the controlling factor of anode, C_a, is nearly negligible. This is because that for the cracked beam in this study, the chloride solution is directly sprayed into anode area which introduces high chloride and moisture content in the anode area, leading to unlimited dissolution rate of iron. Controlling factors of the cathodes range from 23% to 44%; while the controlling factor of concrete resistance C_{el} ranges from 55% to 76%, indicating that the corrosion system is mainly under electrolytic resistance control. This is accordant to the conclusion obtained in Chapter 3. It could also be observed that, the C_{el} of A-C3 is relatively smaller than the other three. This is because that C3 is very close to the crack. The concrete resistivity between anode and C3 is quite small due to high moisture content. The controlling factors in III05360 concrete are similar with I05360 concrete.

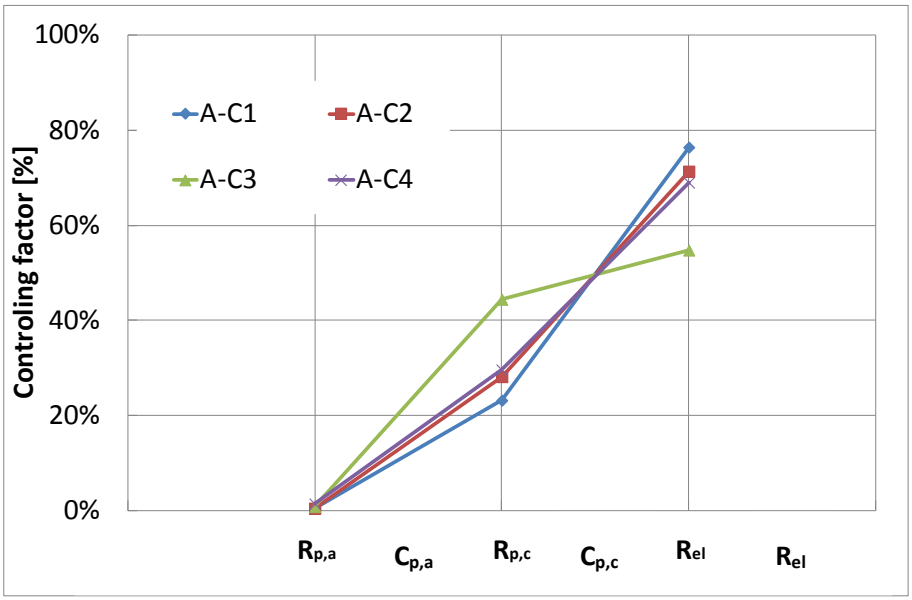

Figure 5-35: Calculated controlling factors of the four branch electrical circuits, I05360, 3 years exposure.

5.4.2 Parametric study

The solution of Laplace's equation with boundary conditions requires that the values of a number of corrosion parameters could be pre-determined. These parameters were originated from the basic corrosion theory which is described as Butler-Volmer equation:

$$i = i_{0,a}\left\{\exp\left[\frac{\ln(10)\left|E_a - E_{a,0}\right|}{\beta_a}\right]\right\} \tag{5.8}$$

$$i = i_{0,c}\left\{\exp\left[\frac{\ln(10)\left|E_c - E_{c,0}\right|}{\beta_c}\right]\right\} \tag{5.9}$$

In which,

β_a and β_c - anodic and cathodic Tafel slopes;

$i_{0,a}$ and $i_{0,c}$ - anodic and cathodic exchange current density;

$E_{0,a}$ and $E_{0,c}$ - free corrosion potential of the anodic and cathodic reaction.

Experimental studies have shown that the parameters in Butler-Volmer equation, i.e. β_a, β_c, i_{0a}, i_{0c}, E_{0a} and E_{0c}, can show significant variations; therefore their selection for modelling purposes can be a challenging task. Environmental factors and the presence of external ions,

such as chlorides, have been shown to affect them. Brem [158] has reported the effect of environmental temperature and relative humidity on the Tafel slopes. Tafel slope also shows variations under varying values of pH. Additionally, concrete resistivity and model geometry also influence the corrosion state.

Based on MCRC program, it becomes possible to conduct a parametric study to identify the effect of the above mentioned parameters on the corrosion rate in concrete. Since there is uncertainty associated with the selection of these parameters, it is intended that the results of this study will provide valuable information to engineers and researchers who model steel corrosion in concrete.

There are some points to be clarified:

1) For parametric study, there is only one variable in each case, while the other factors are kept constant.
2) Not all the parameters in Butler-Volmer equation are discussed in this parametric study. Although Tafel slopes and exchange current density may also have considerable effects on corrosion intensity, they are excluded from discussion. A parametric study of these parameters has been theoretically done by Ge and Isgor [157].
3) For geometry factors, only the concrete cover depth, which is of much concern in this thesis, is discussed. Factors such as anode and cathode area, distance between anode and cathode, rebar diameter etc., are not involved, although the modeling of these factors can be easily achieved by the MCRC program.

   Actually, studying the geometry effect simply by changing the geometry is irrational. It must be combined with its corresponding polarization curves. For example, the polarization curve of rebar varies with concrete cover depth, as have been shown in Figure 5-25.
4) The polarization curves for calculation are one group curves that taken from the I05360 concrete, Figure G-3 (in page 232).

The range of main parameters is illustrated in Table 5-6, with bold character selected as basic values.

Table 5-6: Parameter matrix.

Parameter	Unit	Range
Concrete resistivity, R	$\Omega \cdot m$	150, 300, **500**, 1000, 5000, 10000
Driving potential, ΔE	mV	300, 400, **500**, 600, 700
Concrete cover, d	cm	2, 3.5, **5**

Concrete resistivity

Figure 5-36 shows the effect of concrete resistivity on macro-cell corrosion current. As expected, the corrosion current density shows a strong dependence on concrete resistivity. A half logarithm relationship could be observed and mathematically fitted as:

$$i_{corr} = 8.6 - 2.1\lg(\rho) \tag{5.10}$$

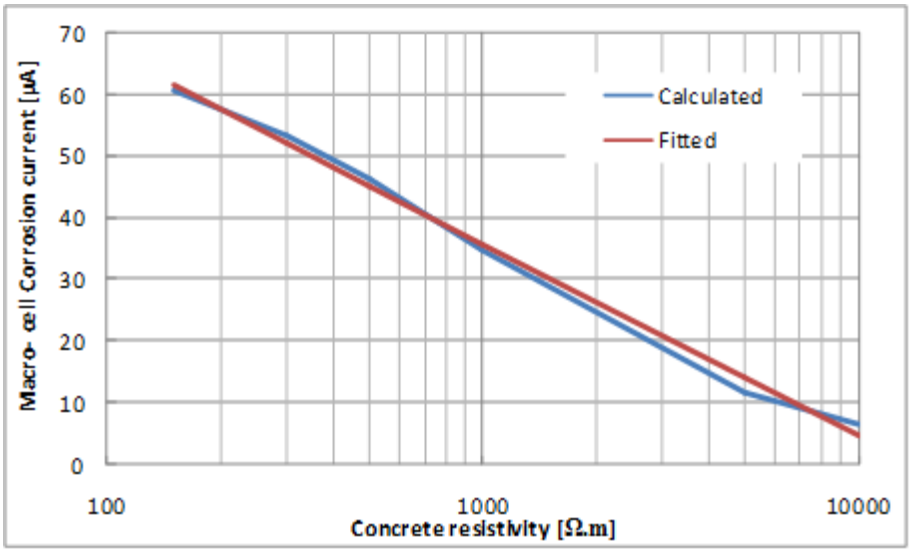

Figure 5-36: The effect of concrete resistivity on macro-cell corrosion current, calculated with uniform resistivity field

The distribution of macro-cell corrosion current among the electrodes which are modelled with uniform resistivity fields are shown in Figure 5-37. The four diagrams in Figure 5-37 are calculated with different resistivity levels, ranging from 150 $\Omega \cdot$m to 5000 $\Omega \cdot$m. As could be seen in Figure 5-37 (a) and (b), cathodes C1, C2 and C3 share nearly the same current portion when resistivity are in the low level (ρ=150 and 500 $\Omega \cdot$m, respectively); when the resistivity increases, the distribution of corrosion currents among the cathodes varies. At higher resistivity levels, as shown in Figure 5-37 (c) and (d), the closer cathode C3 grabs more and more quotient of the total currents. The current distribution among cathodes demonstrates more and more distance-dependence when the concrete resistivity increases,

indicating a growing resistance control of the corrosion system. If a comparison is made between Figure 5-34 and Figure 5-37, a conclusion could be drawn that simply assuming uniform resistivity field in modelling the corrosion in cracked concrete may lead to inaccurate results, especially at low resistivity level. The over-simplified assumption will lead to under-estimation of the corrosion state for the reinforcement in low resistivity region (crack vicinity zone) and over-estimation in high resistivity region.

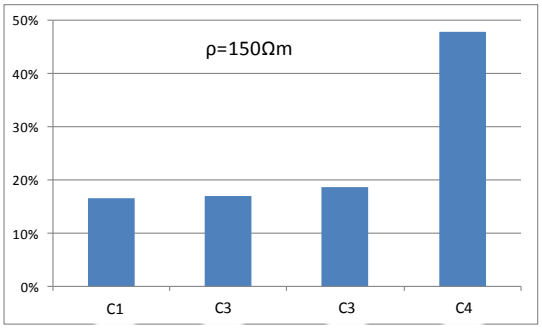

(a) $\rho = 150\Omega m$

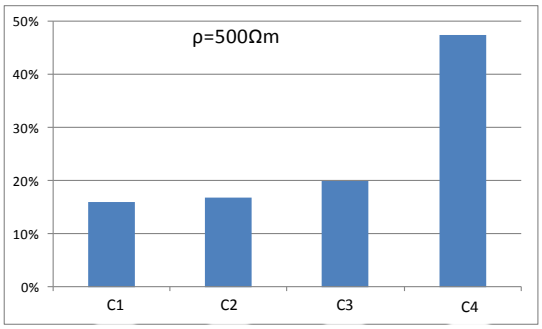

(b) $\rho = 500\Omega m$

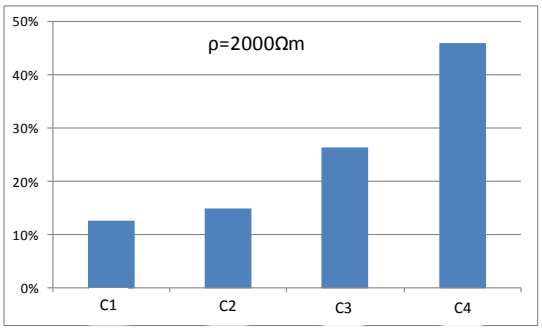

(c) $\rho = 2000\Omega m$

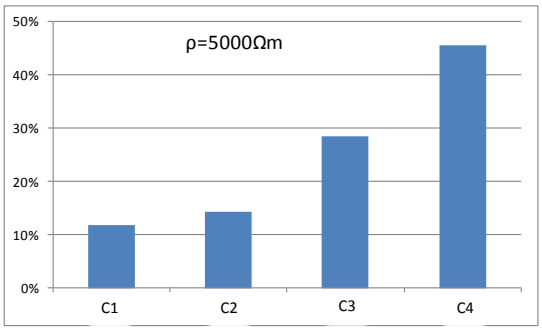

(d) $\rho = 5000\Omega m$

Figure 5-37: Distribution of macro-cell corrosion currents among electrodes, with uniform concrete resistivity field.

The influence of concrete resistivity on the controlling factors of the corrosion system is shown in Figure 5-38. The anodic controlling factor $C_{p,a}$ is quite low; C_{el} increases with increasing concrete resistivity as expected; $C_{p,c}$ consequently decreases with increasing concrete resistivity.

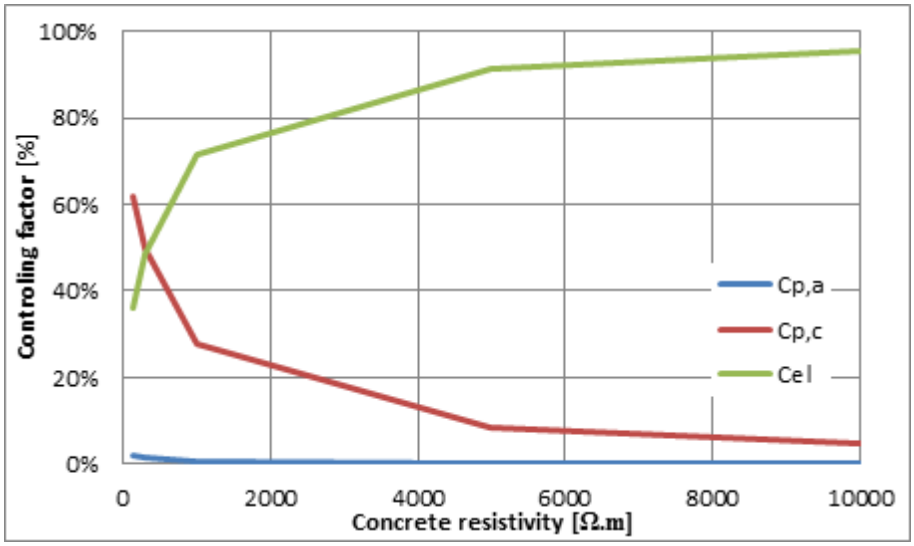

Figure 5-38: Dependence of controlling factors on concrete resistivity, I05360, 3 years exposure duration

Driving potential

A linear relationship between driving potential and macro-cell corrosion current was observed, as shown in Figure 5-39.

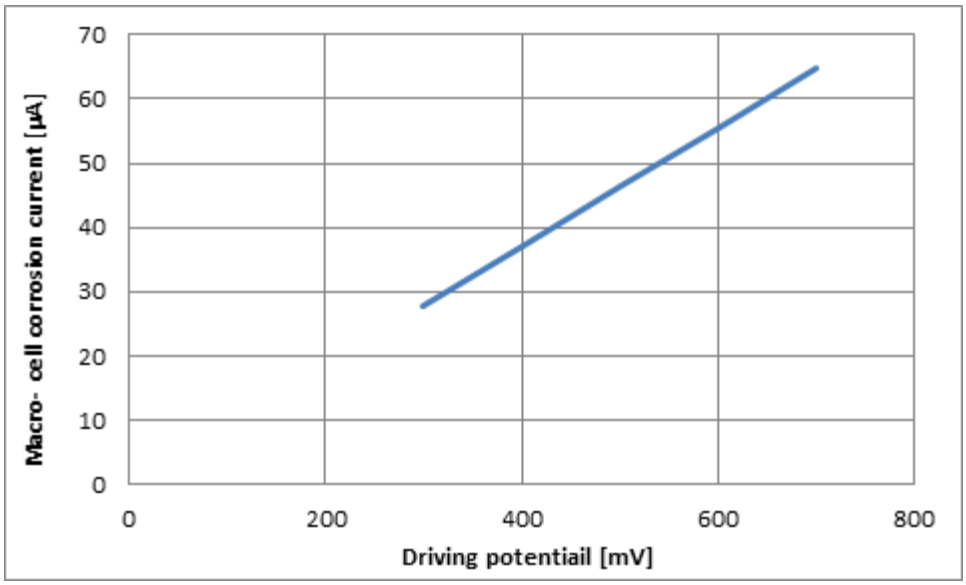

Figure 5-39： Influence of driving potential on macro-cell corrosion current, I05360, 3 years exposure duration

Concrete cover depth

The influences of concrete cover depth on the corrosion intensity, in a numerical point of view, are that:

1) The concrete resistivity around the embedded reinforcement is different, due to the different pore moisture content at different cover depths;
2) The polarization curves should be different for the reinforcement embedded in different cover depth, due to the different moisture content at different cover depth.
3) When calculating, the electrolyte domain that involves in the calculation is different.

Both experimental results in chapter 3 and numerical results in this chapter show an increase of corrosion current with increasing cover depth. This tendency is supposed to be the combined effect of the above mentioned three aspects. Point 1) and 2) are considered as the main aspects. The effect of the third aspect, i.e. the electrolyte domain that involves in the charge transportation, is not clear. Therefore, a case study was conducted to investigate this effect when the cover depth varies. In this case, the only variable is the concrete cover depth. The concrete resistivity and polarization curves are kept constant. It could be seen in Figure 5-40 that macro-cell corrosion current shows only a slight increase with increasing cover depth. The concrete domain that involves in the charge transportation is slightly larger when concrete cover is deeper. However, this effect is negligible.

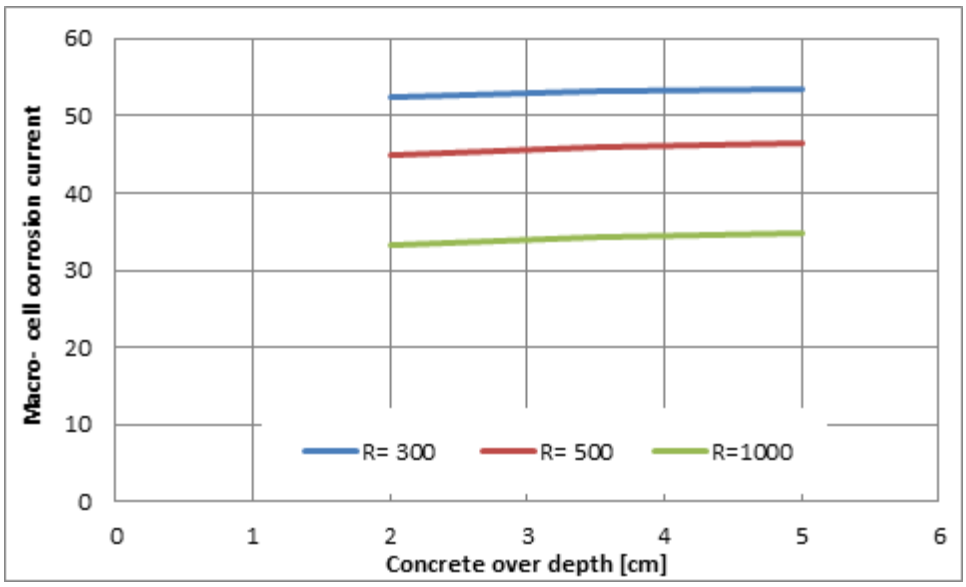

Figure 5-40: Influence of the involved concrete domain on macro-cell corrosion current, uniform resistivity field

5.5 Summary

In order to evaluate the corrosion conditions of steel bars in concrete elements and to validate the experimental results of Chapter 3, numerical simulation was carried out with a self-developing FEM program 'MCRC', i.e., the 'Macro-cell Corrosion of Reinforcement in

Concrete'. This program is written in FORTRAN. Galerkin method is employed to solve the Laplace equations, when a certain boundary conditions are given. A validation of the MCRC program is conducted by modelling the same case presented by Warkus, *et al* [129] and Redaelli, *et al* [134]. The results calculated by MCRC are in great accordance with those reported by J.Warkus (modelled with BEM software Beasy) and E.Redaelli (modelled by FEM software, FEMLAB).

Attention was focused on the selection of proper values of the parameters to describe the electrochemical behaviour of steel in the different conditions of exposure. As boundary condition, polarization curves are measured on the cracked concrete beams of both I05360 and III05360 concrete. Polarization curves are found to be influenced by concrete composition and rebar location. Anodic and cathodic polarization curves for rebar in CEM I concrete is more steeper than those in CEM III concrete; while the polarization curves of the cathodes which is close to crack is slightly steeper than those further away from the crack. No clear dependence of driving potential on concrete mixture or electrode location is observed yet. The location-dependent resistivity field of the cracked beam was obtained by combing the numerically modelled moisture distribution in Chapter 4 and the resistivity data that measured in a parallel project.

As main output data, the potential and corrosion current contour on both electrodes and bulk concrete could be determined. The numerically calculated macro-cell current agrees well with experimental results of Chapter 3. This accordance validates the experimental results and meanwhile, proves the validity of the MCRC program.

Based on the output data, anodic and catholic polarization resistance could be calculated. Controlling factors of anode, cathode and electrolyte could be thereby calculated. It is found that the corrosion in the cracked beam which is subjected to chloride wetting-drying cycle is under concrete resistance control. This is accordant with the findings in Chapter 3.The anode controlling factor is nearly negligible.

In parametric study, a half logarithm relationship between the calculated corrosion current and concrete resistivity was found, by assuming a uniform concrete resistivity distribution. The controlling factor of concrete resistance increases with increasing resistivity.

The effects of cover depth on calculated macro-cell corrosion current are mainly focused on its effects on polarization curves and concrete resistivity field. The pure effect of concrete domain that involved in charge transfer is negligible.

The numerical calculation in this chapter only reflects the state of the measuring moment. It could not reveal the time dependence of corrosion process. To describe the time development of corrosion process, frequently measurement should be performed.

MCRC is effective and valid numerical tool for modelling macro-cell corrosion. Results show that MCRC provided results practically identical to those obtained using other exiting commercial software. However, MCRC is superior with the potential for future development for corrosion simulation. The advantage of MCRC is that it could model macro-cell corrosion in concrete with arbitrary geometry and arbitrary resistivity distribution. Meanwhile, as self-developing program, the output is more flexible than commercial software. Combine with the numerical program CPUCC, which has been introduced in Chapter 4, the prediction of both the initiation and propagation period is possible.

Chapter 6 Conclusions and Recommendations

6.1 Conclusions

When cracks occur, a preferable path for corrosion promoting substances (CO_2, Cl ions, etc.) is created and corrosion is thereby enabled. Through the experimental and numerical study in this research, the physical mechanisms underlying the corrosion process of reinforcement in cracked concrete subjected to cyclic chloride contamination is better understood and meanwhile, numerical tools that could serve as a complement to engineering decisions related to durability-based design and assessment of cracked/sound reinforced concrete structures were developed.

During laboratory study, corrosion relating terms are collected and analyzed. The effects of factors such as concrete composition (cement type, w/c ratio), exposure conditions (cyclic chloride contamination, cyclic water exposure, and natural unsheltered exposure), and member geometry (distance between anode and cathode, cathode size, concrete cover depth) are quantified. It is found that:

1) Penetration of chloride solution though crack is rather fast, indicating a short initiation period.
2) The mechanism of reinforcement corrosion in cracked concrete is macro-cell corrosion under concrete resistance control. With the chloride solution directly sprayed into crack, chloride concentration and moisture at anode is abundant. With atmospheric exposure and moderate concrete cover, the oxygen supply to cathode is adequate as well. Experimental results reveal that the relationship between the anode-to-cathode resistance and corrosion intensity is nearly inverse proportional, indicating that the corrosion system in cracked concrete is under resistance control.
3) According to the test results, corrosion intensity depends on environmental conditions, concrete composition (cement type, w/c ratio), specimen geometry and etc.. Cyclic chloride contamination is the most severe exposure condition, especially when combined with carbonation.
4) CEM I w/c 0.5 concrete is more vulnerable than CEM III 0.5 concrete when subjected to chloride induced corrosion. Concretes with lower w/c ratio demostrate superior corrosion resistance. Both the effect of cement type and w/c ratio could be attributed to the effect of concrete resistivity. The higher the concrete resistivity,

the lower the corrosion intensity. A half logarithm linear relationship was found between the macro-cell corrosion current and concrete resistivity.

5) The development of corrosion current over exposure duration was characterized by a 3-phase model, i.e. the ascending phase, the descending phase and the equilibrium phase. In equilibrium phase, the corrosion is steady due to the static state of related conditions, which makes the prediction of propagation period possible.
6) Corrosion pattern in the two types of concrete is different: Corrosion product in CEM III concrete distributes more dispersive and spread along steel-concrete interface, but remains more locally in CEM I concrete. Therefore, the damage pattern in cracked concrete is probably the loss of steel cross section in CEM I concrete and loss of bond strength in CEM III concrete. The possibility of corrosion product induced cover spalling and cracking is quite low, since the existed crack could release the stress induced by the voluminous corrosion product and act as a 'drainage' for the corrosion product.
7) The effects of cover depth on corrosion are found to be interesting. Corrosion intensity is found to be more severe on steels embedded with thicker concrete cover. The chloride profiles taken in destructive tests also show higher total chloride content in deeper crack. This was attempted to explain as: with chloride solution directly sprayed into crack 1 hour per week, it is probably that more moisture is kept in the deep crack, while the moisture in outside crack is dried out due to the effect of evaporation. Meanwhile, the chloride penetration duration into concrete from crack flank is consequently longer in deeper crack. Those hypotheses were proved by the experiments and numerical simulation in chapter 4.

The penetration of moisture and chloride into unsaturated cracked concrete are numerically simulated by a self-developed FDM program CPUCC. The transportation mechanisms are considered to be diffusion and convection. Based on the Fick's 1st law and mass conservation, two dimensional differential equations of chloride penetration coupled with moisture diffusion were built, considering chloride binding which obeys Freundlich and Langmuir binding isotherm. The diffusion coefficients of chloride and moisture are obtained by a factorial approach. To determine the moisture condition in crack, an experimental method was developed to test the water evaporation rate in crack, using electrolytic resistance as an indicator of moisture. The water evaporation rate in crack was found to obey a half logarithm relationship with exposure time.

Based on the numerical model and boundary conditions, the chloride/ moisture penetration process were studied. The following conclusions could be drawn:

With the self-developed program CPUCC, concrete pore RH, total chloride content C_t, free chloride content C_f, as well as moisture diffusion coefficient D_h and chloride diffusion coefficient D_c could be output as contour plot. In contour plot, the above mentioned terms could be easily determined at any time and any location.

Numerical calculated total chloride profiles were compared with experimental results of Chapter 3 and agree well with each other. Moisture content and chloride concentration were found to be higher in deeper crack. The unconventional phenomenon that corrosion was more intensive on reinforcements that embedded with thicker cover depth has been explained.

The correspondence of numerical results and experimental results proves the validity of the experimental data in Chapter 3. Meanwhile, the reliability of the numerical model is testified. It could be believed that CPUCC is a trustworthy tool in predicting the moisture distribution and chloride penetration in both uncracked concrete and cracked concrete.

Numerical simulation of the corrosion state in propagation period was carried out with a self-developed FEM program 'MCRC'. A validation of the MCRC program is conducted by modelling the same case with published scientific reports. As boundary condition, polarization curves are measured on the cracked concrete beams. Polarization curves are found to be influenced by concrete composition and rebar location. Anodic and cathodic polarization curves of rebar in CEM I concrete is steeper than those in CEM III concrete; while the polarization curves of the cathodes which is close to crack is slightly steeper than those apart from the crack. No clear dependence of driving potential on concrete mixture or electrode location is observed. A 3-dimensional-location-dependent resistivity field in the cracked beam was obtained by combing the numerically modelled moisture distribution in Chapter 4 and the resistivity data that measured in a parallel project.

As main output data, the potential and corrosion current contour on both electrodes and bulk concrete could be determined. The numerically calculated macro-cell current agrees well with experimental results of Chapter 3. This accordance validates experimental results and at the same time, proves the validity of the MCRC program. MCRC is effective and valid tool for modelling macro-cell corrosion.

Based on the output data, anodic and catholic polarization resistance could be calculated. Controlling factor of anode, cathode and electrolyte could be thereby calculated. It is found that the corrosion in the cracked beam which is subjected to a chloride wetting- drying cycle is under concrete resistance control, which is accordant with one of the conclusions in Chapter 3. The anode controlling factor is nearly negligible.

The laboratory study and numerical simulation validated each other and together integrate all of the aspects related to chloride induced corrosion of reinforcing steel, namely the time to steel depassivation, the process of active corrosion, and the damage patterns thereafter. It was an objective to formulate the model upon general physical laws so it would not be limited to a specific type of concrete or environmental conditions. Therefore, not only unsaturated but also saturated, not only cracked but also uncracked concrete could be modelled.

The research work in this study provides a possibility of modelling both the initiation and propagation period of structures subjected to chloride contamination with arbitrary geometry and arbitrary environmental conditions, as long as the boundary conditions could be obtained from field tests.

6.2 Recommendations for future research

Based on the findings of this study, works for future research are suggested as follow:

- More experiments should be carried out to examine the pitting factor in cracked concrete. To enable a statistical analysis, the number of specimens shouldn't be rare.
- Investigation should be carried on the combined effect of carbonation and chloride contamination on corrosion.
- More contribution is needed on the influences of plenty factors on chloride/moisture diffusion coefficient, to complete the factorial approach.
- Further refinement of equations describing the process of convection in concrete. Is needed. This also includes a better quantification of the critical parameters involved as well as measurements of field moisture profiles.
- The moisture evaporation rate tests should be carried out with various crack geometry, especially different crack width. This is quite important for the modelling of chloride/moisture ingression into cracked concrete, and the corrosion state simulation thereafter.

- More investigation should be conducted on the polarization curves in different conditions. A polarization curve data base should be built.

Other corrosion induced deterioration model for cracked concrete should be considered.

Appendix A Theoretical Aspects of Numerical Modelling on Chloride & Moisture Transportation into Concrete

A.1 Basic Equations

As has been stated in Chapter 3, the cracked concrete beams are subjected to a wetting-drying cycle with 1% chloride solution directly sprayed into crack area 1 hour per week. Except of the 1 hour's wetting, cracked beams are exposed in laboratory environment with an average temperature 25°C and RH 40%.

The chloride penetration process in this research is from crack flank into the non-saturated concrete, instead of the commonly discussed chloride penetration into saturated concrete from casting surface. The main transportation mechanisms are diffusion and convection with flowing moisture. Thereby, the coupled moisture movement has to be modelled as well.

In unsaturated concrete, at any point there exists an infinitesimal element whose centre located at the point, as shown in Figure A-1.

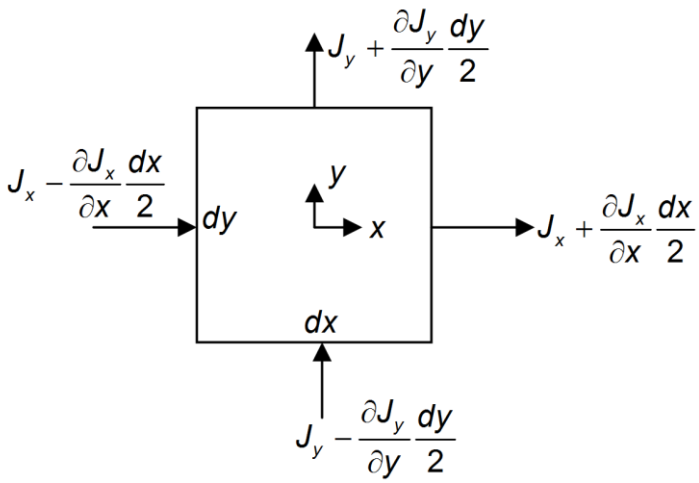

Figure A-1: Chloride penetration flux on a typical element

Chloride ions flow into the element through some edges and flow out through the others. According to the principle of mass conservation, the incremental chloride iron during an infinitesimal period should be equal to the difference between the inlet chloride quantity and the outlet chloride quantity, and can be expressed as:

$$\Delta C_t \cdot dxdy = \left(\left(J_x - \frac{\partial J_x}{\partial x}\frac{dx}{2} \right) dy + \left(J_y - \frac{\partial J_y}{\partial y}\frac{dy}{2} \right) dx \right) \cdot \Delta t - \left(\left(J_x + \frac{\partial J_x}{\partial x}\frac{dx}{2} \right) dy + \left(J_y + \frac{\partial J_y}{\partial y}\frac{dy}{2} \right) dx \right) \cdot \Delta t \tag{A.1}$$

Or, simply written as:

$$\frac{\partial J_x}{\partial x} + \frac{\partial J_y}{\partial y} = -\frac{\partial c_t}{\partial t} \tag{A.2}$$

In which,

c_t - the total chloride concentration (g of Cl/g of concrete), which is the summation of the free chloride concentration (c_f) and the bound chloride concentration (c_b)

$$c_t = c_f + c_b \tag{A.3}$$

J_x and J_y – chloride penetration flux along x and y direction respectively, in (g of chloride iron per cm^2 per day).

Considering the two transportation mechanisms involved in unsaturated concrete, the flux are composed of two parts: chloride diffusion due to the gradient of chloride concentration, and the convection induced by moisture diffusion. Expressed as:

$$J_c = \begin{Bmatrix} J_x \\ J_y \end{Bmatrix} = \begin{Bmatrix} -D_c \dfrac{\partial c_f}{\partial x} \\ -D_c \dfrac{\partial c_f}{\partial y} \end{Bmatrix} + \mu \begin{Bmatrix} c_f \cdot J_x' \\ c_f \cdot J_y' \end{Bmatrix} \tag{A.4}$$

In which,

D_c - chloride diffusion coefficient (cm^2/s);

μ - pore solution content, i.e., mass ratio of concrete to pore solution, in (g of concrete/g of pore solution);

J_x' and J_y' - moisture flux along x and y direction (g of pore water per cm^2 per s), which are mainly induced by the moisture gradients around the point.

$$\overline{J}_w = \begin{Bmatrix} J_x' \\ J_y' \end{Bmatrix} = \begin{Bmatrix} -D_h \dfrac{\partial h}{\partial x} \\ -D_h \dfrac{\partial h}{\partial y} \end{Bmatrix} \tag{A.5}$$

In which,

h - pore relative humidity;

D_h - humidity diffusion coefficient (cm²/s).

The moisture flux could also be determined by combining with mass conservation. Similar with the chloride ions, during the same infinitesimal period, the moisture would flow into the infinitesimal element through some edges and flow out the element through others. The incremental moisture quantity should be equal to the difference between the inlet moisture and the outlet moisture, and can be expressed as:

$$\begin{aligned}\Delta w \cdot dxdy = &\left(\left(J_x^{'} - \frac{\partial J_x^{'}}{\partial x}\frac{dx}{2}\right)dy + \left(J_y^{'} - \frac{\partial J_y^{'}}{\partial y}\frac{dy}{2}\right)dx\right)\cdot \Delta t \\ &-\left(\left(J_x^{'} + \frac{\partial J_x^{'}}{\partial x}\frac{dx}{2}\right)dy + \left(J_y^{'} + \frac{\partial J_y^{'}}{\partial y}\frac{dy}{2}\right)dx\right)\cdot \Delta t\end{aligned} \tag{A.6}$$

And simplified as

$$\frac{\partial J_x^{'}}{\partial x} + \frac{\partial J_y^{'}}{\partial y} = -\frac{\partial w}{\partial t} \tag{A.7}$$

In which,

w- moisture content (g of solution/g of concrete), including both evaporable water and non-evaporable water.

Subsisting Eq.(A.5) into Eq.(A.7) obtains

$$\frac{\partial w}{\partial t} = \frac{\partial w}{\partial h}\frac{\partial h}{\partial t} = div\left[D_h \cdot grad(h)\right] \tag{A.8}$$

In which, $\frac{\partial w}{\partial h}$ is concrete moisture capacity.

Subsisting Eq.(A.4) into Eq.(A.2) obtains:

$$\frac{\partial c_t}{\partial t} = \frac{\partial c_t}{\partial c_f}\frac{\partial c_f}{\partial t} = div\left[D_c \cdot grad\left(c_f\right) + \mu c_f D_h \cdot grad(h)\right] \tag{A.9}$$

In which, $\frac{dc_t}{dc_f}$ is chloride binding capacity, which reflects the relationship between the bound chloride concentration and the free chloride concentration.

Eq.(A.8) and Eq.(A.9) are the basic equations for moisture and chloride transportation, by which the main required variables h and c_f could be solved, if the boundary and initial conditions are known. D_h,D_c, $\frac{\partial w}{\partial h}$,and $\frac{\partial c_t}{\partial c_f}$ are the main coefficients. In the following sections, the four coefficients will be discussed in detail.

A.2 Determination of Main Coefficients

To solve the unknown variables h and c_f from Eq.(A.8) and Eq.(A.9), four main coefficients have to be predetermined. However, the four coefficients are not constant which is purely defined by material, but also dependent on the two variables, which causes the equations heavily nonlinear to solve. In order to simplify the solution, the values of h and c_f obtained from the previous time step are used to determine the four coefficients, and then use the coefficients to solve the equation and obtain new values of h and c_f for current time step, which should be sufficiently accurate when the time step is small enough.

Strictly speaking, the four coefficients might be different for different specimens and should be determined with corresponding lab experiments. However, due to the time limitation, a factorial approach was adopted based on existing theory or empirical formula.

Chloride diffusion coefficient, D_c

Diffusivity of chloride is complex material property which is not only influenced by the concrete composition and curing conditions but also varies with the relative humidity and free chloride concentration. It could be modelled as a multi-factor function [159]:

$$D_c = f_1(w/c, t_0) f_2(g_i) f_3(h) f_4(T) f_5(c_f) \tag{A.10}$$

where f_1 is the effect of water cement ratio (w/c) and curing time [t_0] [160]:

$$f_1(w/c, t_0) = \frac{28 - t_0}{62500} + \left[\frac{1}{4} + \frac{28 - t_0}{300}\right]\left(\frac{w}{c}\right)^{6.55} \tag{A.11}$$

f_2 is the effect of concrete composition of aggregate and cement paste [159]:

$$f_2(g_i) = D_{c,cp}\left(1 + \frac{g_i}{[1 - g_i]/3 + 1/[D_{c,agg}/D_{c,cp} - 1]}\right) \tag{A.12}$$

in which

g_i - the volume fraction of aggregates of the concrete;

$D_{c,agg}$ and $D_{c,cp}$ - chloride diffusion coefficient of aggregate and cement paste respectively .

f_3 is the effect of pore relative humidity in concrete [161]:

$$f_3(h)=\left[1+\left(\frac{1-h}{1-h_c}\right)^4\right]^{-1} \tag{A.13}$$

in which,

h_c - critical humidity at which the diffusion coefficient drops halfway between its maximum and minimum values (h_c=0.75)

f_4 is the effect of temperature. According to Arrhenius' law:

$$f_4(T)=\exp\left[\frac{U}{8.314}\left(\frac{1}{296}-\frac{1}{T}\right)\right] \tag{A.14}$$

where, U is activation energy.

f_5 is the effect of free chloride concentration [160]:

$$f_5(c_f)=1-8.33(c_f)^{0.5} \tag{A.15}$$

Applying the empirical formula to the specimens and condition which the study uses, the diffusion coefficient of chloride penetration could be obtained, as shown in Figure A-2 and Figure A-3.

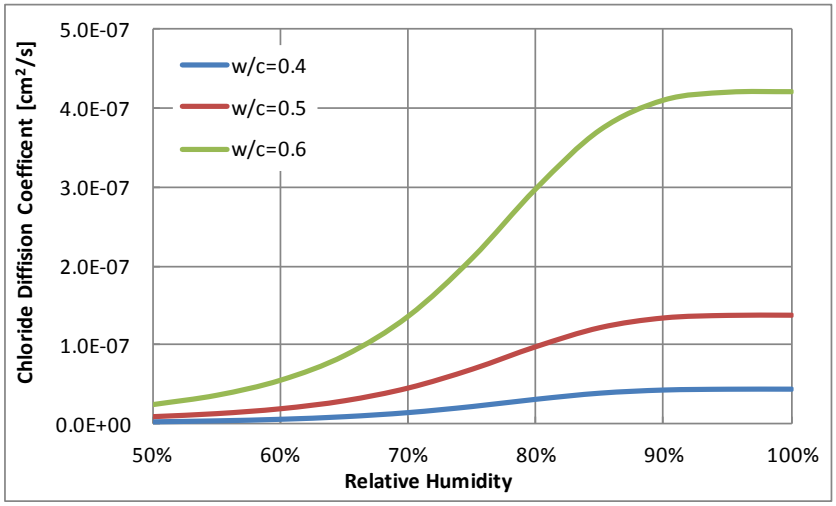

(a) CEM I, g_i=0.70

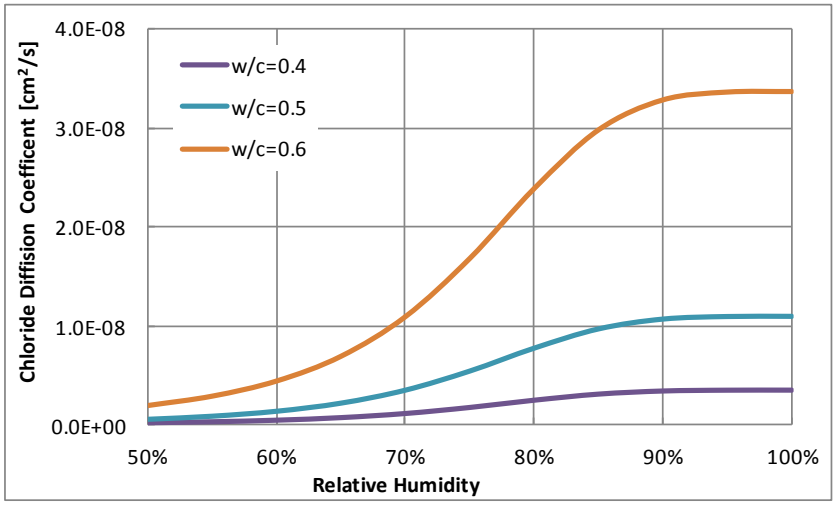

(b) CEM III, g_i=0.70

Figure A-2: Effect of w/c ratio and relative humidity on chloride diffusion coefficient

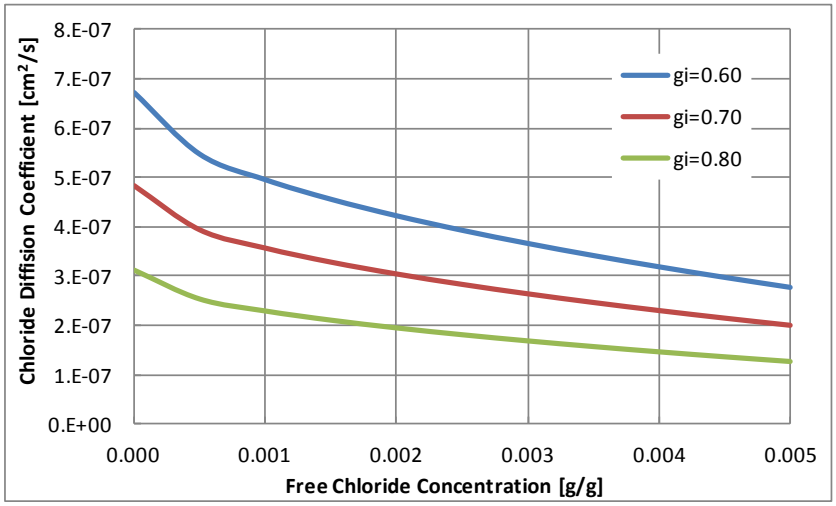

(a) CEM I, w/c=0.5

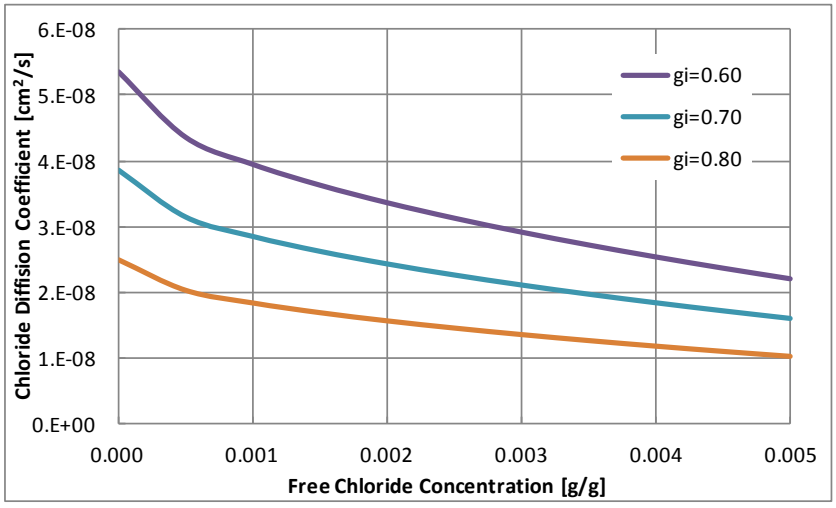

(b) CEM III, w/c=0.5

Figure A-3: Effect of aggregate volume fraction and free chloride concentration on chloride diffusion coefficient

Chloride binding capacity, $\frac{\partial c_t}{\partial c_f}$

Only the chlorides dissolved in the pore solution, i.e. the free chlorides can move freely through the concrete cover and hence responsible for depassivation of the embedded reinforcement. When chloride penetrates from environment into concrete, part of them will be bound by the porous cement matrix either by chemical reaction or by physical adsorption. The relationship between total chloride and free chloride could be described by binding isotherm. In this study, the Freundlich binding isotherm developed by Tang and Nilsson [153] is adopted. The Freundlich binding isotherm is found to fit the data very well when free

chloride concentrations ranges of from 0.10 to 1 mol/L, which covers the most important range orders of free chloride concentration in sea water.

$$\log(c_b) = A\log(c_f) + B \quad \text{or} \quad c_b = (c_f)^A 10^B \tag{A.16}$$

In which

c_b - bound chloride concentration in milligram of Cl per gram of C-S-H;

c_f - free chloride concentration in moles per liter of pore solution, [mole/l].

Parameters A and B are purely empirical coefficients from a non-linear regression. No physical meaning can be drawn from them. Their values depend on concrete compositions. However, the experimental results been reported are rare.

In Eq.(A.16), c_b and c_f use different units of chloride concentrations. In order to unify the units, a series of parameters have to be introduced:

$$c_b = \frac{f_b \cdot \beta_{C-S-H}}{1000}\left(\frac{c_f}{35.45\beta_{sol}}\right)^{\beta} \tag{A.17}$$

In which

β_{sol} - the ratio of pore solution to concrete, in litters of pore solution per gram of concrete [L/g]

$$\beta_{sol} = \frac{V_{sol}}{w_{conc}} = \frac{w_{sol}}{\rho_{sol} w_{conc}} = \frac{n(h)}{\rho_{sol}} \tag{A.18}$$

where

ρ_{sol} - density of solution [g/l], which is simply taken as water density [1000g/l];

V_{sol} - the volume of solution;

w_{sol} - weight of solution;

w_{conc} - weight of concrete.

The ratio between w_{sol} and w_{conc} depends on the relative humidity in concrete$n(h)$.

Considering concrete is a two-phases composite material which is composed by aggregate and cement paste, the function n(h) could be written as:

$$n(h) = f_{agg} \cdot n_{agg}(h) + f_{cp} \cdot n_{cp}(h) \tag{A.19}$$

where

f_{agg} and f_{cp} - weight fraction of aggregate and cement paste;

β_{C-S-H} - the weight ratio of $C-S-H$ gel to concrete [g/g].

$$\beta_{C-S-H} = \frac{w_{C-S-H}}{w_{conc}} = \frac{w_{C-S-H}/w_{cp}}{w_{conc}/w_{cp}} \approx \alpha\left(1-f_{agg}\right) \tag{A.20}$$

where

w_{C-S-H} and w_{cp} - weight of C-S-H gel and cement paste respectively in [g];

α - the degree of hydration of the cement.

Table A-1: Calculated binding constants f_b and β

Cement type	f_b	β
100% OPC	3.57	0.38
30% Slag+70% OPC	3.82	0.37
50% Slag+50% OPC	5.87	0.29
30% Flyash+70% OPC	5.73	0.29

Freundlich isotherm fits well only when c_f is large. When c_f is under a certain value, Langmuir isotherm fits better than Freundlich isotherm.

$$\frac{1}{C_b} = \frac{1000}{\beta_{C-S-H}} \frac{35.45\beta_{sol}}{k^{'}C_{bm}} \frac{1}{C_f} + \frac{1}{C_{bm}} \tag{A.21}$$

where

$k^{'}$ - adsorption constant;

C_{bm} - bound chloride content at saturated monolayer adsorption.

When C_f approaches zero, binding capacity $\frac{dC_f}{dC_t}$ approaches $\frac{1}{1+\frac{k^{'}C_{bm}\beta_{C-S-H}}{35450\beta_{sol}}}$ .Tang and Nilsson [153] reported the value of the parameters: $k^{'}=75.841$, and $C_{bm}=5.4083$.

Therefore a piecewise function is adopted for binding capacity:

$$\frac{\partial c_f}{\partial c_t} = \begin{cases} \dfrac{1}{1+\dfrac{\beta_{C-S-H}}{86.4\beta_{sol}}} & c_f \le 2\times10^{-6} \\ \dfrac{1}{1+\dfrac{f_a\cdot\beta\cdot\beta_{C-S-H}}{35450\beta_{sol}}\left(\dfrac{c_f}{\beta_{sol}}\right)^{\beta-1}} & c_f > 2\times10^{-6} \end{cases} \tag{A.22}$$

It is applied to the specimens in this study as illustrated in Figure A-4.

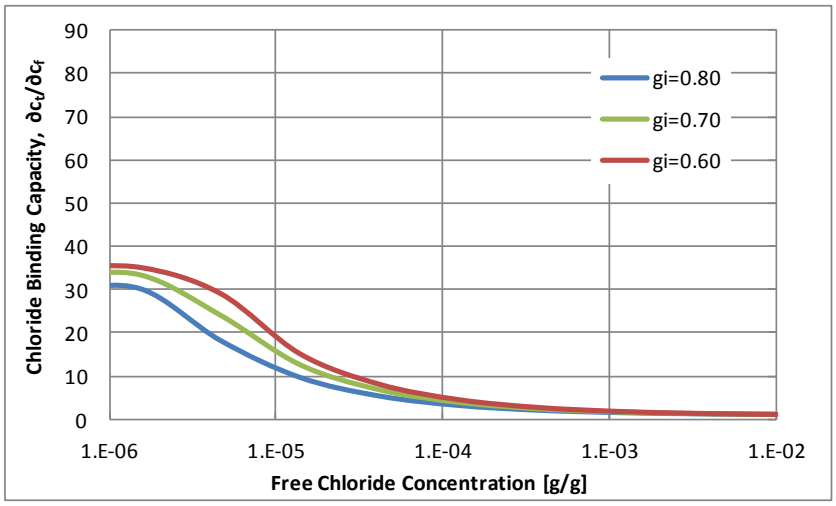

(a) CEM I, w/c=0.5

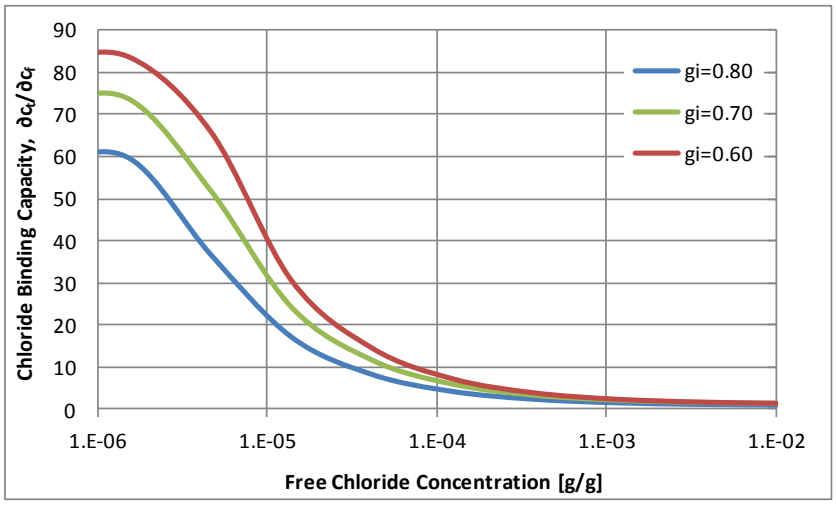

(b) CEM III, w/c=0.5

Figure A-4: Effect of aggregate volume fraction and free chloride concentration on chloride binding capacity

Diffusivity of relative humidity, D_h

The effective diffusion coefficient of relative humidity is also a complex parameter which is influenced by many factors. It could be represented by a two-phase model [159]:

$$D_h = D_{h,\,cp}\left(1+\frac{g_i}{\left[1-g_i\right]/3+1/\left[D_{h,\,agg}/D_{h,\,cp}-1\right]}\right) \tag{A.23}$$

in which,

$D_{h,cp}$and $D_{h,agg}$ - the diffusion coefficient of humidity of the cement paste and aggregate respectively, in [cm^2/s].

The moisture diffusion coefficient of aggregate is taken as zero since the pore structure of aggregate is quite un-connective and dense compared to cement paste.

The diffusion coefficient of cement paste $D_{h,cp}$ could be empirically estimated [102, 103] as

$$D_{h,\,cp} = \alpha_h + \beta_h\left[1-2^{-10^{\gamma h(h-1)}}\right] \tag{A.24}$$

The humidity diffusivity coefficient of the specimens in this study is illustrated in Figure A-5 and Figure A-6.

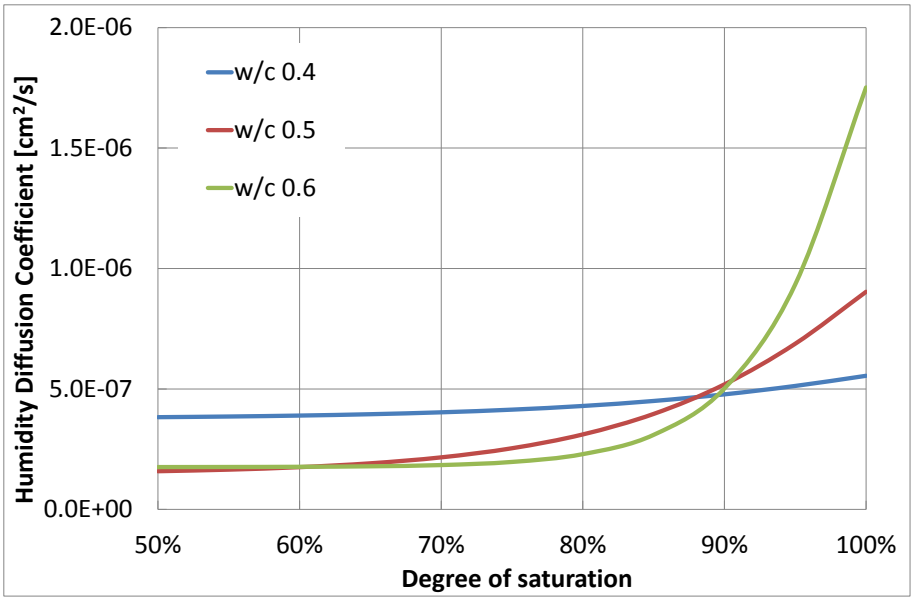

Figure A-5: Effect of water cement ratio and relative humidity on humidity diffusion coefficient, CEMI

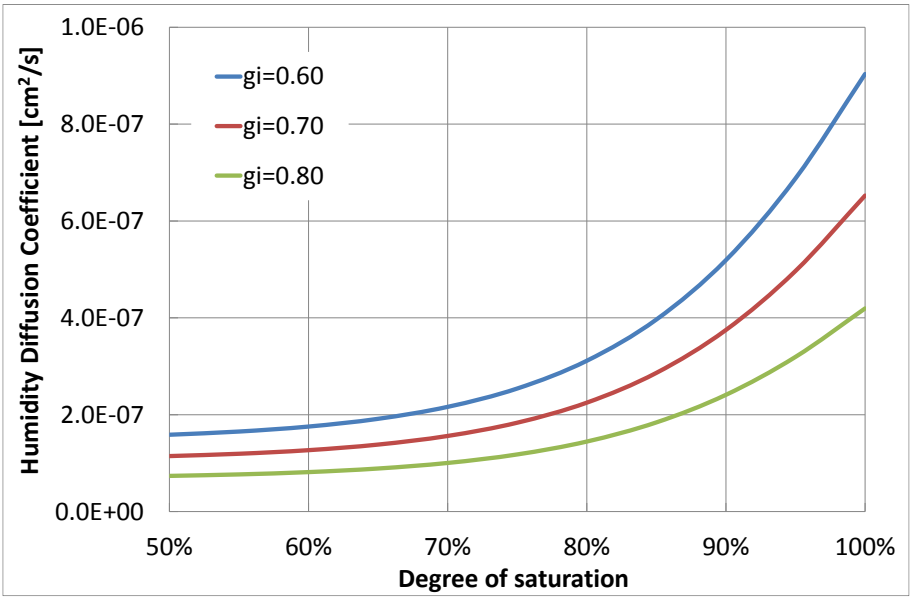

Figure A-6: Effect of aggregate volume fraction and relativity humidity on humidity diffusivity coefficient, CEMI

Moisture capacity, $\frac{\partial w}{\partial h}$

Moisture capacity could be modelled as two-phase:

$$\frac{\partial w}{\partial h} = f_{agg}\left(\frac{\partial w}{\partial h}\right)_{agg} + f_{cp}\left(\frac{\partial w}{\partial h}\right)_{cp} \tag{A.25}$$

in which

$\left(\frac{\partial w}{\partial h}\right)_{agg}$ and $\left(\frac{\partial w}{\partial h}\right)_{cp}$ - the moisture capacity of aggregate and cement paste respectively, which could be determined with the model developed by Xi, *et al* [102, 103] and Xi [100, 101], and is illustrated in Figure A-7 and Figure A-8.

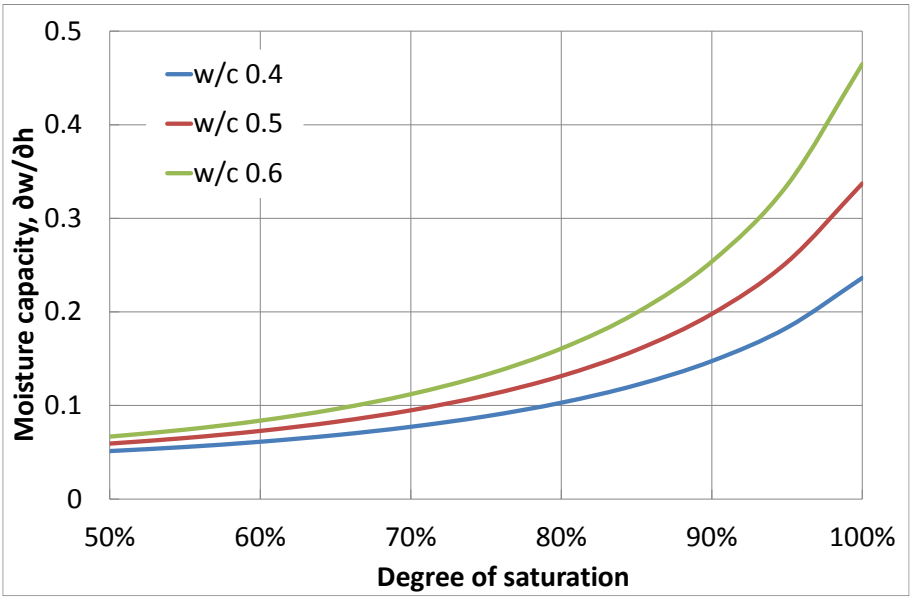

(a) CEM I

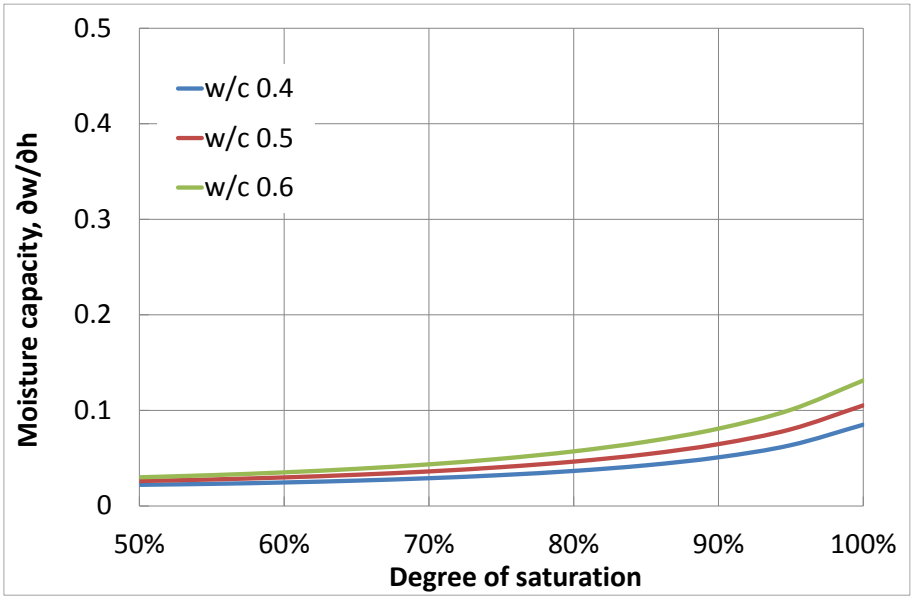

(b) CEM III

Figure A-7: Effect of water cement ratio and relativity humidity on moisture capacity

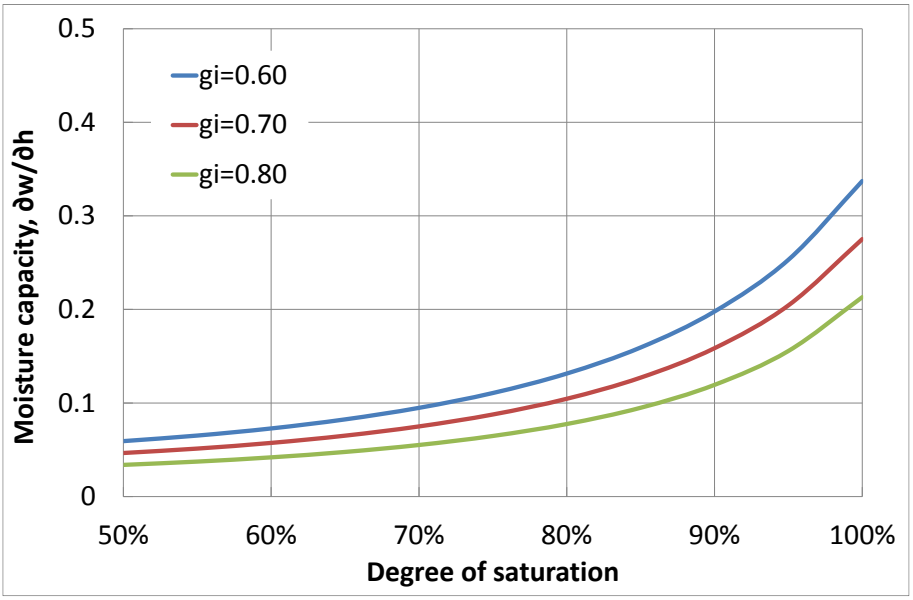

(a) CEM I

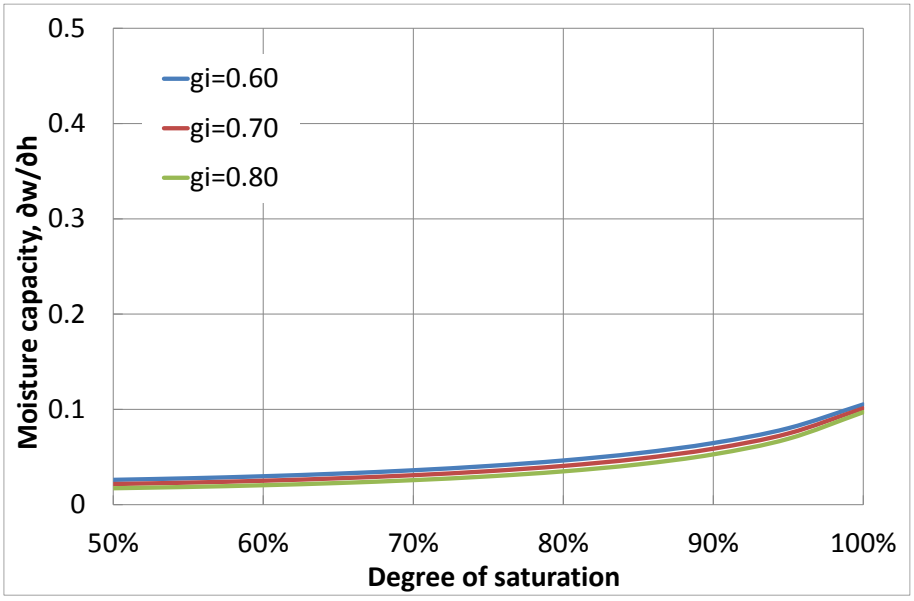

(b) CEM III

Figure A-8: Effect of aggregate volume fraction and relativity humidity on moisture capacity

Appendix B Numerical Simulation for Chloride Penetration in Unsaturated Concrete

Even with the four known coefficients obtained from the previous section, it's still very difficult to get a closed analytical solution for cracked concrete with a time-dependent boundary condition. Therefore numerical method for solving the basic equations is needed. In this study, the calculated concrete domain is simplified as a two dimensional area and finite difference method is used to solve the penetration equation at meshed points as shown in Figure 4-6 in page 109.

B.1 Alternating-direction Implicit Finite Difference Method

In order to reduce the calculation work and obtain stable results, the alternating-direction implicit (ADI) finite-difference method [162] is employed to solve the equations, which is to split the finite difference equations into two: one with the x-derivative taken implicitly and the next with the y-derivative taken implicitly. The advantage of the ADI method is that the equations that have to be solved in each step have a simpler structure and can be solved efficiently with the tridiagonal matrix algorithm.

For clear illustration, rewriting Eq.(A.8) as

$$\frac{\partial h}{\partial t}=\frac{\partial h}{\partial w}\left[D_h\frac{\partial^2 h}{\partial x^2}+\frac{\partial D_h}{\partial x}\frac{\partial h}{\partial x}+D_h\frac{\partial^2 h}{\partial y^2}+\frac{\partial D_h}{\partial y}\frac{\partial h}{\partial y}\right] \tag{B.1}$$

Applying ADI method, it can be solved using two difference equations over two successive time steps, each of duration $\Delta t/2$

$$\frac{h_{i,j}^{*}-h_{i,j}^{n}}{\Delta t/2}=\left(\frac{\partial h}{\partial w}\right)_{i,j}^{n}\times\left[\begin{array}{l} D_{i,j}^{n}\times\dfrac{h_{i+1,j}^{*}-2h_{i,j}^{*}+h_{i-1,j}^{*}}{(\Delta x)^2}+\dfrac{D_{i+1,j}^{n}-D_{i,j}^{n}}{\Delta x}\times\dfrac{h_{i+1,j}^{*}-h_{i,j}^{*}}{\Delta x} \\ +D_{i,j}^{n}\times\dfrac{h_{i,j+1}^{n}-2h_{i,j}^{n}+h_{i,j-1}^{n}}{(\Delta y)^2}+\dfrac{D_{i,j+1}^{n}-D_{i,j}^{n}}{\Delta y}\times\dfrac{h_{i,j+1}^{n}-h_{i,j}^{n}}{\Delta y} \end{array}\right] \tag{B.2}$$

$$\frac{h_{i,j}^{n+1}-h_{i,j}^{*}}{\Delta t/2}=\left(\frac{\partial h}{\partial w}\right)_{i,j}^{n}\times\left[\begin{array}{l} D_{i,j}^{n}\times\dfrac{h_{i+1,j}^{*}-2h_{i,j}^{*}+h_{i-1,j}^{*}}{(\Delta x)^{2}}+\dfrac{D_{i+1,j}^{n}-D_{i,j}^{n}}{\Delta x}\times\dfrac{h_{i+1,j}^{*}-h_{i,j}^{*}}{\Delta x} \\ +D_{i,j}^{n}\times\dfrac{h_{i,j+1}^{n+1}-2h_{i,j}^{n+1}+h_{i,j-1}^{n+1}}{(\Delta y)^{2}}+\dfrac{D_{i,j+1}^{n}-D_{i,j}^{n}}{\Delta y}\times\dfrac{h_{i,j+1}^{n+1}-h_{i,j}^{n+1}}{\Delta y} \end{array}\right] \tag{B.3}$$

Douglas [163] discussed the stability of the ADI method and pointed out that this method is unconditionally stable and the solution converges within a discretization error of $o((\Delta t)^2+(\Delta x)^2+(\Delta y)^2)$.

For computer to calculate, Eq.(B.2) and Eq.(B.3) could be written as matrix form,

$$\left[-\left(\frac{\partial h}{\partial w}\right)_{i,j}^{n}\times D_{i,j}^{n}\times\frac{\Delta t}{(\Delta x)^{2}}\quad\left(\frac{\partial h}{\partial w}\right)_{i,j}^{n}\times\left(D_{i+1,j}^{n}+D_{i,j}^{n}\right)\times\frac{\Delta t}{(\Delta x)^{2}}+2\quad-\left(\frac{\partial h}{\partial w}\right)_{i,j}^{n}\times D_{i+1,j}^{n}\times\frac{\Delta t}{(\Delta x)^{2}}\right]\begin{Bmatrix}h_{i-1,j}^{*}\\h_{i,j}^{*}\\h_{i+1,j}^{*}\end{Bmatrix}$$
$$=\left(\frac{\partial h}{\partial w}\right)_{i,j}^{n}\times D_{i,j}^{n}\times\frac{\Delta t}{(\Delta y)^{2}}\left(h_{i,j-1}^{n}-h_{i,j}^{n}\right)+\left(\frac{\partial h}{\partial w}\right)_{i,j}^{n}\times D_{i,j+1}^{n}\times\frac{\Delta t}{(\Delta y)^{2}}\left(h_{i,j+1}^{n}-h_{i,j}^{n}\right)+2h_{i,j}^{n} \tag{B.4}$$

and

$$\left[-\left(\frac{\partial h}{\partial w}\right)_{i,j}^{n}\times D_{i,j}^{n}\times\frac{\Delta t}{(\Delta y)^{2}}\quad\left(\frac{\partial h}{\partial w}\right)_{i,j}^{n}\times\left(D_{i,j+1}^{n}+D_{i,j}^{n}\right)\times\frac{\Delta t}{(\Delta y)^{2}}+2\quad-\left(\frac{\partial h}{\partial w}\right)_{i,j}^{n}\times D_{i,j+1}^{n}\times\frac{\Delta t}{(\Delta y)^{2}}\right]\begin{Bmatrix}h_{i,j-1}^{n+1}\\h_{i,j}^{n+1}\\h_{i,j+1}^{n+1}\end{Bmatrix}$$
$$=\left(\frac{\partial h}{\partial w}\right)_{i,j}^{n}\times D_{i,j}^{n}\times\frac{\Delta t}{(\Delta x)^{2}}\left(h_{i,j-1}^{*}-h_{i,j}^{*}\right)+\left(\frac{\partial h}{\partial w}\right)_{i,j}^{n}\times D_{i,j+1}^{n}\times\frac{\Delta t}{(\Delta x)^{2}}\left(h_{i,j+1}^{*}-h_{i,j}^{*}\right)+2h_{i,j}^{*} \tag{B.5}$$

Every point(i,j)could obtain two equations, and all these equations could be assembled as a whole equation system with unknown variable vectors $\{h^{*}\}$ and $\{h^{n+1}\}$. The coefficients are tridiagonal matrix and the equation systems can be easily solved with tridiagonal matrix algorithm.

Similarly, Eq.(A.9) can be rewritten as:

$$\frac{\partial c_f}{\partial t}=\frac{\partial c_f}{\partial c_t}\left[D_c\frac{\partial^2 c_f}{\partial x^2}+\frac{\partial D_c}{\partial x}\frac{\partial c_f}{\partial x}+D_c\frac{\partial^2 c_f}{\partial y^2}+\frac{\partial D_c}{\partial y}\frac{\partial c_f}{\partial y}+\mu c_f\frac{\partial w}{\partial t}\right] \tag{B.6}$$

Applying ADI method

$$\frac{c_{i,j}^{*}-c_{i,j}^{n}}{\Delta t/2}=\left(\frac{\partial c_f}{\partial c_t}\right)_{i,j}^{n}\times\left[\begin{array}{l} D_{i,j}^{n}\times\dfrac{c_{i+1,j}^{*}-2c_{i,j}^{*}+c_{i-1,j}^{*}}{(\Delta x)^2}+\dfrac{D_{i+1,j}^{n}-D_{i,j}^{n}}{\Delta x}\times\dfrac{c_{i+1,j}^{*}-c_{i,j}^{*}}{\Delta x}+D_{i,j}^{n}\times\dfrac{c_{i,j+1}^{n}-2c_{i,j}^{n}+c_{i,j-1}^{n}}{(\Delta y)^2} \\ +\dfrac{D_{i,j+1}^{n}-D_{i,j}^{n}}{\Delta y}\times\dfrac{c_{i,j+1}^{n}-c_{i,j}^{n}}{\Delta y}+\left(\dfrac{1}{w}\right)_{i,j}^{n}\left(\dfrac{\partial w}{\partial h}\right)_{i,j}^{n}\dfrac{h_{i,j}^{*}-h_{i,j}^{n}}{\Delta t/2} \end{array}\right] \tag{B.7}$$

$$\frac{c_{i,j}^{n+1}-c_{i,j}^{*}}{\Delta t/2}=\left(\frac{\partial c_f}{\partial c_t}\right)_{i,j}^{n}\times\left[\begin{array}{l} D_{i,j}^{n}\times\dfrac{c_{i+1,j}^{*}-2c_{i,j}^{*}+c_{i-1,j}^{*}}{(\Delta x)^2}+\dfrac{D_{i+1,j}^{n}-D_{i,j}^{n}}{\Delta x}\times\dfrac{c_{i+1,j}^{*}-c_{i,j}^{*}}{\Delta x}+D_{i,j}^{n}\times\dfrac{c_{i,j+1}^{n+1}-2c_{i,j}^{n+1}+c_{i,j-1}^{n+1}}{(\Delta y)^2} \\ +\dfrac{D_{i,j+1}^{n}-D_{i,j}^{n}}{\Delta y}\times\dfrac{c_{i,j+1}^{n+1}-c_{i,j}^{n+1}}{\Delta y}+\left(\dfrac{1}{w}\right)_{i,j}^{n}\left(\dfrac{\partial w}{\partial h}\right)_{i,j}^{n}\dfrac{h_{i,j}^{n+1}-h_{i,j}^{*}}{\Delta t/2} \end{array}\right] \tag{B.8}$$

Then

$$\begin{aligned} &\left[-\left(\frac{\partial c_f}{\partial c_t}\right)_{i,j}^{n}\times D_{i,j}^{n}\times\frac{\Delta t}{(\Delta x)^2}\quad\left(\frac{\partial c_f}{\partial c_t}\right)_{i,j}^{n}\times\left(D_{i+1,j}^{n}+D_{i,j}^{n}\right)\times\frac{\Delta t}{(\Delta x)^2}+2\quad-\left(\frac{\partial c_f}{\partial c_t}\right)_{i,j}^{n}\times D_{i+1,j}^{n}\times\frac{\Delta t}{(\Delta x)^2}\right]\begin{Bmatrix} c_{i-1,j}^{*} \\ c_{i,j}^{*} \\ c_{i+1,j}^{*}\end{Bmatrix} \\ &=\left(\frac{\partial c_f}{\partial c_t}\right)_{i,j}^{n}\times D_{i,j}^{n}\times\frac{\Delta t}{(\Delta y)^2}\left(c_{i,j-1}^{n}-c_{i,j}^{n}\right)+\left(\frac{\partial c_f}{\partial c_t}\right)_{i,j}^{n}\times D_{i,j+1}^{n}\times\frac{\Delta t}{(\Delta y)^2}\left(c_{i,j+1}^{n}-c_{i,j}^{n}\right) \\ &+2c_{i,j}^{n}+2\left(\frac{\partial c_f}{\partial c_t}\right)_{i,j}^{n}\left(\frac{1}{w}\right)_{i,j}^{n}\left(\frac{\partial w}{\partial h}\right)_{i,j}^{n}\left(h_{i,j}^{*}-h_{i,j}^{n}\right) \end{aligned} \tag{B.9}$$

$$\begin{aligned} &\left[-\left(\frac{\partial c_f}{\partial c_t}\right)_{i,j}^{n}\times D_{i,j}^{n}\times\frac{\Delta t}{(\Delta y)^2}\quad\left(\frac{\partial c_f}{\partial c_t}\right)_{i,j}^{n}\times\left(D_{i,j+1}^{n}+D_{i,j}^{n}\right)\times\frac{\Delta t}{(\Delta y)^2}+2\quad-\left(\frac{\partial c_f}{\partial c_t}\right)_{i,j}^{n}\times D_{i,j+1}^{n}\times\frac{\Delta t}{(\Delta y)^2}\right]\begin{Bmatrix} c_{i,j-1}^{n+1} \\ c_{i,j}^{n+1} \\ c_{i,j+1}^{n+1}\end{Bmatrix} \\ &=\left(\frac{\partial c_f}{\partial c_t}\right)_{i,j}^{n}\times D_{i,j}^{n}\times\frac{\Delta t}{(\Delta x)^2}\left(c_{i,j-1}^{*}-c_{i,j}^{*}\right)+\left(\frac{\partial c_f}{\partial c_t}\right)_{i,j}^{n}\times D_{i,j+1}^{n}\times\frac{\Delta t}{(\Delta x)^2}\left(c_{i,j+1}^{*}-c_{i,j}^{*}\right)+2c_{i,j}^{*} \\ &+2c_{i,j}^{n}+2\left(\frac{\partial c_f}{\partial c_t}\right)_{i,j}^{n}\left(\frac{1}{w}\right)_{i,j}^{n}\left(\frac{\partial w}{\partial h}\right)_{i,j}^{n}\left(h_{i,j}^{n+1}-h_{i,j}^{*}\right) \end{aligned} \tag{B.10}$$

B.2 Implementation of the Calculation with Program

In this study, the chloride penetration theory and alternating-direction implicit finite element method are implemented with FORTRAN program CPUCC (Chloride Penetration in Unsaturated Cracked Concrete). The whole program includes four functional parts as following:

1) Read Necessary Information from INP File

In this part, the program reads the calculation information from an '.inp' file and allocates the calculation matrixes. The .inp file includes five records:

The first record is to control calculation size, includes (1) number of nodes along x direction, (2) number of nodes along y direction, and (3) number of time steps. With this information, the program could allocate the calculation matrixes.

The second record is to define the geometry of the calculation model, includes (4) node space along x-direction (unit: cm), (5) node space along y-direction (unit: cm), (6) width of half crack, (7) time length per step (unit: day). In this study, the chloride penetrates mainly along y direction, so the meshed nodes along y-direction are denser than it in x-direction. 0.1 cm node space along x-direction and 0.05 cm node space along y direction are adopted. Theoretically, the time step should be infinitesimal for accurate solution, but it's practically difficult to achieve. After trying several different time steps, it's found that stable results could be obtained when the time step is shorter than 0.0003 days. Therefore, time step of 0.0001 days is adopted. The geometry size and penetration period are defined by the first and second records.

The third record is to define the concrete properties, includes (8) cement type, (9) water cement ratio, (10) cement mass fraction, (11) aggregate mass fraction, (12) curing time (unit: day), (13) initial relative humidity, (14) initial free chloride density (g of chloride ions/ g of concrete), and (15) environmental temperature (unit: K). These information is used to determine the four main coefficients described in section 4.3.

The fourth record is (16) surface chloride density, i.e., the chloride density in crack solution (g of Cl ions/ g of solution).

The fifth record is for boundary condition, including relative humidity and free chloride concentration along all edges.

After reading all the information and allocate the calculation matrixes, the initial relative humidity and free chloride concentration of the specimen are used to define the matrixes value as the previous humidity and free chloride concentration for the first step calculation.

With the initial values as the beginning, the program will go through the following four parts iteratively for each time step until the time step number arrives at the required one.

2) Determine Coefficients of Penetration at Each Node

The concrete properties and the relative humidity and free chloride concentration obtained from initial value of previous step calculation are used to determine the four main coefficients at all nodes with the formula provided in Section 4.3.

3) Form Coefficients Matrix and Solve Equation Systems

For each row of nodes, Eq.(B.4) is developed at every node to form a tri-diagonal equation system. The equation system, combined with the boundary conditions at right and left edge, could be solved with matrix chase-after method to obtain a temporary vector$\{h^*\}$ for the corresponding row node. Repeating this process for all rows of node could obtain the value of h^* for all nodes. Using the same method to Eq.(B.9) could obtain the value of c^* for all nodes. Then, with each column of node, it's to solve h^{n+1} and c_f^{n+1} with Eq.(B.5) and Eq.(B.10) for all nodes.

In Eq.(A.22), using $\Delta c_f = c_f^{n+1} - c_f^n$ could obtain c_t^{n+1}, the total chloride concentration in each point.

4) Output Simulation Results

Output of the relative humidity, free chloride concentration and total chloride concentration at all nodes in all time steps is possible. Meanwhile, the chloride diffusion coefficient and moisture diffusion coefficient at any time and any location could be obtained as well.

Part 2, part 3 and part 4 consist of a time step, after which the newly obtained h^{n+1} and c_f^{n+1} could be used for next time step calculation.

(Blank Page)

Appendix C Test Data of Individual Sample for Water Evaporation Test

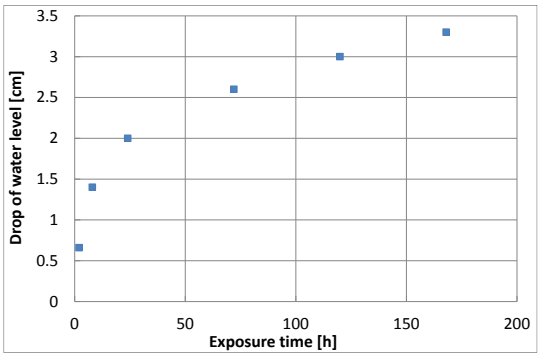

(a) I05360 A

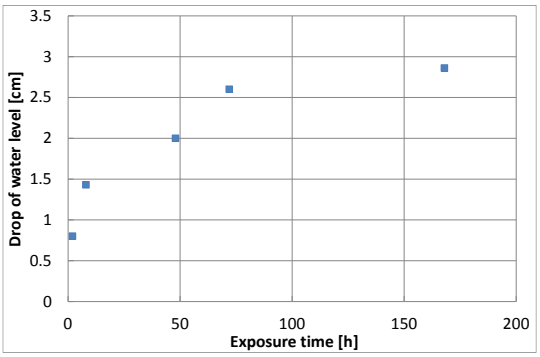

(b) I05360 B

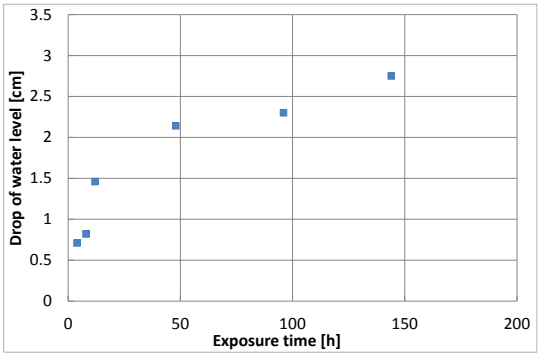

(c) III05360 A

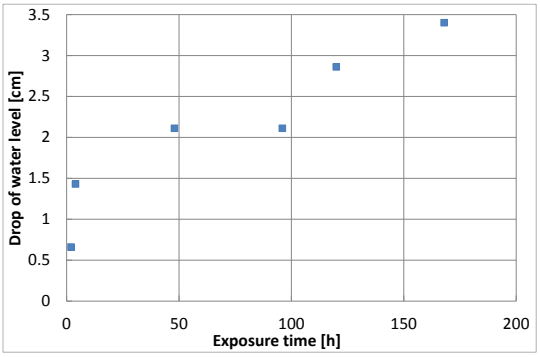

(d) III05360 B

Figure C-1: Water evaporation rate of individual specimens.

(Blank Page)

Appendix D Simulation Results of Chloride Diffusion for III05360

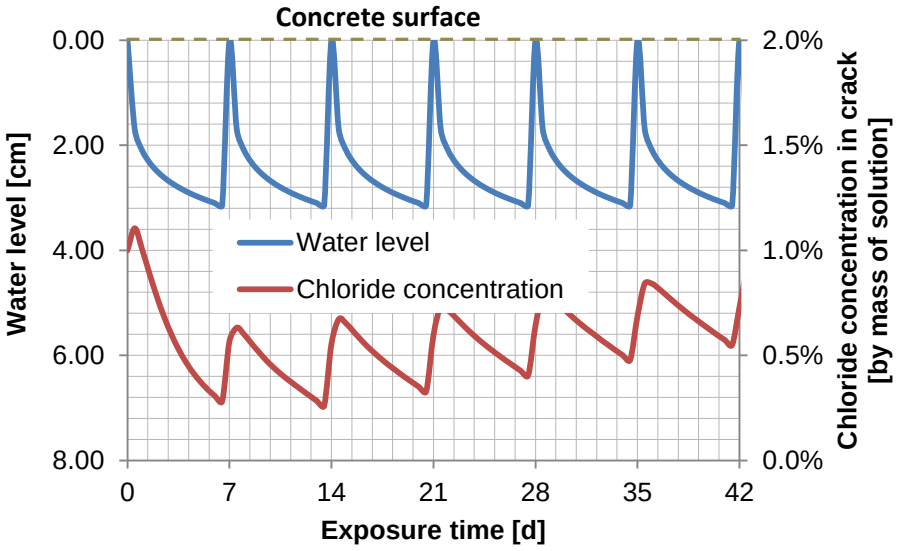

Figure D-1: Variation of water level and chloride concentration in crack solution with time, III05360.

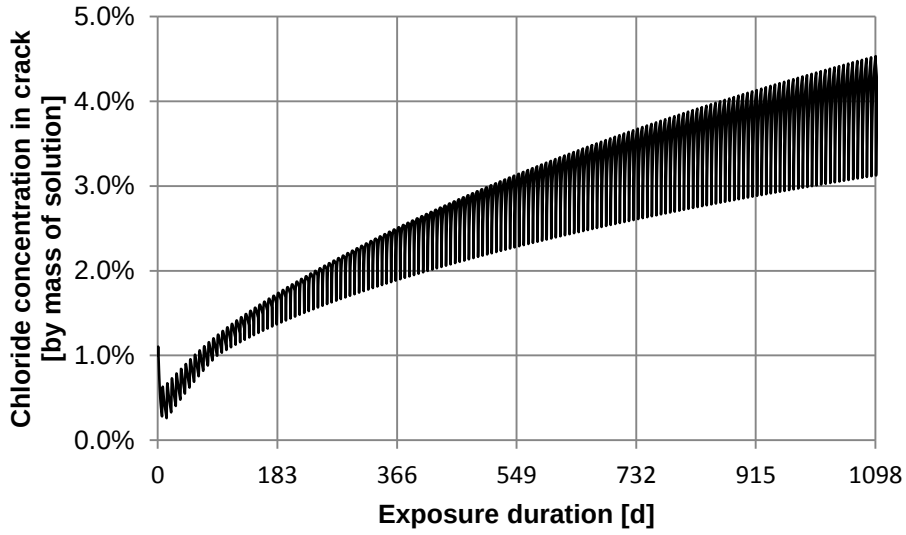

Figure D-2: Variation of chloride concentration in crack solution within 3 years exposure duration, III05360.

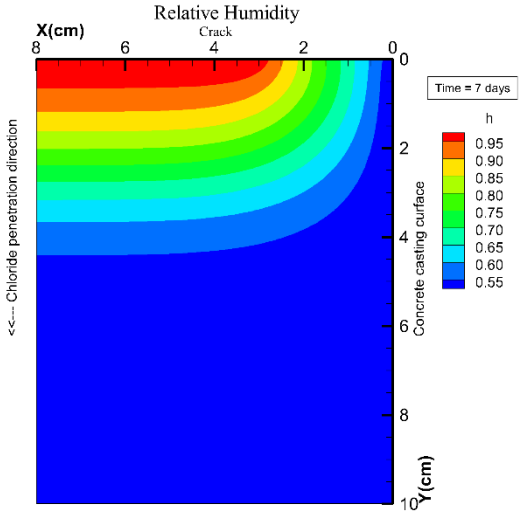

(a) 1 week

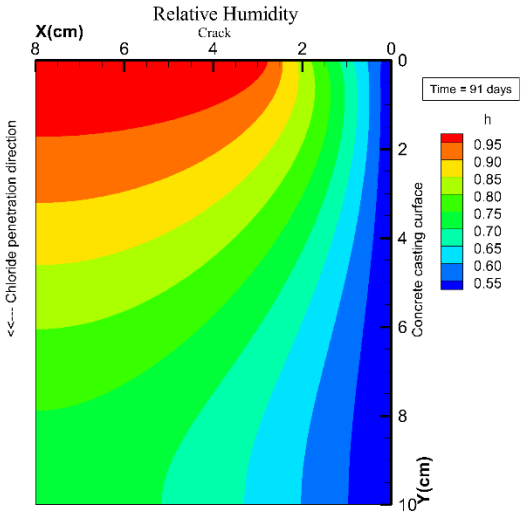

(b) 3 months

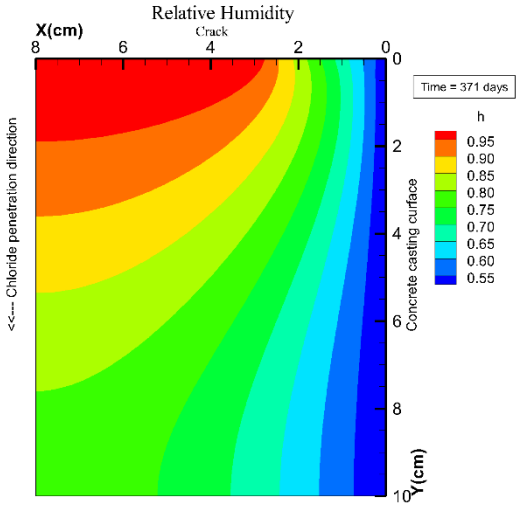

(c) 1 year

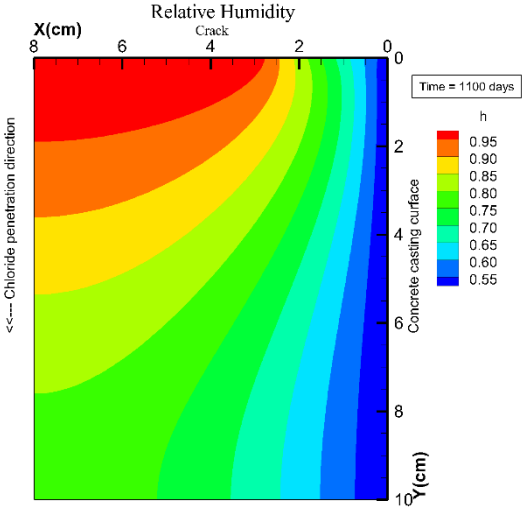

(d) 3 years

Figure D-3: Contour plots of pore RH, III05360.

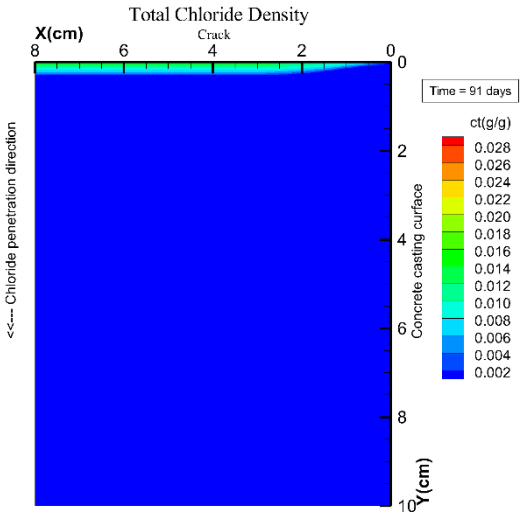

(a) 3 months

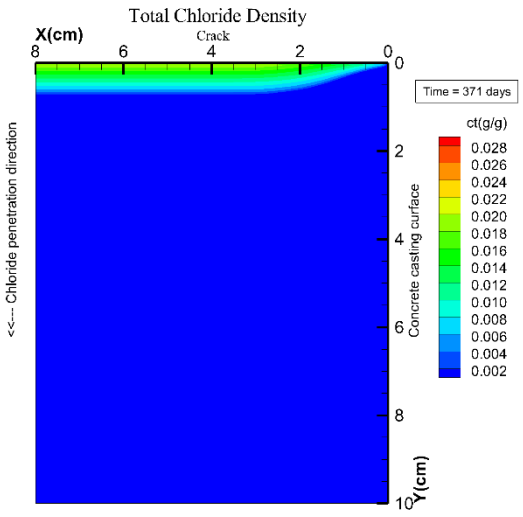

(b) 1 year

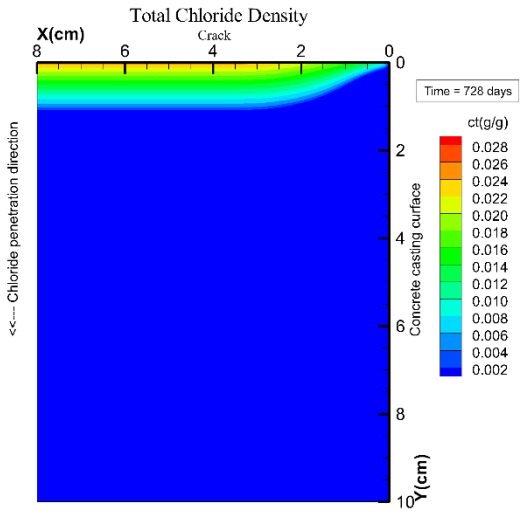

(c) 2 years

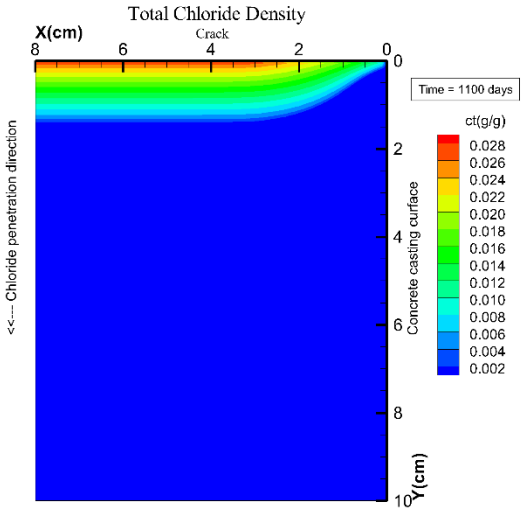

(d) 3 years

Figure D-4: Contour plots of total chloride concentration C_t, III05360, [g Cl^-/g cement]

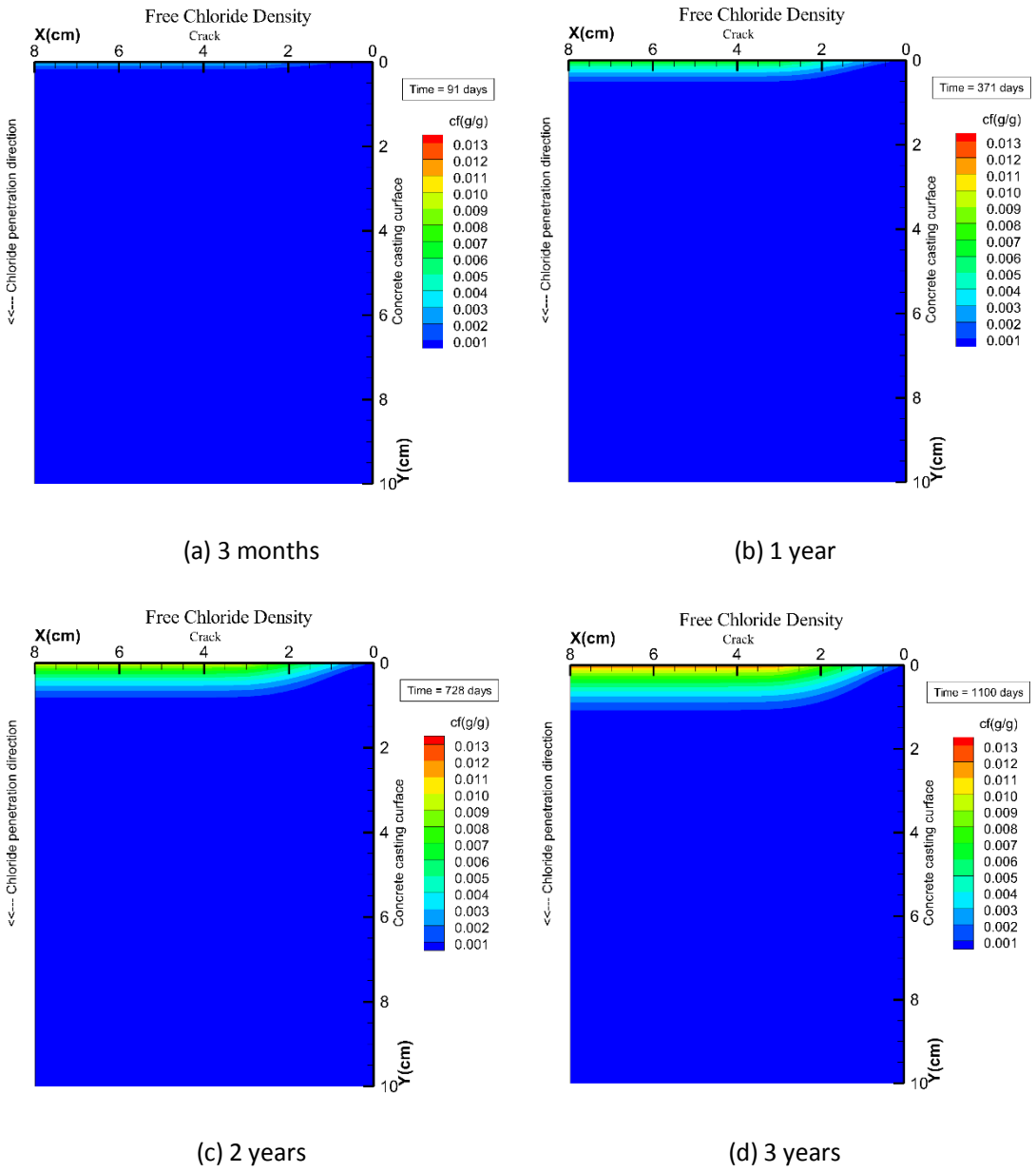

Figure D-5: Contour plots of free chloride concentration C_f , III05360, [g Cl^-/g cement]

Appendix E Fundamentals on FEM Modeling

Numerical modelling of reinforcement corrosion in concrete involves solving Laplace's equation for electrical potentials with required boundary conditions and thereby calculating current density on the steel surface using these potentials. An implementation of this process can be found in reference [164].

Macro-cell corrosion occurs at the interface between steel bar and concrete. However, corrosion simulation is studied by simulating of electrical field in bulk concrete based on electrical conservation and Ohm's law.

As shown in Figure E-1, at any point in the concrete field, applying the principle of current conservation to the surrounding infinitesimal volume that the inlet charge equals to the outlet charge, results in:

$$i_x dydz + i_y dzdx + i_z dxdy = \left(i_x + \frac{\partial i_x}{\partial x}dx\right)dydz + \left(i_y + \frac{\partial i_y}{\partial y}dy\right)dzdx + \left(i_z + \frac{\partial i_z}{\partial z}dz\right)dxdy \qquad (E.1)$$

Simplified as

$$\frac{\partial i_x}{\partial x} + \frac{\partial i_y}{\partial y} + \frac{\partial i_z}{\partial z} = 0 \qquad (E.2)$$

This is the equilibrium equation for electrical current.

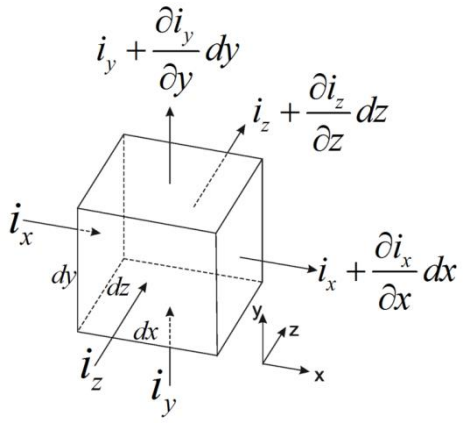

Figure E-1: Schema of element

According to Ohm's law, at this point, the electric current density in each direction can be expressed as

$$\vec{i}=\begin{Bmatrix} i_x \\ i_y \\ i_z \end{Bmatrix}=\begin{Bmatrix} k_x \dfrac{\partial \phi}{\partial x} \\ k_y \dfrac{\partial \phi}{\partial y} \\ k_z \dfrac{\partial \phi}{\partial z} \end{Bmatrix} \tag{E.3}$$

In which

$\phi(x,y,z)$ - the electrical potential;

k_x, k_y, k_z - the concrete electric conductivities along x, y, z directions which are assumed to be identical in this study:

$$k_x = k_y = k_z = k \tag{E.4}$$

Substituting Eq.(E.3) into Eq.(E.2) obtains:

$$k\nabla^2\phi = k\left(\frac{\partial^2\phi}{\partial x^2}+\frac{\partial^2\phi}{\partial y^2}+\frac{\partial^2\phi}{\partial z^2}\right)=0 \tag{E.5}$$

This is the Laplace equation which is steady-state electrical conduct equation and should be satisfied in the whole domain of the electrical field.

The corresponding boundary conditions of the calculating electrical field could be generally expressed as:

$$\begin{aligned} \phi &= \bar{\phi} && \text{at} \quad S_\phi \\ k\frac{\partial \phi_x}{\partial x}n_x + k\frac{\partial \phi_y}{\partial y}n_y + k\frac{\partial \phi_z}{\partial z}n_z &= \bar{i}_n && \text{at} \quad S_i \end{aligned} \tag{E.6}$$

S_ϕ - the partial boundary with constant electrical potential, $\bar{\phi}$;

S_i - the other parts of boundary through which the electrical current density is fixed as $\bar{i}_n$. Usually, there is no union sets between S_ϕ and S_i while their unit set should cover all the boundary of the electrical field.

A closed solution for Eq.(E.5) could be found only with some specified geometry domain and simple boundary condition. For most cases, however, it's very difficult, if possible, to solve Eq.(E.5) directly. Therefore, numerical methods have been developed to solve Eq.(E.5) for general geometry and boundary conditions, such as boundary element method (BEM), finite difference method (FDM) and finite element method (FEM).

In BEM only the interfaces that involved in the problem are considered. In FEM, also the bulk phase of the concrete and if desired also the steel can be modelled. Therefore with FEM all three aspects: interfacial properties, transport though and changes of the concrete and the geometrical design can be accounted for. This constitutes the drawback of BEM compared to FEM: bulk properties cannot be modelled explicitly but can only be taken into account implicitly at best [134, 165]. The drawback of FEM, however, is that the numerical size of the model can become impractically large for practical situations [166].

In Issue 8 Volume 57 of Materials and Corrosion (August, 2006), different aspects of modelling steel corrosion in concrete along with a number of numerical and empirical implementations of the process have been discussed in detail by a number of researchers [17, 129, 134, 167].In this study, FEM is employed to solve Eq.(E.5) and simulate the electrical conduct in the concrete field.

Firstly, a weak form equation of Eq.(E.5) and boundary condition Eq.(E.6) is developed based on weighted residual method. The essence of this method, which is an optimization process, is the multiplication of weighting functions w_i to the governing differential Eq.(E.5) and minimizing the errors thus obtained over the volume of the element while satisfying the essential boundary conditions. The resulting integral for the element equilibrium can be written as

$$\iiint_V \left(w_j k \nabla^2 \phi \right) dV = 0 \tag{E.7}$$

Based on the theory of partial integration and Green function, Eq.(E.5) could be divided as

$$\iint_S w_j k \nabla \phi dS - \iiint_V \left(\nabla w_j k \nabla \phi \right) dV = 0 \tag{E.8}$$

Combining with the boundary conditions Eq.(E.6), Eq.(E.8) could be rewritten as

$$\iiint_V \left(\nabla w_j k \nabla \phi \right) dV = \iint_{S_i} w_j \bar{i}_n dS \tag{E.9}$$

As to the actual problem with complicated simulation domain, it's still difficult or impossible to satisfy Eq.(E.9) in the entire domain. Finite element method is employed to divide the entire domain into small elements with simple geometry and require the electrical potential to satisfy Eq.(E.9) in each element. In the element, the electrical potential and its gradient at any point could be interpolated with the corresponding values at the nodes:

$$\phi = \sum N_j \phi_j = [N]\{\phi_m\} \tag{E.10}$$

and

$$\nabla\phi = [\nabla N]\{\phi_m\} \tag{E.11}$$

In this study, eight-node hexahedral element is adopted to discrete the whole calculation domain field, as shown in Figure E-2. Each element has eight interpolation functions, named as shape function:

$$[N] = [N_1 \quad N_2 \quad N_3 \quad N_4 \quad N_5 \quad N_6 \quad N_7 \quad N_8] \tag{E.12}$$

In which

$$\begin{aligned}
N_1 &= \left(1-\frac{x}{a}\right)\left(1-\frac{y}{b}\right)\left(1-\frac{z}{c}\right) & N_5 &= \left(1-\frac{x}{a}\right)\frac{y}{b}\left(1-\frac{z}{c}\right) \\
N_2 &= \left(1-\frac{x}{a}\right)\left(1-\frac{y}{b}\right) & N_6 &= \left(1-\frac{x}{a}\right)\frac{y}{b}\frac{z}{c} \\
N_3 &= \frac{x}{a}\left(1-\frac{y}{b}\right)\frac{z}{c} & N_7 &= \frac{x}{a}\frac{y}{b}\frac{z}{c} \\
N_4 &= \frac{x}{a}\left(1-\frac{y}{b}\right)\left(1-\frac{z}{c}\right) & N_8 &= \frac{x}{a}\frac{y}{b}\left(1-\frac{z}{c}\right)
\end{aligned} \tag{E.13}$$

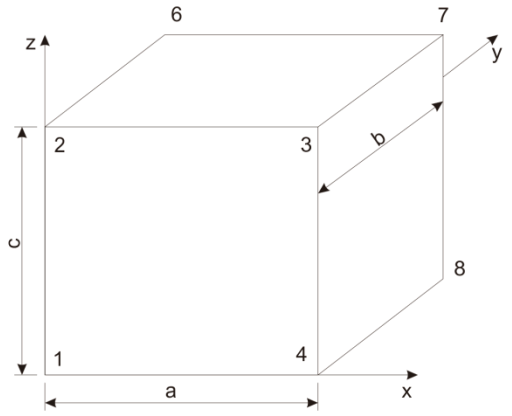

Figure E-2: Eight-node hexahedral element [168]

Substituting Eq.(E.10) and Eq.(E.11) into Eq.(E.9), obtains

$$\sum_{elem} \iiint_{V_e} \left(\nabla w_j k[\nabla N]\right) dV \{\phi_m\} = \sum_{elem} \iint_{S_{ie}} w_j \{\bar{i}_n\} dS \tag{E.14}$$

In order to solve Eq.(E.14), it is necessary to choose a suitable weighting function w_j. In this study, Galerkin's weighted residual method [169], in which the weighting function is chosen to be the same as the shape function N_j of the element, is used to obtain approximate solutions to Eq.(E.14). This leads to

$$\sum_{elem} \iiint_{V_e} \left([\nabla N]^T k[\nabla N]\right) dV \{\phi_m\} = \sum_{elem} \iint_{S_{ie}} [N]^T \{\bar{i}_n\} dS \tag{E.15}$$

It could be written as typical finite element matrix formulation

$$[K]\{\Phi\} = \{I\} \tag{E.16}$$

where $\{\Phi\}$ is the vector of electrical potential at each node, and $\{I\} = \sum_{elem} \iint_{S_{ie}} [N]^T \{\bar{i}_n\} dS$ is the vector of electric current flowing in/out at each node; $[K] = \sum_{elem} \iiint_{V_e} \left([\nabla N]^T k[\nabla N]\right) dV$ is the corresponding conductivity matrix.

Combining with suitable boundary conditions, the electrical potential at all nodes could be obtained. All other electrical characteristics, including the current density in the concrete domain and steel- concrete interface could be thereafter calculated based on the potential data.

However, in simulating the electrical conduction in concrete, the boundary conditions at the steel-concrete interface are not directly given as Eq.(E.6), like most ordinary FEM problem does, but a nonlinear relationship between the potential and current. This makes the problem special and difficult. This difficulty is solved by introducing an interface layer on steel- concrete interface, which is given in detail in section 5.2.1.

Appendix F Implementation for Program 'MCRC'

The numerical theory described in the previous section is developed to a three-dimensional finite element program, named as 'MCRC' (Macro-cell Corrosion in Reinforcement Concrete), written in FORTRAN language. MCRC could simulate corrosion of reinforcement with arbitrary geometry and/or arbitrary electrical resistance distribution. The output of this self-developed program is more flexible than other commercial FEM software.

MCRC includes three functional parts: 1) Input of model information; 2) Main calculation procedure; and 3) Results output. Each function part is described in details as follow:

The model information input

This part consists of reading the control information and boundary conditions. The control information includes the model geometry, detailed information of nodes and elements, the required precision of the calculation, the convergent tolerance and the maximum iteration number.

The boundary condition refers to the concrete resistivity field in modelling domain and the anodic and cathodic polarization curves. As a self-developed FEM program, MCRC has the advantage to deal with arbitrary distribution of electrolytic resistivity in the concrete domain which could be either linear or nonlinear varied in either single or multiple directions, or interpolated within several sub-domains. This is of fundamental importance for the simulation of corrosion in cracked concrete which is induced by cyclic chloride attack. It has been confirmed in Chapter 4 that the moisture condition in the cracked beam is non-uniform, which indicates a non-uniform concrete resistivity field. The input polarization information is composed by several series of corrosion current density-potential data for anode/cathodes.

The current version of this program only focuses on FEM calculation which, however, doesn't offer the function of generating meshes. Meshing of the model could be completed by commercial FEM software, such as ABAQUS or ANSYS. In this research, ANSYS was adopted to finish the geometry building and meshing task. MCRC only reads the mesh information from a formatted input file which is composed with nodes coordination and element composition.

The main calculation part

In this part the potential at each node is solved and assembled according to equation set Eq.(E.16). Each eight-node hexahedral element has eight Gauss integration points located at$x = a/\sqrt{3}\ or\ 2a/\sqrt{3}$, $y = b/\sqrt{3}\ or\ 2b/\sqrt{3}$, $z = c/\sqrt{3}\ or\ 2c/\sqrt{3}$. At each integration point within each element, the value of $[\nabla N]$ could be easily calculated with local coordination and the value of k could be determined with the input information according to the test data. Then the integral kernel $[\nabla N]^T k[\nabla N]$ could be determined. Applying Gauss integration method to each element, the element conductivity matrix could be integrated with the kernel value at the eight integration points:

$$[K]^e = \iiint_{V_e} \left([\nabla N]^T k[\nabla N]\right) dV = \sum_{j=1}^{8} \left([\nabla N]^T k[\nabla N]\right)_j \cdot |J|_j \cdot \alpha_j \qquad \text{(F.1)}$$

In which,

$[J]$- the Jacobi matrix for integration point transferring from global coordination to local coordination;

α - the integration weighting coefficient.

All element conductivity matrixes are assembled into the global matrix based on the node order. Each row or each column of the global matrix corresponds to one node, and the item of the global matrix is the sum of the element matrix item corresponding to the same node. Details of the element assemblies could be referred to 'programming the finite element method' by Smith and Griffiths [168].

$$[K] = \sum_{elem} [K]^e \qquad \text{(F.2)}$$

In Eq.(E.16), each node has two variables: electrical potential Φ and nodal inflow/outflow electrical current. For the internal nodes and the nodes at the concrete surface, there is no net electrical current flow in or out, which means that the corresponding item of {I} is equal to zero. However, nodes at the steel-concrete interface have two unknown variables. The two variables follow a specified nonlinear relationship which is described as polarization curves. This kind of boundary conditions are much more difficult to deal with than those

ordinary BCs described in Eq.(E.6) . The treatment of the polarization curve is the most challenging part and makes this program special from the normal Laplace's FEM program.

In this study, a very thin interfacial layer is introduced between concrete and steel bar to simulate polarization curve, as shown in Figure F-1. The interfacial layer acts as the carrier of the polarization resistances.

This thin interface layer is also discrete into eight-node hexahedral elements. Polarization resistance could be calculated with the tangent or secant line of the polarization curve according to corresponding corrosion current density level:

$$\frac{1}{k_{in}}=\begin{cases}\left|\frac{dE}{di}\right|\Big/t & i=i_0\\ \left|\frac{E-E_0}{i}\right|\Big/t & i>i_0\end{cases} \tag{F.3}$$

In which

$1/k_{in}$ - the equivalent resistance of the interface layer, which represents the anodic or cathodic polarization resistance;

i - the corrosion current density $[A/m^2]$;

E - the corresponding potential on the polarization curve $[mV]$;

E_0 - the free corrosion potential $[mV]$ of either anode or cathode;

i_0 - either the anodic or cathodic exchange current density; and

t - the thickness of the interface layer.

The nonlinear relationship between the potential and current density, i.e. the polarization curves, is described by:

$$E=f(i) \tag{F.4}$$

Please note that there are two interfacial layers in one corrosion system which belong to anode and cathode respectively.

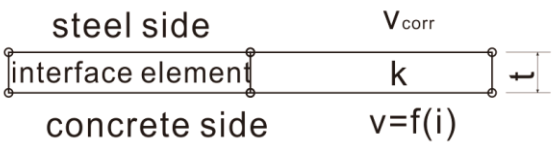

Figure F-1: Illustration of interface element

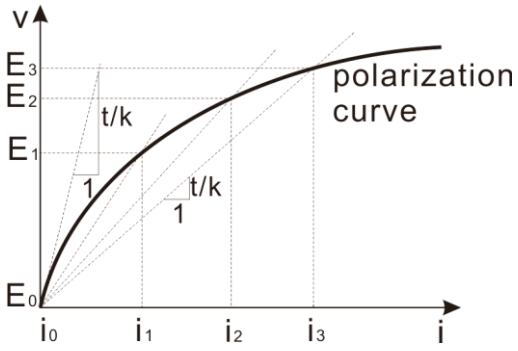

Figure F-2: Determination of polarization resistance, take anode as an example

As the polarization curve is nonlinear and the polarization resistance $\frac{t}{k_{in}}$ is dependent on the corrosion current density, the global equation system is consequently also nonlinear. Therefore, iterative method is needed to solve the global equation system. The procedure is described as follow:

1) The solution starts at the equilibrium state. By assuming the current density equal to i_0 at the steel side of the interface layer, the polarization resistance $R_{p,a}^0$ and $R_{p,c}^0$ (i.e. $1/k_{in}$) are considered as the tangent at (i_0,E_0) of anodic and cathodic polarization curves, as shown in Figure F-2.
2) Combing the polarization resistance from 1) and the concrete electrolytic resistance to form the global conductivity matrix $[K]=\sum_{elem}\iiint_{V_e}(\nabla N k \nabla N)dV$ and equation system Eq.(E.16).
3) Apply the free corrosion potential E_0 at the steel-bar-side nodes of the interfacial layer, and use wave front method to solve the equation system to obtain electrical potential $\{\Phi\}$ at all nodes.
4) Use Eq.(E.3) to calculate the electrical current density $\vec{\imath}$ and $i=\sqrt{i_x^2+i_y^2+i_z^2}$ at the integral points of interface element.
5) Use Eq.(F.3) to find the polarization resistance $1/k_{in}$ on the polarization curves corresponding to the corrosion current density i obtained from 4).
6) Use the newly obtained polarization resistance to repeat step 2) to 5) until the difference between current density of current step and previous step is smaller than the required tolerance 0.1%.

Data output

The final part of MCRC is to output calculated results for post process. Besides the nodal electrical potential, the nodal current and nodal current density vector are also calculated and output. Substituting the solved $\{\Phi\}$ into Eq.(E.16), nodal current density $\{I\}$ could be obtained. Use Eq.(E.11) and Eq.(E.3) to calculate the electrical current density i at the integral points of all concrete elements with which the electrical current vector and stream traces in the concrete could be plotted with the commercial software Tecplot 360. The sum of the items, whose corresponding nodes are on the steel-side of the anodic interface layer, is the corrosion current.

(Blank page)

Appendix G Polarization Curves of Individual Anode and Cathodes

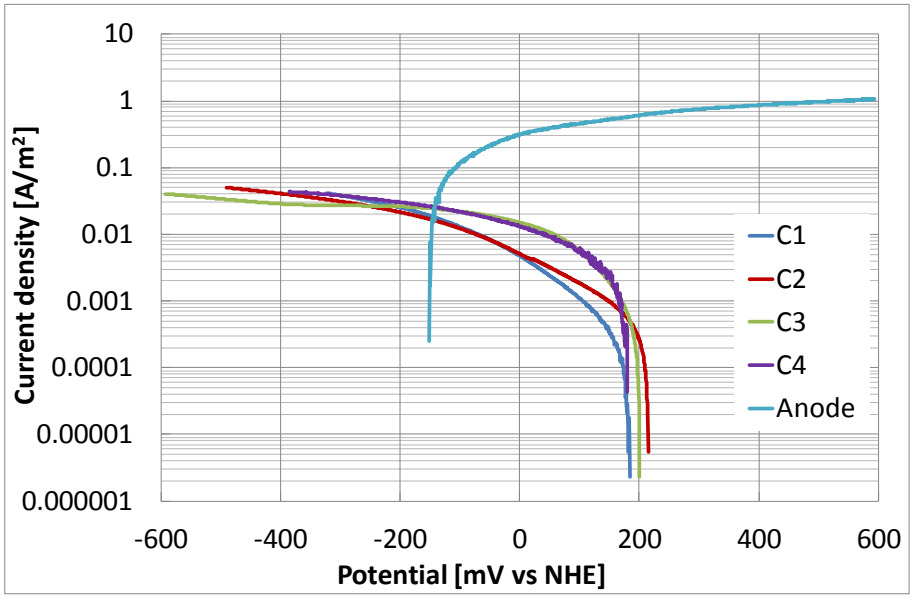

Figure G-1: I05360, cover=2 cm, 3 years exposure duration

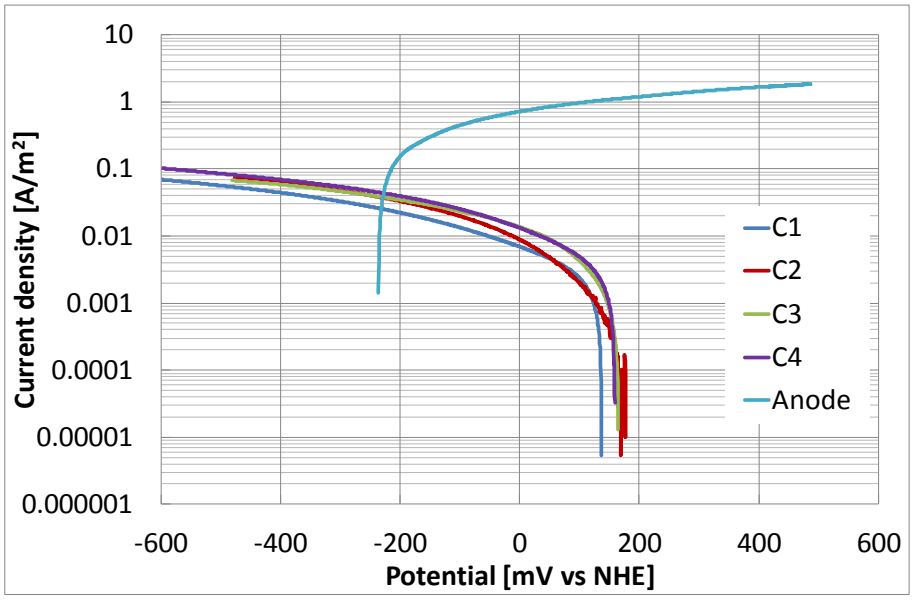

Figure G-2: I05360, cover=3.5 cm, 3 years exposure duration

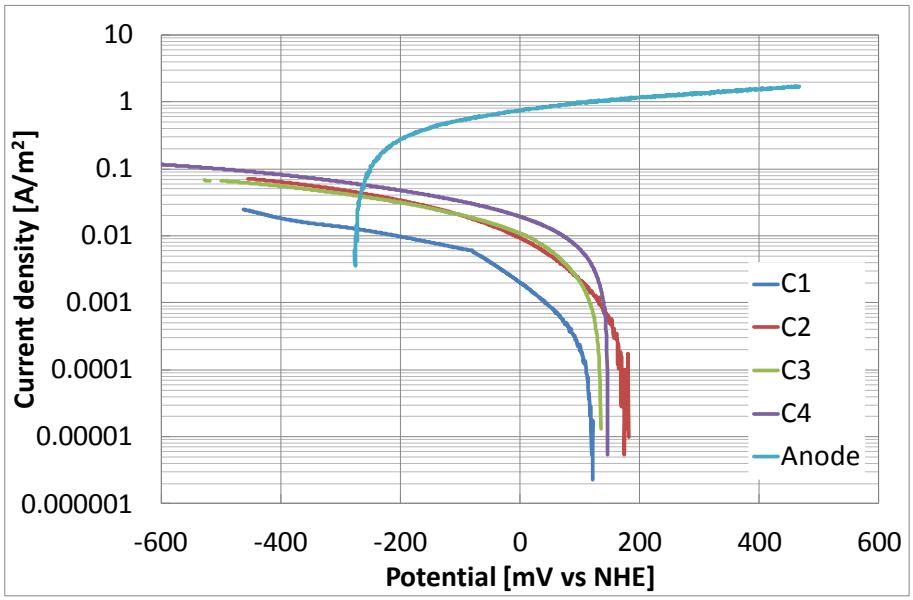

Figure G-3: I05360, cover=5 cm, 3 years exposure duration

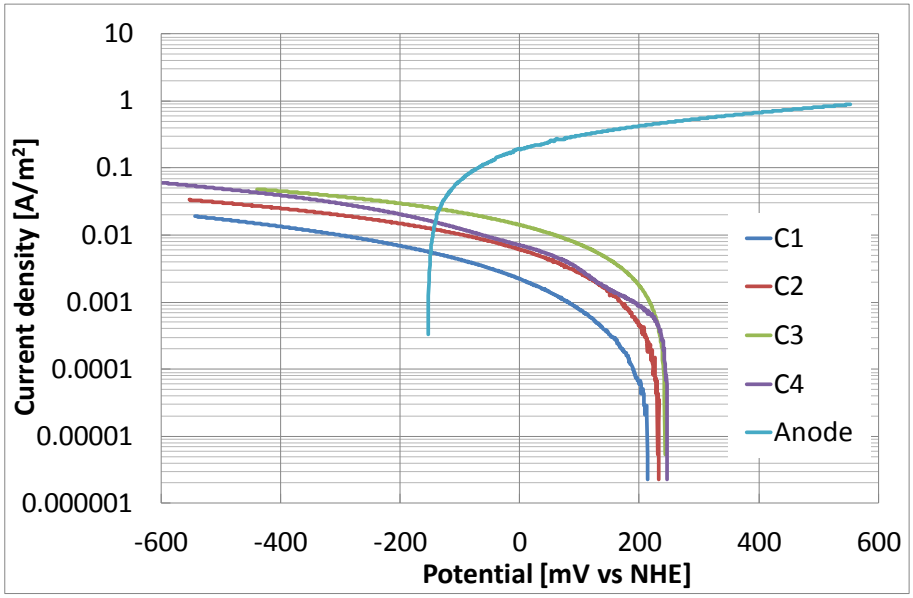

Figure G-4: III05360, cover=5 cm, 3 years exposure duration

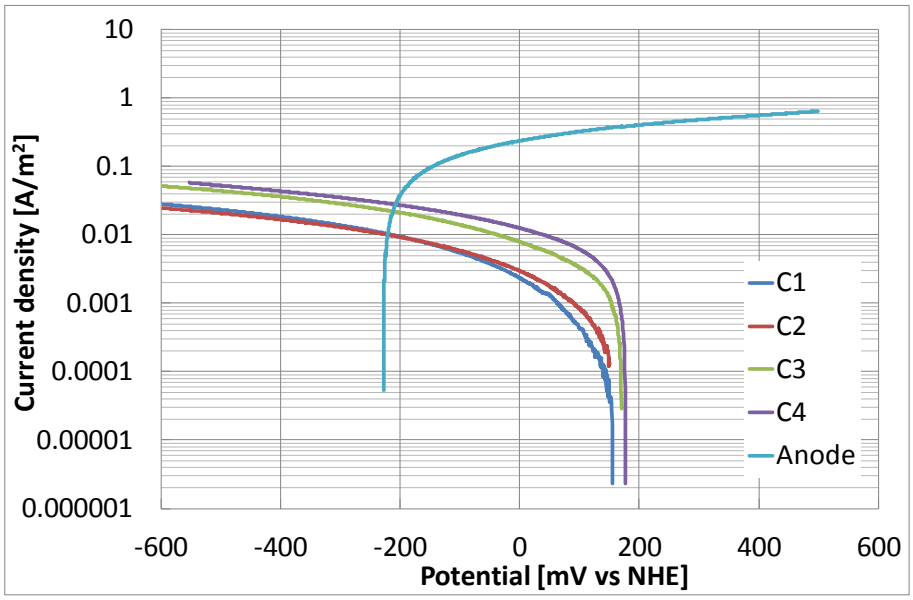

Figure G-5: III05360, cover=5 cm, 3 years exposure duration

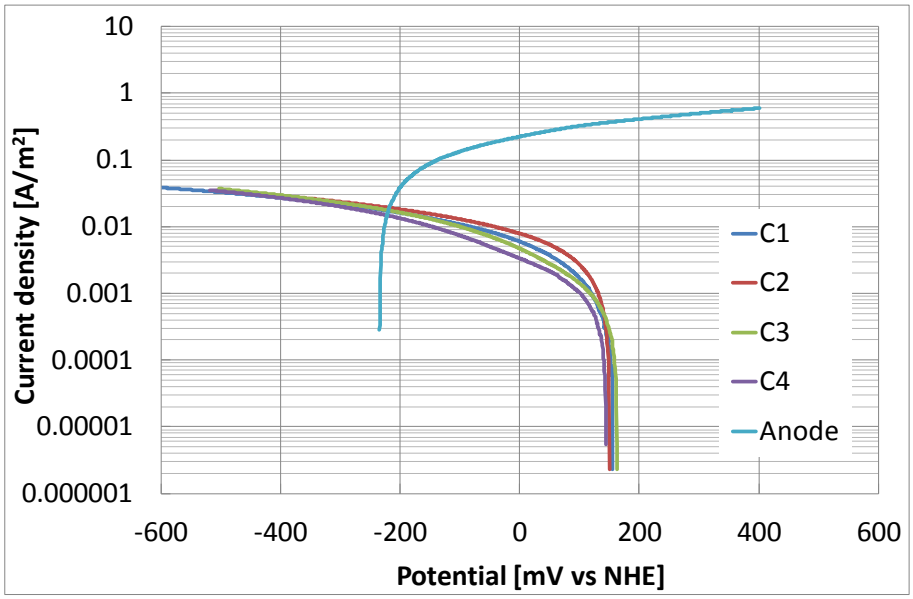

Figure G-6: III05360, cover=5 cm, 3 years exposure duration

(Blank page)

References

[1] C. Alonso, Andrade, C. and González, J. A., *Relation between resistivity and corrosion rate of reinforcements in carbonated mortar made with several cement types.* Cement and Concrete Research, 1988. **18**(5): p. 687-698.

[2] C. Andrade and González, J. A., *Quantitative measurements of corrosion rate of reinforcing steels embedded in concrete using polarization resistance measurements.* Materials and Corrosion, 1978. **29**(8): p. 515-519.

[3] C. Arya and Ofori-Darko, F. K., *Influence of crack frequency on reinforcement corrosion in concrete.* Cement and Concrete Research, 1996. **26**(3): p. 345-353.

[4] John P. Broomfield, *Corrosion of steel in concrete : understanding, investigation and repair*. 1997, London: Spon. 240 p.

[5] N. Carino, *Nondestructive Techniques to Investigate Corrosion Status in Concrete Structures.* Journal of Performance of Constructed Facilities, 1999. **13**(3): p. 96-106.

[6] M. Raupach, *Corrosion of steel in the area of cracks in concrete – Laboratory tests and calculations using a transmission line model*, in *Corrosion of Reinforcement in Concrete Construction*, C.L. Page, P. Bamforth, and J.W. Figg, Editors. 1996. p. 13-23.

[7] M. Raupach, *Chloride-induced macro-cell corrosion of steel in concrete—theoretical background and practical consequences.* Construction and Building Materials, 1996. **10**(5): p. 329-338.

[8] P. Schießl and Raupach, M., *Chloride induced corrosion of steel in concrete — investigations with a concrete corrosion cell*, in *The Life of Structures: The Role of Physical Testing, International Seminar*. 1989: Brighton, UK.

[9] K. Tuutti, *Corrosion of steel in concrete*. 1982: Swedish Cement and Concrete Research Institute.

[10] B Borgard, WARREN, C, Somayaji, S and Heidersbach, R, *CORRELATION BETWEEN CORROSION OF REINFORCING STEEL AND VOIDS AND CRACKS IN CONCRETE STRUCTURES.* Transportation Research Record, 1989. **1211**: p. 1-11.

[11] K Suzuki, Ohno, Y, Praparntanatorn, S and Tamura, H, *MECHANISM OF STEEL CORROSION IN CRACKED CONCRETE*, in *THE THIRD INTERNATIONAL SYMPOSIUM ON "CORROSION OF REINFORCEMENT IN CONCRETE CONSTRUCTION"*. 1990, CICC Publications: BELFRY HOTEL, WISHAW, WARWICKSHIRE. p. 19-28.

[12] E. Vesikari, Service life of concrete structures with regards to corrosion of reinforcement, VTT research report 553, 1988

[13] K. Osterminski, Schießl, P., Volkwein, A. and Mayer, T. F., *Modelling reinforcement corrosion – usability of a factorial approach for modelling resistivity of concrete.* Materials and Corrosion, 2006. **57**(12): p. 926-931.

[14] C. Arya and Vassie, P. R. W., *Influence of cathode-to-anode area ratio and separation distance on galvanic corrosion currents of steel in concrete containing chlorides.* Cement and Concrete Research, 1995. **25**(5): p. 989-998.

[15] A. A. Sagüés and Kranc, S. C., *Computer modeling of effect of corrosion macro-cells on measurement of corrosion rate of reinforcing steel in concrete.* ASTM Special Technical Publication, 1996. **1276**: p. 58-73.

[16] P. Schießl and Raupach, M., *Laboratory studies and calculations on the influence of crack width on chloride-induced corrosion of steel in concrete.* ACI Materials Journal, 1997. **94**(1): p. 56-62.

[17] M. Raupach, *Models for the propagation phase of reinforcement corrosion - an overview.* Materials and Corrosion-Werkstoffe Und Korrosion, 2006. **57**(8): p. 605-613.

[18] M. RAUPACH and DAUBERSCHMIDT, C., *Modelling of chloride-induced corrosion of reinforcement in cracked high-performance concrete based on laboratory investigations*, in *Corrosion of reinforcement in concrete: Monitoring, prevention and rehabilitation techniques*, M. Raupach, et al., Editors. 2006, Woodhead.

[19] P. Schießl and Osterminski, K., *DFG-research-group: Modelling reinforcement corrosion – overview of the project.* Materials and Corrosion, 2006. **57**(12): p. 911-913.

[20] J. Gulikers, *Theoretical considerations on the supposed linear relationship between concrete resistivity and corrosion rate of steel reinforcement.* Materials and Corrosion, 2005. **56**(6): p. 393-403.

[21] W. Elkey and Sellevold, E.J, Electrical resistivity of concrete, No.80, 1995

[22] D.A Whiting and Nagi, M.A., Electrical Resistivity of Concrete – A Literature Review, R&D Serial No.2457, 2003

[23] H. T. Cao and Sirivivatnanon, V., *Corrosion of steel in concrete with and without silica fume.* Cement and Concrete Research, 1991. **21**(2–3): p. 316-324.

[24] Syed Ehtesham Hussain and Rasheeduzzafar, *Corrosion Resistance Performance of Fly Ash Blended Cement Concrete.* ACI Materials Journal, 1994. **91**(3): p. 264-272.

[25] A.M. Neville, *Properties of concrete*. 1996: John Wiley & Sons.

[26] B. P. Hughes, Soleit, A. K. O. and Brierley, R. W., *NEW TECHNIQUE FOR DETERMINING THE ELECTRICAL-RESISTIVITY OF CONCRETE.* Magazine of Concrete Research, 1985. **37**(133): p. 243-248.

[27] I. L. H. Hansson and Hansson, C. M., *Electrical resistivity measurements of Portland cement based materials.* Cement and Concrete Research, 1983. **13**(5): p. 675-683.

[28] S. G. Millard, *Effects of temperature and moisture upon concrete permeability and resistivity measurements*, in *Workshop on Insitu Measurement of Concrete Permeablity*. 1989: University of Lounghborough.

[29] Odd E. Gjorv, Vennesland, Oystein and El-Busaidy, A. H. S., *ELECTRICAL RESISTIVITY OF CONCRETE IN THE OCEANS.* Proceedings of the Annual Offshore Technology Conference, 1977. **1**: p. 581-588.

[30] C.L. Page and Cunningham, P.J., *Electro-Chemical Methods of Corrosion Monitoring for Marine Concrete Structures*. 1988: Stationery Office.

[31] P. Schießl, Corrosion of steel in concrete : report of the Technical Committee 60 CSC, RILEM, 1988

[32] C. L. Page, *Corrosion mechanisms*, in *Proc. 1st Int. Conf. Deterioration and repair of reinforced concrete in the Arabian Gulf*. 1985, Bahrain Society of Engineers/Construction Industry Research and Information Association: London. p. 413-425.

[33] P. Gjörv, *Steel Corrosion in Marine Environment – an overview*, in *Proceedings Gerwick Symposium on Durability of Concrete in Marine Environment*, P.K. Mehta, Editor. 1989: Berkeley, California. p. 77-89.

[34] P. Schießl and Gehlen, Ch., DuraCrete, Document BE95-1347/R4-5, 1998

[35] Seung Yup Jang, Kim, Bo Sung and Oh, Byung Hwan, *Effect of crack width on chloride diffusion coefficients of concrete by steady-state migration tests.* Cement and Concrete Research, 2011. **41**(1): p. 9-19.

[36] J. Bisschop and van Mier, J. G. M., *How to study drying shrinkage microcracking in cement-based materials using optical and scanning electron microscopy?* Cement and Concrete Research, 2002. **32**(2): p. 279-287.

[37] T. Shiotani, Bisschop, J. and Van Mier, J. G. M., *Temporal and spatial development of drying shrinkage cracking in cement-based materials.* Engineering Fracture Mechanics, 2003. **70**(12): p. 1509-1525.

[38] F. O. Slate and Hover, K. C., *Microcracking in concrete*, in *Fracture mechanics of concrete: Material characterization and testing*, A. Carpinteri and A.R. Ingraffea, Editors. 1984, Springer Netherlands. p. 137-159.

[39] S. J. Jaffer and Hansson, C. M., *The influence of cracks on chloride-induced corrosion of steel in ordinary Portland cement and high performance concretes subjected to different loading conditions.* Corrosion Science, 2008. **50**(12): p. 3343-3355.

[40] M. Prezzi, Monteiro, P. J. M. and Sposito, G., *The alkali-silica reaction, part I: Use of the double-layer theory to explain the behavior of reaction-product gels.* ACI Materials Journal, 1997. **94**(1): p. 10-17.

[41] Benoit Fournier and Bérubé, Marc-André, *Alkali-aggregate reaction in concrete: a review of basic concepts and engineering implications.* Canadian Journal of Civil Engineering, 2000. **27**(2): p. 167-191.

[42] E G Swenson and Gillott, J E, ALKALI-CARBONATE ROCK REACTION, No45, 1964

[43] R. E. Beddoe and Setzer, M. J., *A low-temperature DSC investigation of hardened cement paste subjected to chloride action.* Cement and Concrete Research, 1988. **18**(2): p. 249-256.

[44] Mette R. Geiker and Laugesen, Peter, *On the effect of laboratory conditioning and freeze/thaw exposure on moisture profiles in HPC.* Cement and Concrete Research, 2001. **31**(12): p. 1831-1836.

[45] Stefan Jacobsen, Marchand, Jacques and Hornain, Hugues, *Sem observations of the microstructure of frost deteriorated and self-healed concretes.* Cement and Concrete Research, 1995. **25**(8): p. 1781-1790.

[46] Zongjin Li and Shah, Surendra P., *Localization of microcracking in concrete under uniaxial tension.* ACI Materials Journal, 1994. **91**(4): p. 372-381.

[47] N. K. Raju, *Microcracking in concrete under repeated compressive loads.* Building Science, 1970. **5**(1): p. 51-56.

[48] K. M. Nemati, Monteiro, P. J. M. and Scrivener, K. L., *Analysis of compressive stress-induced cracks in concrete.* ACI Materials Journal, 1998. **95**(5): p. 617-630.

[49] Kapilesh Bhargava, Ghosh, A. K., Mori, Yasuhiro and Ramanujam, S., *Modeling of time to corrosion-induced cover cracking in reinforced concrete structures.* Cement and Concrete Research, 2005. **35**(11): p. 2203-2218.

[50] A. W. Beeby, *The Prediction of Crack Widths in Hardened Concrete.* The Structural Engineer, 1979. **57**(1): p. 9-17.

[51] ACI Committee, 224.1R-07 Causes, Evaluation, and Repair of Cracks in Concrete Structures, 2007

[52] British Standards Institute, BS 8110 - Structural use of concrete, 1985

[53] Canadian Standards Association, Staff, Canadian Standards Association, Canada, Standards Council of and Staff, Standards Council of Canada, *Canadian Highway Bridge Design Code*. 2006: Canadian Standards Association.

[54] R. Francois and Maso, J. C., *EFFECT OF DAMAGE IN REINFORCED-CONCRETE ON CARBONATION OR CHLORIDE PENETRATION.* Cement and Concrete Research, 1988. **18**(6): p. 961-970.

[55] A. Bentur, Berke, N. and Diamond, S., *Steel Corrosion in Concrete: Fundamentals and civil engineering practice*. 1997: Taylor & Francis.

[56] A. W. Beeby, *CORROSION OF REINFORCING STEEL IN CONCRETE AND ITS RELATION TO CRACKING.* Structural Engineer-Part A, 1978. **56**(3): p. 77-81.

[57] C. Arya, Sa'id-Shawqi, Q. and Vassie, P. R. W., *Factors influencing electrochemical removal of chloride from concrete.* Cement and Concrete Research, 1996. **26**(6): p. 851-860.

[58] A.J. Bard and Faulkner, L.R., *Electrochemical Methods: Fundamentals and Applications*. 2001: Wiley.

[59] Mingdong Bi, *Corrosion of reinforcing steel in cracked concrete*. 2008, City University of New York: United States -- New York. p. 197.

[60] N.S. Berke, Dallaire, M.P., Hicks, M.C. and Hoopes, R.J., *Corrosion of Steel in Cracked Concrete.* NACE International corrosion, 1993. **49**(11): p. 934-943.

[61] Bhaskar Sangoju, Gettu, Ravindra, Bharatkumar, B. H. and Neelamegam, M., *Chloride-induced corrosion of steel in cracked OPC and PPC concretes: experimental study.(ordinary portland cement, portland pozzolana cement).* Journal of materials in civil engineering, 2011. **23**(7): p. 1057.

[62] C. Gehlen and Pabsch, G, Updating through measurement and incorporation of sensitive variables, 2003

[63] Kolluru V. Subramaniam and Bi, Mingdong, *Investigation of steel corrosion in cracked concrete: Evaluation of macro-cell and micro-cell rates using Tafel polarization response.* Corrosion Science, 2010. **52**(8): p. 2725-2735.

[64] P. Schießl, *Zur Frage der zulässigen Rißbreite und der erforderlichen Betondeckung im Stahlbetonbau unter besonderer Berücksichtigung der Karbonatisierung des Betons*. 1976: Ernst.

[65] N. Gowripalan, Sirivivatnanon, V. and Lim, C. C., *Chloride diffusivity of concrete cracked in flexure.* Cement and Concrete Research, 2000. **30**(5): p. 725-730.

[66] Ema Kato, Kato, Yoshitaka and Uomoto, Taketo, *Development of simulation model of chloride ion transportation in cracked concrete.* Journal of Advanced Concrete Technology, 2005. **3**(1): p. 85-94.

[67] T. U. Mohammed, Otsuki, N. and Hamada, H., *Oxygen permeability in cracked concrete reinforced with plain and deformed bars.* Cement and Concrete Research, 2001. **31**(5): p. 829-834.

[68] Vincent Picandet, Khelidj, Abdelhafid and Bellegou, Herve, *Crack effects on gas and water permeability of concretes.* Cement and Concrete Research, 2009. **39**(6): p. 537-547.

[69] Kejin Wang, Jansen, Daniel C., Shah, Surendra P. and Karr, Alan F., *Permeability study of cracked concrete.* Cement and Concrete Research, 1997. **27**(3): p. 381-393.

[70] Pa Pa Win, Watanabe, Makiko and Machida, Atsuhiko, *Penetration profile of chloride ion in cracked reinforced concrete.* Cement and Concrete Research, 2004. **34**(7): p. 1073-1079.

[71] T. Lorentz and French, F., *CORROSION OF REINFORCING STEEL IN CONCRETE - EFFECTS OF MATERIALS, MIX COMPOSITION, AND CRACKING.* Aci Materials Journal, 1995. **92**(2): p. 181-190.

[72] R. François and Arliguie, G., *Influence of Service Cracking on Reinforcement Steel Corrosion.* Journal of Materials in Civil Engineering, 1998. **10**(1): p. 14-20.

[73] R. François and Arliguie, G., *Effect of microcracking and cracking on the development of corrosion in reinforced concrete members.* Magazine of Concrete Research, 1999. **51**(2): p. 143-150.

[74] S. Yoon, Wang, K. J., Weiss, W. J. and Shah, S. P., *Interaction between loading, corrosion, and serviceability of reinforced concrete.* Aci Materials Journal, 2000. **97**(6): p. 637-644.

[75] T. Mohammed, Otsuki, N., Hisada, M. and Shibata, T., *Effect of Crack Width and Bar Types on Corrosionof Steel in Concrete.* Journal of Materials in Civil Engineering, 2001. **13**(3): p. 194-201.

[76] C. M. Aldea, Shah, S. P. and Karr, A., *Permeability of cracked concrete.* Materials and Structures, 1999. **32**(5): p. 370-376.

[77] C. Aldea, Shah, S. and Karr, A., *Effect of Cracking on Water and Chloride Permeability of Concrete.* Journal of Materials in Civil Engineering, 1999. **11**(3): p. 181-187.

[78] B. Gérard, Breysse, D., Ammouche, A., Houdusse, O. and Didry, O., *Cracking and permeability of concrete under tension.* Materials and Structures, 1996. **29**(3): p. 141-151.

[79] B. Gerard and Marchand, J., *Influence of cracking on the diffusion properties of cement-based materials - Part I: Influence of continuous cracks on the steady-state regime.* Cement and Concrete Research, 2000. **30**(1): p. 37-43.

[80] Stefan Jacobsen, Marchand, Jacques and Boisvert, Luc, *Effect of cracking and healing on chloride transport in OPC concrete.* Cement and Concrete Research, 1996. **26**(6): p. 869-881.

[81] R. Gagné, François, R. and Masse, P., *Chloride penetration testing of cracked mortar samples*, in *Concrete under severe conditions*, N. Banthia, K. Sakai, and O.E. Gjory, Editors. 2001: University of British Columbia, Vancouver p. 198-205.

[82] P. Kumar Mehta and Gerwick Jr, Ben C., *CRACKING-CORROSION INTERACTION IN CONCRETE EXPOSED TO MARINE ENVIRONMENT.* Concrete International, 1982. **4**(10): p. 45-51.

[83] A. Djerbi, Bonnet, S., Khelidj, A. and Baroghel-bouny, V., *Influence of traversing crack on chloride diffusion into concrete.* Cement and Concrete Research, 2008. **38**(6): p. 877-883.

[84] A. Castel, Francy, 0., Francois, R. and Arliguie, G., *Chloride Diffusion in Reinforced Concrete Beam Under Sustained loading.* ACI Special Publication: Fifth CANMET/ACI Conference on Recent Advances in Concrete Technology-Proceeding, Fifth International Conference, 2001. **200**.

[85] C.M. Aldea, Rapoport, J., Shah, S.P. and Karr, A., *Combined Effect of Cracking and Water Permeability of Fiber Reinforced Concrete*, in *Proceedings of the Third International Conference on Concrete Under Severe Conditions, CONSEC'01*, N. Banthia, K. Sakai, and O.E. Gjorv, Editors. 2001. p. 198-205.

[86] M. Ismail, Toumi, A., François, R. and Gagné, R., *Effect of crack opening on the local diffusion of chloride in cracked mortar samples.* Cement and Concrete Research, 2008. **38**(8–9): p. 1106-1111.

[87] I. S. Yoon and Schlange, E., *Long / short term experimental study on chloride penetration in cracked concrete*. 2010. p. 765-768.

[88] Nataliya Hearn, *Self-sealing, autogenous healing and continued hydration: What is the difference?* Materials and Structures, 1998. **31**(8): p. 563-567.

[89] Peter Schieβl and Raupach, Michael, *Influence of temperature on the corrosion rate of steel in concrete containing chlorides*, in *First international conference on reinforced concrete materials in hot climates*. 1994, United Arab Emirates University: Alain, U.A.E.

[90] Tarek Uddin Mohammed, Otsuki, Nobuaki and Hamada, Hidenori, *Corrosion of Steel Bars in Cracked Concrete under Marine Environment.* Journal of materials in civil engineering, 2003. **15**(5): p. 460-469.

[91] T. D. Marcotte and Hansson, C. M., *The influence of silica fume on the corrosion resistance of steel in high performance concrete exposed to simulated sea water.* Journal of Materials Science, 2003. **38**(23): p. 4765-4776.

[92] M. Ismail, Toumi, A., François, R. and Gagné, R., *Effect of crack opening on the local diffusion of chloride in inert materials.* Cement and Concrete Research, 2004. **34**(4): p. 711-716.

[93] K. Audenaert, Marsavina, L. and De Schutter, G., *Influence of cracks on the service life of concrete structures in a marine environment*. 2009. p. 153-160.

[94] B. Savija, Pacheco Farias, J. and Schlangen, H.E.J.G., *Lattice based simulation of chloride ingress in uncracked and cracked concrete: Model validation*, in *FraMCos-8: Proceedings of the 8th International Conference on Fracture Mechanics of Concrete and Concrete Structures*. 2013: Toledo, Spain.

[95] Alireza Akhavan, Shafaatian, Seyed-Mohammad-Hadi and Rajabipour, Farshad, *Quantifying the effects of crack width, tortuosity, and roughness on water permeability of cracked mortars.* Cement and Concrete Research, 2012. **42**(2): p. 313-320.

[96] Andre Küter, Geiker, Mette Rica, Olesen, John Forbes, Stang, Henrik, Dauberschmidt, Christoph and Raupach, Michael, *Chloride Ingress in Concrete Cracks under Cyclic Loading*, in *3rd International Conference on Construction Materials*. 2005, University of British Columbia: Vancouver, Canada.

[97] L. Tang, *Electrically accelerated methods for determining chloride diffusivity in concrete - Current development.* Magazine of Concrete Research, 1996. **48**(176): p. 173-179.

[98] B. Martín-Pérez, Pantazopoulou, S. J. and Thomas, M. D. A., *Numerical solution of mass transport equations in concrete structures.* Computers & Structures, 2001. **79**(13): p. 1251-1264.

[99] Yu Wang, Li, Long-yuan and Page, C. L., *Modelling of chloride ingress into concrete from a saline environment.* Building and Environment, 2005. **40**(12): p. 1573-1582.

[100] Y. Xi, *A model for moisture capacities of composite materials Part I: formulation.* Computational Materials Science, 1995. **4**(1): p. 65-77.

[101] Y. Xi, *A model for moisture capacities of composite materials Part II: application to concrete.* Computational Materials Science, 1995. **4**(1): p. 78-92.

[102] Yunping Xi, Bažant, Zdenňek P., Molina, Larissa and Jennings, Hamlin M., *Moisture diffusion in cementitious materials Moisture capacity and diffusivity.* Advanced Cement Based Materials, 1994. **1**(6): p. 258-266.

[103] Yunping Xi, Bažant, Zdeněk P. and Jennings, Hamlin M., *Moisture diffusion in cementitious materials Adsorption isotherms.* Advanced Cement Based Materials, 1994. **1**(6): p. 248-257.

[104] L. Marsavina, Audenaert, K., De Schutter, G., Faur, N. and Marsavina, D., *Experimental and numerical determination of the chloride penetration in cracked concrete.* Construction and Building Materials, 2009. **23**(1): p. 264-274.

[105] ACI Committee, 222R-01: Protection of Metals in Concrete Against Corrosion, 2010

[106] T. Vidal, Castel, A. and François, R., *Analyzing crack width to predict corrosion in reinforced concrete.* Cement and Concrete Research, 2004. **34**(1): p. 165-174.

[107] ACI Committee, 224R-01, Control of cracking in concrete structures, American Concrete Institute, 2001

[108] N. Otsuki, Miyazato, S. I., Diola, N. B. and Suzuki, H., *Influences of bending crack and water-cement ratio on chloride-induced corrosion of main reinforcing bars and stirrups.* ACI Structural Journal, 2000. **97**(4): p. 454-464.

[109] A.C. Burdall and Sharp, J.V, *Some aspects of revisions to the U.K. guidance not for offshore concrete structures*, in *Proceedings, International Conference on Concrete in the Marine Environment*. 1986, The Concrete Society: London. p. 37-48.

[110] Kiyoshi Okada, Koyanagi, Wataru and Miyagawa, Toyoaki, *CHLORIDE CORROSION OF REINFORCING STEEL IN CRACKED CONCRETE.* Proceedings of the Japan Society of Civil Engineers, 1979. **1979**(281): p. 75-87.

[111] A. Raharinaivo, Brevet, P., Grimaldi, G. and Pannier, G., *RELATIONSHIPS BETWEEN CONCRETE DETERIORATION AND REINFORCING-STEEL CORROSION.* Durability of Building Materials, 1986. **4**(2): p. 97-112.

[112] A. W. Beeby, *Cracking, Cover, and Corrostion of Reinforcement.* Concrete International, 1983. **5**(2): p. 35-40.

[113] L. Bertolini, Elsener, B., Pedeferri, P., Redaelli, E. and Polder, R.B., *Corrosion of Steel in Concrete: Prevention, Diagnosis, Repair*. 2013: Wiley.

[114] K. Pettersson, *Criteria for cracks in connection with corrosion in high-strength concrete*, in *Fourth International Symposium on Utilisation of High Strength/High Performance Concrete*. 1996: Paris. p. 509-517.

[115] S. Jacobsen, Marchand, J. and Gerard, B., *Concrete cracks. I. Durability and self - healing—a review*, in *Proceedings of the Second International Conference on*

Concrete Under Severe Conditions, Environment and Loading, O.E. Gjorv, K. Sakai, and N. Banthia, Editors. 1998: Tromso, Norway. p. 217-231.

[116] James T. Houston, Ergin Atimtay and Ferguson, P.M., Corrosion of Reinforcing Steel Embedded in Structural Concrete, Research Report No. 112-1-F, 1972

[117] C. E. Bird and Callaghan, B. G., *Corrosion of Reinforcing Steel and Other Metals in Concrete, and the Possible Effects of Galvanic and Stray Currents*, in *Conference on Concrete in Aggressive Environments*. 1977: Pretoria.

[118] G. Hartl and Lukas, W., *Untersuchung zur Chlorideindringung in Beton und zum Einfluß von Rissen auf die chloridinduzierte Korrosion der Bewehrung.* BFT Betonwerk Fertigteil-Technik, Concrete Plant Precast Technology 1987. **53**(7): p. 497-506.

[119] R. Weiermair, Hansson, C.M., Seabrook, P.T. and Tullmin, M., *Corrosion Measurements on Steel Embedded in High Performance Concrete Exposed to a Marine Environment*, in *Third CANMET/ACI International Conference on Performance of Concrete in Marine Environment*, V.M. Malhotra, Editor. 1996, American Concrete Institute: St. Andrews by the Sea, New Brunswick, Canada.

[120] C.M. Hansson and Okulaja, S.A, *Corrosion of Reinforcing Steel in Cracked High Performance Concrete*, in *Advances in Cement and Concrete*, D.A. Lange, K.L. Scrivener, and J. Marchand, Editors. 2003, University of Illinois at Urbana-Champaign: Copper Mountain, Colorado, USA.

[121] S. C. Kranc and Sagüés, Alberto A., *Detailed modeling of corrosion macro-cells on steel reinforcing in concrete.* Corrosion Science, 2001. **43**(7): p. 1355-1372.

[122] M. D. Koretsky, Abooameri, F. and Westall, J. C., *Effect of Concrete Pore Saturation on Cathodic Protection of Steel-Reinforced Concrete Bridges.* Corrosion, 1999. **55**(1): p. 52-64.

[123] Erik B. Muehlenkamp, *Electrochemical modeling of cathodic protection systems applied to reinforced concrete structures*, in *Chemical Engineering*. 2006, Oregon State University.

[124] S. C. Kranc and Sagüés, A. A., *Computation of Reinforcing Steel Corrosion Distribution in Concrete Marine Bridge Substructures.* Corrosion, 1994. **50**(1): p. 50-61.

[125] G. Beer, Smith, Ian and Duenser, Christian, *The boundary element method with programming : for engineers and scientists*. 2008, Wien, Austria: Springer. xiv, 494 p.

[126] K. Amaya and Aoki, S., *Effective boundary element methods in corrosion analysis.* Engineering Analysis with Boundary Elements, 2003. **27**(5): p. 507-519.

[127] N. G. Zamani and Chuang, J. M., *Optimal control of current in a cathodic protection system: A numerical investigation.* Optimal Control Applications and Methods, 1987. **8**(4): p. 339-350.

[128] Martin Brem, *Numerische Modellierung der Korrosion in Stahlbetonbauten*. 2004, ETH Zurich.

[129] J. Warkus, Brem, M. and Raupach, M., *BEM-models for the propagation period of chloride induced reinforcement corrosion.* Materials and Corrosion, 2006. **57**(8): p. 636-641.

[130] J. Warkus and Raupach, M., *Modelling of reinforcement corrosion - geometrical effects on macro-cell corrosion.* Materials and Corrosion-Werkstoffe Und Korrosion, 2010. **61**(6): p. 494-504.

[131] Je-Woon Kyung, Tae, Sung-Ho and Lee, Han-Seung, *Potential and current flow of double steel bars in concrete by 2-D BEM.* Isij International, 2007. **47**(10): p. 1497-1503.

[132] O. Abootalebi, Kermanpur, A., Shishesaz, M. R. and Golozar, M. A., *Optimizing the electrode position in sacrificial anode cathodic protection systems using boundary element method.* Corrosion Science, 2010. **52**(3): p. 678-687.

[133] A. M. Hassanein, Glass, G. K. and Buenfeld, N. R., *Protection current distribution in reinforced concrete cathodic protection systems.* Cement and Concrete Composites, 2002. **24**(1): p. 159-167.

[134] E. Redaelli, Bertolini, L., Peelen, W. and Polder, R., *FEM-models for the propagation period of chloride induced reinforcement corrosion.* Materials and Corrosion-Werkstoffe Und Korrosion, 2006. **57**(8): p. 628-635.

[135] M. H. Zhang and Canmet, *Microstructure, crack propagation, and mechanical properties of cement pastes containing high volumes of fly ashes.* Cement and Concrete Research, 1995. **25**(6): p. 1165-1178.

[136] Y. Yuan and Wan, Z. L., *Prediction of cracking within early-age concrete due to thermal, drying and creep behavior.* Cement and Concrete Research, 2002. **32**(7): p. 1053-1059.

[137] Peter Schieβl and Raupach, Michael, *Laboratory Studies and Calculations on the Influence of Crack Width on Chloride-Induced Corrosion of Steel in Concrete.* ACI Materials Journal, 1997. **94**(1): p. 56-61.

[138] P. Schieβl and Raupach, M., *Macro-cell steel corrosion in concrete caused by chlorides*, in *Second CANMET/ACI Internatioanl Conference on Durability of Concrete*, V.M. Malhotra, Editor. 1991: Canmet, Montreal. p. 565–583.

[139] P. Schieβl and Raupach, M., *Influence on of the type of cement on the corrosion behaviour of steel in concrete*, in *9th International Congress on the Chemistry of Cement*. 1992: New Delhi. p. 296.

[140] V. K. Gouda and Halaka, W. Y., *Corrosion and Corrosion Inhibition of Reinforcing Steel: II. Embedded In Concrete.* British Corrosion Journal, 1970. **5**(5): p. 204-208.

[141] P Schieβl and Breit, W., *Local repair measures at concrete structures damaged by reinforcement corrosion – aspects of durability*, in *Proceedings of the 4th international symposium on corrosion of reinforcement in concrete construction*, T.R.S.o. Chemistry, Editor. 1996: Cambridge. p. 524-559.

[142] An Cheng, Huang, Ran, Wu, Jiann-Kuo and Chen, Cheng-Hsin, *Influence of GGBS on durability and corrosion behavior of reinforced concrete.* Materials Chemistry and Physics, 2005. **93**(2–3): p. 404-411.

[143] Elke Gruyaert, Van den Heede, Philip and De Belie, Nele, *Carbonation of slag concrete: Effect of the cement replacement level and curing on the carbonation coefficient – Effect of carbonation on the pore structure.* Cement and Concrete Composites, 2013. **35**(1): p. 39-48.

[144] J. A. González, Andrade, C., Alonso, C. and Feliu, S., *Comparison of rates of general corrosion and maximum pitting penetration on concrete embedded steel reinforcement.* Cement and Concrete Research, 1995. **25**(2): p. 257-264.

[145] C. Andrade, Diez, J.M. and Alonso, C., *Modelling of skin effects on diffusion processes in concrete*, in *RILEM International Workshop on Chloride Penetration into Concrete*, L.-O. Nilsson and J.-P. Ollivier, Editors. 1995.

[146] W. Morris, Vico, A. and Vázquez, M., *Chloride induced corrosion of reinforcing steel evaluated by concrete resistivity measurements.* Electrochimica Acta, 2004. **49**(25): p. 4447-4453.

[147] G. K. Glass, Page, C. L. and Short, N. R., *Factors affecting the corrosion rate of steel in carbonated mortars.* Corrosion Science, 1991. **32**(12): p. 1283-1294.

[148] W. López and González, J. A., *Influence of the degree of pore saturation on the resistivity of concrete and the corrosion rate of steel reinforcement.* Cement and Concrete Research, 1993. **23**(2): p. 368-376.

[149] P. S. Mangat and Gurusamy, Kribanandan, *Chloride diffusion in steel fibre reinforced marine concrete.* Cement and Concrete Research, 1987. **17**(3): p. 385-396.

[150] G. K. Glass and Buenfeld, N. R., *The influence of chloride binding on the chloride induced corrosion risk in reinforced concrete.* Corrosion Science, 2000. **42**(2): p. 329-344.

[151] Sang-Soon Park, Kwon, Seung-Jun, Jung, Sang Hwa and Lee, Sang-Woong, *Modeling of water permeability in early aged concrete with cracks based on micro pore structure.* Construction and Building Materials, 2012. **27**(1): p. 597-604.

[152] Hailong Ye, Jin, Nanguo, Jin, Xianyu and Fu, Chuanqing, *Model of chloride penetration into cracked concrete subject to drying–wetting cycles.* Construction and Building Materials, 2012. **36**(0): p. 259-269.

[153] L. Tang and Nilsson, Lars-Olof, *Chloride binding capacity and binding isotherms of OPC pastes and mortars.* Cement and Concrete Research, 1993. **23**(2): p. 247-253.

[154] L. Tang and Nilsson, L.-O. , *A numerical method for prediction of chloride penetration into concrete structures*, in *The Modeling of Microstructure and Its Potential for Studying Transport Properties and Durability* H. Jennings, J. Kropp, and K. Scrivener, Editors. 1996, Kluwer Academic Publishers: The Netherlands. p. 539-552.

[155] L. Tang, *Chloride Transport in Concrete-Measurement and Prediction*, in *Department of Building Materials*. 1996, Chalmers University of Technology.

[156] O.C. Zienkiewicz, Taylor, R.L. and Taylor, R.L., *The Finite Element Method: The Basis*. 2000: Oxford [etc.] : Butterworth Heinemann.

[157] J. Ge and Isgor, O. B., *Effects of Tafel slope, exchange current density and electrode potential on the corrosion of steel in concrete.* Materials and Corrosion-Werkstoffe Und Korrosion, 2007. **58**(8): p. 573-582.

[158] M. Brem, *NUMERISCHE MODELLIERUNG DER KORROSION IN STAHLBETONBAUTEN*. 2004, ETH Zu¨rich.

[159] A. Ababneh, Benboudjema, F. and Xi, Y. P., *Chloride penetration in nonsaturated concrete.* Journal of Materials in Civil Engineering, 2003. **15**(2): p. 183-191.

[160] Y. Xi and Bažant, Z., *Modeling Chloride Penetration in Saturated Concrete.* Journal of Materials in Civil Engineering, 1999. **11**(1): p. 58-65.

[161] Z. P. Bažant and Najjar, L. J., *Nonlinear water diffusion in nonsaturated concrete.* Matériaux et Construction, 1972. **5**(1): p. 3-20.

[162] D. Peaceman and Rachford, Jr., H., *The Numerical Solution of Parabolic and Elliptic Differential Equations.* Journal of the Society for Industrial and Applied Mathematics, 1955. **3**(1): p. 28-41.

[163] Jr. Douglas, J., *On the numerical integration of uxx+ uyy= utt by implicit methods.* Journal of the Society of Industrial and Applied Mathematics, 1955. **3**: p. 42-65.

[164] O. Burkan Isgor and Razaqpur, A. Ghani, *Modelling steel corrosion in concrete structures.* Materials and Structures, 2006. **39**(3): p. 291-302.

[165] E. Divo and Kassab, A.J., *Boundary Element Method for Heat Conduction: With Applications in Non-homogenous Media*. 2003: WIT.

[166] L.C. Wrobel and Brebbia, C.A., *Boundary element methods in heat transfer*. 1992: Computational Mechanics Publications.

[167] J. Gulikers and Raupach, M., *Numerical models for the propagation period of reinforcement corrosion - Comparison of a case study calculated by different researchers.* Materials and Corrosion-Werkstoffe Und Korrosion, 2006. **57**(8): p. 618-627.

[168] I.M. Smith and Griffiths, D.V., *Programming the Finite Element Method*. 2005: Wiley.

[169] B.A. Finlayson, *The Method of Weighted Residuals and Variational Principles: With Applications in Fluid Mechanics, Heat and Mass Transfer*. 1972: Academic Press.

(the end)